Physik-Department

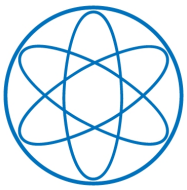

Evaluation and Optimization of a Digital Calorimetric Trigger and Analysis of Pion-Photon-Interactions in π^-Ni $\rightarrow \pi^-\pi^0\pi^0$Ni Reactions at COMPASS at CERN

Dissertation von Markus Christian Krämer

Technische Universität München

TECHNISCHE UNIVERSITÄT MÜNCHEN
Physik-Department E18

Evaluation and Optimization of a Digital Calorimetric Trigger and Analysis of Pion-Photon-Interactions in $\pi^-\mathrm{Ni} \to \pi^-\pi^0\pi^0\mathrm{Ni}$ Reactions at COMPASS at CERN

Markus Christian Krämer

Vollständiger Abdruck der von der Fakultät für Physik der Technischen Universität München zur Erlangung des akademischen Grades eines

Doktor der Naturwissenschaften (Dr. rer. nat.)

genehmigten Dissertation.

Vorsitzender:

apl. Prof. Dr. Norbert Kaiser

Prüfer der Dissertation:

1. Univ.-Prof. Dr. Stephan Paul
2. Univ.-Prof. Shawn Bishop, PhD

Die Dissertation wurde am 01.12.2015 bei der Technischen Universität München eingereicht und durch die Fakultät für Physik am 24.05.2016 angenommen.

Abstract

One important physics topic addressed by the COMPASS collaboration at CERN is the investigation of so-called Primakoff reactions. This class of reactions is studied by impinging high-energetic pions on a nuclear target. Exploiting the equivalence of the electromagnetic field of a relativistic charged particle and a pulse of radiation, the interaction of the pions and the electromagnetic field of the nucleus is described by the exchange of quasi-real photons. This effect is quantitatively described by the Weizsäcker-Williams equivalent-photon approximation.

A short pilot run in 2004 with a lead target revealed important insights, which were taken into account for the Primakoff measurement in 2009. This measurement lasted roughly two weeks and used a nickel target. The measurement focused on final states with neutral particles, which requires a suitable trigger. The requirements have been matched by developing a digital trigger, which is sensitive to the energy deposit in the electromagnetic calorimeter.

An event sample with one negatively charged and two neutral pions in the final state has been selected from the recorded data. This event sample is used to measure the differential cross section of the process $\pi^-\gamma \to \pi^-\pi^0\pi^0$ near the three-pion threshold. In order to do so, the contribution of Primakoff events to the event sample, which is dominated by diffractive dissociation, is determined. The Primakoff production, having a significantly different momentum transfer t' dependence than strong processes, peaks at very small t'. On the one hand, this is exploited to determine the contribution of Primakoff production by studying the t' spectrum. On the other hand a partial-wave decomposition in the range of $t' \leq 0.002\,\mathrm{GeV}^2/c^2$ has been conducted, where quasi-real one-photon exchange exhibits a spin projection $M = 1$. Production by diffractive dissociation is proportional to t'^M. Consequently, at small momentum transfer contribution to amplitudes with $M \neq 0$ are suppressed. In the study of the t' spectrum the contribution of Primakoff events is determined matching the production signature. In case of the partial-wave decomposition the event distribution in the phase-space of the final state is studied. Thus, these two methods represent two complementary approaches to determine the contribution of Primakoff production. In order to measure the differential cross section the integrated luminosity is determined by analyzing decays of beam kaons into the $\pi^-\pi^0\pi^0$ final state. The measured differential cross section is compared to predictions from chiral perturbation theory.

Kurzfassung

Die Untersuchung von sogenannten Primakoff-Reaktionen ist ein Forschungsschwerpunkt der COMPASS Kollaboration am CERN. Diese Reaktionen werden mit Hilfe eines hoch-energetischen Teilchenstrahls aus negativ geladenen Pionen untersucht. Primakoff-Reaktionen zeichnen sich dadurch aus, dass das hochenergetische Pion mit dem elektromagnetischen Feld eines Atomkerns wechselwirkt. Die Wirkung des elektromagnetischen Feldes ist äquivalent zu der Wirkung eines Strahlungspulses aus Photonen. Quantitativ wird dieser Effekt durch die Weizsäcker-Williams Äquivalent-Photon-Näherung beschrieben. Das Primakoff-Programm am COMPASS Experiment deckt durch die Untersuchung verschiedener Endzustände ein breites physikalisches Spektrum im Bereich der Quanten-Chromodynamik bei niedrigen Energien.

Eine erste Testmessung im Jahr 2004, bei der ein Blei-Target zum Einsatzt kam, brachte wichtige Erkenntnisse für die Primakoff Messung im Jahr 2009. Bei der etwa zweiwöchigen Messung wurde das Blei- durch ein Nickel-Target ersetzt. Die Messung konzentrierte sich auf Reaktionen mit neutralen Teilchen im Endzustand. Daher benötigte man ein Trigger-System, das auf diese Teilchen sensitiv ist. Um dies zu erreichen wurde ein digitaler Ereignis-Trigger entwickelt, der sensitiv auf den Energie-Eintrag im elektromagnetischem Kalorimeter ist.

Im Rahmen dieser Arbeit wurde der differentielle Wirkungsquerschnitt der radiativen Produktion des $\pi^-\pi^0\pi^0$ Endzustands bestimmt. Das beobachtete Spektrum wird durch Prozesse der starken Wechselwirkung, vorwiegend diffraktive Dissoziation, dominiert. Davon muss der Beitrag radiativer Produktion separiert werden. Dies geschieht mittels zweier unterschiedlicher Methoden. Primakoff-Reaktionen finden bei sehr kleinem Vierer-Impuls-Übertrag statt. Die Verteilung der Impuls-Überträge t' unterscheidet sich deutlich von der Verteilung, die bei Prozessen der starken Wechselwirkung auftreten. Dies wird zur Bestimmung mittels Untersuchung des Impulsübertrags-Spektrum genutzt. Anderseits wird eine Partialwellen-Zerlegung bei kleinen Impulsüberträgen $t' \leq 0.002\,\mathrm{GeV}^2/c^2$ zur Identifikation radiativer Prozesse an Hand der Spin-Projektion genutzt. Die Spin-Projektion $M = 1$ radiativer Prozesse ist durch die Eigenschaften des quasi reellen Photons gegeben. Bei kleinen Impulsüberträgen ist diffraktive Dissoziation mit $M \neq 0$ unterdrückt. Um den Wirkungsquerschnitts zu bestimmen benötigt man dieintegrierte Luminosität. Dies geschieht durch die Analyse von Kaon-Zerfällen. Der Messung des Wirkungsquerschnitts werden Vorhersagen der chiralen Störungsrechnung gegenübergestellt.

Contents

Part I

Introduction

Chapter 1

Physics Motivation

The discovery of nuclear decays and the produced radiation at the end of the 19^{th} century opened up new fields of research. Rutherford used the α radiation produced in nuclear decays to investigate the structure of atomic matter. Based on his observations he developed an atomic model with a positively charged compact atomic nucleus surround by electrons [Rut11]. Furthermore, he suggested, that the nucleus is made up of positively charged particles, *protons*, and neutral particles, *neutrons*, of approximately the same mass [Rut20]. This, however, rises the question, which force holds the nucleus together. Hideki Yukawa answered this question in the framework of quantum field theory by introducing the charged u-particle as mediator of this *strong force* [Yuk35]. The *pion*, which was finally discovered in cosmic ray experiments, was the first particle of a new family of particles called *mesons*. During the 1950, the development of accelerator experiments led to the discovery of a growing number of new particles, often referred to as *particle zoo*. In the early sixties a pattern based on the $SU(3)$ flavor symmetry, was found by Gell-Mann [GM61], which described the, at that time observed, 25 light and strange hadrons and their properties by arranging them in octets and decuplets .

1.1 The Quark Model and Quantum Chromodynamics

It took a few more years to develop a theory, which could explain the underlying symmetry of the observed pattern. Independently from each other, Georg Zweig [Zwe64] and Gell-Mann [GM64] suggested a theory based on the $SU(3)$ flavor symmetry, postulating that mesons and baryons are build from point-like particles, which follow the Fermi-Dirac statistics. Following the nomenclature introduced by Gell-Mann these fermions with spin $S = 1/2$ are today called *quarks* q . The quarks are organized in a unitary triplet, which consists of an isopin singlet s with isopin $I = 0$ and an isopin doublet (u, d) with $I = 1/2$. The charges

of the quarks are correlated, thus by choosing the charge of the singlet s to z, the charges of the u and d quarks are given by $z+1$ and z respectively. The choice consistent with the electric charge of the observed composed objects is the non-integer charge $z = -1/3$. The anti-quarks $\overline{q}$ have opposite signed charges, of course. The parity P of quarks and anti-quarks is $P = +1$ and $P = -1$ respectively. Additionally, the new introduced quantum number *strangeness* $\mathcal{S} = -1$ is attributed to the s quark, with $\overline{s}$ having $\mathcal{S} = 1$. The Gell-Mann-Nishijima formula [NN53, GM56]

$$Q = I_z + \frac{Y}{2}, \tag{1.1}$$

which helps to describe regularities of observed particles, relates the electrical charge Q of a particle with the third component of the isospin I_z and the *hypercharge* Y. At that time, knowing only three quark flavors, the hypercharge was defined as sum of the *baryon number* B, where the quarks and anti-quark carry $B = 1/3$ and $B = -1/3$ respectively, and the strangeness $\mathcal{S}$. Today three more quark flavors – c, b and t – are known. The associated quantum numbers are added to the sum, which defines the hypercharge

$$Y = B + \mathcal{S} + \mathcal{C} + \mathcal{B} + \mathcal{T}. \tag{1.2}$$

Baryons are constructed by combining quarks and anti-quarks to have Baryon number $B = 1$, i.e. any combination of qqq, $qqqq\overline{q}$ etc. Mesons are required to have $B = 0$ and can therefore be constructed of states having an equal amount of quarks and anti-quarks, i.e. $q\overline{q}$, $qq\overline{qq}$ etc.

This theory did not only describe the known *particle zoo*, but also provides predictive power. The Ω^- Baryon was discovered soon after the prediction by Gell-Mann to complete the $S = 3/2$ Baryon decuplet. The Ω^-, being a ground state, has a symmetric space wave function. It is formed by three strange quarks with aligned spins building the total spin of $S = 3/2$ and seems to violate the Pauli principle, which requires an asymmetric wave function. This issue was finally resolved by introducing an additional degree of freedom, the *color*. Thus, for each quark flavor three quarks exist, which differ only in color, extending the number of known quarks from three to nine. This approach did not only solve the Ω^- problem, but also fixed several other discrepancies between prediction and experiments as for example the cross section of electron-positron annihilation. Soon after, the basis of *Quantum Chromodynamics* (QCD) was set by treating the color group as gauge group, with an octet of gauge bosons, called *gluons*, mediating the strong force [FGM72]. The gluons carry color charges and are therefore self interacting, which is a big difference to *Quantum Electrodynamics* (QED). This does not only imply, that in principle states composed of gluons, so-called glueballs, or states composed of quarks and gluons, so-called hybrids, may exist, it is also responsible for the fact, that the strong coupling $\alpha_s(Q^2)$ gets smaller for high energies, i.e. small distances, leading to *asymptotic freedom*.

This allows to treat the high energetic regime within a perturbation theory. On the other hand $\alpha_s(Q^2)$ is large for low energies, which leads to *confinement*, i.e. the fact, that no free object with a net color charge can exist. QCD, based on the $SU(3)$ color symmetry also implies, that the structure of hadrons is more complicated than the *constituent quark* model suggests. The properties of hadron are defined by so-called *valence quarks* and possibly *valence gluons*[1], which are accompanied by a rich dynamic structure formed by so-called *sea quarks* and *sea gluons*. Today we know three more quark flavors - charmed c, bottom b and top t. Reflecting the observed transition probabilities and mass hierarchies the six quarks are similar to leptons arranged in three families each with an up-like quark (electrical charge 2/3) and a down-like (electrical charge $-1/3$) quark, i.e. (u, d), (c, s) and (t, b).

The search for states beyond the known $q\bar{q}$ and qqq states, such as tetra-quark or penta-quark states as well as states with valence gluons, is a topic of active research and one of the topics addressed by the COMPASS collaboration [BKT96, GHK$^+$10]. These states are called exotic states. Mixing with the known states, it is difficult to discover exotic states with the same quantum number as known states, thus one actually searches for states with quantum number not allowed for $q\bar{q}$ and qqq, so called spin exotics such that exotic nature is obvious.

1.2 Chiral Perturbation Theory

At low momentum transfer Q^2, i.e. large distances, the coupling constant $\alpha_s(Q^2)$ of the strong interaction gets large and QCD becomes non-perturbative. However, confinement suggests, that in this regime the relevant degrees of freedom are given by hadrons, which are color neutral, rather than quarks and gluon. In *chiral perturbation theory* (ChPT) the $SU(3)_L \times SU(3)_R \times U(1)_V$ symmetry of the QCD Lagrangian for vanishing masses of u, d and s quarks is spontaneously broken down to $SU(3)_V \times U(1)_V$. The Goldstone theorem gives rise to an octet of massless Goldstone bosons, which have the same quantum properties as the octet of the light pseudoscalar mesons, i.e. pions, kaons and the eta. In order to expand the Greens function in terms of the quark masses m_u, m_d and m_s, the light quark u, d and s are assumed massless, while the heavy quarks are assigned to their physical masses. By assigning finite masses to the u, d and s quarks, chiral symmetry is not only spontaneously but also explicitly broken, such that the Goldstone bosons acquire masses. In contrast to fundamental gauge theories, where the perturbative treatment is done in expansion of a small coupling constant, ChPT, doing an expansion in particle momentum, is an effective field theory. ofHowever, renormalization of ChPT on a given finite order can be achieved by calculating contact terms. All inner dynamic is described by *low-energy constants* (LECs). These LECs have to be determined by experimental observaoftion.

[1] In principle allowed by the theory, up to now no such state is established.

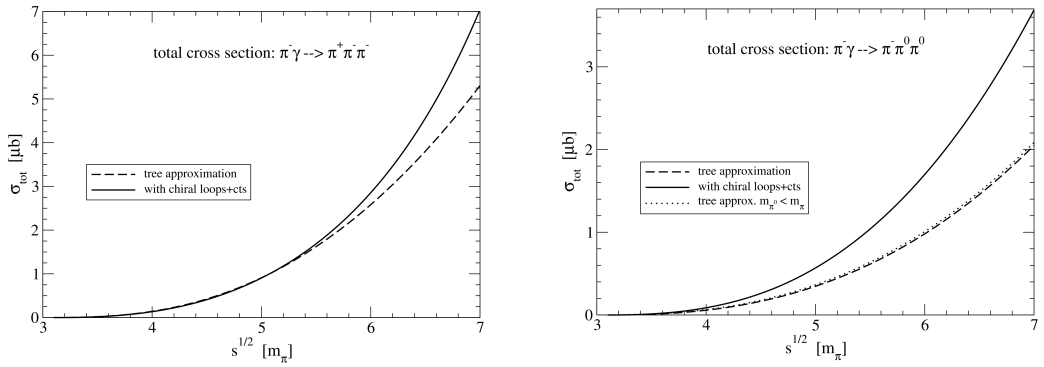

(a) $\pi^-\gamma \to \pi^-\pi^-\pi^+$ (b) $\pi^-\gamma \to \pi^-\pi^0\pi^0$

Figure 1.1: Chiral perturbation theory prediction of the differential cross section for $\pi^-\gamma \to \pi^-\pi^-\pi^+$ (a) and $\pi^-\gamma \to \pi^-\pi^0\pi^0$ (b). The prediction in leading order (dashed line) and next-to-leading-order calculation (solid line) are shown. The dotted line shows the effect of isospin breaking, i.e. $m_{\pi^0} \neq m_\pi$, for the tree approximation of $\pi^-\gamma \to \pi^-\pi^0\pi^0$. (From [Kai10]).

Strong interaction conserves the flavor current, thus in many cases it is sufficient to restrict to the two-flavor sector of QCD and the chiral symmetry is given by $SU(2)_L \times SU(2)_R$ rather than $SU(3)_L \times SU(3)_R$. Applying ChPT to the two-flavor sector one speaks about $SU(2)$ ChPT. In this case the s is treated as heavy quark and gets its physical mass assigned. The $SU(2)_L \times SU(2)_R$ chiral symmetry gets spontaneously and explicit broken to $SU(2)_V$, giving a rise to three Goldstone bosons with $J^P = 0^-$. The Goldstone bosons are identified as π^-, π^+ and π^0. Within the $SU(2)$ ChPT, the LECs required for tree level calculations, which are given by the mass m_π of the pion and the pion decay constant f_π, are known to high precision. The six LECs $l_1, l_2, ..., l_6$, which are required for next-to-leading order (NLO) calculations, are known with varying precisions and can be potentially improved by further experimental input.

In order to prove that the low-energy dynamic of QCD is correctly described by ChPT, theoretical predictions have to be verified by measurements, as it was achieved for the pion-pion scattering length, where accurate predictions of two-loop calculations [CGL01] are confirmed by experimental results [PAA+03] [BCK+08] [BCK+09]. Besides the scattering of strong interacting particles ChPT also allows predictions in the field of electromagnetic processes as for example the $\pi\gamma$ scattering, which is related to the measurements of pion polarizability in $\pi\gamma \to \pi\gamma$ (see 4.1.1) or the chiral axial anomaly in $\pi^\pm\gamma \to \pi^\pm\pi^0$ processes. Also the $\pi\gamma \to 3\pi$ process has already been subject to ChPT calculations [KF08, Kai10]. This calculation does not only cover the $\pi^-\gamma \to \pi^-\pi^-\pi^+$ reaction, which has been investigated at COMPASS 2004 data (see 4.1.3), but also the non-resonant production of the $\pi^-\pi^0\pi^0$ final state, which is subject to the analysis of the data

presented in chapter 13. Figure 1.1 shows the prediction for the cross sections of both processes, which are obtained by leading and next-to-leading order calculations. As discussed in section 3.3, π^--photon reactions are accessible in π^- nucleus scattering exploiting *Primakoff reactions*, which are subject to this thesis. Due to the relevance of this calculation, it is discussed in more detail in the following concentrating on the $\pi^-(p_1) + \gamma(k, \epsilon) \to \pi^-(p_2) + \pi^0(q_1) + \pi^0(q_2)$ process. The prediction of the cross section $\sigma_{\text{tot}}(s)$ is obtained by integrating the the squared T-matrix T over the three-pion phase space. In order to represent NLO terms, one has to start with the general form of the T-matrix, which in Coulomb-gauge can be decomposed

$$T = \frac{2e}{f_\pi^2} \left[\vec{\epsilon} \cdot \vec{q}_1 A_1 + \vec{\epsilon} \cdot \vec{q}_2 A_2 \right], \tag{1.3}$$

where A_1 and A_2 are two dimensionless products, which depend on the squared center-of-mass energy $s = (p_1 + k)^2$ and $\vec{\epsilon}$ the unit vector in direction of the momentum of the photon. The independent Mandelstam variables s_1, s_2, t_1 and t_2 are given by

$$s_1 = (p_2 + q_1)^2 \ , \quad s_2 = (p_2 + q_2)^2 \ , \quad t_1 = (q_1 - k)^2 \ , \quad t_2 = (q_2 - k)^2. \tag{1.4}$$

This choice allows to describe the permutation of the two identical π^0 conveniently. Going to the center-of-mass frame, all diagrams where the photon couples to the incoming π^- vanish, leaving only one tree diagram contributing to the amplitude. This Feynman diagram is depicted in figure 1.3(a). The leading-order amplitude can then be written as [Kai10]

$$A_1^{(\text{tree})} = A_2^{(\text{tree})} = \frac{2m_\pi^2 + s - s_1 - s_2}{3m_\pi^2 - s - t_1 - t_2}. \tag{1.5}$$

Figure 1.3(b) and 1.3(c) show examples for loop diagrams, which contribute to the NLO amplitude. In case of the LO calculations, A_1^{LO} and A_2^{LO} are used to calculate the T-matrix (see Eq. 1.3). The LO amplitudes are given by the tree level amplitudes

$$\begin{aligned} A_1^{\text{LO}} &= A_1^{(\text{tree})} \qquad \text{and} \\ A_2^{\text{LO}} &= A_2^{(\text{tree})}, \end{aligned} \tag{1.6}$$

Going to the next-to-leading-order calculations, the contributions from loop diagrams $A_1^{(\text{loop})}$ and $A_2^{(\text{loop})}$ and counter terms $A_1^{(\text{ct})}$ and $A_2^{(\text{ct})}$ have to be added

$$\begin{aligned} A_1^{\text{NLO}} &= A_1^{(\text{tree})} + A_1^{(\text{loop})} + A_1^{(\text{ct})} \\ A_2^{\text{NLO}} &= A_2^{(\text{tree})} + A_2^{(\text{loop})} + A_2^{(\text{ct})}. \end{aligned} \tag{1.7}$$

The exact parametrization of the loop contribution and counter terms can be found in [Kai10]. The differential cross section as function of the squared center-

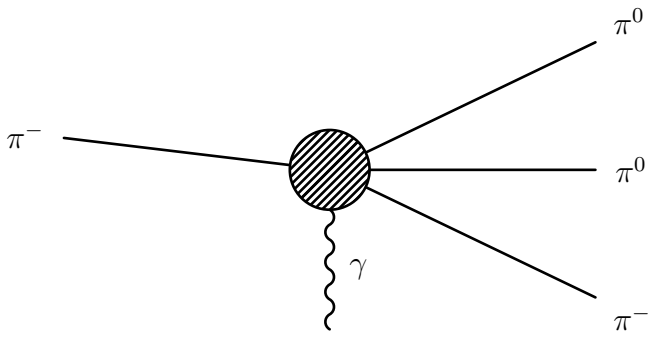

Figure 1.2: Schematic drawing of $\pi^-\gamma\to\pi^-\pi^0\pi^0$ as subject to the calculations within ChPT.

of-mass energy $s = m_{3\pi}^2$ is then given as

$$\sigma(s) = \frac{\alpha}{32\pi^2 f_\pi^4 (s - m_\pi^2)} \iint\limits_{z^2<1} \mathrm{d}w_1 \mathrm{d}w_2 \int_{-1}^{1} \mathrm{d}x \int_0^\pi \mathrm{d}\phi \left| \hat{k} \times (\vec{q}_1 A_1 + \vec{q}_2 A_2) \right|^2 \quad (1.8)$$

with $w_{1,2}$ being the energies of the outgoing π^0s and $\vec{q}_{1,2}$ their momenta. $\hat{k}$ denotes the unit vector in the direction of the incoming photon. The squared cross products expressed in terms of the direction cosines x, y and z are given by

$$\left(\hat{k} \times \vec{q}_1\right)^2 = q_1^2(1-x^2), \ \left(\hat{k} \times \vec{q}_2\right)^2 = q_2^2(1-y^2) \text{ and } \left(\hat{k} \times \vec{q}_1\right)\cdot\left(\hat{k} \times \vec{q}_2\right) = q_1 q_2 (z-xy), \quad (1.9)$$

with $q_{1,2} = (w_{1,2}^2 - m_\pi)^{1/2}$. Applying the relations

$$q_1 q_2 z = w_1 w_2 - \sqrt{s}(w_1 + w_2) + \frac{s + m_\pi^2}{2} \quad \text{and} \quad y = xz + \sqrt{(1-x^2)(1-z^2)}\cos\phi \quad (1.10)$$

the Mandelstam variables $s_{1,2}$ and $t_{1,2}$ are given by

$$s_{1,2} = s + m_\pi^2 - 2\sqrt{s} w_{2,1} \quad \text{and} \quad t_{1,2} = m_\pi^2 + \frac{m_\pi^2 - s}{\sqrt{s}} \left(w_{1,2} - q_{1,2} x_{1,2}\right). \quad (1.11)$$

with $x_1 = x$ and $x_2 = y$. Including even higher order diagrams, based on the calculation presented in [EU02], contributions from single and double ρ exchange can be included. A few examples of diagrams contributing to this calculations are shown in figure 1.3. The chiral amplitudes are known in the fully differential form, thus these calculations can be included in partial-wave analysis as depicted in 3.2.3. The detailed parametrization[2] of the ρ contributions as it is used in the partial-wave analysis is given in appendix A.

[2]Kindly provided by the author of [Kai10].

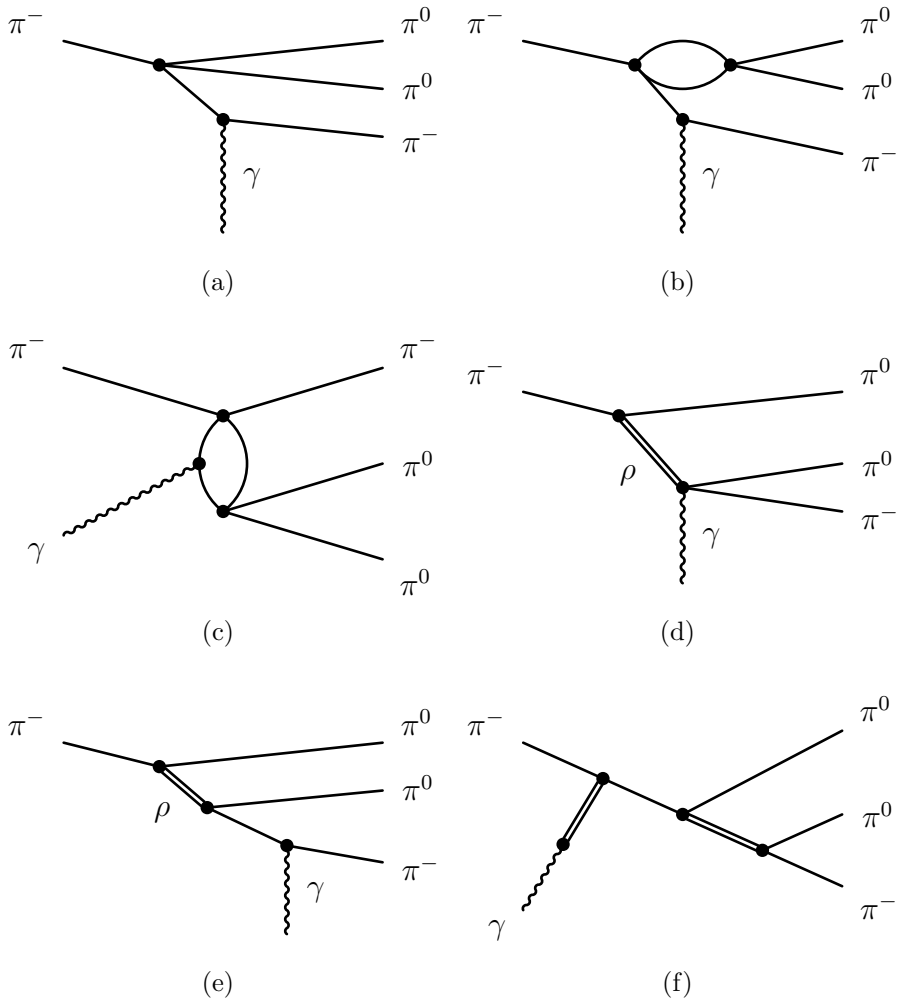

Figure 1.3: Examples of Feynman diagrams contributing to the $\pi^-\gamma \to \pi^-\pi^0\pi^0$ cross section in leading order (a), next-to-leading order (b),(c) as well as single (d),(e) and double (f) ρ exchange. Not all possible contribution are shown. Please refer to [Kai10] and [EU02] for a complete list.

Chapter 2

Meson Spectroscopy

The identification of meson resonances and their properties, called *meson spectroscopy*, is a fundamental method to investigate the nature of strong interaction. Today, one can distinguish two types of experiments, which are done in this field. In *formation experiments*, two reaction partners form such a state. In this type of experiment, the quantum numbers of the formed state are given by the parent particles. The invariant mass and the orbital angular momentum L is varied by the impact parameter of the reaction partners, being either two colliding beam particles or a beam particle impinging on a target. The second class of experiments are *production experiments*. They are typically done by scattering high-energetic hadronic beams on nuclear targets. In contrast to formation experiments, where one studies resonances by investigating the cross section, in production experiments the reaction is studied by investigating the final state, being either the resonance itself or, in case of short lived resonances, its decay products. Production experiments make a wide spectrum of kinematics and physical processes available for investigation. The COMPASS experiment (see chapter 4) is following this approach. The dominating process in this reaction is the production of an intermediate state X, a short lived state often referred to as resonance, which decouples production and decay processes. Due to its relevance for the analysis of the data set described in chapter 8, the underlying physics is shortly depicted in the following.

2.1 Meson Resonances

The mesons resonances established today can in the constituent-quark model, be described as color-neutral $q\overline{q}$ pairs. They are characterized by the quantum numbers J^{PC}. The total angular momentum J is composed of the relative angular momentum L between the $q\overline{q}$ pair and the total intrinsic spin S

$$|L - S| \leq J \leq |L + S|. \tag{2.1}$$

Thereby, the spin components of the quark and the anti-quark couple to the total intrinsic spin $S = 1$ ($|\uparrow\uparrow\rangle$) or $S = 0$ ($|\uparrow\downarrow\rangle$). The parity P is given by

$$P = (+1)(-1)(-1)^L = (-1)^{L+1}, \tag{2.2}$$

where the factors $(+1)(-1)$ are accounting for the intrinsic parity of the quark and anti-quark, respectively. The *naturality* η is defined as

$$\eta = P(-1)^J. \tag{2.3}$$

The C-parity C defines the behavior under charge conjugation. As this symmetry exchanges particles with their antiparticles, the C-parity eigenstates are built of a quark and its anti-quark.

$$C = (-1)^{L+S} \tag{2.4}$$

Only for neutral $q\overline{q}$ systems the C-parity is properly defined. However, as convention, the charged mesons have the C-parity of their neutral isospin partners. Being conserved in strong interactions the additional quantum numbers I^G, i.e. the Isospin I and the G-parity G, are considered. The G-parity is a generalization of the C-parity, which is defined for all meson multiplets. It is a combination of charge-conjugation followed by a rotation of 180 degrees around the I_y axis in the isospin space

$$G = C \cdot e^{i\pi I_y} = C(-1)^I. \tag{2.5}$$

Following these rules, not all spin parity states can be constructed from $q\overline{q}$ pairs. The mesons with the quantum numbers

$$J^{PC} = 0^{--}, odd^{-+}, even^{+-} \tag{2.6}$$

cannot be formed by $q\overline{q}$ pairs and therefore are called *spin exotic*. As there is no overlap with $q\overline{q}$ states the *exotic* nature of the state is obvious. These states may be either multi-quark states such as tetra-quark states ($qq\overline{q}\overline{q}$) or states with valence gluons. States like $q\overline{q}g$, which have both valence quarks and gluons are called *hybrids*. States formed only from gluons like gg are called *glueballs*. In principle exotic states are not forbidden by QCD and therefore should exist. Exotic states, which have quantum numbers allowed for $q\overline{q}$ pairs, are experimentally difficult to distinguish from the $q\overline{q}$, which gives rise to the search for spin exotic states. Evidences for such states have been report by different experiments, also at COMPASS, but require further clarification.

2.2 Parametrization of Resonances

Resonances are mathematically described as pole in the scattering amplitude. However, in contrast to stable or meta-stable particles, which have poles on or near the real axis of the complex s-plane, the poles of resonances have a signif-

icant deviation from the real axis and therefore a finite life-time. These short lived resonances are often described using relativistic Breit-Wigner functions (see section 11.2). Thereby the features of the Breit-Wigner function are respecting the fact, that a resonance is not only characterized by an enhancement in the production cross section, but also by a phase motion, where the phase changes by π. The steepness of the phase motion is connected to the width of the resonance. Wide resonances show a slow phase motion, while narrow resonance show a faster phase change. In many experiments, like production experiments, it is not possible to measure absolute phases, but often it is possible to measure relative phases between different resonances, which still allow to observe the expected phase motion. Thus one has to consider that non-resonant processes like the deck process (see 3.2.3) may influence the observed relative phase.

2.3 Decay of Resonances

For final states with more than two particles, enhancements in agreement with the mass and width of known resonances are often observed in the mass spectra of subsystems, which gives rise to the *isobaric* decay model. In the isobaric model, the decay of a resonance is described as a chain of subsequent two particle decays. A detailed discussion of this decay model is given in section 10.5.

Chapter 3

Scattering Processes

Typical reactions investigated in production experiments are exclusive scattering processes of a high energetic beam a from a nuclear target b as depicted in figure 3.1(a). The exchange particle $\mathcal{R}$ transfers momentum, angular momentum L and possibly other quantum numbers between the target and the beam particle. Due to the fact, that for elastic scattering the momentum transfer is smaller than typical nuclear excitation energies, the target, which recoils with low momentum d, stays intact, while the beam is exited to the short lived state c, which is often called a resonance.

$$a + b \rightarrow c + d \tag{3.1}$$

The resonance c then decays into an n-particle final state.

$$c \rightarrow 1 + 2 + ... + n, \tag{3.2}$$

$1, 2, ..., n$ denote the single particles of the observed final state. Under the assumption that neither the resonance c nor its decay products interact with the recoil particle d, production and decay of the resonance c are decoupled. At low momentum transfer the transferred energy is very small, thus the energy of the beam particle E_a equals in good approximation the energy of the resonance E_c, which is given by the sum of the energies E_i of the final state particles

$$E_a \approx E_c = \sum_{1}^{n} E_i. \tag{3.3}$$

Starting with a short introduction to S-matrix and Regge theory, the production mechanism of the strong interaction, which dominates the observed spectra, is discussed below. A nice introduction of this topic can also be found in [Haa14]. This is followed by a short excursion to electrodynamics introducing the Weizsäcker-Williams-Method of virtual quanta, which allows to access radiative processes in pion-nucleus scattering in so-called *Primakoff Reactions*.

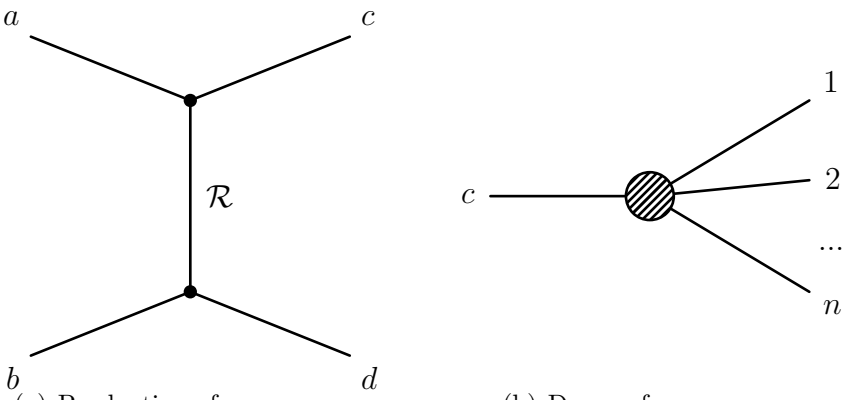

(a) Production of resonance c. (b) Decay of resonance c.

Figure 3.1: Schematic drawing of the scattering of beam a from target b. $\mathcal{R}$ mediates the interaction. The target recoils at low momentum d, while the beam gets excited to the resonance c (a). The resonance c subsequently decays into a n-particle final state (b).

3.1 Introduction to S-Matrix and Regge Theory

The scattering process is described by the *scattering matrix* S, a Lorentz-invariant linear operator, which transforms the initial state $|i\rangle$ into the final state $|f\rangle$.

$$S|i\rangle = |f\rangle \tag{3.4}$$

The S-matrix can be written as the sum of the identity operator I and the *transition matrix* T multiplied by i

$$S = I + \mathrm{i}T, \tag{3.5}$$

with the matrix elements

$$S_{if} = \delta_{if} + \mathrm{i}T_{if} \tag{3.6}$$

The T-matrix can be separated into a δ function, accounting for the four momentum conservation and the scattering amplitude $A_{if}(s,t)$.

$$T_{if} = i(2\pi)^4\delta^4(p_f - p_i)A_{if}(s,t) \tag{3.7}$$

The scattering amplitude depends on s and t, two of the three Lorentz-invariant *Mandelstam variables*

$$s = (p_a + p_b)^2 = (p_c + p_d)^2, \tag{3.8}$$

$$t = (p_a - p_c)^2 = (p_b - p_d)^2 \text{ and} \tag{3.9}$$

$$u = (p_a - p_d)^2 = (p_b - p_c)^2. \tag{3.10}$$

It is possible to investigate relativistic scattering amplitudes in different reference frames, which are named s-channel ($a + b = c + d$), t-channel ($a + \overline{c} = \overline{b} + d$) and u-channel ($a + \overline{d} = \overline{b} + c$) according to the corresponding Mandelstam invariants. An incoming particle x with momentum p can be regarded as its outgoing anti-particle $\overline{x}$ with momentum $-p$. This property is called crossing symmetry and implies, that the amplitude does not change, when looking at the same process in the three different channels. This means, that for analytical amplitudes the channel can be chosen freely for the parametrization of an amplitude. The partial-wave expansion of the scattering amplitude $A_{if}(s,t) = A(s,t)$ in the t-channel is defined as

$$A(s,t) = A(s, \cos\theta_t) = \sum_{l=0}^{\infty} (2l+1) A_l(t) P_l(\cos\theta_t) \tag{3.11}$$

with the cosine of the scattering angle

$$\cos\theta_t = 1 + \frac{2s}{t - 4m^2}. \tag{3.12}$$

$A_l(t)$ are the partial-waves and $P_l(\cos\theta_t)$ the corresponding Legendre polynomials. Investigating the *Regge limit*, i.e. fixed t and $s \to \infty$, the Legendre polynomials behave like

$$P_l(\cos\theta_t) \underset{s\to\infty}{\sim} s^l, \tag{3.13}$$

which leads to the phenomenon, that the expansion 3.11 diverges at high energies

$$A(s,t) \underset{s\to\infty}{\sim} \sum_l A_l(t) s^l. \tag{3.14}$$

Originally *Regge theory* aimed to calculate this sum in the non-relativistic case [Reg59]. Regge described bound states in a framework of non-relativistic quantum mechanics as poles of the partial-wave amplitude $a_l(k)$. Thereby the bound states are according to their angular momentum l grouped into families. The partial-wave amplitude $a(l,k)$ can formally be extended to complex numbers of l, such that for integer values of l the relation $a(l,k) = a_l(k)$ is fulfilled. For certain kinds of potentials, the *Regge poles* are lying on the *Regge trajectory* $\alpha(k)$, i.e.

$$l = \alpha(k). \tag{3.15}$$

It was found, that under certain hypotheses this ansatz can be adapted to relativistic scattering processes described by the S-matrix formalism. Therefore, the relativistic partial-wave amplitude $A_l(t)$ is advanced to $A(l,t)$, which has poles at

$$l = \alpha(t). \tag{3.16}$$

As each of these poles contribute to the scattering amplitude, the scattering process is described by the exchange of a whole family of resonances. For fixed

t, $A(s,t)$ is proportional to $s^{\alpha(t)}$.

$$A(s,t) \underset{s\to\infty}{\sim} \sum_l s^{\alpha(t)} \tag{3.17}$$

Here, each Regge trajectory is described by the linear equation

$$\alpha(t) = \alpha(0) + \alpha' \cdot t. \tag{3.18}$$

An important theorem in hadron-hadron scattering process is the *Froissart-Martin bound* [Fro61][Mar63], which claims that the total cross section of such scattering processes is limited by

$$\sigma_{tot} \leq \frac{\pi}{m_\pi^2} ln^2 s, \quad \text{with } s \to \infty. \tag{3.19}$$

This theorem is fulfilled for Regge trajectories with

$$\alpha(0) < 1. \tag{3.20}$$

Looking at single Regge exchange, the scattering amplitude $A(s,t)$ can be written as

$$A(s,t) = \beta(t)\eta_\xi(t)s^{\alpha(t)}. \tag{3.21}$$

The *residue* $\beta(t) = g_{ab}(t)g_{cd}(t)$ is factorized into the couplings at the two vertices. $\eta_\xi(t)$ is called *signature factor* after the *signature* ξ, a quantum number connected with the angular momentum l, being $+1$ or -1 for even and odd l respectively

$$\eta_\xi(t) = \begin{cases} -\frac{\exp(-i\frac{\pi}{2}\alpha(t))}{\sin(\frac{\pi}{2}\alpha(t))} & \text{if } \xi = +1 \\ -\frac{\exp(-i\frac{\pi}{2}\alpha(t))}{\cos(\frac{\pi}{2}\alpha(t))} & \text{if } \xi = -1 \end{cases}. \tag{3.22}$$

The *optical theorem*

$$\sigma_{tot} = \frac{1}{s}\Im(A_{\text{el}}(s, t = 0)) \tag{3.23}$$

is one of the key features of S-matrix theory. It relates the cross section to the imaginary part of the elastic scattering amplitude $A_{\text{el}}(s,t)$ in the forward limit $t = 0$ and avoids the theoretically unlimited summation over all possible inelastic terms. Applying this to the Regge theory, the cross section of single Regge exchange is proportional to $s^{\alpha(0)-1}$

$$\sigma_{tot} \sim s^{\alpha(0)-1}. \tag{3.24}$$

This, however, lead to a contraction between experiment and theory. On the one hand experimental observation show a flat minimum in the cross section at center-of-mass energies $\sqrt{s}\approx 10 - 20\text{GeV}/c^2$. On the other hand know Regge

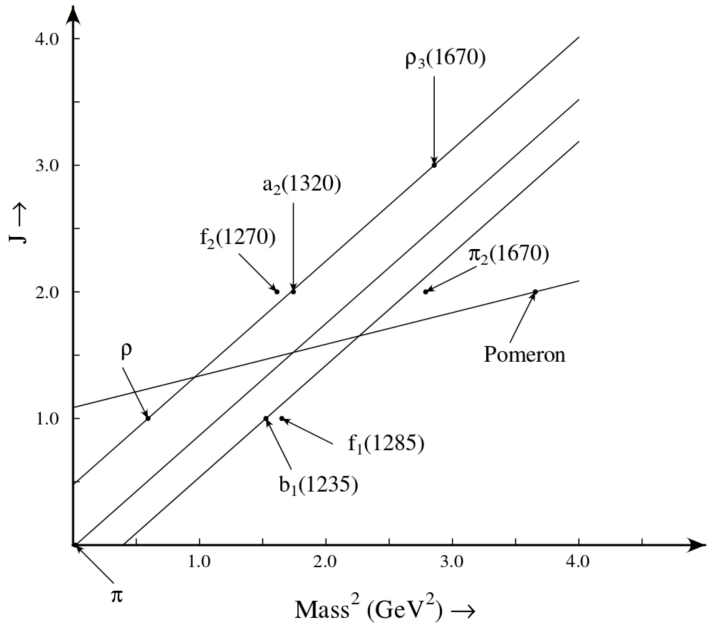

Figure 3.2: Chew-Frautschi plot showing examples of Regge trajectories. The trajectory of the Pomeron is among the shown trajectories (From [Chu08]).

trajectories had an intercepts $\alpha(0)\leq 0.6$, which suggest a decreasing cross section. In order to resolve this contradiction Gribov introduced a Regge trajectory with an intercept around one, which he named *pomeron* after his former student Isaac Pomeranchuck. Besides the intercept, this trajectory has two other properties, which significantly differ from all other known Regge trajectories. On the one hand it has a much flatter slope, which makes the Pomeron the dominant exchange particle at high energies, on the other hand no known meson resonance lies on the Pomeron trajectory[1]. Figure 3.2 shows the Chew-Frautschi plot for several Regge trajectories include the Pomeron trajectory. The Pomeron carries the quantum numbers of the vacuum $J^{PC} = 0^{++}$ and $J^{PC} = 2^{++}$, which suggest, that it is a glue rich state. Fitting experimental data, the Pomeron trajectory is parametrized as [DDLN02]

$$\alpha(t)\approx 1 + \epsilon_{\mathbb{P}} + 0.25(\mathrm{GeV}/c)^2 \cdot t \quad \text{with } \epsilon_{\mathbb{P}}\approx 0.06\text{-}0.08 \tag{3.25}$$

Due to its intercept being larger than one, which is required to describe the slow increase of the cross section at high energies, this trajectory is violating the Froissart-Martin bound (equation 3.19). Up to now this discrepancy between experimental data and theory is unresolved. As mentioned before, due to the large intersect and shallow slope the Pomeron is the leading trajectory at large

[1] A glueball candidate, which would lie on the Pomeron trajectory was reported , but needs confirmation [AAB+94].

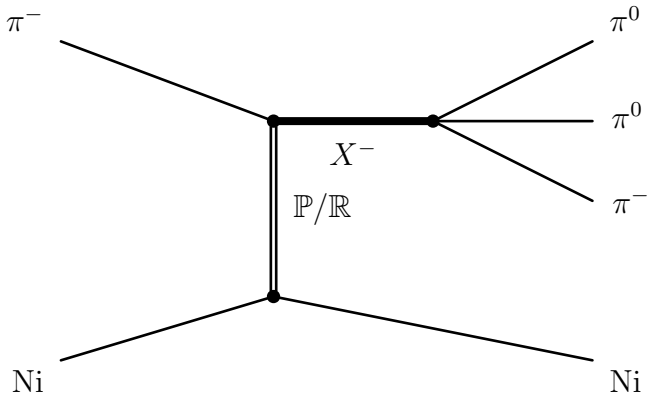

Figure 3.3: Schematic drawing of diffractive dissociation of π^- into $\pi^-\pi^0\pi^0$ in π^--Ni scattering.

s. The Pomeron contribution to the scattering processes is dominant at center-of-mass energies of $\sqrt{s}\approx 19\,\mathrm{GeV}$, which are investigated at COMPASS, such that the strong processes can be regarded as being mediated by the Pomeron $\mathbb{P}$.

3.2 Production Mechanisms of the Strong Interaction

As discussed previously, the scattering processes in the strongly interacting sector can be described by Regge exchange. At the center-of-mass energy reached at COMPASS, this reactions are dominated by Pomeron exchange. Three different production mechanisms can be distinguished. The *diffractive dissociation* is the leading process and the only one considered relevant for the analysis of the data set presented in chapter 8. The following discussion is extended to *central* and *non-resonant production*. All examples schematics are given for the $\pi^-\,\mathrm{Ni}\to\pi^-\pi^0\pi^0\,\mathrm{Ni}$, which is the process under investigation.

3.2.1 Diffractive Dissociation

Single-diffractive dissociation, depicted in 3.3 is a single Regge exchange between the incoming pion and the nucleus, where the pion gets excited to the intermediate resonance X, while the target nucleus stays intact. Within the *triple Regge limit*

$$s \gg m_{3\pi} \gg t, \tag{3.26}$$

which is fulfilled by the COMPASS data under investigation, the scattering amplitudes behaves as

$$A(s,t) \underset{s\to\infty}{\sim} \sum_i g_{aX}(t) g_{bd}(t) \eta_i \left(\frac{s}{m_{3\pi}^2}\right)^{\alpha_i(t)}, \tag{3.27}$$

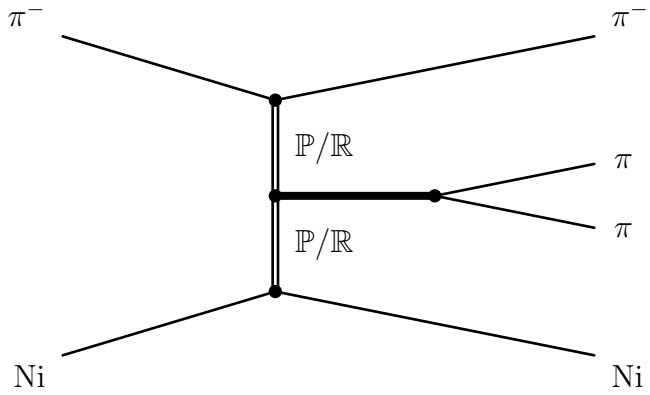

Figure 3.4: Schematic drawing of central production of a three-pion final state in π^--Ni scattering.

where $m_{3\pi} = m_X$ is the invariant mass of the resonance. The sum accounts for the contribution of different Regge trajectories. For the center-of-mass energy $s \approx 150\,\mathrm{GeV}^2/c^4$ reached in π^--Ni collisions at COMPASS, the Pomeron trajectory is the leading Regge trajectory. Momenta and angular momenta are exchanged. Due to the quantum properties of the Pomeron charge and flavor remain unchanged. Thus the excitation of the pion only changes spin J and parity P. Due to the expected t-dependence [Per74]

$$\frac{\mathrm{d}\sigma}{\mathrm{d}t} \propto t^M e^{-bt} \tag{3.28}$$

excitations with spin projections $M > 0$ are suppressed for very small values of t.

3.2.2 Central Production

Central production is a multi-Regge exchange, where two Regge an intermediate resonance is produced in a fusion of two Reggeons. Thereby one Reggeon is emitted by the pion, the other one by the target. Figure 3.4 shows this process for scattering of a π^- beam off a nickel target with three-pions in the final state. Due to the production mechanism, one expects to observe a fast negatively charged pion and a slower neutral subsystem. This reactions can be identified by their experimental signature. A helpful quantity, to do this, is the *rapidity*

$$y = \frac{1}{2}\ln\frac{E + p_\parallel}{E - p_\parallel}. \tag{3.29}$$

E is the energy of a particle or subsystem and $p_\parallel$ the component of the corresponding momentum, which is parallel to the incoming beam. The scattered beam pion has a significant higher rapidity, then the other two pions. This can be used to identify contribution from central production.

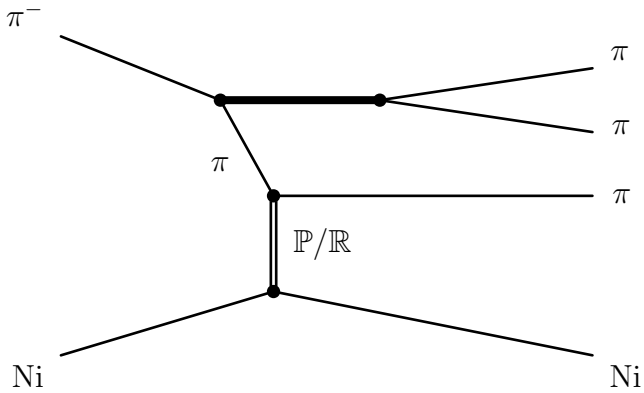

Figure 3.5: Schematic drawing of one possible non-resonant production mechanism, which is embedded in π^--Ni scattering and produces a three-pion final state.

3.2.3 Non-resonant Production

An important source of possible contributions is the non-resonant production of the final state under investigation. These contributions to the observed spectrum are not necessary flat. Thus it is hard to disentangle them from resonant contributions. For the three-pion final state a possible source of non-resonating production is the process depicted in figure 3.5, where the beam pion dissociates into an intermediate state decaying into a two pion system and a pion, which scatters of the nucleus. This reaction also called *Deck effect* was proposed as alternative explanation of the experimentally observed $a_1(1260)$ shortly after its discovery [Dec64].

3.3 Weizsäcker-Williams-Method of Virtual Quantum

The *method of virtual quantum* was independently developed by Weizsäcker [Wei34] and Williams [Wil33]. It exploits the fact, that the electromagnetic field of a charged particle moving at relativistic velocity is similar to a pulse of radiation. This allows to relate the effect induced by a relativistic charged particle with the one induced by radiation. At the COMPASS experiment, this allows to study pion-photon interaction embedded in hadron-nucleus scattering processes. Applying Lorentz transformation, one finds, that the field of an incoming particle with charge q traveling at relativistic velocity $v \simeq c$ in x_1 direction passing a struck

system S at impact parameter b is given by [Jac62]

$$\begin{aligned} E_2(t) &= q\frac{\gamma b}{(b^2+\gamma^2 v^2 t^2)^{3/2}} \\ B_3(t) &= \beta E_2(t) \\ E_1(t) &= -q\frac{\gamma v t}{(b^2+\gamma^2 v^2 t^2)^{3/2}}. \end{aligned} \tag{3.30}$$

$\beta = vc^{-1}$ and $\gamma = (1-\beta^2)^{-1}$ denotes the quantities, which are typical for special relativity calculations. In the ultra-relativistic approximation $\beta \simeq 1$, $E_2(t)$ and $B_3(t)$ are equal. Such that these two components form a field, which is equivalent to a linearly polarized radiation P_1 impinging on S in the x_1 direction. In order to form a radiation P_2 together with $E_1(t)$ one has to introduce an additional field, which in principle modifies the problem. However, P_2 involves γ^{-2}. Thus, the resulting radiation pulse vanishes in the ultra-relativistic case. Thus the electromagnetic interaction is described by the exchange of quasi real photons. Therefore this approach is also called *equivalent-photon method*. Deducing the dependence of the cross section on the squared momentum transfer $t = t' + t_{\min}$ one finds

$$\frac{\mathrm{d}\sigma}{\mathrm{d}t'} \propto \frac{t}{(t'+t_{\min})^2}, \tag{3.31}$$

where $t_{\min}$ is the minimal squared momentum, which is required to excite the pion to the higher mass s and t' is the by $t_{\min}$ reduced squared momentum transfer. The function peaks at $t' = t_{\min}$ or $t = t' + t_{\min} = 2 \cdot t_{\min}$, respectively. For a beam scattering of a target with the target staying intact $t_{\min}$ is given by

$$t_{\min} = \frac{\left(s - m_{\text{beam}}^2\right)^2}{4\left|\vec{p}_{\text{beam}}\right|^2}. \tag{3.32}$$

For the Primakoff measurement in COMPASS the values of $t_{\min}$ reach from $\mathcal{O}(10^{-7})\mathrm{GeV}^2/c^2$ at $\sqrt{(s)} = 0.4\,\mathrm{GeV}/c^2$ to $\mathcal{O}(10^{-4})\mathrm{GeV}^2/c^2$ at $\sqrt{(s)} = 2.5\,\mathrm{GeV}/c^2$.

The intensity of the radiation and therefore the flux of quasi-real photons depends on the charge q and the velocity v of the relativistic particle. Investigating radiative processes in hadron nucleon scattering, one typically looks at the rest frame of the hadron, in which the nucleon with charge $q = Z$ moves with relativistic velocity v. Knowing the reaction partners, it is convenient to use the center-of-mass energy s as parameter. The Weizsäcker-Williams equivalent photon approximation, which is deduced from this approach, relates the experimentally observed cross section $\sigma_{\pi,\text{nucleus}}$ of pion-nucleon scattering to the one of pion-photon scattering $\sigma_{\pi,\gamma}$ [PS61]

$$\frac{\mathrm{d}\sigma_{\pi,\text{nucleus}}}{\mathrm{d}s\mathrm{d}t\mathrm{d}\Phi} = \frac{\alpha \cdot Z^2}{\pi(m_\pi)^2} \cdot F_{\text{eff}}^2(t'+t_{\min}) \cdot \frac{t'}{(t'+t_{\min})^2} \cdot \frac{\mathrm{d}\sigma_{\pi,\gamma}(s)}{\mathrm{d}\Phi}. \tag{3.33}$$

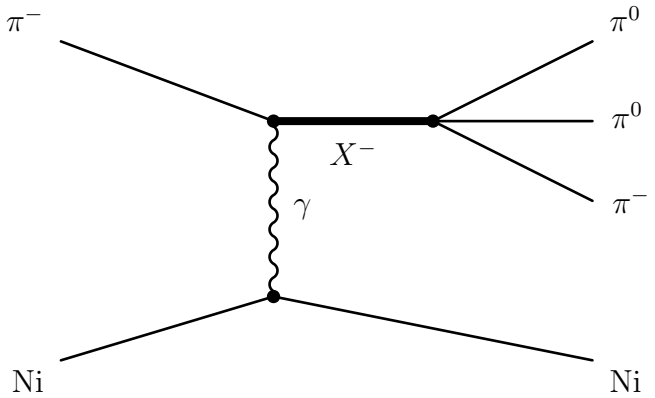

Figure 3.6: Schematic drawing of Primakoff reaction $\pi^-\gamma \to \pi^-\pi^0\pi^0$ in π^--Ni scattering.

where $F_{\text{eff}}(t')$ is the elastic form factor. In the limit of very small momentum transfer, where the cross section peaks, the elastic form factor can be approximated by the form factor of a sphere with sharp radius

$$F_{\text{eff}}(t') = \left[\frac{3}{(qr)^3}\left(\sin(qr) - qr\cos(qr)\right)\right]^2 \quad \text{with } q = \sqrt{t'}. \tag{3.34}$$

The radius of the nucleus is given by

$$r = r_0 \cdot A^{1/3}. \tag{3.35}$$

r_0 can be slightly different for different nuclei, with $r_0 = 1.25\,\text{fm}$ being a good approximation for most nuclei. For the nickel target a radius $r = 4.8\,\text{fm}$ is used. As the Weizsäcker-Williams distribution peaks at very small values of t', *Primakoff production* gets visible at low three-pion mass, where no resonances are present. The fact, that this peak is much sharper than the comparatively shallow t' dependence of strong processes, can be exploited to separate radiative and strong processes. Due to the helicities of $\lambda_\gamma = \pm 1$ of quasi real photon, their exchange exhibits a spin projection $|M| = 1$. This gives an additional handle to distinguish radiative from strong processes. Where for the later contribution with $M \neq 0$ are suppressed at low t'. The resonant production via excitation of the beam pion (see figure 3.6), allows to access the radiative width of the resonance produced in Primakoff reactions. This, however, requires a deep understanding of the interference between production processes. Investigating non-resonant contributions, especially in absence of resonances, i.e. at low $m_{3\pi}$, the interference term between different production mechanisms is negligible. Comparison of the experimental findings to the ChPT calculations (see section 1.2) can provide valuable input. As the calculations are given in differential form, not only the total differential cross section, but also phase space-behavior, can be compared.

Part II

Instrumentation

Chapter 4

COMPASS

The *Common Muon and Proton Apparatus for Structure and Spectroscopy* (COMPASS) is a fixed target experiment at CERN studying the quark and gluon structure of nucleons and other hadrons. The experiment addresses a wide range of physics topics in the non-perturbative regime of Quantum Chromo-Dynamics (QCD) by performing measurements of nucleon structure functions and hadron spectroscopy.

Originally proposed in 1996 [BKT96], combining the efforts of the CHEOPS [ABB95, Pau96] and HMC [HMC95] experiments, COMPASS was approved by CERN in the same year. The proposal for the successor physics program of COMPASS-II [GHK$^+$10], was approved in 2010, while the recording of physics data for the original COMPASS proposal, starting in 2002 and ending in 2011, was still on going. The measurements for COMPASS-II started in the following year 2012.

Section 4.1 will give an overview of the physics program addressed at COMPASS, concentrating on the hadron program, which is most relevant for this thesis. The layout of the COMPASS experiment, which was used during the COMPASS Primakoff measurements in 2009, i.e. the setup used to record the data on which the event selection presented in chapter 8 is based, will be described in 4.2. Having an experimental setup, which can be adapted to different measurements with only small changes, the setup for other measurements is similar to the one presented. However this setup has a feature, which is unique for COMPASS measurements – a digital electromagnetic-calorimetric trigger. Due to its relevance for this work, this trigger will be discussed in a separate chapter (see chapter 6). Section 4.4 will give an overview of the different software frameworks, which are used in the COMPASS experiment.

4.1 Physics Program

The COMPASS collaboration addresses a wide variety of physics topics in the non-perturbative regime of QCD. Due to the large variety of physics addressed

at COMPASS, the following discussion can only cover a small part of the COMPASS research program and restricts to the topics, which are most relevant for the presented work. Are more complete picture of the topics addressed by the COMPASS collaboration can be found in [BKT96, GHK+10].

4.1.1 Pion Polarizability

Chiral perturbation theory (ChPT) is an effective theory deduced from QCD, which describes the non-perturbative regime of QCD (see section 1.2). While some of the calculations done in the framework of ChPT, like the pion-pion scattering length, which was measured in Kaon decays, could already be confirmed experimentally, some still need confirmation. The measured value of $\alpha_\pi = (2.0 \pm 0.6_{\text{stat}} \pm 0.7_{\text{syst}}) \cdot 10^{-4} \text{fm}^3$ [AAA+15b] is in good agreement with calculation done in the framework of ChPT. However some tension with previous measurements remain. In order to reduce uncertainties a data set with roughly ten times the number of events was recorded in 2012 and is subject to a similar on-going analysis.

4.1.2 Measurement of Radiative Width

The radiative decay is an important tool to study the distribution of electric and magnetic currents within mesons and therefore their internal structure. Deduced from the few days of hadron data taking at COMPASS in 2004, a measurement of the radiative decays $a_2(1320) \to \pi\gamma$, a magnetic quadrupole transition, and $\pi_2(1670) \to \pi\gamma$, an electric quadrupole transition, had been performed and is discussed in more details in [Krä14] and [AAA+14b]. The COMPASS measurement adds an important contribution to the measurements of the radiative width $\Gamma_0(a_2(1320) \to \pi\gamma)$, which was measured several time before (see [MAA+77], [CBB+82] and [MAA+01]) and predicted using various models (see [Ros81], [AO88] and [IYO89]). $\Gamma_0(\pi_2(1670) \to \pi\gamma)$, being measured at COMPASS for the first time, can only be compared to model predictions, which can be found in [MYO+13]. The typically low cross section and numerous background processes make the direct measurement of radiative decays of a resonance X to a $\pi\gamma$ final state is difficult to accomplish. Thus the COMPASS measurement exploits the Primakoff effect. The radiative production cross section of the resonance X is measured in π^--Lead interactions by studying the $\pi^-\pi^-\pi^+$ final state. Partial-wave analysis techniques are used to distinguish diffractive and radiative processes. 3 million exclusive $\pi^-\pi^-\pi^+$ events in the small squared our-momentum transfer regime ($t' < 0.01\,\text{GeV}^2/c^2$), which were recorded in 2004 using 190 GeV π^- beam, enters the partial-wave analysis.

The differential cross section for Primakoff production of a broad resonance X is given by

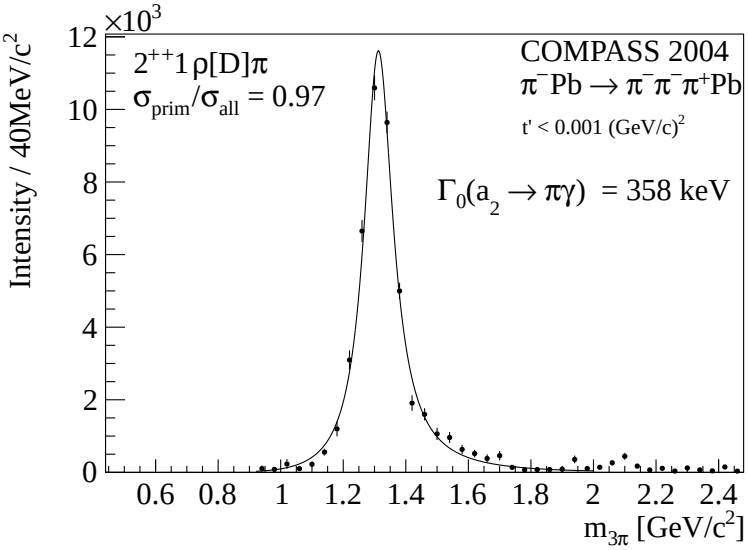

(a) Coherent sum of waves with $J^{PC} M\,\xi\,L\,\pi = 2^{++}1\,\rho\,D\,\pi$.

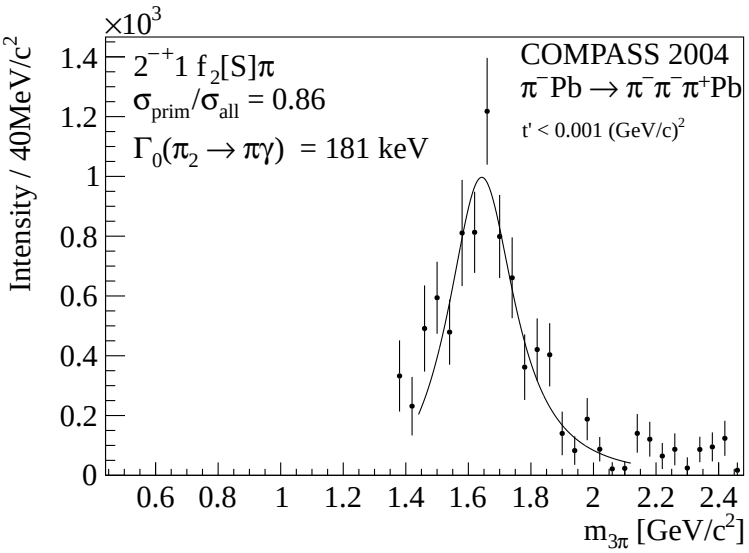

(b) Coherent sum of waves with $J^{PC} M\,\xi\,L\,\pi = 2^{-+}1\,f_2\,S\,\pi$.

Figure 4.1: Total waves intensities of $J^{PC} M\,\xi\,L\,\pi = 2^{++}1\,\rho\,D\,\pi$ waves (a) and $J^{PC} M\,\xi\,L\,\pi = 2^{-+}1\,f_2\,S\,\pi$ (b) waves. The intensities are fitted with Breit-Wigner shapes. From [AAA+14b].

$$\frac{\mathrm{d}\sigma}{\mathrm{d}m\mathrm{d}t'} = 16\alpha Z^2 \left(\frac{m}{m^2 - m_\pi^2}\right)^3 \frac{m_0^2 \Gamma_{\pi\gamma}(m)\Gamma_{\mathrm{final}}(m)}{\left(m^2 - m_0^2\right)^2 + m_0^2 \Gamma_{\mathrm{total}}(m)^2} \frac{t'}{\left(t' + t_{\mathrm{min}}\right)^2} |F(t')|^2. \tag{4.1}$$

$\Gamma_{\mathrm{total}}(m)$ denotes the the total mass-dependent width of the resonance X. $\Gamma_{\mathrm{final}}(m)$ is the mass-dependent width of resonance X decaying to the investigated final state. Here $\Gamma_{\pi\gamma}(m) = f_{\pi\gamma}^{dyn}(m) \cdot \Gamma_0(X \to \pi\gamma)$ is the mass-dependent radiative width, with the factor $f_{\pi\gamma}^{dyn}(m)$ accounting for the mass-dependence.

Thus the total cross section in a certain mass and t' range given by the product of a normalization integral C_X and the radiative width $\Gamma_0(X \to \pi\gamma)$ of the resonance.

$$\sigma_{\mathrm{Primakoff}} = \int_{m_1}^{m_2} \int_{t_1'=0}^{t_2'} \frac{\mathrm{d}\sigma}{\mathrm{d}m\mathrm{d}t'} \mathrm{d}t'\mathrm{d}m = \Gamma_0(X \to \pi\gamma) \cdot C_X, \tag{4.2}$$

and it can be determined experimentally as

$$\sigma_{\mathrm{Primakoff}} = \frac{N_x/\epsilon}{\mathcal{L} \cdot CG^2 \cdot BR(X \to \pi^-\pi^-\pi^+) \cdot \epsilon_{\mathrm{resol}}}. \tag{4.3}$$

Here, the integrated luminosity $\mathcal{L}$ is measured analyzing decays of beam kaons. The branching fraction of the resonance X decaying into the three-pion final state $BR(X \to \pi^-\pi^-\pi^+)$ is taken from the PDG [B$^+$12], CG denotes the respective Clebsch-Gordan coefficient. $\epsilon_{\mathrm{resol}}$ accounts for effects of the experimental resolution. The quantity N_x/ϵ is determined by fitting Breit-Wigners functions to the acceptance-corrected intensity obtained by a mass independent partial-wave analysis, similar to the analysis described in section 10, in the four momentum range $t' \leq 0.001\,\mathrm{GeV}^2/c^2$ in bins of the invariant mass of the outgoing three-pion mass $m_{3\pi}$. The radiative width of the $a_2(1320)$ is extracted by fitting the mass-dependence of the $J^{PC}M = 2^{++}1\rho[\mathrm{D}]\pi$ total waves intensities[1] (see figure 4.1(a)) and that of the $\pi_2(1670)$ by fitting the mass-dependence of the $J^{PC}M = 2^{-+}1\mathrm{f}_2[\mathrm{S}]\pi$ total waves intensities (see figure 4.1(b)), were $J^{PC}M$ are the quantum numbers of the resonance X as described in chapter 10. The normalization is obtained by measuring the decay of kaons, present in the beam. For the radiative width, one gets

$$\Gamma_0(a_2(1320) \to \pi\gamma) = (358 \pm 6 \pm 42)\,\mathrm{keV}/c^2 \tag{4.4}$$

and

$$\Gamma_0(\pi_2(1670) \to \pi\gamma) = (181 \pm 11 \pm 27)\,\mathrm{keV}/c^2 \cdot 0.56/BR_{f_2\pi}. \tag{4.5}$$

In case of the $\pi_2(1670)$, the factor $0.56/\mathrm{BR}_{f_2\pi}$ accounts for the uncertainty of

[1] The coherent sum of all partial-waves with the described properties.

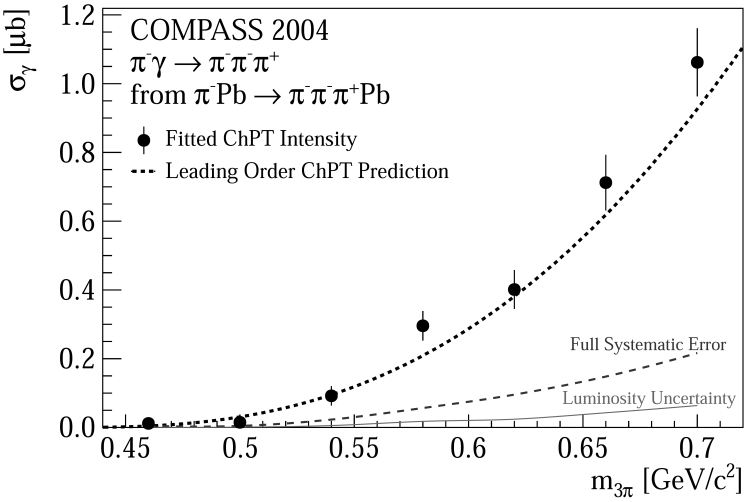

Figure 4.2: Dependence of the cross section of $\pi^-\gamma \to \pi^-\pi^-\pi^+$ on the center of mast energy $\sqrt{s} = m_{3\pi}$ measured at COMPASS 2004. The error bars shows only the statistical uncertainty, while the total systematic uncertainties is given as dashed line at the bottom of the histogram. From [AAA+12].

the branching ratio $\mathrm{BR}_{f_2\pi}$, which was given as 0.56 by PDG at the time of the analysis.

4.1.3 Chiral-Dynamics Near Threshold

Similar to the work presented in this thesis, the partial-wave analysis used for extracting radiative widths (see section 4.1.2) can be applied for three-pion masses down to the three-pion threshold. Extending the isobar model of partial-waves, with a non-isobaric chiral wave, the total cross section of $\pi^-\gamma \to \pi^-\pi^-\pi^+$ is measured. In the range, in which ChPT is expected to be applicable, i.e. up to a few pion masses above threshold, the result is used to verify the prediction of ChPT calculations (see section 1.2). The observed cross section (see figure 4.2) is in good agreement with leading-order calculations of chiral perturbation theory. However, in case the final state contains three charged pion the cross section expected from LO and NLO calculation (see figure 1.1), lie close together. Thus experimentally it is difficult to distinguish the two solutions. A more detailed discussion of this analysis can be found in [AAA+12] and [Gra12].

4.2 Experimental Setup

The COMPASS experiment is located at the *M2 beam line* in the CERN north area. It is an approximately 60 m long two staged spectrometer (see figure 4.3) and can be divided into three parts. The part upstream the target, the *large angle*

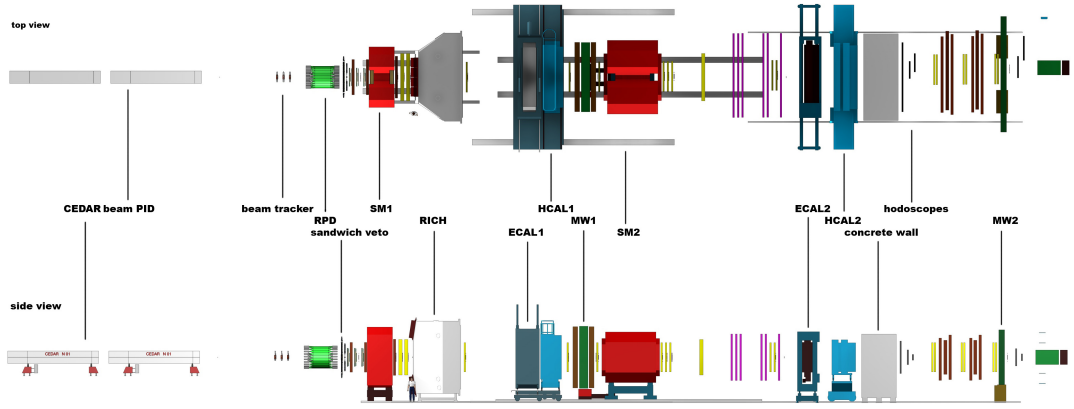

Figure 4.3: Schematic view of the COMPASS spectrometer. The beam enters from the left. The CEDARs on the very left are positioned 30 m upstream of the target. (From [AAA+14a]).

spectrometer (LAS), which provides the large angular acceptance of 180 mrad, and the *small angle spectrometer* (SAS), which allows precise measurement of particles with momentum larger than 5 GeV/c. Each of the two spectrometers are build around a dipole magnet, preceded and followed by tracking telescopes, and are equipped with electromagnetic and hadronic calorimetry as well as muon identification. A *Ring Imaging Cherenkov Detector* (RICH) located in the LAS provides particle identification for particles with momentum starting at a few GeV/c up to approximately 45 GeV/c.

The apparatus can be adapted to the requirements of the different physics measurements, having in common the requirement for a high-rate capability and large angular acceptance. During the years, the apparatus has undergone several upgrades. Besides it flexibility, the apparatus configuration as used during the period of 2009 Primakoff data taking will be described here.

The M2 beam line is described in section 4.2.1. Section 4.2.2 will describe the *beam telescope*, followed by the description of the *LAS* (section 4.2.3) and *SAS* (section 4.2.4). Section 4.3 will give a short overview of the detectors in use. A detailed description of the initial spectrometer setup can be found in [AAA+07], while [AAA+15a] focuses on the setup for measurements with hadron beams.

4.2.1 Beam Line

For its physics program, COMPASS uses high intensity beams of tertiary muon or secondary hadron with a nominal momentum of approximately 160 and 190 GeV/c, respectively. These beams are delivered by the CERNs *Super Proton Synchrotron* (SPS) to the *M2* beam line. A beam of low energetic electrons is used for detector calibrations.

In order to produce a beam of secondary hadrons, protons with momenta of

400 GeV/c are extracted from the *SPS* during a period of 9.6 s and guided to the primary production target *T6*, where the conversion to a beam of secondary hadrons takes place. Depending on other users of the SPS, this process is repeated every 30 to 48 s, giving the so-called *spill* structure. The primary production target *T6* is interchangeable from so called empty or air target, i.e. absence of any solid target material, up to a 500 mm-thick beryllium target. By inserting a hadron absorber, a beam of tertiary muons can be extracted. The momentum of the extracted beam particles as well as their charge are selected by adjusting the optics of the beam line. The COMPASS hadron program uses high intensity hadron beams with 190 GeV/c and typically $5 \cdot 10^6$ particles/s, which are realized by impinging $9 \cdot 10^{12}$ protons/cycle onto the 500 mm thick Beryllium production target. The number of protons per cycle and thus the intensity of the beam may vary dependent on other SPS users and technical issues.

4.2.2 Target Region and Beam Telescope

The Beam Telescope starts around 100 m upstream of the target with the *Beam Momentum Station* (BMS), which measures the momentum of individual particles contained in the muon beam. The BMS consists of six *Scintillating Fibre* (SciFi) detectors grouped around an analyzing magnet and is removed for hadron beams due to the large interaction length of the SciFi. The 2009 setup includes two *cherenkov differential counters with achromatic ring* (CEDAR), which are located around 30 m meters upstream of the target. These detectors provide particle identification for beam particles. The beam telescope in front of the target consists of fast trackers, i.e. two SciFi detector and three cryogenic silicon microstrip detector stations. Scintillating veto counters define the beam diameter and separate the beam from the beam halo. The target is surrounded by a *recoil proton detector* (RPD), which, in case of proton targets, allows to detect the recoil particle. Due to the properties of solid nuclear targets, this detector does not play an important role for the 2009 Primakoff measurement, which uses a 4.2 mm thin nickel disc as target. The disc is mounted into the RPD using the detector as part of the holding structure.

4.2.3 The Large Angle Spectrometer

The second part of the spectrometer, the large angle spectrometer, is built around *SM1*, a 1.1 m long dipole magnet with an integrated field strength of 1.0 Tm located 4 m downstream of the target. The LAS is designed to ensure a polar acceptance of 180 mrad. The preceding tracker telescope starts shortly behind the target with two stations of cryogenic silicon microstrip detectors, which ensure a good vertex resolution, followed by a set of various small and medium-sized gas detectors. Downstream of *SM1*, the setup is completed with the *RICH* detector, providing particle identification, an electromagnetic calorimeter (*ECAL1*), a

hadronic calorimeter (*HCAL1*) and a muon filter, which allows to identify high energetic muons. Thereby, *ECAL1* and *HCAL1* as well as the muon filter have a central hole matching the acceptance of the SAS.

4.2.4 The Small Angle Spectrometer

The small angle spectrometer is designed to provide good momentum resolution for particles with momenta larger than $5\,\mathrm{GeV}/c$ and has an angular acceptance of $\pm 30\,\mathrm{mrad}$. The analyzing magnet *SM2*, located 18 m downstream of the target, has an integrated field strength of 4.4 Tm. The electromagnetic (*ECAL2*) and hadronic (*HCAL2*) calorimeter are positioned at the downstream end of the SAS and are followed by a muon identification system.

4.3 Particle Detection at COMPASS

The following section gives a short overview of the detectors used for the different parts of the COMPASS spectrometer. A more comprehensive discussion can be found in [AAA+07, AAA+15a].

4.3.1 The Tracking System

The tracking system of COMPASS consists of planar tracking detectors, which are grouped in stations. Each detector station consists of multiple tracking detectors of the same type, which are mounted at approximately the same z-position[2], but with different orientation. In order to provide a large acceptance for slow particles, detectors with several square-meters of active area are required. On the other hand, going to small scattering angles, the particle rates quickly increase with decreasing distance to the beam. Thus, a variety of different detectors technologies and sizes is used at COMPASS. Several types of wire-based gaseous drift detectors such as multiwire proportional chambers (MWPCs), drift chambers (DC) and straw tubes provide the large-area tracking. Going closer to the beam, two types of micro-pattern gas detectors with stripe readout are used – micromegas and gas electron multipliers (GEMs). In the beam area itself, the particle rate exceeds $10^5\,\mathrm{mm}^{-2}\,\mathrm{s}^{-1}$, which exceeds the rates possible to readout with the detectors mentioned so far. This area is covered by scintillating fibre detectors and GEM detectors with pixel readout and in the target area, as mentioned before, with silicon stripe detectors, which are operated at cryogenic temperatures.

[2]With the z-axis pointing along the axis of the incoming beam.

4.3.2 Particle Identification

An important aspect of the COMPASS spectrometer is the particle identification (PID). Different identification schemes are applied. The identification of the beam pions and kaons is provided by two CEDAR detectors, which are installed several meters upstream of the target. They rely on the Cerenkov effect. Another Cerenkov detector, the RICH, can identify charged pions, kaons and protons with a momentum up to 45 GeV/c. Muon identification is provided by a combination of iron (Muon-Filter 1) and concrete (Muon-Filter 2) absorbers and drift tube detectors, namely Muon-Wall 1 (MW1) and 2 (MW2). Last but not least, photons are detected in the two electromagnetic calorimeters and can be identified by using information of the tracking system.

4.4 Software

Taking approximately 0.5 PByte of raw data per year, COMPASS relies on several pieces of software, which are used during data recording and for the analysis of the data. In the following, an overview of the software components and frameworks used at COMPASS will be given, concentrating on the components relevant for the work presented in this thesis.

4.4.1 ConfigServer - A Distributed Frontend Configuration Service

Most of the frontend electronics used in COMPASS need to be programmed or configured before they can be used. While this, in principle can be done manually or partial manually using scripts, due to the total number of front ends, different settings and the expert knowledge required, this is practically not achievable.

Thus, this task is taken over by the *ConfigServer*, a process which runs on all frontend computers, with a direct programming interface to the electronics [Kuh07]. The configuration is stored in a database, which is consulted by the ConfigServer processes retrieving a list of frontend modules, which are connected to the frontend computer, it is executed on, and the required settings. These modules identified by integer numbers, so-called *srcid*s, are registered to a master process via the *Distributed Information Management System* (DIM) developed at CERN[3]. All control commands are distributed via this interface.

The program, written in C++, has a modular design, which handles the loading and controlling of different type of frontends. The core program handles the communication via DIM and provides some general interfaces like database connection, VMEbus (Versa Module Europa bus) and I^2C (Inter-Integrated Circuit)

[3] dim.cern.ch

access. The functionality of retrieving configuration as well as writing the configuration to the frontend is then implemented in these modules. This design provides a maximum of flexibility to adapted the software to the requirements of different frontend electronics.

4.4.2 The Online Filter Cinderella

Cinderella is a framework, developed in ANSI C, which provides online filtering capability to the data acquisition system (DAQ) of COMPASS [Nag05]. Being part of the COMPASS data acquisition system, every event, which is acquired from the frontend electronics upon a trigger signal, is processed online by this software, using a computer farm at the experimental cite. Due to the fact, that events are processed online, there are strong time constraints.

In order to provide flexibility for different experimental setups as well as different physics channels, the framework is designed modular with inter module dependencies. The configuration is managed via XML files. CINDERELLA acts not only as a second level trigger, but also as an online monitoring system, as in the case of monitoring of the configuration parameters of the digital trigger (see chapter 6).

4.4.3 The ROOT framework

ROOT [BRo14, ABB+09], developed at CERN and written in C++, is an object orientated software framework, which provides basic functionality and utilities for analysis of large amounts of data in high energy particle physics and is used by many COMPASS software projects.

4.4.4 Event Reconstruction with CORAL

Event reconstruction at COMPASS is done using CORAL[4]. The detector response of real data or Monte Carlo simulation is taken as input to reconstruct full event information, i.e. particle tracks, vertices, calorimeter clusters, particle IDs. The reconstruction is done in several steps. The first step is the *decoding*. During decoding, detector hits are formed out of digitized detector signals, applying detector mappings and calibrations. For some detectors, like calorimeters, this includes pulse shape analysis. During the next step, *clustering*, hits within one detector, which, by the expected detector response are assumed to origin from the same particle trajectory, are combined into clusters. The *pattern recognition* combines clusters of different detectors into track-lets, i.e. straight tracks in certain spectrometer regions. Those track-lets are combined during *bridging*. A *Kalman filter* is used to get the best track parameters. Upon the track parameter the *vertexing* algorithm determines interaction points. Calorimeter hits,

[4] **CO**MPASS **R**econstruction and **A**na**L**ysis project

which are excluded from tracking, are made up into calorimeter showers, which describes the energy deposit as well as time and position of the detected particle. If a track crosses the calorimeter in the region of a calorimeter cluster, the cluster will be associated with the track. The results are stored in Data Summary Trees (DST) using the I/O functionality of the ROOT framework. There is the possibility to store additional detector information, like raw data and detector hits of specific information, which might be used for detector analysis. For physics analysis the so-called minimal Data Summery Trees (mDST) are used, which contain all relevant information. For the here presented work revision 13489 of the CORAL framework, which except some fixes for Monte-Carlo data is identical to the revision used for the initial data production (see chapter 8), is used.

4.4.5 Monte-Carlo Simulations with COMGEANT

COMGEANT simulates particle reactions, including detector response, within the COMPASS spectrometer. It is used to accomplish Monte-Carlo studies for COMPASS. Currently, it is based on the well established GEANT 3.21 Monte Carlo framework, which is used to simulate particle interactions in high-energy physics. All relevant interactions in the COMPASS spectrometer are simulated using material and magnetic field maps. Internal or external event generators may be used as starting point of the event simulation. The output files contain a list of detector hits, which can be processed with CORAL doing the event reconstruction. For the presented work revision 384 of COMGEANT is utilized. This revision contains all general available tuning for the 2009 Primakoff data taking period.

4.4.6 The Analysis Framework PHAST

The *PHysics Analysis Software Tools* (PHAST), an object oriented COMPASS specific analysis framework written in C++, provides a convenient way to access and analyze the content of DSTs. The framework provides a plugin mechanism for user defined analysis functions and an easy to use interface to the ROOT I/O stack for the purpose of storing the results.

Chapter 5

ECAL2

Calorimeters are detectors, which measure the energy of an incoming particle. In contrast to tracking detectors, where it is desirable to have a minimum impact to the passing particle, measuring the energy of a particle is a destructive measurement. In high-energy particle physics two types of calorimeters play an important role – *electromagnetic* and *hadronic calorimeters*. The principle of operation of these types of calorimeters will be described in this section. As mentioned before both the *LAS* and *SAS* of COMPASS are equipped with electromagnetic and hadronic calorimeters. All COMPASS calorimeters have similar design and function principles. ECAL2, the electromagnetic calorimeter of the small angle spectrometer, plays a prominent role for the work presented in this thesis. Therefore the discussion will concentrate on the specific properties of this detector and its setup during the Primakoff run in 2009 (see section 5.2). But before discussing the details of ECAL2 a short introduction to the fundamental working principle of electromagnetic and hadronic calorimeters (section 5.1) is given. The readout system of ECAL2, which is similar to other calorimeters used at COMPASS, is then discussed in section 5.3, followed by a more detailed discussion (section 5.4) of the *mezzanine sampling ADC* (*MSADC*), which plays a central role in the trigger scheme, which is used for the Primakoff measurement and discussed in chapter 6.

5.1 Principle of Particle Detection

Electromagnetic calorimeters are used to measure the energy of electrons, positrons and photons. For electrons and positrons at energies of more than a few 100 MeV the dominant process of energy loss is the emission of photons due to the deceleration in the electric field of the nucleus. This process is called *Bremsstrahlung*. The dominant reaction for photons at these energies is the production of e^+-e^- pairs. By successive combination of these two processes an electromagnetic shower is generated, which can be detected by its ionization or light signal. The signal is proportional to the deposited energy and can be detected by suitable

readout systems.

Hadronic calorimeters are used to measure the energy of hadrons, which generate hadronic showers by series of inelastic reactions. Hadronic calorimeters are usually sampling calorimeters build up of alternating layers of absorbing and detecting materials. Hadronic showers have a large variance in number and type of particles. This and the fact, that only a small part of the energy is actually deposited into the detecting layer, reduces the energy resolution in comparison to electromagnetic calorimeters.

5.2 The Detector Layout of ECAL2

During the Primakoff run in 2009, ECAL2 was equipped with 3068 cells, which were arranged in a grid of 64×48 cells leaving a hole of 2×2 at the position of the undeflected beam. Each cell has a quadratic front surface with of $3.83\,\text{cm} \times 3.83\,\text{cm}$. The length of the cells is 45 cm. The central part of the calorimeter is equipped with 860 Shashlik modules, which are accompanied in the outer part with GAMS and radiation hard GAMS-R modules, as depicted in Figure 5.1. The Shashlik modules are made out of alternating layers of lead, which induce the electromagnetic showers, and scintillating material, which is made out of plastic. Wave-length shifting scintillating fibres transport the signal to photomultiplier tubes (PMTs), which are used to amplify the signal. Figure 5.2 shows the photograph of a Shashlik module as installed in ECAL2. The GAMS and GAMS-R modules are made out of transparent blocks of lead-glass and radiation hard lead-glass, respectively. The signal amplification for the GAMS modules is also realized with PMTs.

5.3 The Readout Chain of ECAL2

The PMTs attached to the calorimeter modules are connected to shaper cards, which transform the analogue PMT pulses into pulses with a rise time of 50 to 62.5 ns and a long falling tail. The shaped analog signals are fed into sampling ADCs (see section 5.4). The 12bit ADCs work with a sampling frequency of 80 MHz. After digitization, pedestals calculated during the off-spill time are subtracted, setting the baseline to 50 ADC channels. Upon a trigger signal a configurable number of samples per module with configurable latency is transferred to the central data acquisition system. Thereby, a zero suppression algorithm reduces the amount of data by only transferring samples from modules, where the signal exceeds a certain threshold.

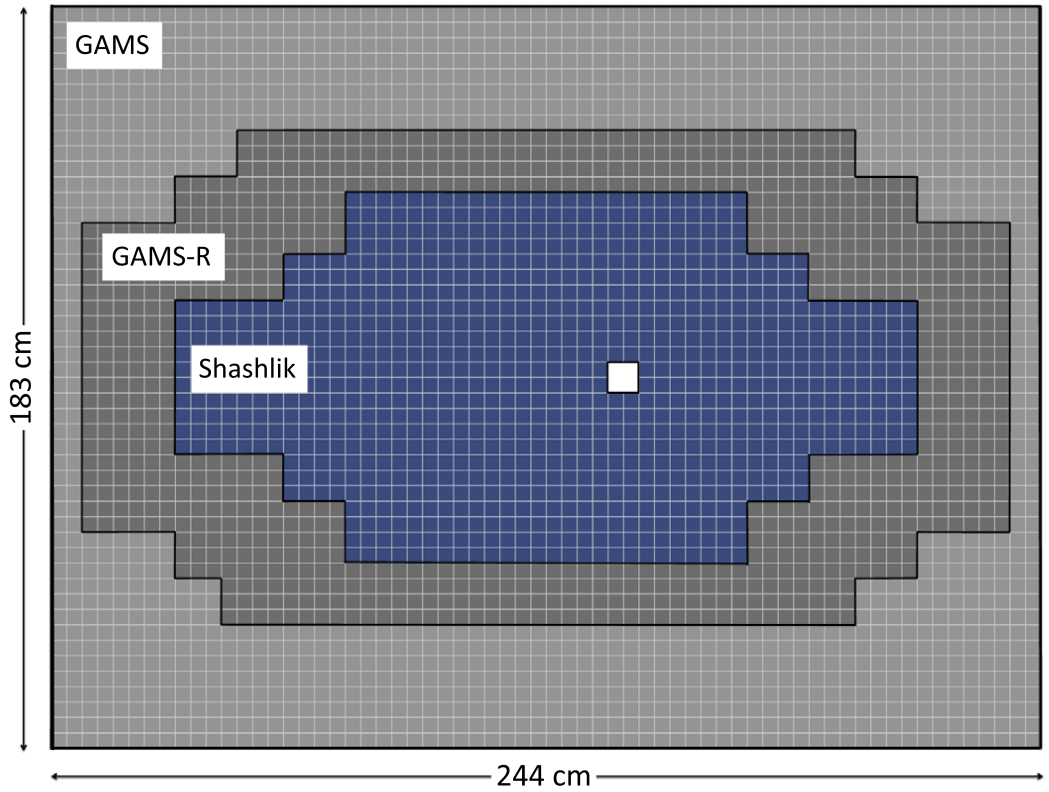

Figure 5.1: Schematic view of ECAL2 showing the cells installed during the 2009 Primakoff data taking period. (From [AAA+15a]).

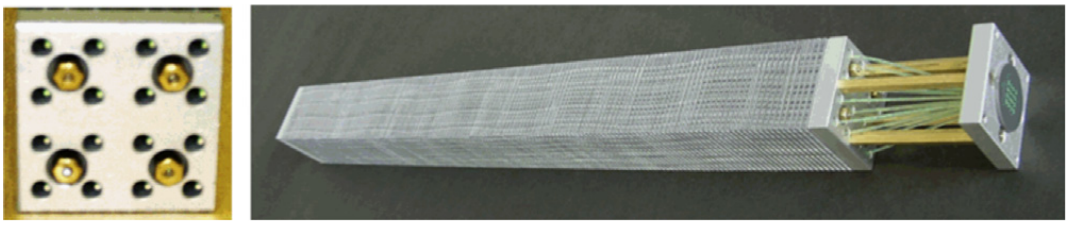

Figure 5.2: Photograph of a Shashlik module as installed in ECAL2. (From [AAA+15a]).

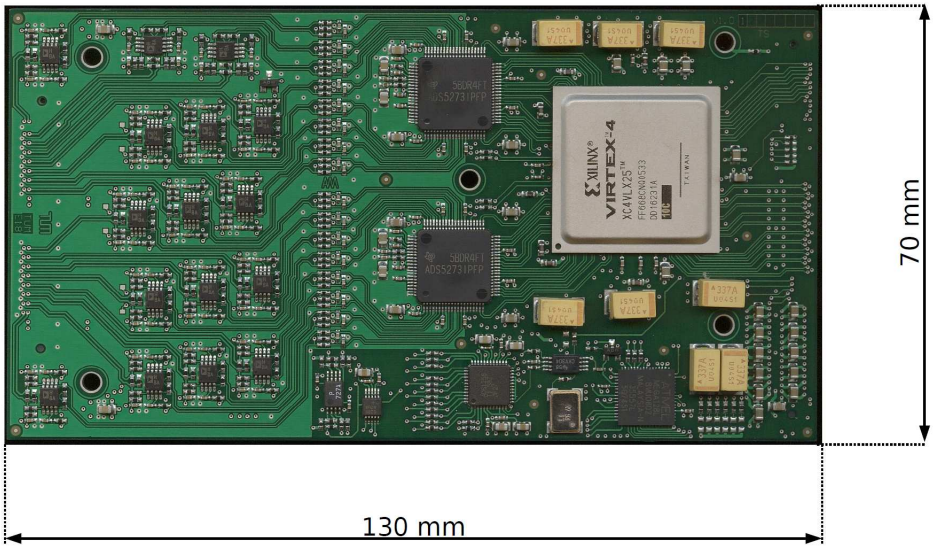

Figure 5.3: Mezzanine sampling ADC module used for ECAL2 readout. (From [FHK+09]).

5.4 The MSADC Readout

Given the advantage of having access to the pulse shape of a signal, versatile sampling Analog to Digital Convert (ADC) modules [MKP07] are used to digitize the signals of ECAL2. These ADCs are mounted on mezzanine cards (see figure 5.3), which makes this card versatile as the mezzanine card can be mounted to different types of carrier cards. This allows to the same ADC cards in small experimental setup with only a few channels, which a readout via a local connection, and large scale setups, like COMPASS. In case of COMPASS the mezzanine cads themselves are mounted to 9U[1] VME[2] carrier cards. The 12bit ADCs chips, which are mounted to the mezzanine card, are capable of sampling 16 input signals at a frequency of 40 MHz. In order to reach a sampling frequency of 80 MHz, two ADC chips run in an interleaved mode. This means both chips are connected the same 16 input channels sampling at 40 MHz, but the clock signal of both chips differ by half a clock cycle. Each mezzanine card mounts four chips and is able to read 16 channels at a combined sampling rate of 80 MHz. The carrier cards holds four mezzanine cards reading 64 channels in total. Each mezzanine card as well as each carrier is equipped with a *Field Programmable Gate Array* (*FPGA*), which is used to control the readout and transfer the data to the upstream data acquisition system. The FPGAs mounted on the mezzanine cards are connected to the FPGA on each carrier card as depicted in the scheme shown in figure 5.4. While the FPGAs are operated at 80 MHz in order to increase the bandwidth,

[1]Height in rack units (1 U = 4.4 cm)
[2]Versa Module Eurocard, IEEE 1014

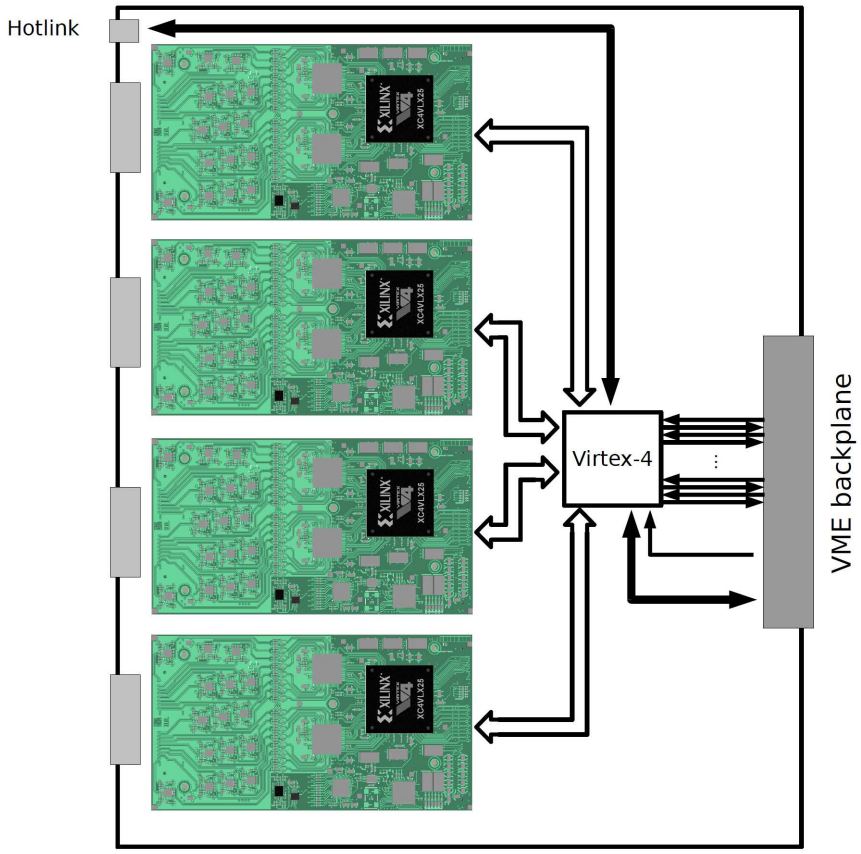

Figure 5.4: Schematic view of the VME carrier card holding the mezzanine sampling ADCs. (From [FHK+09]).

the link between carrier and mezzanine card is driven with 160 MHz. The programming and controlling of the ADCs and FPGAs is done via the VME back plane, enveloping an I^2C interface into the VMEbus interface. The data acquisition itself uses front side connectors running a custom protocol called HOT-LINK [MKA+09].

Chapter 6

The Primakoff Trigger

A suitable trigger setup is required to access the low momentum transfer regime in π^-Ni reactions and therefore Primakoff interaction at COMPASS. For the Primakoff run in 2009, a completely new trigger scheme was developed. This trigger setup was optimized to measure the Pion polarizability in π^- Ni $\rightarrow \pi^-\gamma$Ni reactions, but is also suitable for other physics topics. Aiming for the low transfer momentum regime, the reactions of interest are identified by a clear signature, i.e the emission of a hard photon in forward direction. Due to the relativistic boost the trajectories of the emitted photons pointed towards the center of ECAL2. Thus a calorimetric trigger sensitive to the energy deposit in ECAL2 is a good choice to select interesting events. The trigger scheme discussed in the following was first presented in 2009 [FHK$^+$09]. A more complete discussion with the focus on the FPGA implementation and performance assessment can be found in [Hub10].

The choice of implementing a digital trigger have several advantages over an analog setup. On the one hand time and energy calibrations are used to simplify commissioning (see section 6.1). On the other hand advanced signal detection algorithms and pulse shape analysis improve noise rejection and feature extraction (see section 6.2). The main disadvantage of a digital trigger is its higher latency[1] in comparison to analog trigger. While in COMPASS the latency of 500 ns for the analog triggers are given by the time of flight and signal transmission, the digital trigger was estimated to need additional 500 ns for digitization and processing. The maximum achievable latency is defined by the caching capabilities of the front-end electronics. A latency of 1.2 μs was chosen, which is still compatible with the limitation given by the front-end electronics and provide some safety margin with respect to the estimated latency required by the digital trigger logic.

In order to avoid development and production of new hardware, the functionality of the existing ADC readout as described in section 5.4 had been extended by modifying the firmware of the FPGA. Thereby, the strongest limitation to the

[1]The time between the moment, where the beam particle crosses the target position, and the moment, where the trigger decision reaches the front-end electronics.

implemented trigger logic is the limited communication bandwidth between the FPGAs, which has to be shared with the readout logic. Due to this limitation the trigger logic restricts itself to a rather simple summation scheme. The scheme respects the time and amplitude information, which are obtained by means of pulse-shape analysis, and incorporates the use of energy and time calibrations. In principle all calorimeter cells maybe considered. However the contributing calorimeter cells can be freely chosen by marking active cells. Finally, a trigger decision is formed by comparing the energy sum to a threshold. The newly designed trigger backplane, the only new hardware component, supports the output of two trigger signals with two different thresholds. The threshold had been set to approximately 40 and 60 GeV. The output signals of the backplane are so-called level signals, which are present for the length of a clock cycle of the main reference clock of the COMPASS experiment, i.e. 25.6 ns. They occur synchronous to the 80 MHz clock, which is used to drive the FPGAs. Thus these signals provide only limited time information. A precise trigger time is obtained by building the coincidence of each of this signals with a minimum-bias beam trigger, which uses the coincidence of two SciFi detector stations, which are placed upstream of the target.

6.1 Time- and Energy-Calibrations

In many trigger schemes, the coincidence of signals from different detectors play an important role. This is especially true for a calorimetric trigger, where each cell, which is considered, has its own readout and amplification system and therefore also its own latency. This has to be respected when considering the coincidence of the signals. In contrast to an analog trigger setup, where all latencies have to be adapted to the same value[2], in the digital trigger setup at COMPASS, this is fixed by applying time calibration. In case of a calorimetric trigger, which is sensitive not only to the appearance of a signal but also to the energy deposit, it is important, that all signals have the same or at least similar response to the energy deposit. Building an analog trigger, this requires are fine-tuning of the high voltage setting of the PMTs. For the digital trigger energy calibration are used to account for difference in the gain. Using time and energy calibration instead of fine-tuning cable length and high voltage of individual channels has obviously a big advantages during commissioning and operation of the trigger.

The energy calibrations are obtained during a dedicated calibration procedure, which is used to determine basic calibration for offline analysis and has to be applied in any case. Indeed, the same energy calibrations are used for offline reconstruction and triggering[3]. The programming of the trigger modules is done

[2]Traditionally the cable length and therefore the delay for each individual channel are adapted.

[3]Offline reconstruction however uses additional corrections to the energy calibrations, which

using the ConfigServer, which converts the floating point values stored in the database into 10bit integers as required for the FPGA[4]. An energy equivalent is calculated by multiplying the observed amplitude of a signal with the corresponding calibration value. The algorithm, which converts the floating point values to integer, takes the targeted energy threshold into account making optimal use of the available precision. In general the ConfigServer retrieves the configuration necessary to program the frontends from a database. Thus the calibrations and configurations of the trigger are also stored into a database. In contrast to the calibration files, the database is extended by additional fields. This fields allows on the one hand tracking of the configuration active at a certain time and on the other hand easy management of active and passive cells, i.e. cells used to build the trigger decision and cells, which are ignored.

A similar database holds the time calibrations. The time calibrations are determined by a specific module added to the COMPASS online filter *Cinderella*, which runs on a computer farm at the experimental site providing online analysis capabilities. It also monitors the stability of energy calibrations by evaluating LED pulses injected into the calorimeter. In order to determine the latency of individual cells a software implementation of the constant fraction algorithm (see section 6.2), which accounts for the latency between individual trigger signals and the experimental clock, is used. Evaluating the time distribution of detected signals, the latency is measured on a run by run basis. This allows monitoring of the stability of this quantity and provides a convenient update mechanisms, thus new calibration can be applied easily. For the FPGA programming, a common offset, which allows to adjust the latency with respect to other signals, like the beam trigger, is added to the time calibration. Technically the time calibrations are split into two parts. The first part is a multiple of the clock cycle of 12.86 ns, which directly configures the depth of a delay buffer. The second part is the remainder, which is added to the measured time t_{signal} of individual signals(see section 6.2).

6.2 Signal Detection on an FPGA

One of the key components of the digital trigger is the identification of a signal and extraction of its features, i.e. time and amplitude. This is done on channel level applying an algorithm resembling a *Constant Fraction Discriminator* (*CFD*). A CFD splits the incoming signal into two, delaying and inverting one and attenuating the other one to a fixed fraction. Independent of the signal amplitude the sum of this signals becomes zero at a time, which is fixed to the signal shape and therefore a good measure of the signal time. The amplitude of the sig-

are not available at the time of data recording.

[4]The floating point performance of FPGAs is much worse than their integer performance. Thus floating point operation has to be avoided.

nal is measured at a fixed latency to this time exploiting the fact that all signals have similar shapes. Providing a digital implementation of the algorithm, the algorithm has to be tuned to give good precision and high efficiency. Targeting the FPGA as execution platform the attenuation of the inverted signal is replaced by an amplification of the delayed signal $s(t + \Delta t)$, replacing a division, which is inefficient on FPGAs, by a much more efficient multiplication with factor a. The inversion of signal $s(t)$ is omitted by calculating the difference instead of the sum

$$d(t) = s(t) - a \cdot s(t + \Delta t). \tag{6.1}$$

The time t_{signal} a signal is triggered, is defined by the condition

$$f(t_0) = 0 \text{ AND } f(t_{\text{signal}} - dt) < 0 \text{ AND } f(t_{\text{signal}} + dt) > 0. \tag{6.2}$$

The long exponential tail of the signal, as it comes out of the shaper, does not provide any time information[5]. Thus choosing the two parameters a and Δt in a way that this condition is fulfilled, when $s(t)$ is approaching its maximum, the full information of the rising flank of the signal is used to achieve the best possible time resolution. The sampling structure of the data, which gives the amplitude of the signal at discrete times, requires modification of the algorithm. Thus for each sample i the difference d_i between the pedestal corrected signal s_i at sample time i and the amplified signal $a \cdot s_{i-n}$ at sample time $i - n$ is calculated

$$d_i = s_i - a \cdot s_{i-n}. \tag{6.3}$$

Thereby a signal is triggered under the conditions

$$d_{i-1} > 0 \text{ AND } d_i \leq 0 \text{ AND } s_{i-1} - s_i > b, \tag{6.4}$$

where b is a programmable threshold rejecting noise. This parameter is chosen to 20 (ADC channels), which dependent on the actual energy calibration implements an amplitude threshold of approximately 1 GeV. Figure 6.1 shows the signal s_i and the delayed and amplified signal $a \cdot s_{i-n}$ as well as the resulting difference d_i. The parameters are chosen to $a = 2$ and $n = 2$. This parameters are also used for the final implementation of the trigger algorithm.

Keeping in mind the implementation on the FPGA, the time information are similar to the time calibration, split into a coarse time t_{coarse} given in full clock cycles and a fine time t_{fine}, which provides sub clock cycle information. The coarse time of the signal is given by the sample index i

$$t_{\text{coarse}} = i \tag{6.5}$$

[5]Without prior knowledge of the amplitude

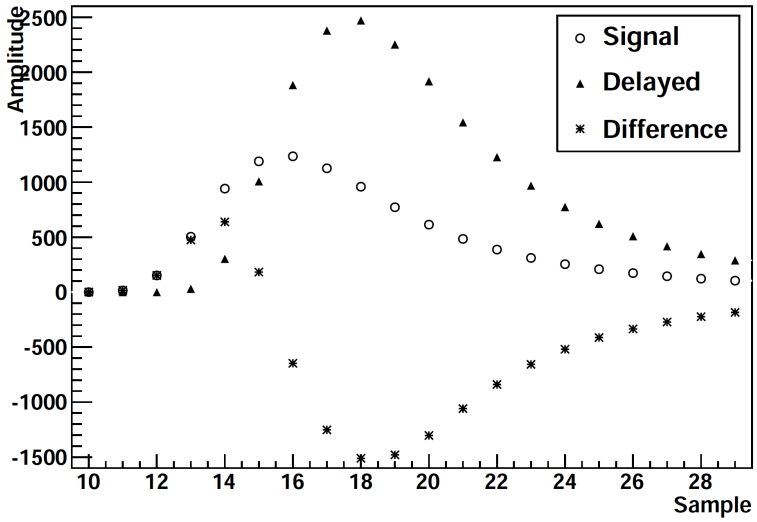

Figure 6.1: The digital constant fraction discriminator. Shown is the signal s_i, the delayed and amplified signal $2 \cdot s_{i-2}$ and the difference d_i of both. Taken from [FHK+09].

while the fine time of the signal is obtained via linear interpolation

$$t_{\text{fine}} = \frac{d_i}{d_{i-1} - d_i}. \tag{6.6}$$

In order to avoid divisions, the calculation of $(d_{i-1} - d_i)^{-1}$ is implemented using a look up table. Note that the fine time is negative, thus the signal time t_{signal} is obtained via summation

$$t_{\text{signal}} = t_{\text{coarse}} + t_{\text{fine}}. \tag{6.7}$$

In order to compensate the dispersion of signals in different channels the earlier discussed time calibration t_{shift} is used to synchronize the signals off all readout channels by calculating the synchronous signal time

$$t_{\text{signal,sync}} = t_{\text{signal}} + t_{\text{shift}}. \tag{6.8}$$

The amplitude s_{max} of the signal is determined by scanning three sample with fixed latency to the coarse time t_{coarse} for its maximum, which is converted to a normalized amplitude a by multiplication with the corresponding energy calibration constant c_{ecalib}

$$a = c_{\text{ecalib}} \cdot s_{\text{max}}. \tag{6.9}$$

The normalized amplitude is filled into time bins according to the measured signal time. Implemented in a synchronized FIFO running at the internal frequency of the FPGA in order to allow for fluctuation two bins are filled. The first bin is filled using the coarse time $t_{\text{coarse,sync}}$ of the synchronous signal time. The second

bin is chosen according to the Most Significant Bit (MSB) of the synchronous fine time. The MSB of the fine time indicates, if the signal appeared in the first or second half of the clock cycle, thus the previous or next bin is chosen to be filled.

6.3 Summation of Signals

As mentioned before, the bandwidth between the mezzanine card and the carrier card as well as between the carrier card and the back plane module is limited. This has to be taken into account when calculating the trigger energy sum. Thereby, not only the piece of hardware, where each summation step is executed, but also the precision of input and output values have to be chosen carefully.

The ADC chip, which is used to digitize the analog signals, has a dynamic range of 12 bit. The normalized amplitude is calculated by multiplying the amplitude of the detected signal given in ADC channels with the corresponding 10 bit calibration value. In order to account for the precision of the measurement, only the 12 most significant bits (MSB) of the result are taken into account. Summing over all connected channels, the first step of summation is executed on the mezzanine cards. The result of the summation has formally a width of 16 bit. Taken into account, that the physically interesting range of the sum is identical with the range of a single cell, only 12 bits are transferred to the carrier card handling an overflow by transferring the maximum value 0xFFF. If no overflow occurs the 12 least significant bits (LSB) are transferred. The transfer to the carrier card is done using a semi-serial connection transferring six bits at 160 MHz. The FPGA on the carrier card is used to calculate the sum of the 64 channels connected to the four attached mezzanine cards. The resulting 15 bit value is reduced to nine bits considering overflows and transferred to the back-plane, where the total sum is calculated. In 2009, the trigger scheme, is restricted to the inner part of ECAL2. Thus only one back-plane module, which is connected to up to eight carrier cards, was used. However the design allows to extend the trigger up to the complete calorimeter by combining multiple back-plane modules. The back-plane module is equipped with two NIM outputs, which are activated, when the sum over all channel exceeds the threshold, which is assigned to the output. The thresholds can be independently assigned to each of the outputs. The described data flow is visualized in figure 6.2.

6.4 Configuration of the Trigger

Figure 6.3 shows the shower occupancy of ECAL2, which was obtained during the 2009 data taking period. The dashed line indicates the area, which was connected to the back-plane and therefore would have been available for the trigger decision. The solid line encloses the area, which was considered for the trigger. It is an area of 12×12 cells in the center of ECAL2, where 3×4 cells, which are located around

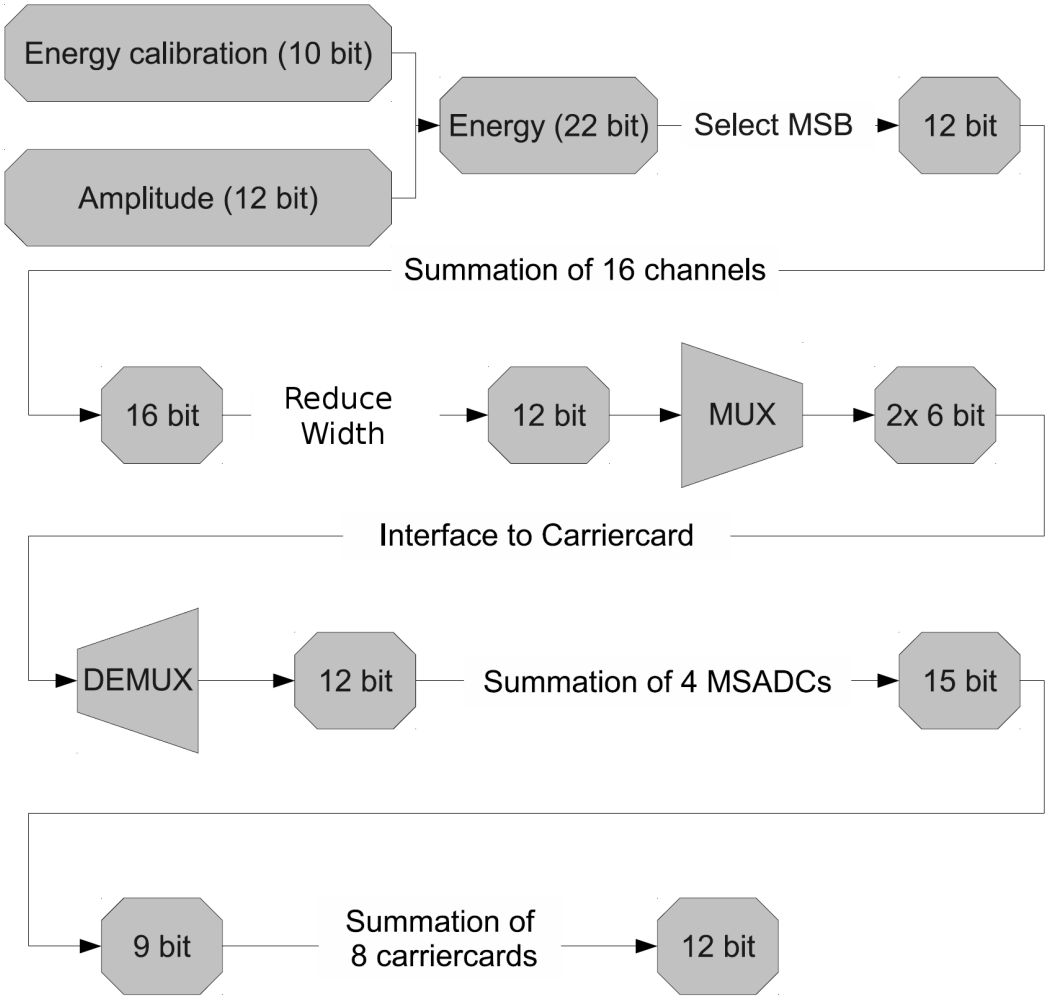

Figure 6.2: Schematic drawing of data flow form the ADCs to the trigger back plane. The flow chart is illustrating the evolution of the data width within each calculation and transmission step. While each calculation increase the width of the intermediate result, the width has to decreased during transmission due to bandwidth limitations. (Based on [Hub10]).

the hole where the undeflected beam pass, are excluded. The correlation between the occupancy and the active area is clearly visible. As mentioned before in 2009 the thresholds for the two independent NIM signals, which occur synchronized to the internal 80 MHz clock, were set to 40 GeV and 60 GeV. The triggers formed with coinciding beam triggers are called *Prim1* (40 GeV threshold) and *Prim2* (60 GeV threshold), respectively. For typical signals and calibration constants, the energy resolution achieved by the summation process is in the order of 1 GeV. In order to match the readout capabilities of the data acquisition system for the *Prim1* trigger only every second trigger attempt is considered.

6.5 Evaluation

Besides the evaluation of general feasibility the expected trigger rate and performance was evaluated before the trigger had been implemented. The results of this study are presented in 6.5.1. In [Hub10] a detailed analysis of the performance finally achieved and of observed problems is presented. Nevertheless in section 6.5.2 an overview of the findings of this analysis will be given.

6.5.1 Performance Expectation

As part of the feasibility study, the expected trigger performance had been evaluated. Thereby, the capability of the online filter Cinderella to run offline, i.e. on recorded data, was exploited. A configurable module, which besides the full evaluation of the trigger scheme allows to determine the time calibrations (see section 6.1), was developed. A central feature of this module is the implementation of the mentioned CFD algorithm, which can be extended to an optional full simulation of the complete trigger algorithm. Further options allow to account for the limited precision of the algorithm implemented on the FPGA. The evaluation is based on a data sample of 50 spills recorded in 2008, when a proton target was in use. Random and beam trigger events are selected to extract a minimal-bias event sample. It is expected, that the spectrum is dominated by strong processes. Thus considering, that the proton and nickel target have similar interaction length, it is assumed, that the proton data allows to estimate trigger rates for different trigger topology and algorithms. Therefore the 32 samples, which are recorded for each channel are evaluated. The trigger rate is estimated on bases of beam trigger events, thus the fraction of beam triggers, which coincide with calorimetric triggers, is obtained. This fraction was estimated to 1.8 % and 1.1 % for *Prim1* and *Prim2* configuration. This numbers can be set in correlation with observed trigger rates. During physics data taking about $2.7 \cdot 10^7$ beam trigger attempts are received during the on spill time of each spill. Having an on-spill time of 9.6 s, this corresponds to trigger frequencies of $\approx$ 50 kHz and $\approx$ 30 kHz, respectively. This is in good agreement with the $4.5{\cdot}10^5$ and $2.7{\cdot}10^5$ trigger attempts per spill,

which were observed in 2009. It should be mentioned, that during the Primakoff run a slightly modified beam trigger with a rate of $2.6 \cdot 10^7$ attempts per spill was used to form the coincidence. Figure 6.4 shows the time residual distribution after applying time calibrations for all signals occurring in the 3068 cells of ECAL2 for the 50 spills event sample used for evaluation. For this small data sample, which was recorded with lower luminosity, the average time resolution $\bar{\sigma}_t$ of ECAL2 is determined to be below 1 ns. Due to various effects, like temperature variation and luminosity effects, the time resolution, which is achievable for an extended run, is expected to be a bit worse. From past experience with ECAL2 it is expected, that time calibrations are quite stable. Further more the time calibration are continuously monitored, allowing for adaptions. Thus also for longer runs a time stability in the order of a few ns is achievable.

6.5.2 Evaluation of the Trigger Performance

A detailed study of the trigger performance was carried out on the basis of the data recorded during the Primakoff data taking period in 2009 [Hub10]. As an outcome of this study the average time resolution is determined to $\bar{\sigma}_t = 1.04\,\text{ns}$ (see [Hub10] section 5.4), which is in the perfect agreement with the expectations (see section 6.5.1).

Besides the time resolution of the signal, the behavior of the threshold plays an important role. This is especially true, when a good understanding of the trigger properties is required. This is the case, when modeling the acceptance of the trigger, where a better defined threshold, finally yield larger statistics and access to events closer to the thresholds. The threshold behavior of the *Prim2* trigger is studied on the basis of the *Prim1* sample, investigating the dependence of the fraction of events, where both Primakoff trigger have fired, to the ones, where at least the *Prim1* tag is set. The dependence of this fraction on energy $E_{\text{thr}} \leq E_{\text{sum}}$ is evaluated (see figure 6.5). The energy sum can be calculated using either the energy calibration available for the hardware trigger (blue) or considering further corrections, which are only available during offline production (yellow). These corrections include corrections based on LED monitoring as well as E- and *time-in-spill*-dependent corrections, which are obtained using a π^0-calibration algorithm. Unfortunately, there is no reference sample with a suitable number of events, which allows to study the *Prim1* threshold. Thus, a similar evaluation of the *Prim1* trigger is impossible.

Already during the data taking some implementation-specific problems have been observed by means of data quality monitoring. The largest impact to the data is a problem of the synchronization between FPGA and ADC. This problem effects always all eight channel connected to one ADC. Due to instabilities, which are for example introduced by thermal effects, the timing of such a channel group may change by a clock cycle, i.e. 12.86 ns. These time jumps can occur from spill to spill. For the recorded data, this can easily be corrected by applying time

calibrations, which account for the time shift. The trigger logic, which is also affected by this time jumps, has some build in robustness against such problems. This is achieved by accounting each detected signal in two consecutive clock cycle and thus extending the signal to 25.6 ns. Thus the effect to the trigger, which is discussed in details in [Hub10], is found to be minimal. Considering a reference frame like the Gottfried-Jackson frame (see section 11.1), no acceptance effects with angular dependencies are introduced. Only a small change of the overall efficiency is expected. A detailed discussion of all problems, which occurred, can be found in [Hub10].

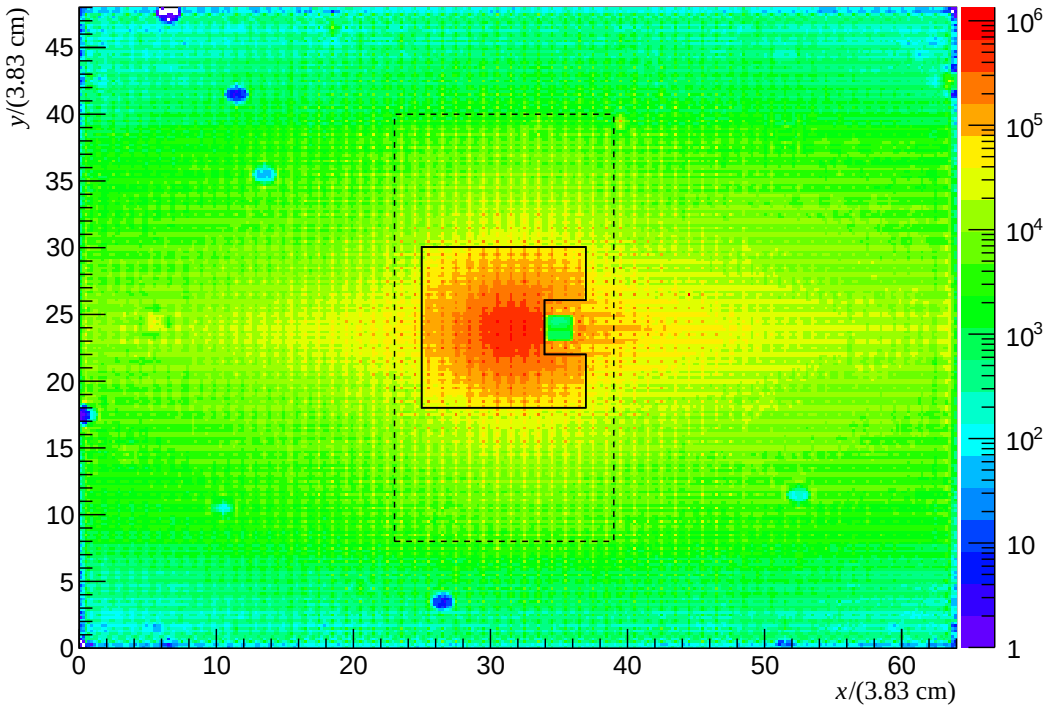

Figure 6.3: Distribution of showers in ECAL2, which are detected during the Primakoff data taking period in 2009. Only showers with energy above 2 GeV are considered. x and y are divided by the cell width of 3.83 cm and the origin of the coordinate system is set to the lower left corner of the calorimeter. The area considered to form the trigger decision is indicated by the polygon. The outer rectangle indicates the area, which is connected to the back plane module, which was installed during the 2009 Primakoff run. The cell structure of the calorimeter is apparent due to clusters, which due to threshold effects on cell level do not provide the full spacial resolution.

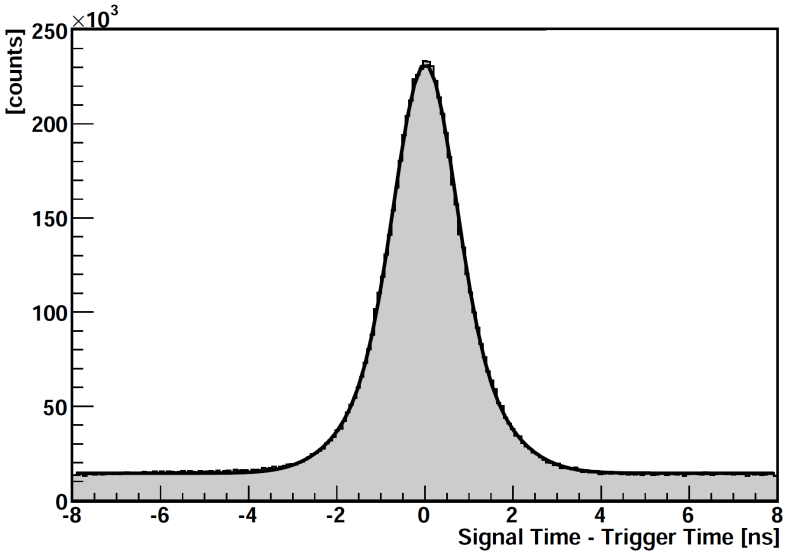

Figure 6.4: Time residual of all 3068 ECAL2 channels after applying time shifts, determined for a 50 spill data sample with Proton target. The ADC threshold for noise rejection is set to 10 ADC channels. (From [FHK+09]).

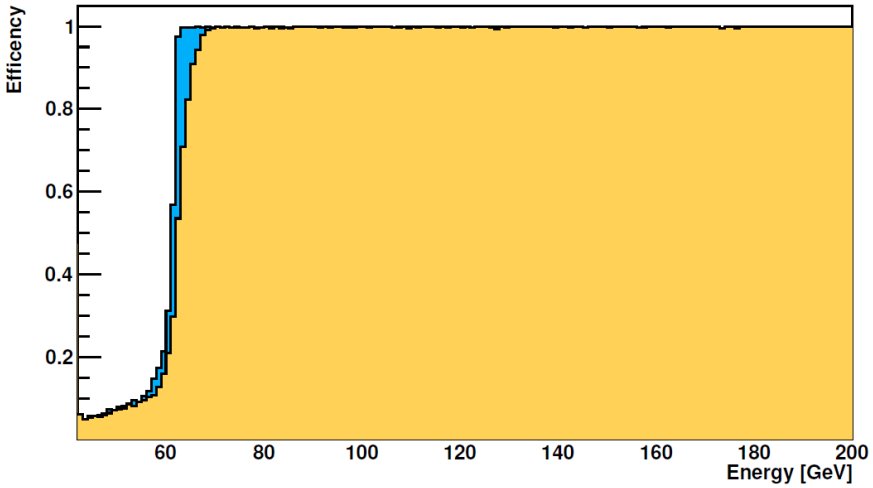

Figure 6.5: Threshold behavior of the *Prim2* trigger for the energy calibration available at the time of data taking (blue) and energy calibrations available for production (yellow). (From [Hub10]).

Part III

Analysis

Chapter 7

Reconstruction of the Pion Beam Energy

While the beam trajectory of the incoming beam particle is determined to high precision, using the silicon beam telescope, due to the removal of the beam momentum station for the hadron beam the momentum and therefore the energy of individual beam particles in the hadron beams is not measured at COMPASS. However the beam momentum has to lie within the momentum distribution imposed by the beam optics, which incorporates correlation between beam energy and trajectory. Extrapolating to the z position of the target at $-72.5\,\mathrm{cm}$ the beam trajectory is defined by its transverse coordinates x and y and its inclination $\mathrm{d}x/\mathrm{d}z$ and $\mathrm{d}y/\mathrm{d}z$. Figure 7.1 shows the dependence of the beam energy, which is determined through analysis of the $\pi^+\pi^-\pi^-$ final state, on each of the parameters of the beam trajectory. Clear correlations are observed. The beam energy, however, depends on all four parameters. Thus the complete picture is much more complex.

Having better knowledge of the beam momentum, as the considerable large spread of 3 % around the mean energy of the beam, namely 191 GeV/c, has considerable impact to many physics analysis, where the beam energy or its momentum, respectively, plays an important role. In order to get a description of the highly non trivial dependency of the beam energy $E(x, y, \mathrm{d}x/\mathrm{d}z, \mathrm{d}y/\mathrm{d}z)$ on the beam trajectory parameters x, y, $\mathrm{d}x/\mathrm{d}z$ and $\mathrm{d}y/\mathrm{d}z$, about 1.37 million events from the 2009 Primakoff data set, which have three charged pions in the final state, are used to train an artificial *neural network* (*NN*). The trained network then can be used to determine the beam energy of beam particles depending on the beam trajectory parameters.

In section 7.1 a short description of the artificial neural networks is given. The focus of this discussion lies on the multilayer perceptron, which is the type of network chosen for this application. The selection of training samples is shortly described in section 7.2. Last but not least the achievements of this approach are presented in section 7.3. A detailed discussion of this topic can also be found in

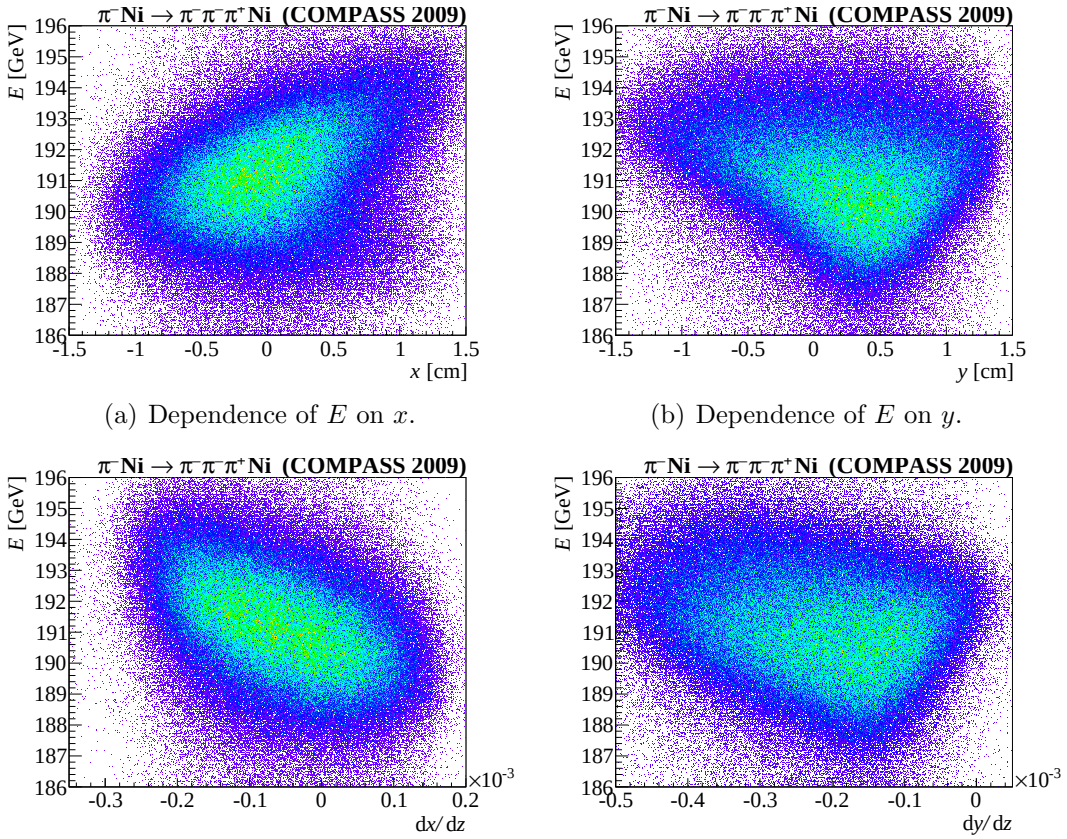

(a) Dependence of E on x.

(b) Dependence of E on y.

(c) Dependence of E on $\mathrm{d}x/\mathrm{d}z$.

(d) Dependence of E on $\mathrm{d}y/\mathrm{d}z$.

Figure 7.1: Dependence of the beam energy measured by final state analysis of $\pi^+\pi^-\pi^-$ events on the parameters of the beam trajectory.

[FK12].

7.1 Neural Networks - Short Introductions

Artificial neural network, inspired by the human brain, consist of neurons with relative simple logic. The neurons process multiple input signals and generate one output signal. The network is formed by connecting the neurons with each other using links, which are often called synapses. Besides the simple logic of the neurons, this kind of networks is an approach to solve problems, which are otherwise computationally difficult to solve. In the following the discussion will focus on *multilayer perceptrons* (*MLP*). MLPs are a class of *feed-forward artificial neural network*, that maps a set of input data onto an appropriate set on output data. It consists out of at least three layers. The input and the output layer have one neuron for each input and output variable, respectively. They are connected via one or more hidden layers with arbitrary number of neurons. Each neuron

of the output and hidden layers are connected to all neurons of the preceding layer. Figure 7.2 shows a simple example of such a MLP. In order to describe the

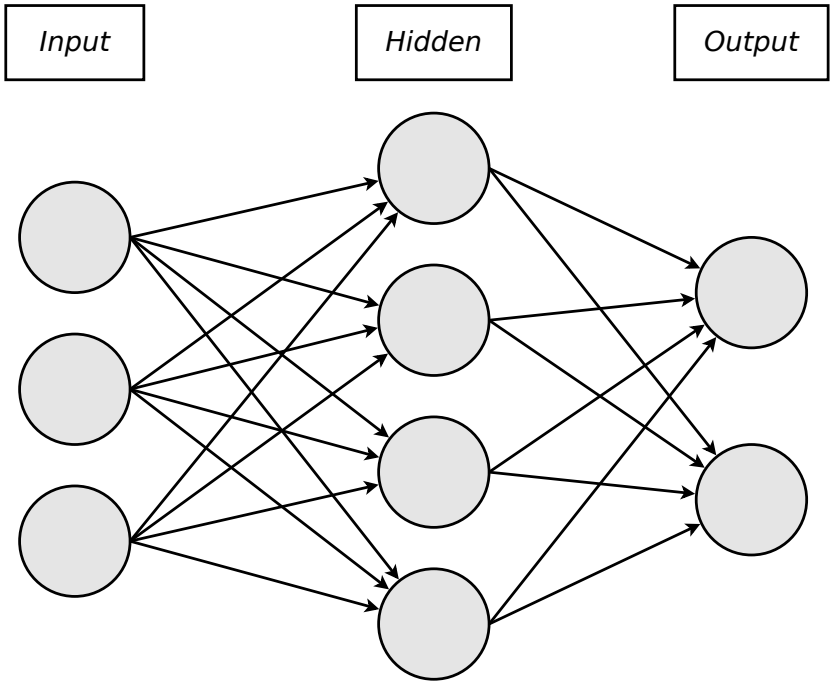

Figure 7.2: Schematic drawing of a multilayer perceptron having three input neurons, two output neurons and one hidden layer, which have four neurons.

topology of a given MLP a commonly used notation is used. The input and output layers are described by a comma separated list of variables. Hidden layers are characterized by the number of neurons. Layers are separated by colons starting from the input layer and ending with the output layer. Using this notation the MLP depicted in figure 7.2 is characterized by $i_1, i_2, i_3 : 4 : o_1, o_2$.

Since otherwise the topology can be reduced to the two layer schema of input and output layer, except for the input and output neurons, all neurons have non-linear *activation functions*. For typical application sigmoids, which are evaluated for a linear combination of the input values, are used. The process to adapt the weights of the input values is called training. MLPs are trained using a *supervised learning* technique called *backpropagation*, which is a least mean square algorithm. This technique thereby uses a set of examples, where input and output values are given, to adapt the weights. The same data set is repeatedly fed to the training algorithm until the error on a test sample, which is split up from the training sample, does not significantly improve any more. Processing the test data set once is called an epoch.

7.2 The Training Sample

In order to get a suitable set of data, which can be used as training sample for the neural network, 1.37 events in the low momentum transfer regime $t' \leq 0.02\,\mathrm{GeV}^2/c^2$ having three charged pions in the final state are selected. Additionally, in order to separate from final states with less particles in the final state, the maximum energy of a single pion in the final state is required to be smaller than 155 GeV. The energy transferred to the target is negligible, the energy sum $E_{\pi^-\pi^-\pi^+}$ of the final state pions equals the energy of the beam due to energy conservation. As the COMPASS spectrometer has a good momentum resolution for charged particles the beam energy for the three-pion events is determined with good accuracy.

The parameters of the beam trajectory are measured with high precision by the silicon beam telescope and extrapolated to the z-position of the target at $-72.5\,\mathrm{cm}$. As the z position is fixed the trajectory is completely described by the coordinates in the x-y-plane perpendicular to the z-axis and the inclination of the beam, which is given by $\mathrm{d}x/\mathrm{d}z$ and $\mathrm{d}y/\mathrm{d}z$.

7.3 The Performance of the Neural Network

The C++ Class *TMultiLayerPerceptron*, which is part of the ROOT framework (see section 4.4.3), provides an implementation of the multilayer perceptron. Several different learning algorithm are included in this implementation. As the systematic of the given problem is not known before hand, a suitable topology for the MLP has to be determined by trial and error. A MLP with four hidden layers is found to be suitable to determine the beam energy. The MLP with the topology [1] *x,y,dx,dy:50:25:6:6:E* is trained utilizing the *stochastic minimization* algorithm until after 100 epochs no further improvements are observed.

Subtracting the energy $E_{\mathrm{NN}} = E(x, y, \mathrm{d}x/\mathrm{d}z, \mathrm{d}y/\mathrm{d}z)$, which is obtained by evaluating the MLP, from the energy $E_{\pi^+\pi^-\pi^-}$ observed in the final state no further systematic correlation are observed (see figure 7.3). This is a huge improvement over using the average beam energy $\overline{E} = 191\,\mathrm{GeV}$, which gets , when looking at the difference between the final state energy $E_{\pi^-\pi^-\pi^+}$ and the beam energy E_{Beam} (see figure 7.4). The width of the so-called exclusivity peak, which is observed in this distributions, is determined by fitting a double Gaussian function with a *tanh* background. By using the neural network the width reduces from 2.0 GeV to 1.5 GeV. This is near the natural Gaussian beam energy spread of 1.2 GeV, which is measured at the production target. The neural network is

[1] Due to some imperfection in the normalization behavior of the input neurons under available learning algorithms the input values for $\mathrm{d}x$ and $\mathrm{d}y$ had to be multiplied by 10^3. Thus all input variables have approximately the same size and spread. This multiplication is finally incorporated into the code of the NN.

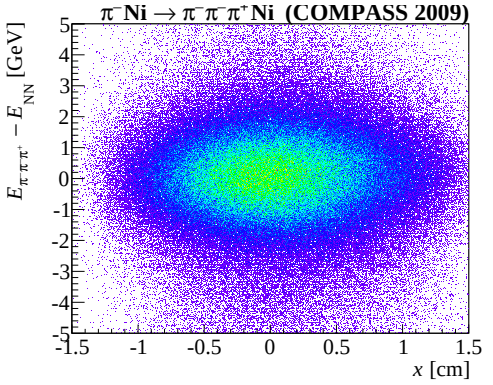

(a) Dependence of $E_{\pi^-\pi^-\pi^+} - E_{\mathrm{NN}}$ on x.

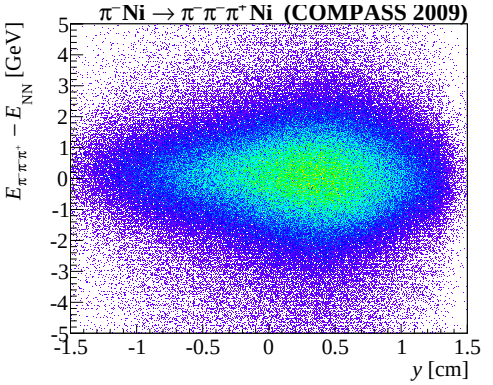

(b) Dependence of $E_{\pi^-\pi^-\pi^+} - E_{\mathrm{NN}}$ on y.

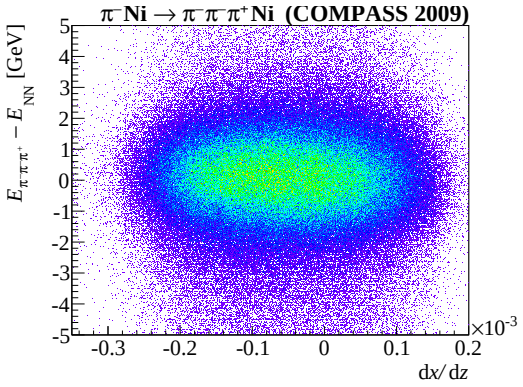

(c) Dependence of $E_{\pi^-\pi^-\pi^+} - E_{\mathrm{NN}}$ on $\mathrm{d}x/\mathrm{d}z$.

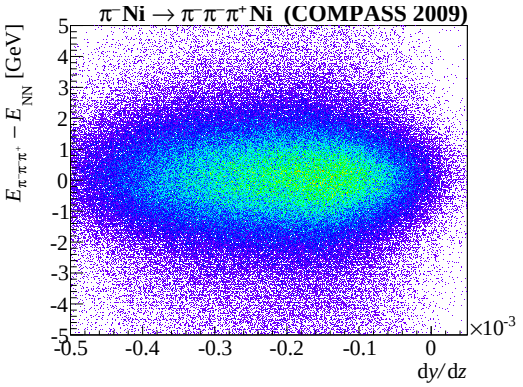

(d) Dependence of $E_{\pi^-\pi^-\pi^+} - E_{\mathrm{NN}}$ on $\mathrm{d}y/\mathrm{d}z$.

Figure 7.3: Dependence of the difference of energy $E_{\pi^-\pi^-\pi^+}$ observed in the final state and the beam energy E_{NN}, which is obtained by evaluating the neural network, on the parameters of the beam trajectory.

calculating the energy of pion particles contained in the beam. The beams optics, which are composed of magnets, act on the momentum of the beam particle. Thus, the energy of other kinds of beam particles can be calculated by accounting for the mass difference of the actual particle and the π^-

$$E_{K^-/\overline{p}} = \sqrt{E_{\mathrm{NN}}^2 + \left(m_{K^-/\overline{p}}^2 - m_{\pi^-}^2\right) \cdot c^4}. \tag{7.1}$$

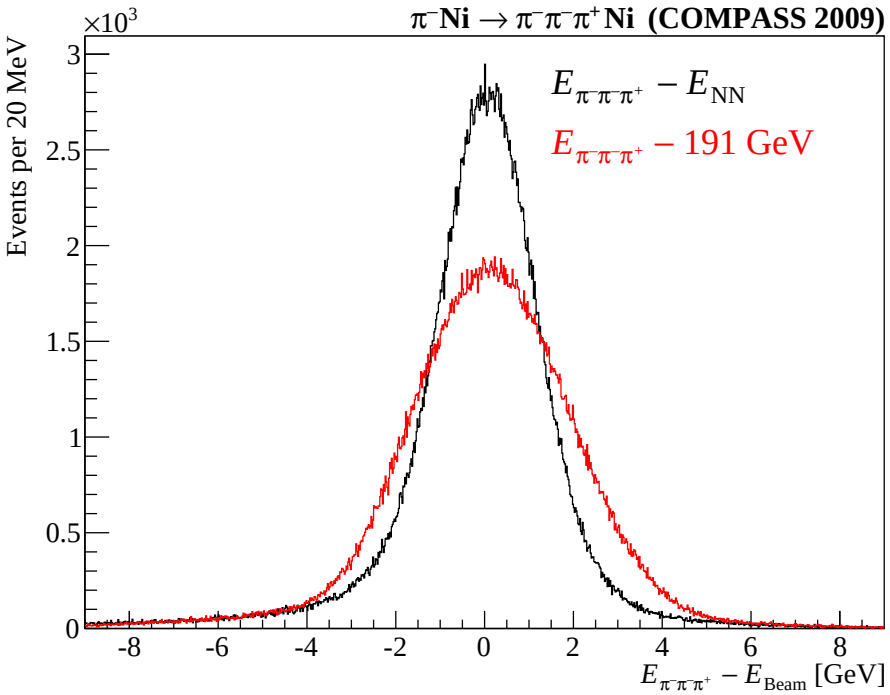

Figure 7.4: Distribution of difference between the energy $E_{\pi^-\pi^-\pi^+}$ of the three-pion final state and the estimated beam energy E_{Beam}. The beam energy is either obtained by evaluating the neural network $E_{\mathrm{Beam}} = E_{\mathrm{NN}}$ (black) or by using the average beam energy of $E_{\mathrm{Beam}} = \overline{E} = 191\,\mathrm{GeV}$ (red).

Chapter 8

Event Reconstruction and Selection

8.1 Data Set

The analysis presented in chapter 13 is based on data recorded during the COMPASS Primakoff run in 2009 using a hadron beam with a mean momentum of 191 GeV/c impinging on a 4.2 mm Nickel target. A set of calorimetric triggers as described in chapter 6 was used to select events, which are recorded. The event selection is based on the so called *t70* production. This production includes the pre-production correction described in section 8.2.

A first event selection is applied by requiring the prerequisites for the later event reconstruction. At least one primary vertex with exactly one incoming and one negatively charged outgoing particle is required. Additionally at least four electromagnetic showers in ECAL2 have to be present. The electromagnetic showers have to fulfill the selection criteria presented in section 8.4. Due to discrepancies between simulation and data, for the current analysis data from ECAL1 are at the moment omitted. The possible increase of the number of events is small ($< 5\,\%$), while the possible impact on systematic uncertainties is considered large. Due to the specific properties of the trigger imposed on the investigated final state, the impact on the covered phase space of this events is small.

8.2 Pre-Production Corrections

In order to get a suitable stable resolution of the energy of final state particles, which rely on detection of neutral particles, the reconstruction performance of the electromagnetic calorimeters ECAL1 and ECAL2 have been improved. The initial energy calibrations are obtained by using mono-energetic electron beams with different energies. At that place a linear energy response is assumed. Upon

this base calibration several corrections of the energy calibrations are applied. This correction are briefly discussed in the following.

8.2.1 Laser and LED Correction

In order to detect and account for temporal fluctuation on time scale of spills, the calorimeter modules are regularly lashed with laser (ECAL1) and LED (ECAL2) pulses [AAA+15a]. This pulses are constant over time, thus fluctuation of the cell response have their origin in the detection and amplification system. Evaluating the change of the response to this pulses allows to correct for temporal instabilities of the calorimeter by applying time dependent corrections.

8.2.2 π^0-Calibration

Another important set of calibrations are the so called π^0-calibrations. This correction are obtained by determining the position $m_{\pi^0,\mathrm{rec}}$ of the π^0 peak observed in the $\gamma\gamma$ invariant mass spectrum. The mean of this peak is expected to coincide with the nominal mass m_{π^0} of the π^0 [Ger12, B+12]. The $\gamma\gamma$ invariant mass spectrum are obtained for each individual calorimeter module. Therefore, the invariant mass of each $\gamma\gamma$ combination is connected with the two main cells[1] of the showers. Assuming that only one shower energy E_i change at a time, the invariant mass $m_{\gamma\gamma}$ is proportional to E_i. The correction factor is then given by

$$a = \frac{m_{\pi^0}}{m_{\pi^0,\mathrm{rec}}} \tag{8.1}$$

and the corrected energy is

$$E_i' = a \cdot E_i. \tag{8.2}$$

This calculation does not take into account, that the calculated invariant mass depend on the calibration of other cell, which are changed at the same time. Thus the π^0-calibration have to be obtained in an iterative procedure. Considering 2 GeV wide bins of shower energy, the obtained calibrations also accounts for energy dependence of the calibration. The spill structure of the beam introduces occupancy effects, which are taken into account by analyzing the time in spill dependence of the calibration. A more detailed description of this method as well as its effects can be found in [Nag12].

8.3 Post-Production Corrections

Before the actual reconstruction and event selection some general post-production correction are applied. Incorrect cell response functions, which show up in a

[1] Here main cell denotes the cell with its center next to the shower center.

displacement of ECAL2 showers, had been used during the *t70* production. This requires a correction of the cluster position. Another important correction, which accounts for the internal structure of the Shashlik modules, is applied to the energies measured by Shashlik cells. The details of these correction are discussed in the following.

8.3.1 Shower Position

Looking at the in-cell position $(x_{\text{ic}}, y_{\text{ic}}) = (x - x_{\text{cell}}, y - y_{\text{cell}})$ of clusters, which is measured relative to the center $(x_{\text{cell}}, y_{\text{cell}})$ of the nearest cell, a uniform distribution is expected due to symmetry. This also applies when looking at a projection of this distribution. However, for low energetic showers there are exceptions due to threshold effects. An obvious example for such an exception are showers, which fired only cells within one row or column. These showers provide only limited information[2] of the position within the row or column, respectively. Thus, their position is set to the center of the row or column. As the threshold effects obviously depend on the shower energy, this is more likely for showers with lower energy E_{shower}.

Besides the expected exceptions due to some hard to cure imperfection of the shower profiles, which are used during production, the observed distributions of showers are not uniform, where they are expected to be. This is accounted by correcting the shower position by applying a additional cell response functions. These cell-response functions add a correction term. In general the corrections depend on the energy E_{shower} of the shower and its position relative to the cell center, i.e. x_{ic} or y_{ic}

$$\begin{aligned} x' &= x + f(E_{\text{shower}}, x_{\text{ic}}) \\ y' &= y + f(E_{\text{shower}}, y_{\text{ic}}). \end{aligned} \tag{8.3}$$

In practice a cubic correction function in the form

$$f(E, x) = a(E) \cdot x^3 + b(E) \cdot x^2 + c(E) \cdot x \tag{8.4}$$

is used. The parameters $a(E)$, $b(E)$ and $c(E)$, are constant for certain ranges of the shower energy E_{shower} and defined individually for x- and y-position. Table 8.1 lists the parameters used during the *t70* production. The corrections for y-position lead to a quite uniform and continuous distribution of clusters (see figure 8.1(b)), which leaves only structures, which are due to threshold effects, construction properties of the Shashlik modules and the value range of the correction function. These effects have only small impact and are in difficult to correct. The distribution along the x-axis in contrast to the distribution along the y-axis shows below 35 GeV a significant reduced number of showers reconstructed at the edge of the cells (see figure 8.1(a)). Furthermore, a non continuous behavior

[2]Depending on the shower energy a bigger or smaller region at the cell borders may be excluded.

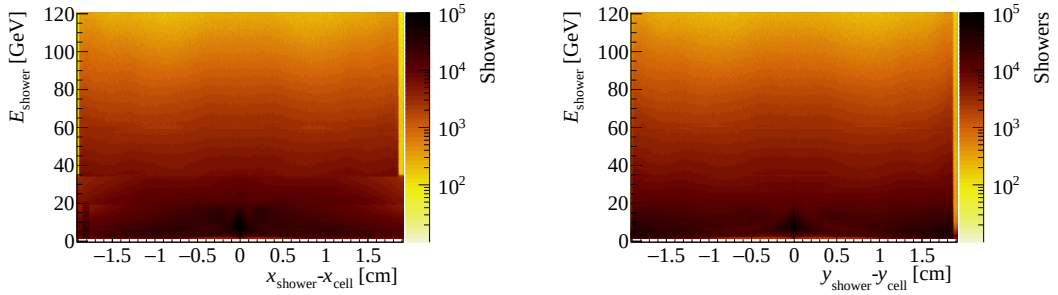

(a) x-position (b) y-position

Figure 8.1: Distribution of the in cell position of electromagnetic showers dependent on the shower energy E_{shower} obtained for the *t70* production. Please note, that the value range of the color scale does not cover the full value range. For values exceeding the range colors saturate at the maximum of the scale.

x/y	$a\,[\text{mm}^{-2}]$	$b\,[\text{mm}^{-1}]$	c	Range
x	$-7.335 \cdot 10^{-4}$	$-2.991 \cdot 10^{-4}$	$2.49 \cdot 10^{-1}$	$E_{\text{Shower}} \leq 20\,\text{GeV}$
x	$7.313 \cdot 10^{-4}$	$2.484 \cdot 10^{-4}$	$-2.460 \cdot 10^{-1}$	$E_{\text{Shower}} > 35\,\text{GeV}$
x	0	0	0	*else*
y	$8.568 \cdot 10^{-4}$	$4.176 \cdot 10^{-4}$	$-2.971 \cdot 10^{-1}$	$E_{\text{Shower}} \geq 0\,\text{GeV}$

Table 8.1: Parameter of cubic cell response function as used for the production.

at 20 GeV and 35 GeV is observed. Due to symmetry considerations it is not expected, that correction for x- and y-coordinate should differ. Thus, the correction, which are proved to work suitable well for the y-coordinate are applied to the x-coordinate. This requires, that the correction applied during production are reverted, before the new ones are applied. Unfortunately the production correction are not vanishing at the cell boarder. Thus, some clusters are moved above the cell borders into neighboring cells. This introduces ambiguities, which cannot be resolved. Thus, some structures are generated near the cell border (see figure 8.2). However only a small number of showers are affect. Thus, the overall effect on the analysis is small. In addition to the in-cell correction a miss alignment of ECAL2 was found during the analysis of the $\pi^-\gamma$ [AAA+15b]. This is compensated by a global shift of $-1.5\,\text{mm}$ of the x-position of ECAL2 showers.

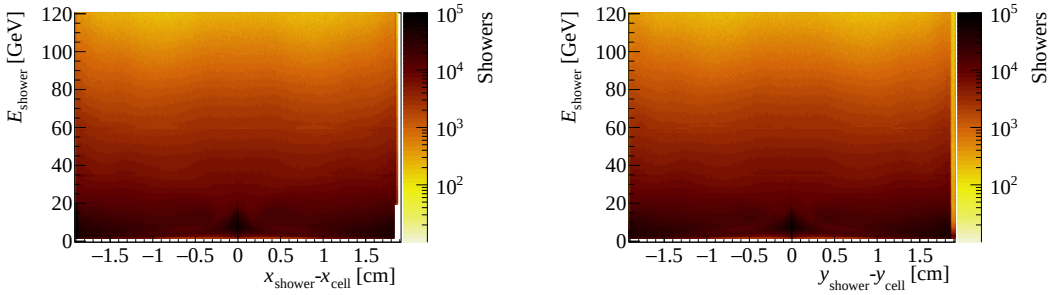

(a) x-position (b) y-position

Figure 8.2: Distribution of the in cell position of electromagnetic showers dependent on the shower energy E_{shower} as obtained after post-production corrections are applied. Please note, that the value range of the color scale does not cover the full value range. For values exceeding the range colors saturate at the maximum of the scale.

8.3.2 Corrections for Shashlik-type Calorimeter Cells

It was found, that the energy measured by Shashlik modules, show some dependence on the in cell position of the cluster. This dependence reflect the inner structure of the modules, which are hold together with rods of inactive material (see figure 5.2). Corrections to compensate this effects are deduced (see [Nag12] section 3.2). This corrections are given by the additive energy correction

$$\begin{aligned} E_{\text{corr}}(x, y, E_\gamma) = p_0(E_\gamma) + p_1(E_\gamma) \cdot (x/\text{cm})^2 + p_2(E_\gamma) \cdot (y/\text{cm})^2 \\ + p_4(E_\gamma) \cdot \exp\left(-\frac{(x/\text{cm} - p_6)^2 + (y/\text{cm} - p_7)^2}{2p_5^2} \right). \end{aligned} \quad (8.5)$$

x and y are the cluster position relative to the nearest cell center after applying the position corrections presented in section 8.3.1. The energy dependent parameters are given as

$$\begin{aligned} p_0(E_\gamma) &= 9.57965 + 6.42201 \cdot arctan\,(7.28429 \cdot (x_{190} - 0.649578)) - 0.64 \\ p_1(E_\gamma) &= -1.89692 - 1.2888 \cdot arctan\,(8.79757 \cdot (x_{190} - 0.638527)) \\ p_2(E_\gamma) &= -1.61223 - 1.13902 \cdot arctan\,(9.43193 \cdot (x_{190} - 0.659991)) \\ p_4(E_\gamma) &= -2.57235 + 15.9715 \cdot x_{190} \\ p_5(E_\gamma) &= 0.214072 - 0.202193 \cdot x_{190} \\ p_6(E_\gamma) &= 1.00 \\ p_7(E_\gamma) &= 0.97 \end{aligned} \quad (8.6)$$

where $x_{190} = E_\gamma/190\,\mathrm{GeV}$ is the normalized shower energy. Due to limits of the calibration method, the correction parameters are calibrated for high energetic showers. Thus the corrected energy E'_γ is applied only for high energetic showers. A smooth transition in the range 60 to 70 GeV is achieved by introducing an additional factor

$$E'_\gamma = E_\gamma + a(E_\gamma) \cdot E_{\mathrm{corr}}(x, y, E_\gamma) \tag{8.7}$$

with

$$a(E) = \begin{cases} 1 & \text{for } E > 70\,\mathrm{GeV} \\ (E \cdot\ \mathrm{GeV}^{-1} - 60)/10 & \text{for } 60\,\mathrm{GeV} \leq E \leq 70\,\mathrm{GeV} \\ 0 & \text{for } E < 60\,\mathrm{GeV}. \end{cases} \tag{8.8}$$

Note, that this is the range, where the absolute value of the average correction energy gets minimal.

8.4 Shower Selection

Showers detected in the electromagnetic calorimeter are not only produced by photons, but also by any kind of charged particles. Thus in order to select electromagnetic showers the tracking system of the spectrometer is used to identify showers produced by photons, by requiring, that no track can be associated with the shower due to the position of the shower. In order to suppress detector noise, a shower energy $E_\gamma \geq 2\,\mathrm{GeV}$ is required. If more than four showers fulfilling this criteria are found, the four showers with the highest energies are considered for reconstruction. Other clusters are ignored.

8.5 Vertex Selection

During event reconstruction, all primary vertices with exactly one outgoing negatively charged particles are considered. In order to select beam-target interaction vertices, which fulfill the target hypothesis are selected

$$|-72.5\,\mathrm{cm} - z_{Vert,rec}| \leq 3 \cdot \sigma_z(\theta(\pi^-_\mathrm{i}, \pi^-_\mathrm{f})). \tag{8.9}$$

Where $z_{Vert,rec}$ is the z-position of the reconstructed vertex. $\sigma_z(\theta(\pi^-_\mathrm{i}, \pi^-_\mathrm{f}))$ describes the resolution achieved for the z-position of the vertex. The z vertex resolution is found to depend on the angle $\theta(\pi^-_\mathrm{i}, \pi^-_\mathrm{f}) = \theta_{i,f}$ between the trajectories of the beam π^-_i and the outgoing negatively charged particle π^-_f. This resolution is described by the empirical function

$$\sigma_z(\theta_{i,f}) = \exp(1.53046e - 855.164 \cdot \theta) + \exp(2.52980 - 3466.52 \cdot \theta) + 0.801737. \tag{8.10}$$

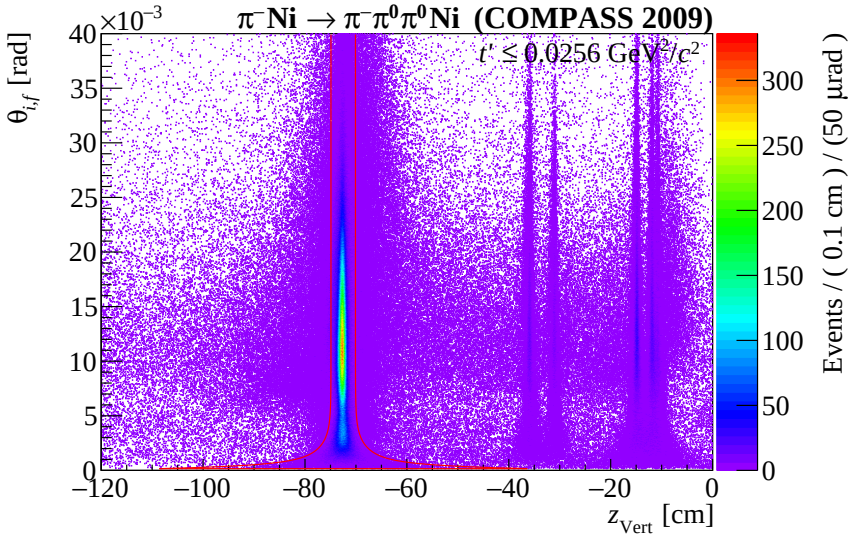

Figure 8.3: Angle $\theta_{i,f}$ between incoming beam pion π_i^- and the charged pion of the final state π_f^- versus z-position of the reconstructed vertex z_{Vert} for the $\pi^-\pi^0\pi^0$ final state. The red lines indicate the cuts applied in the shown variables.

Additional cuts assuring data quality are applied. The selection of scattering angle

$$\theta_{i,f} \geq 1.6 \cdot 10^{-4}\,\text{rad} \tag{8.11}$$

respects the resolution of the beam telescope (see figure 8.3). A cut on the transferred transverse momentum p_{T,π_f^-} of the outgoing π^- accounts for multiple scattering (see figure 8.4)

$$p_{T,\pi_f^-} \geq 15\,\text{MeV}/c. \tag{8.12}$$

Figure 8.3 shows the event distribution in regard to $z_{\text{Vert,rec}}$ and $\theta_{i,f}$. The red line indicates the selection criteria described above. One can also observe the two very thin tungsten targets between -40 and $-30\,\text{cm}$. Above $-20\,\text{cm}$ the detector planes of the beam telescope show up. The enhancements introduced by the tungsten targets are well separated from the nickel target. At small values of $\theta_{i,f}$ the presented cut extends towards the position of the tungsten targets. However, studying the distribution of $z_{\text{Vert,rec}}$ for selected events (figure 8.5) no clear indication of events, which have their origin in interaction of the beam particles with the tungsten targets, are observed. Thus, the number of these events can be estimated to lie in the order of a few dozen. Comparing this to the total amount of evnts, which is approximately 1.1 million, the intensity contribution introduced by scattering on one of the tungsten targets is considered to be negligible.

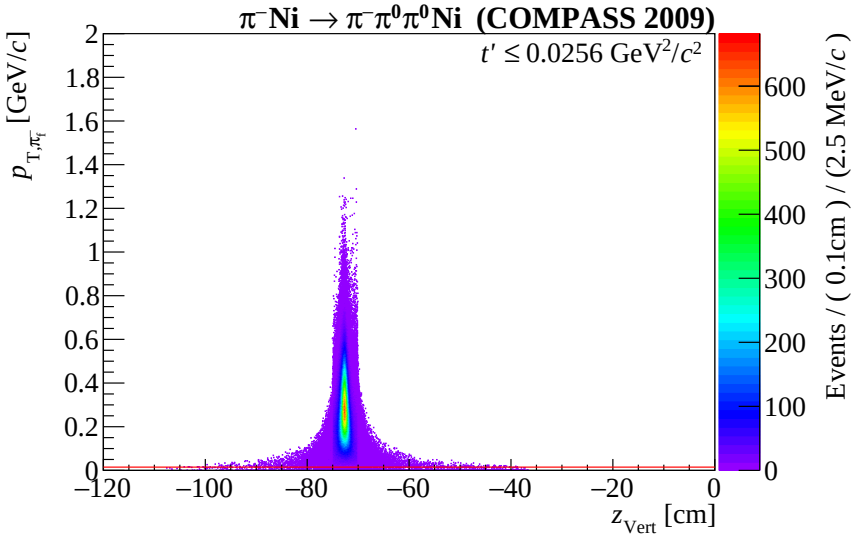

Figure 8.4: Transferred transverse momentum of the outgoing π^- p_{T,π_f^-} vs z-position of the reconstructed vertex for $\pi^-\pi^0\pi^0$ final state. The red line indicate the lower requirement on p_{T,π_f^-}.

8.6 Beam Selection and Beam Particle Identification

Particle identification (PID) for beam particles is provided by a set of two *CEDAR* detectors upstream of the target. During the Primakoff run in 2009, the gas pressure, which allow to modify the identification behavior of the CEDARs, of both detectors has been set to distinguish between pions and kaons. This implies, that it is not possible to identify anti-protons. In [Fri10] a method to determine the PID of a beam particle traversing the cedar detectors is described. This method is relying on a detector response function, which depend on the beam parameters. The method provides a tag, *CPID*, which can have one of the three values *Kaon*,*Pion* or *NULL* (undetermined). The given parameters are optimized to extract a clean Kaon sample. In order to provide a uniform behavior of the beam particle identification algorithm the beam divergence has been limited by requiring, that the divergence of the beam

$$(dx, dy)_i = \left(\frac{p_x}{p_z}, \frac{p_y}{p_z}\right)_i \tag{8.13}$$

is lying within the limits defined by the points given in table 8.2. This limits are indicated in figure 8.6, which shows the *dx*-*dy*-distribution of beam tracks. The given shape thereby provide uniform behavior of the beam PID algorithm and at the same time maximize the acceptance.

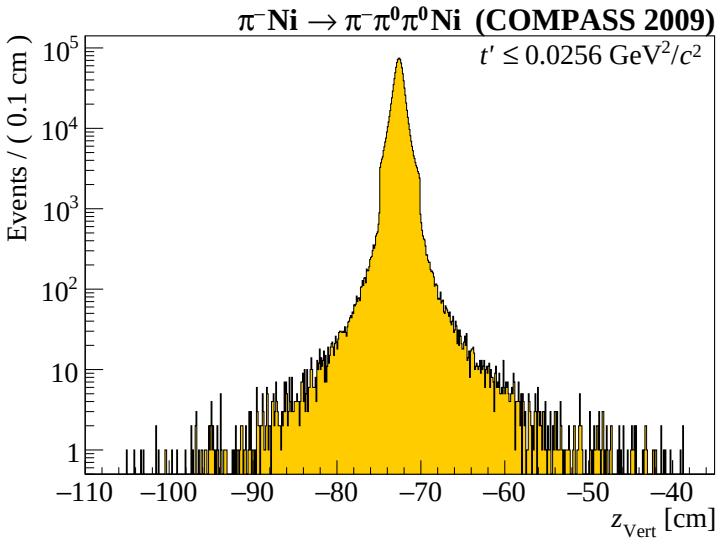

Figure 8.5: Distribution of the z-position of the reconstructed vertex for events in the $\pi^-\pi^0\pi^0$ final state.

8.7 Event Reconstruction and Selection

Event reconstruction assumes, that the beam pion reacts with the nickel target at the position of the primary vertex and form the $\pi^-\pi^0\pi^0$ final state, while the nickel target stays intact. The π^0's are assumed to decay practically instantaneous into two photons. The four momentum vector of the incoming π^--beam is obtained by combining the measured beam position and direction with the beam energy obtained by evaluating the neural network (see chapter 7) and the particle mass m_{π^-} of the π^- as given by the PDG [B+12]

$$p_{\text{beam}} = (E_{NN}^2, \vec{u}_{\text{beam}} \cdot \sqrt{E_{NN}^2 - m_{\pi^-,PDG}^2}). \tag{8.14}$$

$\vec{u}_{\text{beam}}$ is the unit vector parallel to trajectory of the beam. $E_{NN} = E_{\pi^-,i}$ is the beam energy determined with the neural network. The outgoing charged particle is assumed to be also a π^-

$$p_{\pi_f^-} = (\sqrt{|\vec{p}_{\pi^-}|^2 + m_{\pi^-,PDG}^2}, \vec{p}_{\pi^-}). \tag{8.15}$$

$\vec{p}_{\pi^-}$ is the three momentum of the charged particle, which is measured by the spectrometer. Exclusive events are selected by requiring, that the determined energy of the incoming beam particle $E_{beam} = E_{NN}$ and the sum

$$E_f = E_{3\pi} = E_{\pi_f^-} + \sum_{i=1}^{4} E_{\gamma,i,rec} \tag{8.16}$$

$dx \cdot 10^4$	-2.56	-1.61	-0.65	0.1	1.03	1.23	1.23	-0.27	-2.26	-2.56
$dy \cdot 10^4$	-3.95	-5.1	-5.1	-4.6	-4.16	-0.88	-0.88	-0.22	-0.22	-1.97

Table 8.2: Points limiting the area in the x-y-plane of the beam divergence, which is used to select events.

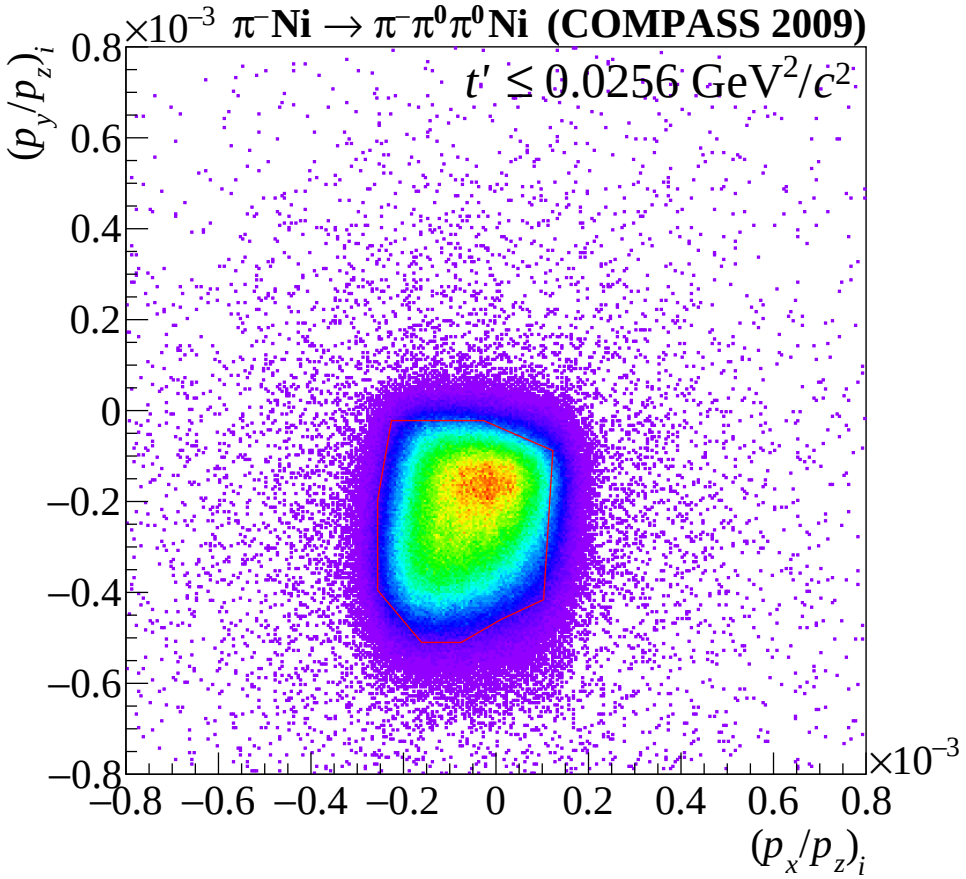

Figure 8.6: Divergence of the incoming beam particle in x-y plane for selected $\pi^-\pi^0\pi^0$ final state. For analysis events within the area indicated by the red lines are considered.

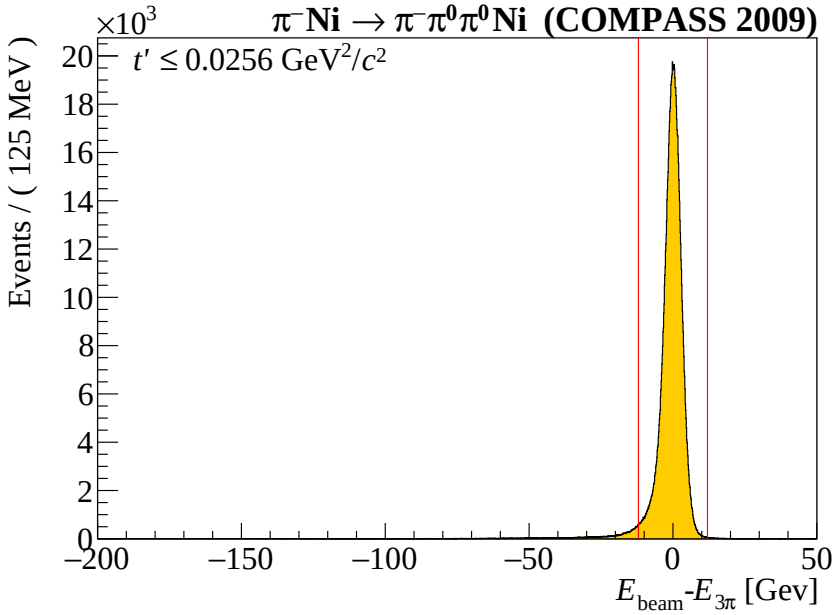

Figure 8.7: $|E_{beam} - E_f|$ of events with $\pi^-\pi^0\pi^0$ final state. The red lines indicate the selection criteria for exclusive events.

of the energies of the detected particles fulfill the condition

$$|E_{beam} - E_f| \leq 12\,\text{GeV}. \tag{8.17}$$

$E_{\gamma,i,rec}$ denote the energies of the electromagnetic showers, where the corrections described in 8.3 are applied. Figure 8.7 shows $|E_{beam} - E_f|$ for events with the $\pi^-\pi^0\pi^0$ final state. It is assumed, that the uncertainty of the measurement of electromagnetic showers is much larger, than the uncertainty of E_{beam} and $E_{\pi_f^-}$. Assuming, that the uncertainty of the photon energy measurement increases linearly with the energy, an exclusivity constraint is applied by multiplying the energies of the photons $E_{\gamma,i,rec}$ with a common factor v

$$E_{\gamma,i} = v \cdot E_{\gamma,i,rec}. \tag{8.18}$$

v is given by

$$v = \frac{E_{beam} - E_{\pi_f^-}}{\sum_{i=1}^{4} E_{\gamma,i,rec}}, \tag{8.19}$$

such that

$$\sum_{i=1}^{4} E_{\gamma,i} = E_{beam} - E_{\pi_f^-}. \tag{8.20}$$

(i,j)	$\sigma_m^{i,j}/(\mathrm{MeV}/c^2)$	$m_{\pi^0}^{i,j}/(\mathrm{MeV}/c^2)$
(sh,sh)	3.7335	135.413
(rlg,rlg)	6.89592	136.752
(lg,lg)	6.26035	136.388
(sh,rlg),(rlg,sh)	5.94527	136.22
(sh,lg),(lg,sh)	7.10832	136.218
(rlg,lg),(lg,rlg)	7.55552	136.536

Table 8.3: Width and mass of the π^0 peak in the $m_{\gamma\gamma}$ mass spectrum for different combination of calorimeter modules.

Each of the selected electromagnetic shower (see section 8.4), is assumed to be caused by a photon, which is generated at the vertex position. Thus the four-momentum of a photon candidate is determined by the energy of the shower $E_{\gamma,i}$ as defined by equation 8.18 and the position of the measured cluster relative to the primary vertex

$$p_\gamma = (E_\gamma, \vec{p}_\gamma) = \left(1, (\vec{x}_{\mathrm{shower}} - \vec{x}_{\mathrm{vertex}})/\sqrt{|\vec{x}_{\mathrm{shower}} - \vec{x}_{\mathrm{vertex}}|^2}\right) \cdot E_\gamma. \tag{8.21}$$

π^0 candidates are built by adding the four-momenta of two photons. All possible pair wise combinations of the four highest-energetic photons are used to identify events with two π^0 in the final state. Therefore the invariant mass $m_{\gamma\gamma}$ of each of the two $\gamma\gamma$ subsystems have to pass a specific cut, which ensures compatibility with the assumption of a π^0 decay. In order to take into account, that the three different types of modules used in ECAL2, i.e. *Shashlik* (sh), *radiation-hard lead glass* (rlg) and *lead glass* (lg), perform differently, each calorimeter cluster is tagged with the module type of its center cell. For each combination the parameters, which define the π^0 mass cut are determined individually by fitting a Gaussian function with a constant background to the observed spectrum (see figure 8.8). The π^0 mass cut is finally given by

$$\left|m_{\pi^0}^{i,j} - m_{\gamma\gamma}\right| \leq 3 \cdot \sigma_m^{i,j} \tag{8.22}$$

where i and j nominates the cell type attributed to the two showers. $m_{\pi^0}^{i,j}$ and $\sigma_m^{i,j}$ are the mean and width of the π^0 mass peak. The actual values are given in table 8.3. In order to identify two π^0 in the final state, this criteria must apply to both $\gamma\gamma$ pairs. Figure 8.8 shows the peaks due to the decay and reconstruction of π^0. Next the mass of the $\gamma\gamma$-subsystems representing a π^0 is constrained by

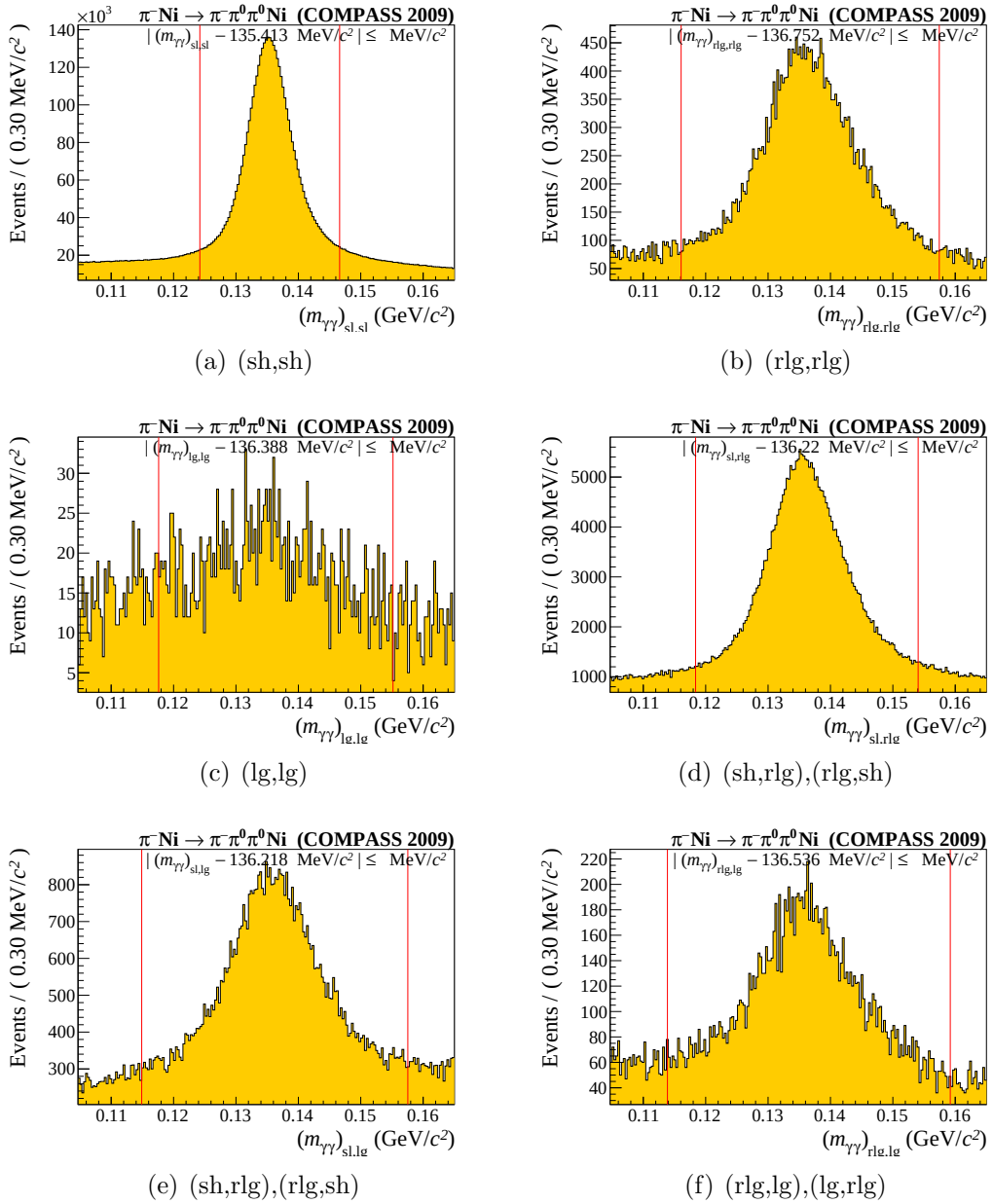

(a) (sh,sh) (b) (rlg,rlg)

(c) (lg,lg) (d) (sh,rlg),(rlg,sh)

(e) (sh,rlg),(rlg,sh) (f) (rlg,lg),(lg,rlg)

Figure 8.8: The $\gamma\gamma$ invariant mass distribution for different combinations of module types of ECAL2 is shown. Red lines indicate the selection range.

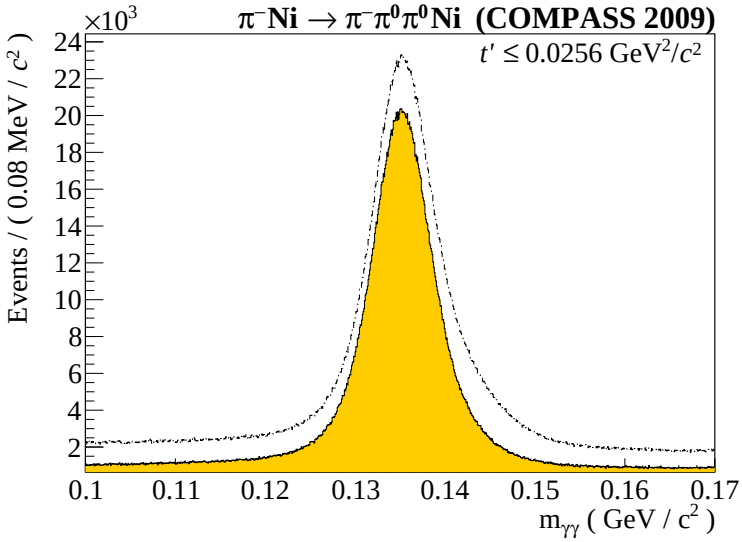

Figure 8.9: The $\gamma\gamma$ invariant mass distribution is shown. The doted line shows the distribution before applying the π^0 mass cut. The solid line shows the distribution after applying the cut on one of the $\gamma\gamma$ subsystems.

rescale the four-vectors to match the mass of the π^0 as given by [B+12]

$$p'_{\pi^0} = \left(\vec{u}_{\gamma\gamma} \cdot \sqrt{E^2_{\gamma\gamma} - m^2_{\pi^0,PDG}}, E_{\gamma\gamma}\right). \tag{8.23}$$

Here $E_{\gamma\gamma}$ is the sum of the rescaled energy of the two photons and $\vec{u}_{\gamma\gamma}$ the unit vector along the sum of the three-momenta $\vec{p}_{\gamma\gamma}$.

A preselection of events with low transferred four momenta t' is done with a loose cut selecting the first diffractive maximum. This cut with

$$t' \leq 0.0256\,\mathrm{GeV}^2/c^2 \tag{8.24}$$

is shown in figure 8.10. Aiming to identify the Primakoff contribution with the help of partial-wave analysis techniques an event select with low interference of Pomeron and photon production is required. As discussed in section 1.2, this can be done by exploiting the fact, that Primakoff reactions, which feature $M = 1$, peak at very low values of t', which follows the Weizsäcker-Williams distribution, while the leading strong production of $M = 1$ states is suppressed by a factor t'. Optimizing the t' cut taking into account the resolution effects, that determines the yield of Primakoff events, for the partial-wave analysis a cut with

$$t' \leq 0.002\,\mathrm{GeV}^2/c^2 \tag{8.25}$$

is applied.

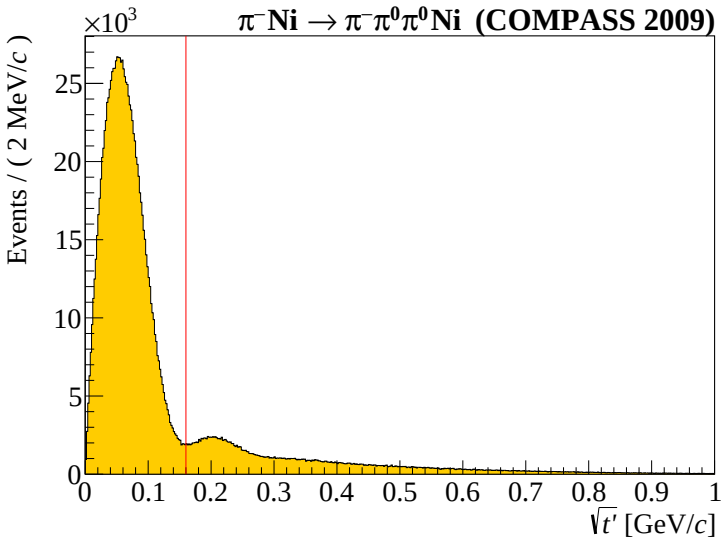

Figure 8.10: $\sqrt{t'}$ distribution. The red line at the first diffractive minimum is indicating the preselection chosen.

8.8 Calorimetric Trigger

During the Primakoff run in 2009 an FPGA based calorimetric trigger was used, which is in detail discussed in chapter 6. The trigger decision is made upon the sum over cell energies, which occurs in a specific area of ECAL2. This sum is then compared to a threshold. Having two thresholds, which are independently set, two triggers are defined. The area covering 12×12 minus 3×4 calorimeter cells in the center of ECAL2 used in 2009 is common to both triggers. The excluded area of 3×4 cells accounts for the increased particle rate around the undeflected beam. Using advanced pulse shape analysis the trigger includes zero subtraction and cell-wise energy and time calibration.

Being a digital logic, the trigger logic can in principle be implemented in software, which matches the hardware implementation one to one. Indeed doing so allows to study the trigger performance. However due to the fact, that showers simulated by the COMPASS Monte Carlo framework have a shower shape with differs from the one observed in the experiment, it is not sensible to use this approach to evaluate the acceptance of the trigger. The observed differences are account during reconstruction by using different cell response function, i.e. shower profiles, for Monte-Carlo and recorded data. By doing so on shower level a good agreement of simulations and data is achieved. Thus, a more restrictive selection based on shower properties is used to superceed the hardware trigger. Applying this selection to both Monte Carlo events and recorded data allows to determine the a common phase space acceptance. Such a selection is defined by summing the energy of those ECAL2 showers, which are lying in the area of the original

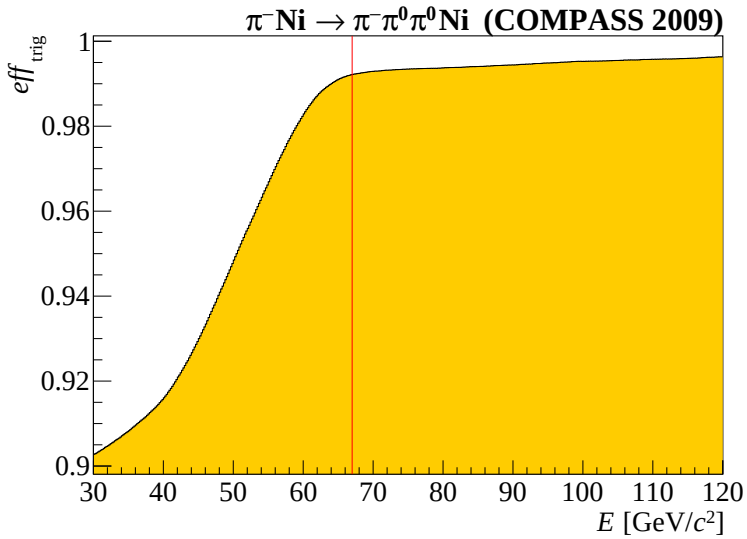

Figure 8.11: Number of events flagged with Prim2 and Prim1 divided by the number of events with Prim1 flag under the condition $E_{\text{Trigger}} \geq E$. Due to the analog part of the primakoff triggers, the Prim1 and Prim2, triggers are not perfectly synchronous. Thus, having a trigger at the edge of the considered time window, it happens, that a Prim2 trigger is not adjuncted to the same clock-cycle as the corresponding Prim1 trigger. This leads to the observed behavior, that instead of a plateau a region with constant slope is reached. The observed slope corresponds to time differences in the order of one picosecond.

trigger. In order to account for the shower size the shower center is required to lie in a slightly smaller area, which is defined by the original area and considers a margin of one cell at each of the borders. In order to reduce influence from background-only clusters, which can be attributed to the final state particles, i.e. the four π^0 showers and a possible energy deposit coming from the π^-, are considered. Evaluating the energy dependence of the sum for the Prim2 trigger a threshold of 67 GeV is determined (figure 8.11). This threshold provides a good purity and a good yield at the same time. As already discussed before due to the lack of a reference sample[3] such an evaluation is not possible for the Prim1 trigger.

8.9 Kinematic Distributions

Studying the three-pion invariant mass $m_{3\pi}$ of the selected events (see figure 8.12(a)) some well-known resonance structure shows up. The spectrum is dominated by a

[3]The possible event sample with minimum-bias and/or random trigger, have to few events with the Prim1 trigger bit set to make a reliable evaluation of the Prim1 threshold.

broad peak with its maximum at around $m_{3\pi} = 1.25\,\mathrm{GeV}/c^2$. This corresponds to the properties of the $a_1(1260)$. The shoulder on the right side of this peak, which gets more prominent, when restricting to smaller values of t', hints for the contribution of the radiatively produced $a_2(1320)$. Going further to even higher masses a small enhancement, which is better visible in case of the relaxed t'-cut, can be observed. The position of this enhancement is roughly at the mass of the $\pi_2(1670)$. The well-visible narrow peak in the low mass region originates from decays of K^-, which are contained in the hadron beam. These events have a t' of zero, which is only affected by experimental resolution. The experimental resolution (see also figure 15.3), that these events are not effected by the presented t'-cuts. Further prove of this conclusion is gained by accounting for the PID of the beam particle. The spectrum for beam particle identified as Kaon (figure 8.12(c)) differs significantly from the total spectrum, while the Kaon decay peak has the same strength as in the spectrum of all events. The spectrum of tagged pion events (figure 8.12(b)) on the other side shows, besides the absence of the Kaon decay peak, the same behavior as the total spectrum. It is assumed, that except of the kaon decay peak the spectrum originates from beam target interaction. The dominant strong interactions conserves strangeness. Thus, the assumption, that the outgoing particle is a pion, does not necessarily apply any more. Instead it is likely, that it is indeed a kaon. In the presented reconstruction these events are reconstructed applying the wrong assumption of the invariant mass of the beam particles. Thus, the kaon spectrum is not expected to show structure, which allow straight forward physical interpretation. As the kaon decay peak is completely removed in the pion spectrum, a pure pion sample can be assumed. Within this analysis a quantitative evaluation is not possible, however in [Fri10] the remaining contribution from kaon events is found to be less than 0.5 %. As a consequence the disturbance of beam kaons is negligible. At this point it should be mentioned, that the applied event selection enriches the pion contribution. Events, where the beam PID could not be determined (figure 8.12(d)), show on the one hand a remaining kaon decay peak and on the other hand the course features of the pion spectrum.

However, not only the $m_{3\pi}$ spectrum, but also the invariant mass spectra of the two pion subsystems can reveal valuable insights to the underlying physics. In this case the charged two pion system reveals a resonance structure, which is dominated by an enhancement showing the mass and width of the well known $\rho(770)$ resonance (see figure 8.13(a) and 8.13(b)). As this enhancement completely disappears for the kaon sample, one can conclude, that the kaon sample has a high purity. The invariant mass spectrum (figure 8.14) of the neutral subsystem on the other hand reveals a spectrum, which shows the features of several light scalar mesons. The spectrum is dominated by the $f_0(500)$, which is also called σ.

A commonly used tool to study three body decays are so called Dalitz plots, where the dependence of two kinematic decay variables on each other are plotted.

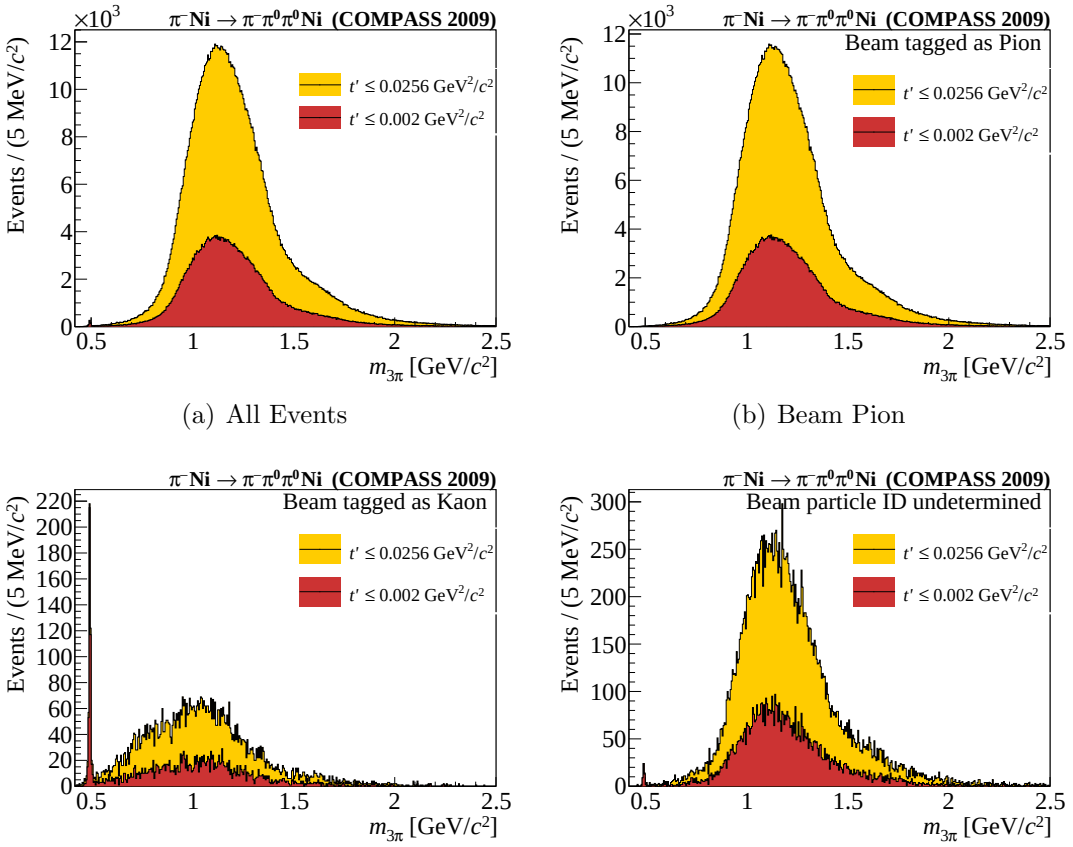

(a) All Events

(b) Beam Pion

(c) Beam Kaon

(d) Beam PID undetermined

Figure 8.12: Distribution of the invariant mass $m_{3\pi}$ of the outgoing $\pi^-\pi^0\pi^0$ system for events with $t' \leq 0.0256\,\mathrm{GeV}^2/c^2$ (yellow) and $t' \leq 0.002\,\mathrm{GeV}^2/c^2$ (red). The mass spectra for all events (a) and for events with different beam PID (π: (b), K: (c), others: (d)) are shown.

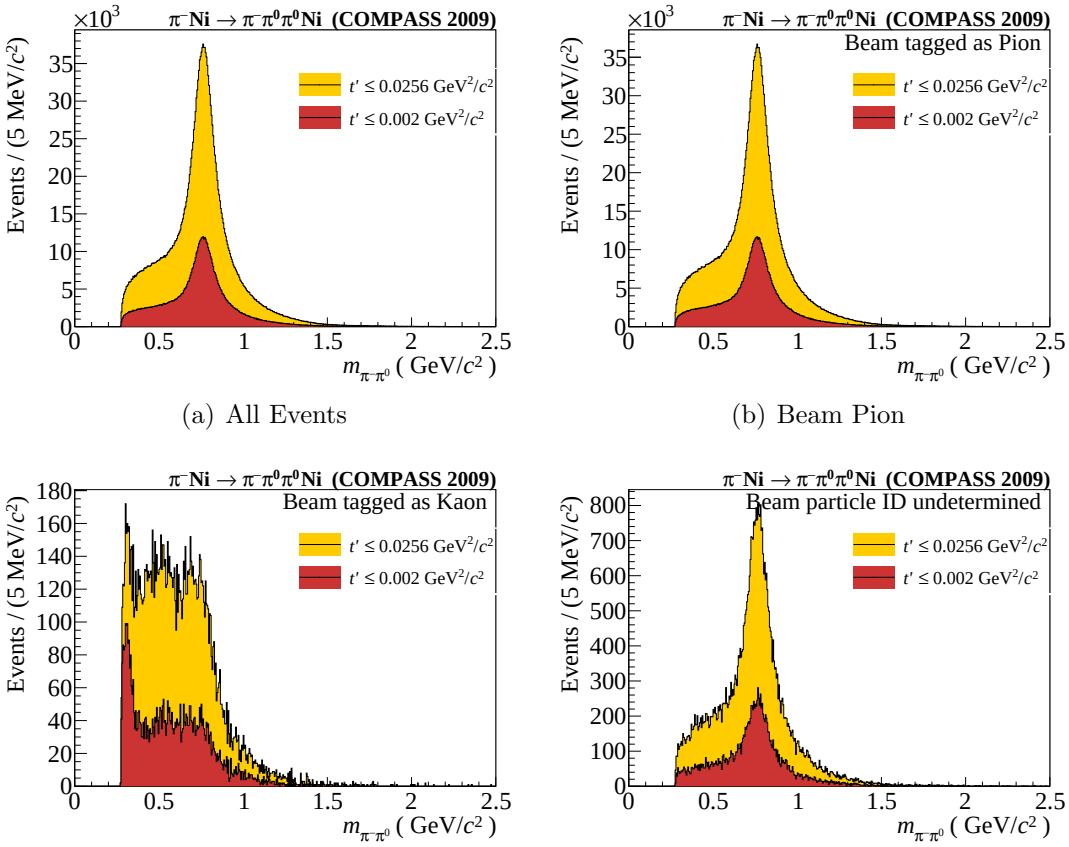

(a) All Events (b) Beam Pion

(c) Beam Kaon (d) Beam PID undetermined

Figure 8.13: Distribution of the invariant mass $m_{\pi^-\pi^0}$ of the charged two pion subsystem for events with $t' \leq 0.0256\,\mathrm{GeV}^2/c^2$ (yellow) and $t' \leq 0.002\,\mathrm{GeV}^2/c^2$ (red). The mass spectra for all events (a) and for events with different beam PID (π: (b), K: (c), others: (d)) are shown.

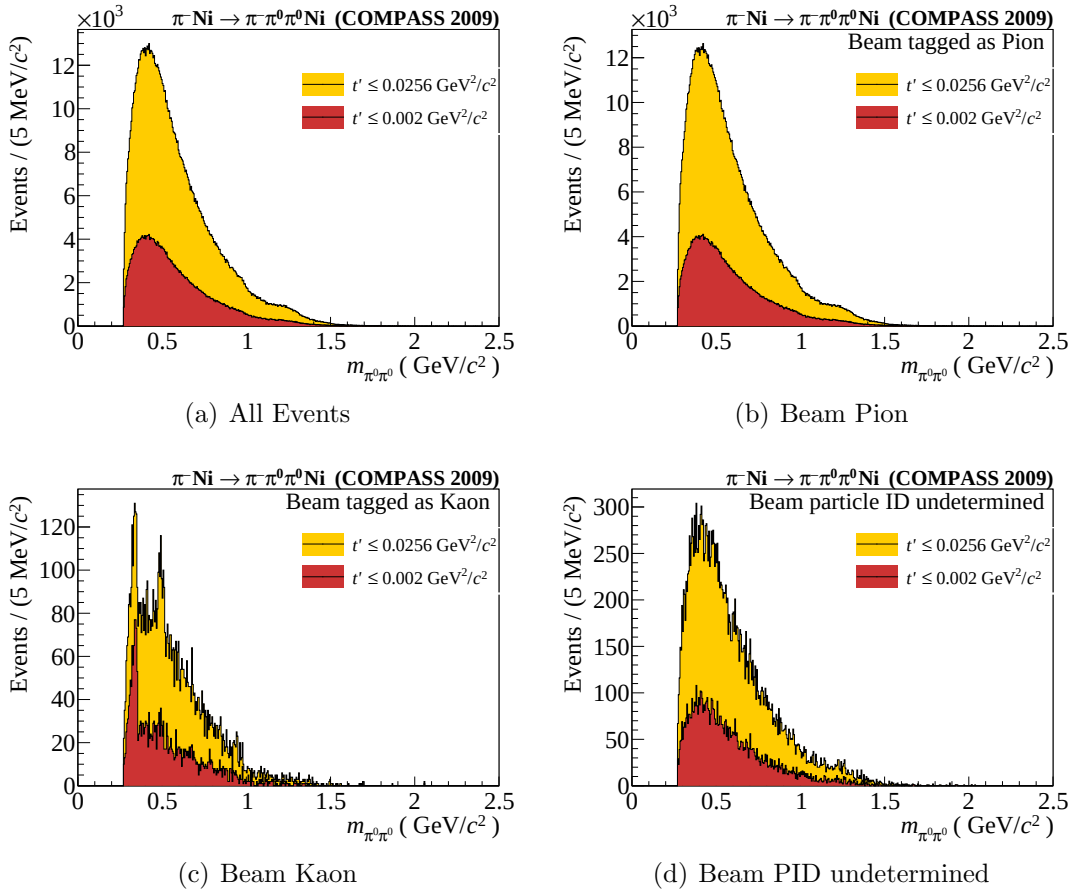

(a) All Events (b) Beam Pion

(c) Beam Kaon (d) Beam PID undetermined

Figure 8.14: Distribution of the invariant mass $m_{\pi^0\pi^0}$ of the neutral two pion subsystem for events with $t' \leq 0.0256\,\mathrm{GeV}^2/c^2$ (yellow) and $t' \leq 0.002\,\mathrm{GeV}^2/c^2$ (red). The mass spectra for all events (a) and for events with different beam PID (π: (b), K: (c), others: (d)) are shown.

.

Traditionally the axis are chosen to be the invariant mass of two-particle subsystems. The observed three-pion decays are, as one can conclude from the two pion invariant mass spectra, dominated by resonant decay processes. In the presence of such processes the Dalitz plots show a non uniform structure. Figure 8.15 shows the Dalitz plots, with the invariant mass of the two charged $\pi\pi$ subsystems used as axis. Four regions of the three-pion mass are shown, ranging from masses near the three-pion threshold, i.e. $0.52\,\mathrm{GeV}/c^2 \leq m_{3\pi} \leq 0.82\,\mathrm{GeV}/c^2$, to the mass region of the $\pi_2(1670)$. Intermediate mass ranges show the behavior at the $\rho\pi$ threshold and around the mass of the $a_1(1260)$ and $a_2(1320)$. In the lowest mass range near the three-pion threshold, but already above the kaon mass, the Dalitz distribution still shows quite uniform behavior. Only slight increase at the lower left edge of the allowed kinematic range indicates the presence of the $f_0(500)$ in the $\pi^0\pi^0$ subsystem[4]. At the $\rho\pi$ threshold, i.e. $0.90\,\mathrm{GeV}/c^2 \leq m_{3\pi} \leq 1.10\,\mathrm{GeV}/c^2$, the typical vertical and horizontal enhancement at the mass of the ρ are observed. The enhancement is increased further, where not only the ρ but also the $f_0(500)$ contributes. This structure evolves further, when going to the mass region of the $a_1(1320)$ or even $\pi_2(1670)$.

[4]Resonant processes in the third two body system show up as diagonal structures.

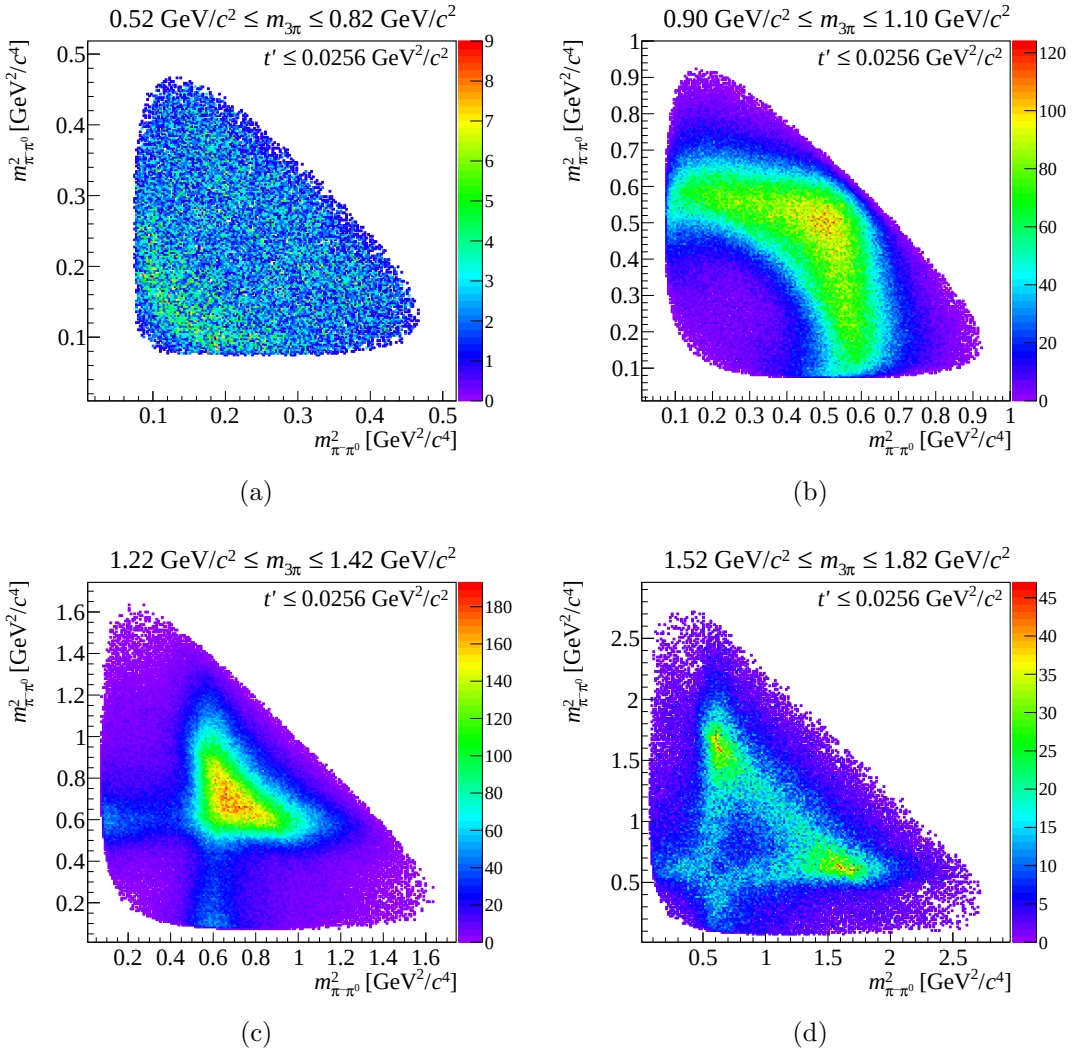

Figure 8.15: Dalitz plots showing the dependence of the invariant masses of the charged $\pi\pi$ subsystems on each other. Events with transferred momenta $t' \leq 0.0256\,\mathrm{GeV}^2/c^2$ and the beam tagged as pionare considered. The dependence is shown for three-pion masses in the range of the $0.52\,\mathrm{GeV}/c^2 \leq m_{3\pi} \leq 0.82\,\mathrm{GeV}/c^2$ (a) and $0.90\,\mathrm{GeV}/c^2 \leq m_{3\pi} \leq 1.10\,\mathrm{GeV}/c^2$ (b) as well as around the $a_1(1320)$ (c) and $\pi_2(1670)$ (d) resonance, i.e. $1.22\,\mathrm{GeV}/c^2 \leq m_{3\pi} \leq 1.42\,\mathrm{GeV}/c^2$ and $1.52\,\mathrm{GeV}/c^2 \leq m_{3\pi} \leq 1.82\,\mathrm{GeV}/c^2$, respectively.

Chapter 9

Phenomenological Fit of the t' Spectrum

Investigating the event selection presented in the previous chapter, the dominating production process is diffractive dissociation, where the dependence of the transferred momentum t' is given by (c.f. section 3.2.1)

$$\frac{\mathrm{d}\sigma}{\mathrm{d}t'} \propto t'^{M} e^{-bt'}. \tag{9.1}$$

At small masses $m_{3\pi}$ the diffractive spectrum is dominated by spin projection $M = 0$ due to the resonance structure. Thus, in first approximation contributions with $M > 0$ can be neglected. However, studying small masses and small momentum transfer another process gets apparent, the Primakoff production. It is visible by an enhancement at very low momentum transfer. This allows to determine the contribution of this radiative process to the spectrum by a fit to the observed t' distribution. In contrast to a partial-wave analysis, which investigates the process by analyzing the angular distributions of the decay particles and therefore investigates the decay, studying the t' distribution, the production process is under investigation.

A crucial input to this fit is the knowledge of the momentum dependence including resolution and reconstruction effects of the different production mechanisms. In case of diffractive dissociation, which has a shallow t' dependence, the distortion has a small impact and the observed dependence can be parametrized as

$$f_{\mathrm{dd}}(t', m_{3\pi}) = e^{a(m_{3\pi}) - b(m_{3\pi})t'} \tag{9.2}$$

with the parameters $a(m_{3\pi})$ and $b(m_{3\pi})$ describing the amplitude and the slope, respectively. Looking at a t' range, where no Primakoff contribution is expected, the parameters can be determined from the data.

9.1 Primakoff t' Distribution

The t' dependence of Primakoff events is given by the Weizsäcker-Williams photon approximation (see equation 3.33), which for masses near threshold is peaking at very small values of t'. This narrow peak cannot be resolved with the experimental resolution achieved at COMPASS. Thus the observed shape, which is used as signature, is dominated by resolution effects. This makes it impossible to use the theoretical t' dependence as given by the Weizsäcker-Williams approximation to describe the data. However processing Monte-Carlo generated events, which follow the t' dependence of the Weizsäcker-Williams approximation and the phase space distribution given by next-to-leading order calculations in chiral perturbation theory, the observed shape can be recovered. For this purpose the COMPASS Monte-Carlo chain accounts for the distortion by resolution and reconstruction effects. The resulting t' distribution is found to be described by the empirical function

$$f_{\text{Primakoff}}(t', m_{3\pi}) = e^{p_0(m_{3\pi})+p_1(m_{3\pi})\cdot t'} + \frac{p_2(m_{3\pi})}{(t' - p_3(m_{3\pi}))^{1.6}}. \tag{9.3}$$

The mass dependent parameters p_i are determined by a fitting individual mass bins. Figure 9.1 show the fit in the most relevant mass bins. The evolution of the parameters are found to be

$$\begin{aligned} p_0(m_{3\pi}) &= -1.10 \cdot m_{3\pi} \cdot \left(\text{GeV}/c^2\right)^{-1} + 7.40 \\ p_1(m_{3\pi}) &= -1.058 \cdot 10^3 \cdot m_{3\pi} \cdot \left(\text{GeV}/c^2\right)^{-1} + 4.076 \cdot 10^3 \\ p_2(m_{3\pi}) &= -7.68 \cdot 10^{-4} \cdot m_{3\pi} \cdot \left(\text{GeV}/c^2\right)^{-1} + 2.89 \cdot 10^{-3} \\ p_3(m_{3\pi}) &= -1.55 \cdot 10^{-3}. \end{aligned} \tag{9.4}$$

Apart from the extraction of the t' dependence, the same Monte-Carlo study also allows to determine the acceptance, which is calculated as the fraction of events matching the selection criteria and generated events. The evaluation is done in mass bins.

$$A_{\text{Primakoff}} = \frac{N_{\text{acc}}}{N_{\text{sim}}} \tag{9.5}$$

The determined efficiency is shown in figure 9.2

9.2 Determination of the Primakoff Contribution

The Primakoff contribution to the observed spectrum is determined by a fit to experimental data. In order to get information about the mass dependence the fit is done in mass bins with $40\,\text{MeV}/c^2$ width. These are the same mass bins, which

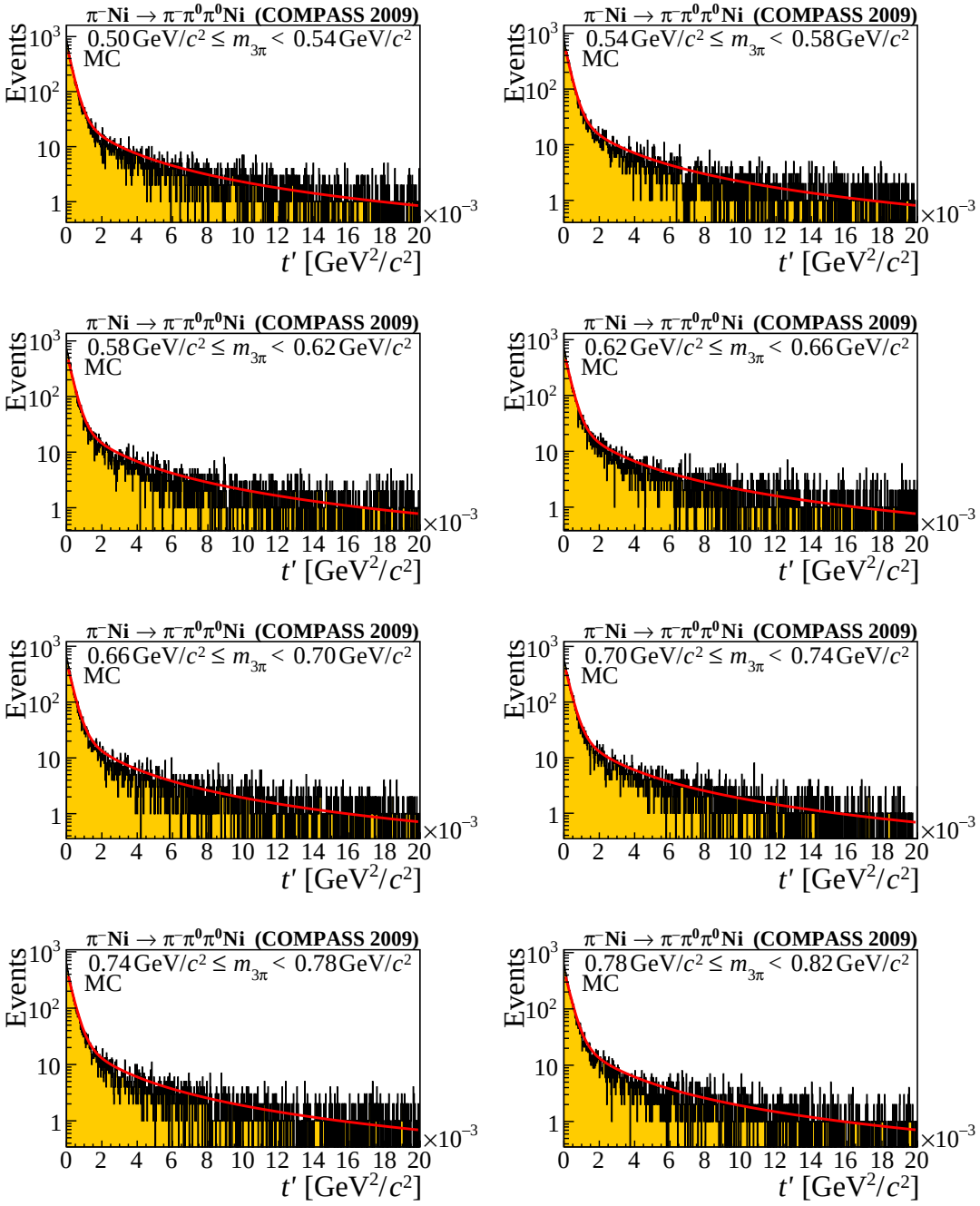

Figure 9.1: Monte-Carlo study of the transferred four momentum of Primakoff $\pi^-\gamma \to \pi^-\pi^0\pi^0$ events. The phase-space behavior of the events follow next-to-leading order chiral perturbation theory calculations. Shown is the t' distribution including resolution and reconstruction effects in the $m_{3\pi}$ mass range from $0.50\,\mathrm{GeV}/c^2$ to $0.78\,\mathrm{GeV}/c^2$. The study is done in mass bins of $40\,\mathrm{MeV}/c^2$ width. The red curve shows the empirical function (equation 9.3) as deduced from the Monte-Carlo study.

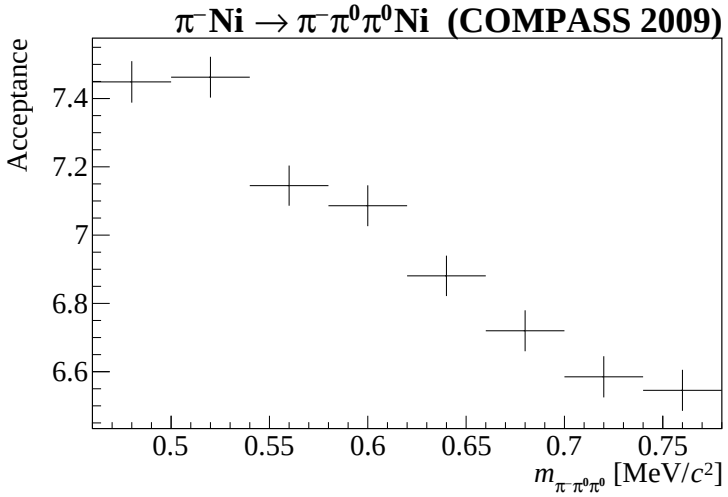

Figure 9.2: Dependence of the acceptance $A_{\text{Primakoff}}$ of Primakoff $\pi^-\gamma \to \pi^-\pi^0\pi^0$ events with a phase-space behavior given by next-to-leading order ChPT calculations. The acceptance is determined in mass bins with a width of $40\,\text{MeV}/c^2$.

are used for the Monte-Carlo study and later on in the partial-wave analysis.

Considering $t' \leq 0.0256\,\text{GeV}^2/c^2$ the t' range exceeds the region, where the Primakoff contribution is important. Thus the parameters, which describes the diffractive dissociation, are determined by the fit. Thereby the starting parameters are determined by fitting an exponential function in the range of $0.004\,\text{GeV}^2/c^2 \leq t' \leq 0.0256\,\text{GeV}^2/c^2$. The shape of the Primakoff contributions is given by equation 9.3 evaluating the parameters (see equation 9.4) for the central value of the mass bin. In order to account for the unknown magnitude of the contribution the Primakoff shape $f_{\text{Primakoff}}(t', m_{3\pi})$ is multiplied a factor $c(m_{3\pi}) = c_m$, which is subject to the log-likelihood fit. The function, which is fitted to the data is then given by

$$F_m(t') = c_m \cdot f_{\text{Primakoff},m}(t') + e^{a_m - b_m t'}. \tag{9.6}$$

The fit parameters a_m and c_m allow to account for the contribution of diffractive and Primakoff production, while the fit parameter b_m allows adjusting the t' dependence of the diffractive contribution, which depends on $m_{3\pi}$. Binning the data into mass bins, the parameters are denoted with an index corresponding to the bin centers. Figure 9.3 shows the fit in the most relevant mass bins, i.e. the same mass bins as shown in figure 9.1 for the Monte-Carlo study. Going beyond the shown mass of range $m_{3\pi} \leq 0.78\,\text{GeV}/c^2$ the background from diffractive dissociate, mainly the rising of the $a_1(1260)$ resonance, vastly increases and the fit becomes unstable. This makes it impossible to derive the Primakoff contribution considering only the t' spectrum. The number of detected Primakoff events within

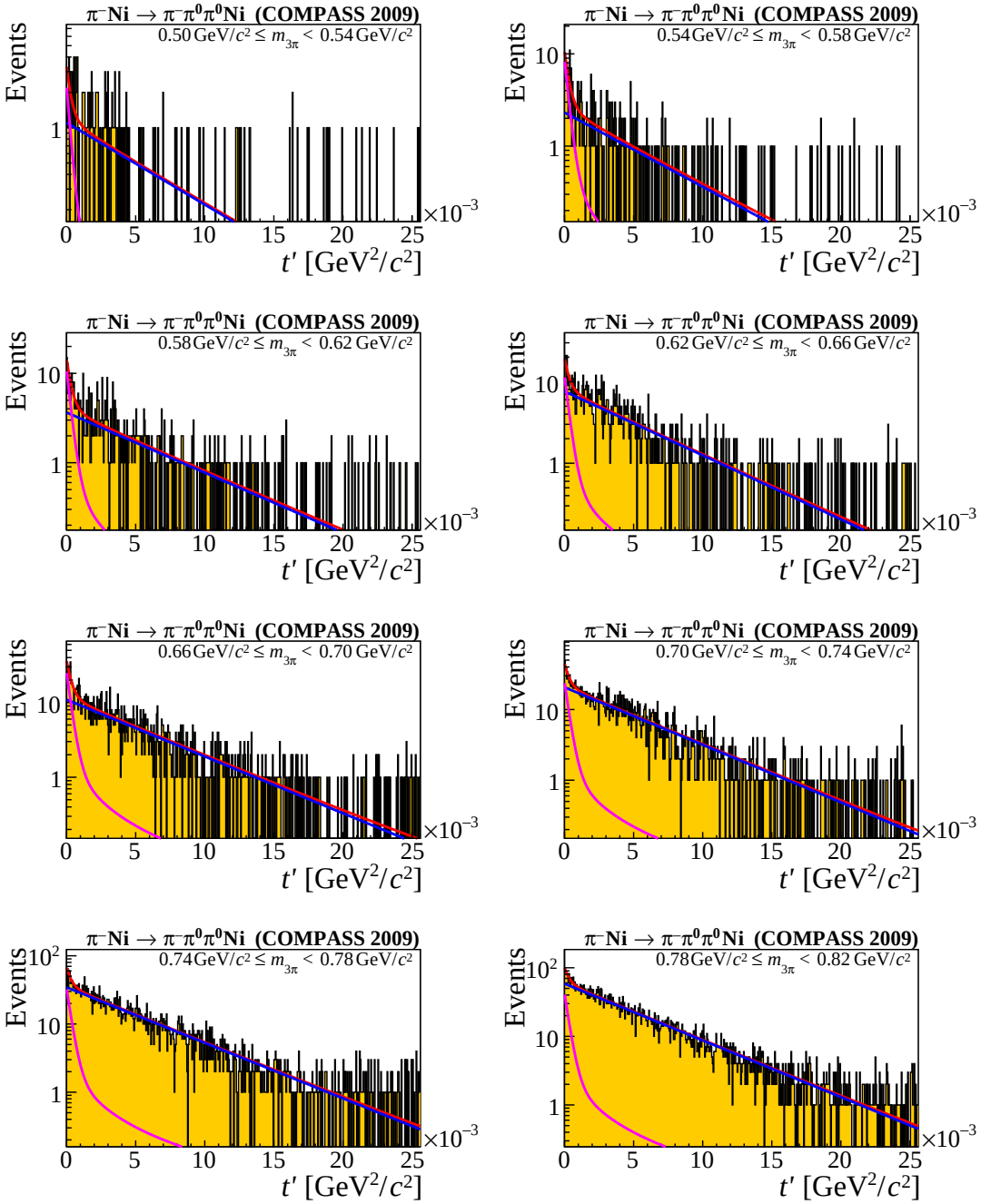

Figure 9.3: The observed distribution of four momentum transfer t' for three-pion masses $m_{3\pi}$ from $0.50\,\mathrm{GeV}/c^2$ to $0.78\,\mathrm{GeV}/c^2$, shown in $40\,\mathrm{MeV}/c^2$ mass bins. The data are fitted with function 9.6 (red line), which accounts for the contribution of radiative production (magenta line) and diffractive dissociation (blue line).

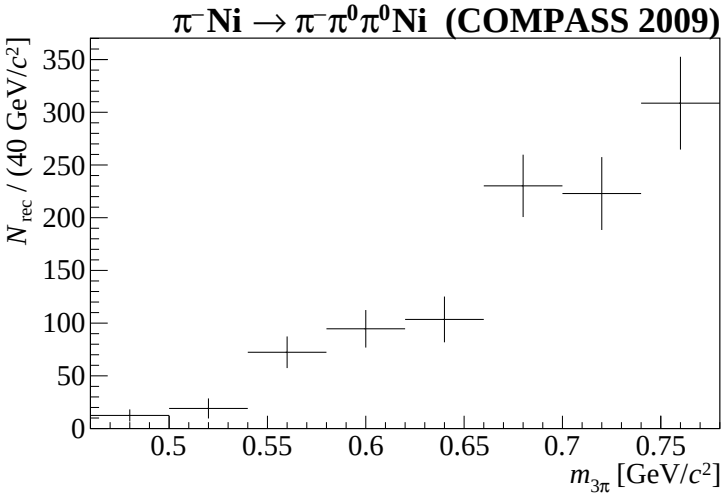

Figure 9.4: Number of detected Primakoff events in bins off invariant mass $m_{3\pi}$.

a mass bin (see figure 9.4) is given by the integral

$$N_{\text{Primakoff,acc}} = \int_{t'=0}^{\infty} c_m \cdot f_{\text{Primakoff},m}(t')\mathrm{d}t'. \tag{9.7}$$

Applying the acceptance derived from the Monte-Carlo study (see section 9.1) the total or accepted corrected number of events

$$N_{\text{Primakoff,tot}} = \frac{N_{\text{Primakoff,acc}}}{A_{\text{Primakoff}}} \tag{9.8}$$

is obtained. Figure 9.5 shows the result in a range of $0.50\,\text{GeV}/c^2$ to $0.78\,\text{GeV}/c^2$. As discussed in chapter 15, this information is an important step towards the determination of the cross section.

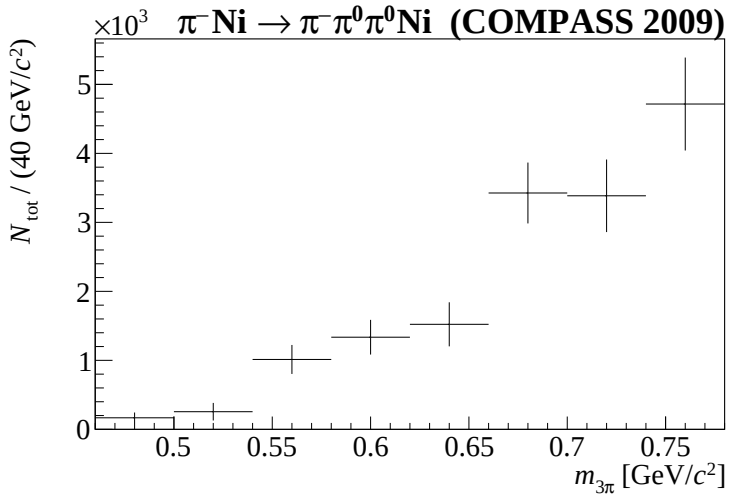

Figure 9.5: Acceptance corrected number of Primakoff events in bins off invariant mass $m_{3\pi}$.

Chapter 10

The Amplitude Analysis Technique

Doing amplitude analysis one aims to identify and characterize all relevant processes present in a given data set, which contribute to a transition from an initial state X to a final state f. The experimentally observed distribution of intensity $\mathcal{I}(m_f, t', \tau)$, which depends on the the invariant mass on m_f of the final state, the transferred momentum t' and a set of other kinematic observables τ, can be expanded in a basis of partial waves ψ_i, which are referred as amplitudes. Thereby the final state is completely determined by m_f and τ[1]. Partial-waves, which describe a transition to the same final state f, interfere with each other. This is taken into account by building the coherent sum

$$\mathcal{I}(m_{3\pi}, t', \tau) = \left| \sum_i \psi_i(m_{3\pi}, t', \tau) \right| . \tag{10.1}$$

Here i runs over all contributing partial waves. Following this idea *partial-wave analysis* (*PWA*) is one of the fundamental methods in spectroscopy. The contributing resonances and their properties (i.e. mass, width and quantum numbers) are determined by fitting predefined correlations of the parameter τ to the data. The parametrization of this correlation is an important input to partial-wave analysis. In the following the basic approach of the chosen partial-wave analysis technique will be presented. A short discussion of the fitting algorithm, i.e. the extended maximum likelihood estimator, and, how the results can be interpretation by calculating observables, follows. After this general introduction some light will be shed on the specific aspects of the underlying model discussing rank and partial coherence as well as the model, which enters the analysis presented in chapter 13.

[1] For a given three particle final state the invariant mass m_f and five independent kinematic variables are required.

10.1 The Partial-Wave Analysis Technique

Dealing with complicated wave sets, a global fit, which accounts for all angular dependencies and the dependencies of mass and transferred momentum at once, is challenging and with available methods technically impossible. Thus, usually the analysis is done in a two step approach. In the first step, which is referred to as *mass-independent PWA*, the data are divided into bins of mass m and transferred momentum t'. Each analysis bin is fitted with the known τ distributions of the partial-waves. The results of this fit are grouped in the *spin-density* matrix, which contains the product of the transition amplitudes and their conjugate complex value. In the second step, the *mass-dependent PWA*, resonance parameters are extracted by studying the spin-density matrix. This is usually done with a χ^2 fit.

10.1.1 Mass-Independent Partial-Wave Analysis

Technically seen, the mass independent PWA is a likelihood maximization fit (see 10.2) to the angular distributions of a data set with a certain final state. Thus, in general, precise measurement of all final state particles is required. The production intensity of a particular intermediate state X in general depends on its mass m and the transferred momentum t'. However, under the assumption, that the production intensity does not change rapidly with these kinematic variables, within suitable small ranges in m and t', the production intensity can be regarded as independent of m and t'. Consequently, within such a bin, the angular distributions are assumed to only depend on the phase-space variables τ.

Under the assumption, that the decay of the resonance X can be decoupled from its production, the total intensity $\mathcal{I}_m$ observed in amass bin is given by

$$\mathcal{I}_m(\tau, t') = \sum_{\epsilon=\pm 1} \sum_{r=1}^{N_r} \left| \sum_i T^{\epsilon}_{ir}(m) \overline{f}^{\epsilon}_i(t', m) \overline{\psi}^{\epsilon}_i(\tau, m) \right|^2 \tag{10.2}$$

with $\overline{\psi}^{\epsilon}_i(\tau, m)$ being the normalized decay amplitudes. The sum over i runs over all partial waves. Again, within a reasonably small analysis bin this quantity is assumed to have no mass dependence. Thus, $\overline{\psi}^{\epsilon}_i(\tau, m)$ depends only on τ. Decay amplitudes are normally used in their normalized form, which is obtained by dividing out the corresponding phase space integral

$$\overline{\psi}^{\epsilon}_i(\tau, m) = \frac{\psi^{\epsilon}_i(\tau, m)}{\sqrt{\int |\psi^{\epsilon}_i(\tau, m)|^2 \, \mathrm{d}\tau}}. \tag{10.3}$$

The factor $\overline{f}^{\epsilon}_i(t', m)$ models the known t' and m dependence of a particular partial

wave i within an analysis bin.

$$\overline{f}_i^{\epsilon}(t', m) = \frac{f_i^{\epsilon}(t', m)}{\sqrt{\int\int |f_i^{\epsilon}(t', m)|^2 \, \mathrm{d}t' \, \mathrm{d}m}}. \tag{10.4}$$

These dependencies are in general unknown and absorbed into the *transition amplitudes* $T_{ir}^{\epsilon}(m)$, which are determined by the fit. $T_{ir}^{\epsilon}(m)$ are complex numbers, which defines the relative strength and phase of a particular wave within the considered mass bin.

A *rank* $N_r > 1$ of the fit introduces additional degrees of freedom by allowing for an incoherent sum over sets of coherent decay amplitudes. In a physics interpretation this parameter accounts for multiple non-interfering processes and has to be chosen to match the coherence of the analyzed scattering process. A discussion in more details is given in section 10.4. The additional quantum number ϵ is the reflectivity and accounts for the parity conservation on the production side (see section 11.3) and therefore for the naturality of the Regge trajectory (see section 2.1). Final states with different reflectivity cannot interfere and are therefore summed incoherently.

10.1.2 Mass-dependent Partial-Wave Analysis

The second step of the partial-wave analysis technique presented here is the so called mass-dependent PWA, which aims to extract resonance parameter by fitting the spin density matrix, which contains the results of the mass-independent fit. In order to extract resonance parameters by a χ^2 fit, the mass dependence of the observed resonance have to be modeled. In the simplest case this is done by exploiting relativistic Breit-Wigner functions. As this step is not part of the presented work, further details will be omitted.

10.2 The Extended Maximum Likelihood Estimator

In the following the technical details of the fit algorithm, which is used to extract the contribution of different amplitudes, will be briefly discussed. A introduction to this topic can be found in [Haa14], partly reproduced for completeness.

The probability to observe a given set of N random variables $x_1, x_2, ..., x_N$, which are distributed according to the same probability density function $\hat{f}(x|a_1, ..., a_k)$ depending on a finite set of constant parameters $a_1, ..., a_k$, is

$$\hat{f}(x_1, ..., x_N|a_1, ..., a_k) = \prod_{l=1}^{N} \hat{f}(x_l|a_1, ..., a_k), \tag{10.5}$$

where the probability density function is normalized

$$\int \mathrm{d}x \hat{f}(x|a_1, ..., a_k) = 1. \tag{10.6}$$

In many cases the outcome of the experiment and therefore the set of observed variables x_l is known, while the constants a_j are not. In order to determine the a_j one introduces the likelihood

$$\hat{\mathcal{L}}(a_1, ..., a_k|x_1, ..., x_N) = \prod_{l=1}^{N} \hat{f}(x_l|a_1, ..., a_k) \tag{10.7}$$

as an function of a_j. Then the most probable parameters are given by the maximum of the likelihood function, which can be obtained by evaluating first and second derivatives. In this case the probability of observing N events is given by the Poisson statistics

$$P(N) = e^{-\lambda} \frac{\lambda^N}{N!}, \tag{10.8}$$

with the expected number of λ of events. Following the discussion presented in [Bar90] the unnormalized probability density function

$$f(x|a_1, ..., a_k) = \lambda \hat{f}(x|a_1, ..., a_k) \tag{10.9}$$

is introduced and equation 10.6 modifies to

$$\int \mathrm{d}x f(x|a_1, ..., a_k) = \lambda. \tag{10.10}$$

Please note, even not written explicitly the expected number of events λ in general depends on the parameters a_j. Now the extended likelihood function $\mathcal{L}(a_1, ..., a_k|x_1, ..., x_N)$ is defined as the product of the likelihood function $\hat{\mathcal{L}}(a_1, ..., a_k|x_1, ..., x_N)$ equation 10.7 and the Poisson probability $P_w(N)$ equation 10.8. With the definition of the unnormalized probability function $f(x|a_1, ..., a_k)$ equation 10.9 the extended likelihood can then be written as

$$\mathcal{L}(a_1, ..., a_k|x_1, ..., x_N) = \frac{e^{-\lambda}}{N!} \prod_{l=1}^{N} f(x_l|a_1, ..., a_k). \tag{10.11}$$

10.2.1 Application to Partial-Wave Analysis

Recalling equation 10.2 and following the discussion in section 10.1.1 the total observed intensity $\mathcal{I}$ in a bin of $m_{3\pi}$ and t' is given by

$$\mathcal{I}(\tau|T) = \sum_{N_r} \sum_{\epsilon=\pm} \left| \sum_i T^{\epsilon}_{ir} \psi^{\epsilon}_i(\tau) \right|^2 \tag{10.12}$$

where the theoretical infinite sum over partial-waves i has has to be limited to certain waves set. In order to allow the fit to determine events, where the contribution to the used wave set can not be identified, a *flat* wave, which is isotropic in phase space, is added incoherently

$$\mathcal{I}(\tau|T) = \sum_{N_r} \sum_{\epsilon=\pm} \left| \sum_i T^{\epsilon}_{ir} \psi^{\epsilon}_i(\tau) \right|^2 + A^2_{\text{Flat}}. \tag{10.13}$$

The flat wave, which is summed incoherently, can technically treated like the sum over a third reflectivity

$$\mathcal{I}(\tau|T) = \sum_{N_r} \sum_{\epsilon=\pm,\text{Flat}} \left| \sum_i T^{\epsilon}_{ir} \psi^{\epsilon}_i(\tau) \right|^2 . \tag{10.14}$$

The expected number $\lambda(T)$ of events is then given by the phase space integral over the intensity

$$\lambda(T) = \int \mathrm{d}\phi(\tau)\ \mathcal{I}(\tau|T)\eta(\tau) \tag{10.15}$$

with the phase space differential $\mathrm{d}\phi(\tau)$ and the *acceptance* $\eta(\tau)$, which accounts for inefficiency of the experimental setup. The phase space integral, thereby runs over the allowed kinematic region. Comparing to equation 10.10 the term $\mathcal{I}(\tau|T)\eta(\tau)$ can be identified as an unnormalized probability density function $f(x|a_1, ..., a_k)$, where the transition amplitudes T are identified by the $a_1, ..., a_k$. The according extended likelihood function is

$$\mathcal{L}(T|\tau_1, ..\tau_N) = \frac{e^{-\lambda}}{N!} \prod_{l=1}^{N} \mathcal{I}(\tau_l|T)\eta(\tau_l). \tag{10.16}$$

In order to determine the maximum of the likelihood function and therefore the optimized set of transition amplitudes T, it is necessary to calculate the first and second derivative of $\mathcal{L}(T|\tau_1, ..\tau_N)$. As the number of events N and expected events λ are potential large, it is convenient to use the natural logarithm of the likelihood for computation. Due to the fact that the logarithm function increases monotonically, the maxima remain unchanged. Applying the logarithm

and dropping the constant factor $1/N$ one gets

$$\ln \mathcal{L} = \sum_{l=1}^{N} \ln \eta(\tau_l) + \sum_{l=1}^{N} \ln \mathcal{I}(\tau_l|T) - \lambda(T). \tag{10.17}$$

The sum over the acceptance is also constant and therefore irrelevant for the determination of the maxima of the likelihood function and consequently dropped from the calculation. Expanding the remaining terms, the log-likelihood function reads

$$\begin{aligned}
\ln \mathcal{L} = \sum_{l=1}^{N} \ln \left[\sum_{r=1}^{N_r} \sum_{\epsilon} \left| \sum_{i} T_{ir}^{\epsilon} \psi_i^{\epsilon}(\tau_l) \right|^2 \right] \\
- \int \mathrm{d}\phi(\tau) \eta(\tau) \sum_{r=1}^{N_r} \sum_{\epsilon} \left| \sum_{i} T_{ir}^{\epsilon} \psi_i^{\epsilon}(\tau_l) \right|^2 \\
= \sum_{l=1}^{N} \ln \left[\sum_{\epsilon} \sum_{qs} \psi_q^{\epsilon}(\tau_l) \psi_s^{\epsilon *}(\tau_l) \sum_{r=1}^{N_r} T_{qr}^{\epsilon} T_{sr}^{\epsilon *} \right] \\
- \sum_{\epsilon} \sum_{qs} \int \mathrm{d}\phi(\tau) \eta(\tau) \psi_q^{\epsilon}(\tau) \psi_s^{\epsilon *}(\tau) \sum_{r=1}^{N_r} T_{qr}^{\epsilon} T_{sr}^{\epsilon *}.
\end{aligned} \tag{10.18}$$

Note that the second expressions is sorted separating the known components and the transition amplitudes, which are determined by the fit.

The computationally expensive part is the calculation of the decay amplitudes $\psi_q^{\epsilon}(\tau_l)\psi_s^{\epsilon *}(\tau_l)$ and the determination of the integral in the second term. As these integrals are independent from the actual transition amplitudes, they have to be calculated only once, and can be reused. In general the analytic form of the phase space integral is not known. Especially the experimental acceptance is usually not known in analytic form. Thus the integrals are computed numerical by using Monte-Carlo integration

$$\int \mathrm{d}\phi(\tau) \eta(\tau) \psi_q^{\epsilon}(\tau) \psi_s^{\epsilon *}(\tau) = I_{A\,qs}^{\epsilon} \approx \frac{V}{N_{\mathrm{MC}}} \sum_{l=1}^{N_{\mathrm{MC}}} \eta(\tau_l) \psi_q^{\epsilon}(\tau_l) \psi_s^{\epsilon *}(\tau_l). \tag{10.19}$$

Here V is the phase space volume. The acceptance is taken into account by evaluating the acceptance for single Monte-Carlo event. In order to derive the acceptance, a simulation, which accounts for all properties of the experimental setup, is required. The purpose of the *normalization integrals* is to cover the whole phase space. Thus, the number N_{MC} of Monte-Carlo events has to be large, as compared to the number of observed events.

Neglecting acceptance effects similar to the normalization integrals *phase*

space integrals are calculated. These integrals allow to normalize the decay amplitude such that a common scale is established. For the normalization only the diagonal terms

$$\int \mathrm{d}\phi(\tau)\, \psi_q^\epsilon(\tau)\psi_q^{\epsilon *}(\tau) = I_{qq}^\epsilon = \frac{V}{N_{\mathrm{MC}}} \sum_{l=1}^{N_{\mathrm{MC}}} \psi_q^\epsilon(\tau_l)\psi_q^{\epsilon *}(\tau_l) \tag{10.20}$$

are needed as the normalized decay amplitudes are given by

$$\overline{\psi}_q^\epsilon(\tau) = \frac{\psi_q^\epsilon(\tau)}{\sqrt{I_{qq}^\epsilon}}. \tag{10.21}$$

The normalization integrals are scaled accordingly

$$\overline{I}_{A\,qs}^\epsilon = \frac{I_{A\,qs}^\epsilon}{\sqrt{I_{qq}^\epsilon I_{ss}^\epsilon}}. \tag{10.22}$$

Applying proper normalization the physical interpretation of the transition amplitudes $T_{qr}^\epsilon T_{sr}^{\epsilon *}$ is straight forward. The summation of this transition amplitudes over the rank, which show up in equation 10.18, are the elements of the *spin-density matrix*

$$\rho_{qs}^\epsilon = \sum_{N_r} T_{qr}^\epsilon T_{sr}^{\epsilon *}. \tag{10.23}$$

Due to the incoherence of partial-waves with different reflectivity the spin density matrix can be written in block diagonal form

$$\rho = \begin{pmatrix} \mathrm{Flat} & 0 & 0 \\ 0 & \rho^+ & 0 \\ 0 & 0 & \rho^- \end{pmatrix}. \tag{10.24}$$

The log-likelihood function can now be written as

$$\ln \mathcal{L} = \sum_{l=1}^{N} \ln \left[\sum_\epsilon \sum_{qs} \overline{\psi}_q^\epsilon(\tau_l) \overline{\psi}_s^{\epsilon *}(\tau_l) \rho_{qs}^\epsilon \right] - \sum_\epsilon \sum_{qs} \rho_{qs}^\epsilon \overline{I}_{A\,qs}^\epsilon. \tag{10.25}$$

The actual maximization of the likelihood is computed by using a modified version of the MINUIT minimization package [JR75], which provides a variety of minimization algorithms.

10.2.2 Comparison of Different Models Through Likelihood

At this place the interpretation of the likelihood must be shortly discussed. The likelihood, by design is meant to optimize a parameter set applying a given model to a given data set. Looking at equation 10.16, the maximum of the likelihood defines the most probable parameters for a given data set fitted with certain model. Due to the fact, that the absolute value of the likelihood dependence on the data set, the likelihood cannot be used to compare fits to different data sets. However, it is possible to compare different models fitted to the same data set, if one of the models contains the other. Thereby the maximum likelihood cannot be decreased by adding additional amplitudes, i.e. free parameters. This can be easily seen, when looking at the case, where the additional parameters are set to zero, which is a valid solution. In this case the extended model reduces to the original model and the likelihood for a given parameter set for both models is identical. In fact as the degrees of freedom increase one also expects an increase of the likelihood.

10.2.3 Determination of Uncertainty

Following the discussion in [EH78], the uncertainty of the maximum likelihood estimator is given by the reciprocal observed Fischer information

$$\mathrm{Cov}(T) = \mathcal{F}^{-1}(T) \tag{10.26}$$

were the observed Fischer information is given by

$$\mathcal{F}_{qs}(T) = -E\left[\frac{\partial^2 \ln \mathcal{L}}{\partial T_q \partial T_s}\right] \tag{10.27}$$

with expectation value E. Neglecting correlations the statistical uncertainties on one σ confidence level of the transition amplitudes T_q are given by the square-root of the diagonal elements of the covariance matrix

$$\sigma_q = \sqrt{\mathrm{Cov}(T)_{qq}}. \tag{10.28}$$

In reality also the non-diagonal terms play a role and have to be considered by applying the rules of error propagation.

10.3 Observables

As the fitted complex transition amplitudes T^{ϵ}_{ij} have no straight forward physical interpretation, it is more convenient to look at derived quantities, which have a

physical interpretation.

Considering equation 10.15 the number λ of expected events, i.e. the accepted corrected number of events is connected to the intensity $\mathcal{I}(\tau)$. Considering equation 10.2 and applying equation 10.20 and 10.23 as well as 10.21 the number of expected events is given by

$$\lambda = \sum_{\epsilon} \sum_{qs} \rho^{\epsilon}_{qs} \overline{I}^{\epsilon}_{qs} \quad \text{with } \overline{I}^{\epsilon}_{qs} = \frac{I^{\epsilon}_{qs}}{\sqrt{I^{\epsilon}_{qq} I^{\epsilon}_{ss}}}. \tag{10.29}$$

Due to the normalization of the decay amplitudes the *intensity* $\mathfrak{I}^{\epsilon}_{q}$ of a particular partial-wave q and reflectivity ϵ is given by the corresponding diagonal element of the spin density matrix

$$\mathfrak{I}^{\epsilon}_{q} = \rho^{\epsilon}_{qq}. \tag{10.30}$$

For $q \neq s$ the *overlap* between two amplitudes is defined as

$$\mathfrak{O}^{\epsilon}_{qs} = 2\Re(\rho^{\epsilon}_{qs} \overline{I}^{\epsilon}_{qs}). \tag{10.31}$$

In production experiments like COMPASS it is not possible to measure the absolute phase, however the phase difference $\Delta\varphi^{\epsilon}_{qs}$ between two partial wave q and s, which have the same reflectivity ϵ, is an important source of understanding the observed resonance structure. $\Delta\varphi^{\epsilon}_{qs}$ is given by the argument function of the spin density matrix elements

$$\Delta\varphi^{\epsilon}_{qs} = \arg(\rho^{\epsilon}_{qs}). \tag{10.32}$$

In many cases it is useful to chose an *anchor wave*, which has a significant contribution in a wide mass range, to investigate the relative phase motion of other waves. Apart from the phase, another important quantity, which is reflected to interference effects, is the *coherence*

$$\mathfrak{Coh}^{\epsilon}_{qs} = \frac{\left|\rho^{\epsilon}_{qs}\right|}{\sqrt{\rho^{\epsilon}_{qq}\rho^{\epsilon}_{ss}}} = \sqrt{\frac{\Re(\rho^{\epsilon}_{qs})^2 + \Im(\rho^{\epsilon}_{qs})^2}{\mathfrak{I}^{\epsilon}_{q}\mathfrak{I}^{\epsilon}_{s}}}. \tag{10.33}$$

The coherence lies in the interval $[0, 1]$, where the diagonal terms $\mathfrak{Coh}^{\epsilon}_{qq}$ are one by definition. In case of a rank one fit, which describes a coherent scattering process, the coherence is one by definition and therefore reveals no further information, while for fits, which uses rank greater than one or partial-coherence (see section 10.4)models, the coherence might reveal important information to understand the resonance structure.

10.4 Rank and Partial Coherence

The rank N_r of a partial-wave decomposition as introduced before (see section 10.1.1), adds an incoherent sum over the partial-wave (c.f. 10.2) and therefore

introduces completely independent sets of transition amplitudes T^{ϵ}_{ir}, which have to be determined by the fit. On a physical point of view a rank $N_r > 1$ accounts for incoherent production processes, which are reflected in different states of the usually unobserved recoil systems. A typical example for processes, where traditionally a $N_r = 2$ is chosen, is scattering of protons, which allows helicity-flip and helicity-non-flip production processes. If the rank exceeds the number of considered decay amplitudes one speaks of an unlimited rank. However, at very small momentum transfer t' the presented scattering process is assumed to be a coherent process, which is represented by a $N_r = 1$. Nevertheless rank two may be considered, as this can also account for experimental resolution effects, which distorted the coherence of a process.

Here the concept of *partial-coherence* is introduced. This gives more freedom to the fit and thus also allows to account for resolution effects. The experimentally observed reduced coherence is thereby reflected by real parameters $r_{ij} \in [0, 1]$ with $r_{ii} = 1$, These parameters are introduced in the coherent sum and determined by the fit, by using the substitution

$$T_i T_j^* \rightarrow r_{ij} T_i T_j^*. \tag{10.34}$$

Obviously the parameters r_{ij} dilute the contribution of interference terms of the amplitudes i and j, while at the same time the phase (see section 10.3) remains unchanged. This is an important difference to a rank-two fit. Tuning of the fit model is applied by fixing some r_{ij}. For obvious reasons the parameters r_{ij} for partial-waves with the same spin projection M is set to one for the given analysis.

10.5 Isobaric Model

Motivated by the experimental observation that nature seems to prefer two-body decays over multi-particle decays, the isobaric model is used to describe decay into multi-particle final states as sequence of two-body decays. Looking at scattering processes at COMPASS an intermediate resonance X with mass m_X and quantum numbers is produced in beam-target interaction (see chapter 3). At high energies neither the resonance nor its decay products interact with the recoil particle, thus the decay of the resonance can be described in the isobaric model.

Considering the process $\pi^-\mathrm{Ni} \rightarrow \pi^-\pi^0\pi^0\mathrm{Ni}$, which is investigated here, the produced resonance decays into an two-pion isobar ξ with mass m_ξ and an spectator pion with an orbital angular momentum L between the decay products. Afterward the isobar decays into two pions, which are part of the final state. The schematics of this decay is shown in figure 10.1. The resonance is characterized by its quantum numbers $J^{PC}M^{\epsilon}$, with J being the total angular momentum, P denoting the parity and C the C-parity. M is the spin projection and ϵ the reflectivity. Due to the nature of the pomeron, which is as the leading Regge trajectory mediating the beam-target interaction, the resonance must have the same I^G as

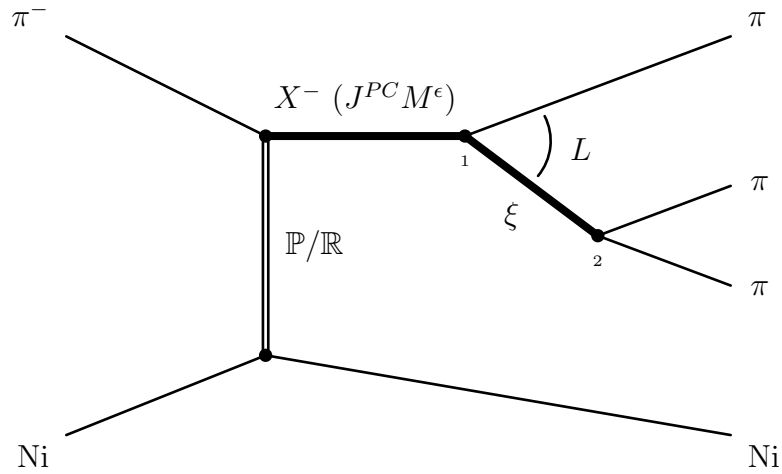

Figure 10.1: The schematic shows the production of resonance X with quantum numbers $J^{PC}M^{\epsilon}$ in π^--nickel scattering and the isobaric decays into a three-pion final state. At vertex 1 X decays into a bachelor pion and an isobar ξ. L is the angular momentum between those two. The isobar ξ then decays at vertex 2 into two pions, which together with the bachelor pion form the final state.

the incoming pion. Thus, a particular partial-wave, describing an isobar decay, is characterized by the quantum numbers of the intermediate state, the isobar and the orbital angular momentum. In the following the notation $J^{PC}M^{\epsilon}\,\xi\,L\,\pi$ shall be used.

Chapter 11

Parametrization of Partial-Waves

An important input to the PWA is the parametrization of the partial-wave amplitudes. Dealing with isobaric partial-waves, each wave is defined by the quantum numbers $I^G J^{PC} M^\epsilon$ of the intermediate state X, the isobar ξ, through which the decay is realized, and the angular momentum L between the isobar and the bachelor pion. The quantum numbers $I^G = 1^-$ are given by the quantum numbers of the incoming pion. Thus, the quantum numbers I^G are omitted in the notation $J^{PC} M^\epsilon \, \xi \, L \, \pi$, which in the following is used to characterize isobaric partial-waves. The so-called helicity formalism is a convenient way to describe the angular dependence of many-body decays, which are realized by consecutive two-body decays. This formalism, which is also applied in the analysis presented in chapter 13, is discussed in the following. The discussion is extended to the description of the parametrization of the mass-dependence of the isobars, which enters the calculations. A brief discourse of the reflectivity ϵ follows. Last but not least the parametrization of a possible non-resonant contribution to the observed spectra is presented.

11.1 The Helicity Formalism

The decay of the resonance X with mass m_X into the $\pi^-\pi^0\pi^0$-final state is fully specified by five additional kinematic variables. Using the *helicity formalism* these variables are chosen to be the decay angles in the *Gottfried-Jackson* frame, i.e. the azimuthal angle, which is called Treiman-Yang angle, ϕ_{TY} and the polar angle θ_{GJ}, the mass m_ξ of the isobar and the decay angles θ_{HF} and ϕ_{HF} in the *helicity frame* of the isobar. The Gottfried-Jackson frame is the rest frame of the resonance X with the z-axis z_{GJ} in direction of the beam momentum and the y-axis being a normal

$$\vec{e}_y = \frac{\vec{p}_{\mathrm{target}} \times \vec{p}_{\mathrm{recoil}}}{|\vec{p}_{\mathrm{target}} \times \vec{p}_{\mathrm{recoil}}|} \tag{11.1}$$

to the production plane, which is defined by the trajectories of the target $\vec{p}_{\text{target}}$ and recoil $\vec{p}_{\text{recoil}}$ particle. The helicity frame is the rest frame of the isobar, with its z-axis z_{hel} along the flight direction of the isobar and the y-axis perpendicular to the plane spanned by the z-axis of the Gottfried-Jackson and helicity frame $y_{\text{hel}} = z_{\text{GJ}} \times z_{\text{hel}}$. For both coordinate system the x, y and z-axis form a right-handed coordinate system $x = y \times z$. Looking at the center-of-mass frame the helicity is given by the spin projection to the reference axis, i.e. $\lambda = s_{z_{\text{hel}}}$, which simplifies the calculation. Considering that the final state is described by $(2s_1+1)(2s_2+1)$ helicity states $|q\lambda_1\lambda_2\rangle$ and the breakup momentum q of the final state particles 1 and 2. λ_1 and λ_2 couple to the spin S with the helicity $\lambda = \lambda_1 - \lambda_2$. The two-body decay amplitude in the helicity formalism is given by

$$A(m, \phi, \theta) = \sum_{\lambda} D^J_{\lambda M}(\phi, \theta, 0) f_\lambda(m, P_R, w_1, p_1, w_2, p_2). \tag{11.2}$$

The angular dependence is described by the *D-function*, trigonometrical function, which allows to write the rotation of the spin state $|JM\rangle$ as linear combination of $|JM'\rangle$ states

$$R(\alpha, \beta, \gamma)|JM\rangle = \sum_{M'=-J}^{J} D^J_{M'M}(\alpha, \beta, \gamma)|JM'\rangle. \tag{11.3}$$

$R(\alpha, \beta, \gamma) = e^{-i\alpha J_z} e^{-i\beta J_y} e^{-i\gamma J_z}$ is the operator of an active rotation with the Euler angle α, β and γ. The magnitude of the total angular momentum with its eigenvalue J is invariant under this rotation. In equation 11.2 the third angle is set to zero, which has no physical implication. The angular dependence of the two-body decay is given by [Chu71]

$$D^J_{\lambda M}(\phi, \theta, 0) = e^{-iM\phi} d^J_{\lambda M}(\theta) \tag{11.4}$$

with

$$\begin{aligned} d^J_{\lambda M}(\theta) = & [(J+\lambda)!(J-\lambda)!(J+M)!(J-M)!]^{1/2} \\ & \cdot \sum_{\kappa} \left[\frac{(-1)^\kappa}{(J-M-\kappa)!(J+\lambda-\kappa)!(M+\kappa-\lambda)!\kappa!} \right. \\ & \left. \cdot \left(\cos\frac{\theta}{2}\right)^{2J+\lambda-M-2\kappa} \left(-\sin\frac{\theta}{2}\right)^{M-\lambda+2\kappa} \right]. \end{aligned} \tag{11.5}$$

The sum runs over all values of κ, for which the term is greater than zero [Ros75].

The non-angular part of the two-body amplitude (see equation 11.2) is given

by

$$f_\lambda(m, P_R, w_1, p_1, w_2, p_2) = \underbrace{\sqrt{2l+1}}_{\text{normalization}} \underbrace{(l0s\lambda|J\lambda)(s_1\lambda_1 s_2\lambda_2|s\lambda)(I_1 I_{1z} I_2 I_{2z}|I_R I_{Rz})}_{\text{Clebsch-Gordon coeff.}} \underbrace{F_l \Delta(m) \alpha_{ls}}_{\text{dynamics}} A_1 A_2. \quad (11.6)$$

A_1 and A_2 are the decay amplitudes of the daughter particles. For final state particles this amplitudes are set to one. The couplings are described by Clebsch-Gordon coefficient. The first one $(l0s\lambda|J\lambda)$ describes the l-s-coupling to the total angular momentum J, with, as l is perpendicular to the reference axis, $l_z = 0$. $(s_1\lambda_1 s_2\lambda_2|s\lambda)$ describes the coupling of the spins s_1 and s_2 of the daughter particles to the total spin s, with its projection to the z-axis being the helicity $\lambda = \lambda_1 - \lambda_2$. The last Clebsch-Gordon coefficient $(I_1 I_{1z} I_2 I_{2z}|I_R I_{Rz})$ stems from the isospin coupling. F_l are the angular momentum barrier factors, which are discussed below. The mass-dependent dynamics are parametrized by $\Delta(m)$. The mass-dependent dynamics of the resonance X are in general unknown and the subject of the mass-dependent partial-wave analysis. Within an analysis bin the partial-wave are assumed to not depend on m. Thus, the m-dependent dynamics of the resonance X are neglected by using $\Delta_X(m) = 1$. The mass-dependence of the isobar ξ is an important input for the partial-wave fit and discussed in section 11.2.

11.2 Parametrization of Mass-Dependent Dynamics

In order to parametrize the mass-dependence of the two-body decay, there are three formalisms, which are commonly used. The most common formalism is the *Breit-Wigner* formalism, which describes a short-lived, i.e. narrow, resonance, by a Breit-Wigner shape, which is sometimes also referred as Cauchy shape. However, for two resonances lying close to each other the *Flatté* formalism, which accounts for two decay modes, gives a better description. Going to a system of heavily overlapping resonances, the *K-matrix* formalism shows its advantage. It regards both the overlap of mother state and their decay modes. Table 11.1 gives an overview of the isobar parametrization relevant for the presented analysis.

11.2.1 The Breit-Wigner Formalism

The Breit-Wigner formalism parametrizes the mass-dependence of a short-lived resonance of mass m_0 and width Γ_0 with a relativistic Breit-Wigner function (see

isobar	**paramters**	**formalism**
$(\pi\pi)_S$ Wave	available at [AMP87]	"M-Solution" K-Matrix-Formalism
$(\pi\pi)_S$ Wave*	available at [AMP87]	"K_1-Solution" K-Matrix-Formalism $f_0(980)$ subtracted from amplitude
$f_0(980)$	$m_0 = 0.98\,\mathrm{GeV}/c^2$ $\Gamma_0 = 0.04\,\mathrm{GeV}/c^2$	Breit-Wigner Formalism
$f_0(980)^*$	$m_\delta = 0.965\,\mathrm{GeV}/c^2$ $g_{\pi\pi} = 0.165\,\mathrm{GeV}/c^2$ $g_{KK} = 4.21 \cdot g_{\pi\pi}$	Flatté Formalism
$f_0(1500)$	$m_0 = 1.507\,\mathrm{GeV}/c^2$ $\Gamma_0 = 0.109\,\mathrm{GeV}/c^2$	Breit-Wigner Formalism
$\rho(770)/\rho$	$m_0 = 0.770\,\mathrm{GeV}/c^2$ $\Gamma_0 = 0.161\,\mathrm{GeV}/c^2$	Breit-Wigner Formalism
$f_2(1270)/f_2$	$m_0 = 1.275\,\mathrm{GeV}/c^2$ $\Gamma_0 = 0.185\,\mathrm{GeV}/c^2$	Breit-Wigner Formalism

Table 11.1: Overview of parametrization of isobars. Isobar parametrization marked with * have been studied, but are not used for the presented analysis. The a_1, a_2 and π_2 are three-pion isobars, which are used for the PWA in t' to model the $m_{3\pi}$ dependence of the resonance X.

2.2). The Breit-Wigner amplitude

$$A_{\mathrm{BW}}(m) = \frac{m_0 \Gamma_0}{m_0^2 - m^2 - i m_0 \Gamma_{\mathrm{tot}}(m)} \tag{11.7}$$

with the mass-dependent width

$$\Gamma_{\mathrm{tot}}(m) = \sum_n \Gamma_0 \frac{m_0}{m} \frac{q_n}{q_{0\,n}} \frac{F_{l_n}^2(q_n)}{F_{l_n}^2(q_{0\,n})} \tag{11.8}$$

describes a mass-dependence $\Delta(m) = A_{\mathrm{BW}}(m)$ of the two-body decay. Here, the sum in principle contains all available decay channels. $q = q(m)$ is the breakup momentum with $q_0 = q(m_0)$ and consequently $\Gamma_{\mathrm{tot}}(m_0) = \Gamma_0$ and $\Delta(m_0) = 1$. The Blatt-Weisskopf centrifugal-barrier factors $F_l(q)$ are accounting for the conservation of the angular momentum, which require a certain breakup momentum between the two daughter particles. In the parametrization suggested by Quigg and Hippel [HQ72] these factors are given by [Chu10]

$$F_l(q) = \frac{h_l^{(1)}(1)}{x h_l^{(1)}(x)} \quad \text{with } x = q/q_R. \tag{11.9}$$

$h_l^{(1)}(x)$ are the spherical Hankel function of the first kind and are given by a power series expansion

$$h_l^{(1)}(x) = \frac{-ie^{ix}}{x^l} \sum_{k=0}^{l} (-1)^k \frac{(l+k)!}{2^k k!(l-k)!} (-ix)^{l-k}. \tag{11.10}$$

Note that $F_l(q_R) = 1$ by definition. The quantity $q_R = 0.1973\,\mathrm{GeV}/c$ corresponds to the effective range of the strong interaction, which is approximately 1 fm. The centrifugal-barrier factors for $l \leq 3$ are [Chu10]

$$F_0(q) = 1 \tag{11.11}$$

$$F_1(q) = \sqrt{\frac{2z}{\sqrt{z+1}}} \tag{11.12}$$

$$F_2(q) = \sqrt{\frac{12z^2}{\sqrt{(z-3)^2 + 9z}}} \tag{11.13}$$

$$F_3(q) = \sqrt{\frac{277z^3}{\sqrt{z(z-15)^2 + 9(2z-5)^2}}} \tag{11.14}$$

with $z = (q/q_R)^2$. Looking at the kinematic boundaries $q \to 0$ and $q \to \infty$ the Quigg-Hippel factors behave like

$$F_l(q)|_{q\to 0} \propto p^l \quad \text{and} \quad F_l(q)|_{q\to\infty} = \text{const}, \tag{11.15}$$

which reproduce the right physical behavior at small values of q by having a finite intensity for large q.

Note for unknown branching ratios, a Breit-Wigner function with constant width Γ_0 can be used as approximation.

11.2.2 The Flatté Formalism

The Flatté formalism [Fla76] parametrize the decay of a two-channel resonance by explicitly accounting both channels and their thresholds. Using the Breit-Wigner parametrization in the coupled channel form the Flatté amplitude of the resonance δ with nominal mass m_δ decaying into the two channels a and b is given by [Chu10]

$$A_{\text{Flatté}}(m) = \frac{|D_\delta(m_t)|}{D_\delta(m)} \tag{11.16}$$

with

$$D_\delta(m) = m_\delta^2 - m^2 - i m_\delta \frac{m_t}{m} \left(g_a^2 q_a + g_b^2 q_b\right). \tag{11.17}$$

The constant m_t is usually chosen to be the threshold of the channel, which opens up, and provides proper normalization, with $A_{\text{Flatté}}(m_t) = 1$. g_a and g_b denote the coupling constants for the resonance coupling to states a and b, respectively. $q_{a,b}$ are the corresponding phase space factors or so-called breakup momenta. If a or b, respectively, is a two-body state $\alpha\beta$ these phase space factors are given by

$$q_a, b = q_{\alpha\beta} = m_{\alpha\beta}^{-2} \sqrt{\left(m_{\alpha\beta}^2 - (m_\alpha + m_\beta)^2\right)\left(m_{\alpha\beta}^2 - (m_\alpha - m_\beta)^2\right)} \tag{11.18}$$

with the invariant mass $m_{\alpha\beta}$ of the two-body system. If this mass is below the threshold of the decay channel $m_{\alpha\beta} < m_\alpha + m_\beta$ the breakup momentum becomes imaginary[1]. This parametrization is especially helpful for resonance with a decay channel opening up near the resonance mass. A prominent example is the $f_0(980)$, which is relevant for the partial-wave analysis of the $\pi^-\pi^0\pi^0$ final state and lies near the $K\overline{K}$ threshold. The two couplings $g_{\pi\pi} = 0.165\,\text{GeV}/c^2$ and $g_{KK} = 4.21 \cdot g_{\pi\pi}$ have been determined by a partial-wave analysis of J/Ψ decaying into $\phi\pi^+\pi^-$ and ϕK^+K^- [ABB$^+$05]. This parametrization has been investigated for the description of the event sample, which obtained by the event selection

[1] Often an additional heavy side function $\Theta(m_{cd} - m_c - m_d)$, which below threshold ensures the phase space factor to be zero, is introduced (see [B$^+$12]). For the present analysis, however, the parametrization introduced by [Fla76], which uses an analytic continuation into the complex plane, is used.

in chapter 8. The simple Breit-Wigner parametrization, however, describes the observed data better. Thus the $f_0(980)$ is described by a simple Breit-Wigner.

11.2.3 The *K*-Matrix Formalism

States with heavily overlapping resonances in the initial state cannot be described with Breit-Wigner shapes. An example for such states are the light scalar mesons. Some of this resonances have a large decay width, which produces significant overlap. An additional complication is the opening up of several decay channels within a short mass interval. The $(\pi\pi)_S$ decay channel, which describes the sector of light scalar mesons, is in the presented analysis parametrized using the *K-matrix* formalism. In the K-matrix formalism the transition amplitude T, which connects the initial and the final state, is written as

$$T = \mathbb{K}(\mathbb{I} - i\rho\mathbb{K})^{-1} \tag{11.19}$$
$$= (\mathbb{M} - i\rho)^{-1}, \tag{11.20}$$

where the K-matrix $\mathbb{K}$ is a real symmetric matrix and $\mathbb{M}$ its inverse. $\mathbb{I}$ is the identity matrix. The elements ρ_1 and ρ_2 of the diagonal ρ-matrix are the weighted average of the neutral and charged phase-space factors. Multiple solutions for the $(\pi\pi)_S$ parametrization had been obtained fitting to $\pi\pi$ scattering data [AMP87]. For this fit the elements of the 2×2 K-matrix is given by

$$K_{ij} = \frac{s - s_0}{4m_K^2} \sum_p \frac{f_i^p f_f^p}{(s_p - a)(s_p - s_0)} + \sum_{n=0} c_{ij}^n = (s - s_0)\hat{K}_{ij}. \tag{11.21}$$

with the squared center-of-mass energy $s = m^2$. Alternatively the M-matrix is parametrized as

$$M_{ij} = \frac{a_{ij}}{s - s_0} + \sum_p \frac{f_i'^p f_f'^p}{s_p' - s} + \sum_{n=0} c_{ij}'^n \left(\frac{s}{4m_K^2} - 1\right)^n. \tag{11.22}$$

The M solution[2] from [AMP87] is found to deliver the best description of the present data set and is consequently used to describe the $(\pi\pi)_S$ waves in the partial-wave fit presented in chapter 13. In addition the parametrization using the K_1 solution from the same publication has been studied. In contrast to the M solution the K_1 solution contains besides the wide scalar mesons also the $f_0(980)$, which is treated as a single resonance. Thus using the K_1 solution the $f_0(980)$ described by a Breit-Wigner with $m_0 = 0.9855\,\mathrm{GeV}/c^2$ and $\Gamma_0 = 0.0449\,\mathrm{GeV}/c^2$ is subtracted from the $(\pi\pi)_S$ line-shape

$$A_{\pi\pi} \to A_{\pi\pi} - c \cdot A_{f_0(980)} \quad \text{with } c = -0.3878 + 0.2991i. \tag{11.23}$$

[2]Please refer to the original publication for the exact parametrization.

11.3 Reflectivity

As discussed in section 2.1 for strong processes in the light quark sector the G-Parity is a good quantum number. The parity P in contrast is a quantum number, which can be used regardless of the actual meson content or the nature of the observed process. It is useful to describe processes like $A + B \to X + C$ regarding their behavior under reflection on the production plane. In any rest frame of X with the y axis perpendicular to the production plane the reflection operator is connected with the parity by a rotation by π through the y-axis

$$\Pi_y = P \exp(-i\pi J_y). \tag{11.24}$$

Let ψ^ϵ_{JM} be an eigenstate of Π_y. The behavior of ψ^ϵ_{JM} under the rotation operator is then described by the reflectivity ϵ, which is defined by

$$\Pi_y \psi^\epsilon_{JM} = -\epsilon \psi^\epsilon_{JM}. \tag{11.25}$$

Here the eigenstates of Π_y are given by linear combinations of states with opposite spin projection M

$$\psi^\epsilon_{JM} = c(M) \left(\psi_{JM} - \epsilon P \psi_{J-M} \right). \tag{11.26}$$

The reflectivity for $M = 0$ states is $\epsilon = +$ per definition. For $M > 0$ the reflectivity can take values of $\epsilon = \pm$. The factor

$$c(M) = \begin{cases} \frac{1}{2} & \text{, for } M = 0 \\ \frac{1}{\sqrt{2}} & \text{, for } M > 0 \end{cases} \tag{11.27}$$

establishes proper normalization. Looking at the high energy limit within the Gottfried-Jackson frame the reflectivity and the naturality coincide [Sch12].

Due to the nature of the photon exchange for small values of $m_{3\pi}$ and t' the reflectivity observed in Primakoff reaction is expected to be positive, i.e. $\epsilon = +$. However at small masses $m_{3\pi}$ and low transferred momentum t' the experimental resolution does not allow to measure the production plane precisely, thus a leakage into negative reflectivity waves is expected.

11.4 Non-Resonant Contributions

Besides the resonant contributions, which are described by the isobar model, there are also non-resonant contributions, like the Deck effect (see section 3.2.3). If the angular dependence of such a contribution is known in differential form, it can be introduced as a partial-wave. In the present analysis this is achieved for the $\pi^- \gamma \to \pi^- \pi^0 \pi^0$, which is calculated in the framework of chiral perturbation theory.

11.4.1 Parametrization of the Chiral-Waves

Looking at equation 1.8 the total differential form of the chiral amplitude is given by

$$\vec{\mathcal{A}} = \sqrt{\frac{\alpha}{32\pi^3 f_\pi^4 (s - m_\pi^2)}} \left(\hat{k} \times (\vec{q}_1 A_1 + \vec{q}_2 A_2) \right). \tag{11.28}$$

In the chosen reference frame, i.e. the Gottfried-Jackson frame, the direction vector of the photon $\hat{k} = (0, 0, -1)$ has vanishing x and y components. Thus the z component of $\vec{\mathcal{A}}$ is zero. Considering the behavior under the reflectivity operation, the negative reflectivity part $\epsilon = -1$ of the amplitude is given by the x component of $\vec{\mathcal{A}}$, which change sign. The y component, which remains unchanged under the reflectivity operator, corresponds to $\epsilon = +1$. The partial-wave decay amplitudes $\psi^\epsilon_{\text{ch}}$ are then given by

$$\psi^-_{\text{ch}} = -\sqrt{\frac{\alpha}{32\pi^3 f_\pi^4 (s - m_\pi^2)}} \left((q_1)_x A_1 + (q_2)_x A_2 \right) \tag{11.29}$$

and

$$\psi^+_{\text{ch}} = \sqrt{\frac{\alpha}{32\pi^3 f_\pi^4 (s - m_\pi^2)}} \left((q_1)_y A_1 + (q_2)_y A_2 \right). \tag{11.30}$$

$A_{1,2}$, in general sum all possible Feynman diagrams. This sum is usually truncated at a given order. For the presented analysis four different flavors of the chiral-waves are available, which corresponds to the ChPT calculation presented in section 1.2. For each flavor two partial waves are calculated, one with positive and one with negative reflectivity. The different flavors of the chiral wave describe the same process and thus have to be used mutually exclusive. The resulting partial-waves are denoted as $(\text{ChPT})^\epsilon_\Lambda$, where $\Lambda \in \{\text{LO}, \text{NLO}, \rho, \rho\rho\}$ is the flavor of the chiral waves.

11.4.2 Properties of the Chiral Waves

The chiral wave waves exhibit spin projection $M = 1$ due to the nature of quasi-real photon exchange. At low values of t', physically only waves with positive reflectivity contribute. Consequently, in the following the chiral waves with positive reflectivity are studied. Thus, if not stated explicitly, the given discussion and quantity refer to $\epsilon = +1$.

Figure 11.1 shows the Dalitz plot of the normalized intensity for the different flavors of chiral-waves at the three-pion mass $m_{3\pi} = 0.7\,\text{GeV}/c^2$. The masses of the two charged $\pi\pi$ subsystems are drawn on the x and y axis. Near the three-pion production threshold and well below the $\rho\pi$ threshold the Dalitz plots of the four chiral waves are similar. This is especially true for those of the chiral waves, which include higher order corrections. The leading-order calculation feature a diagonal shape, which does not fade at the kinematic limits, where one of the two

pion masses is approaching its minimum. Higher-order calculation still reveal a diagonal structure, which, however, show elliptic shapes. Studying three-pion masses in the region of $1\,\mathrm{GeV}/c^2$, in case of the double ρ amplitude the influence of ρ exchange becomes apparent (see figure 11.2). Favoring two-pion masses around the rest mass m_ρ of the ρ meson a significant deviation from the elliptic shape is observed. While the principle shape of LO and NLO chiral waves remain unchanged, the Dalitz plots of chiral waves including single ρ exchange shows a small distortion. Stepping further to $1.3\,\mathrm{GeV}/c^2$ gives rise to the characteristic structure connected to the ρ resonances for both the single and double ρ exchange calculations (figure 11.3).

Besides the Dalitz plots another set of distribution, which show the dependence of the normalized intensity on the decay angles in the Gottfried-Jackson frame θ_{GJ} and ϕ_{TY}, gives further impression of the behavior of partial-waves. Being a $M = 1$ process the dependence on ϕ_{TY} shows the $\cos^2$ structure, which is typical for this spin projection. The $\cos^2$ structure is observed for all flavors of chiral waves and all three-pion masses. Figure 11.4, 11.5 and 11.6 show the dependence of the squared normalized decay amplitude $|\overline{\psi}^+_{\mathrm{ch}}|^2$ of the chiral waves on the decay angles in the Gottfried-Jackson frame. The dependence is shown for three-pion mass $m_{3\pi}$ of $0.7\,\mathrm{GeV}/c^2$, $1.0\,\mathrm{GeV}/c^2$ and $1.3\,\mathrm{GeV}/c^2$, respectively. Besides the dominating $M = 1$ behavior, which generates two maxima at $\phi_{\mathrm{TY}} = 0$ and $\phi_{\mathrm{TY}} = \pm\pi$, one can observe, that all chiral-waves tend to prefer high values of θ_{GF}. At $0.7\,\mathrm{GeV}/c^2$ the LO and NLO wave still extend to smaller values of θ_{GJ}, LO more than NLO. These waves show only one maximum inn θ_{GJ}. Due to the $M = 1$ behavior, which leads to a $\cos^2$ modulations in ϕ_{TY}, two distinct maxima are formed. In case of the LO calculation the θ_{GJ}-position of the maxima is at ≈ 2.3, while for NLO one finds a slightly higher value of ≈ 2.4. The observed structure in general reminds of a fork. The structure of the chiral-waves including ρ-exchange shifts the maxima to $\theta_{\mathrm{GJ}} \approx 2.7$. Besides the two global maxima local maxima at $\theta_{\mathrm{GJ}} \approx 0.4$ are formed. At a three-pion mass of $1.0\,\mathrm{GeV}/c^2$ the ρ amplitudes have converged to a structure similar to the one observed for LO and NLO calculation for all masses and extend towards slightly smaller azimuthal angles. With LO and NLO extending to slightly higher azimuthal angles all flavors of chiral waves reveal similar angular dependencies at $1.0\,\mathrm{GeV}/c^2$. The maxima are found at $\theta_{\mathrm{GJ}} \approx 2.6$. Going to $m_{3\pi} = 1.3\,\mathrm{GeV}/c^2$ the general shape does not change any more, however, the maxima move to $\theta_{\mathrm{GJ}} \approx 2.7$ and a much faster depletion towards small angles is observed. In case of the NLO local maxima at $\theta_{\mathrm{GJ}} \approx 0.6$ show up.

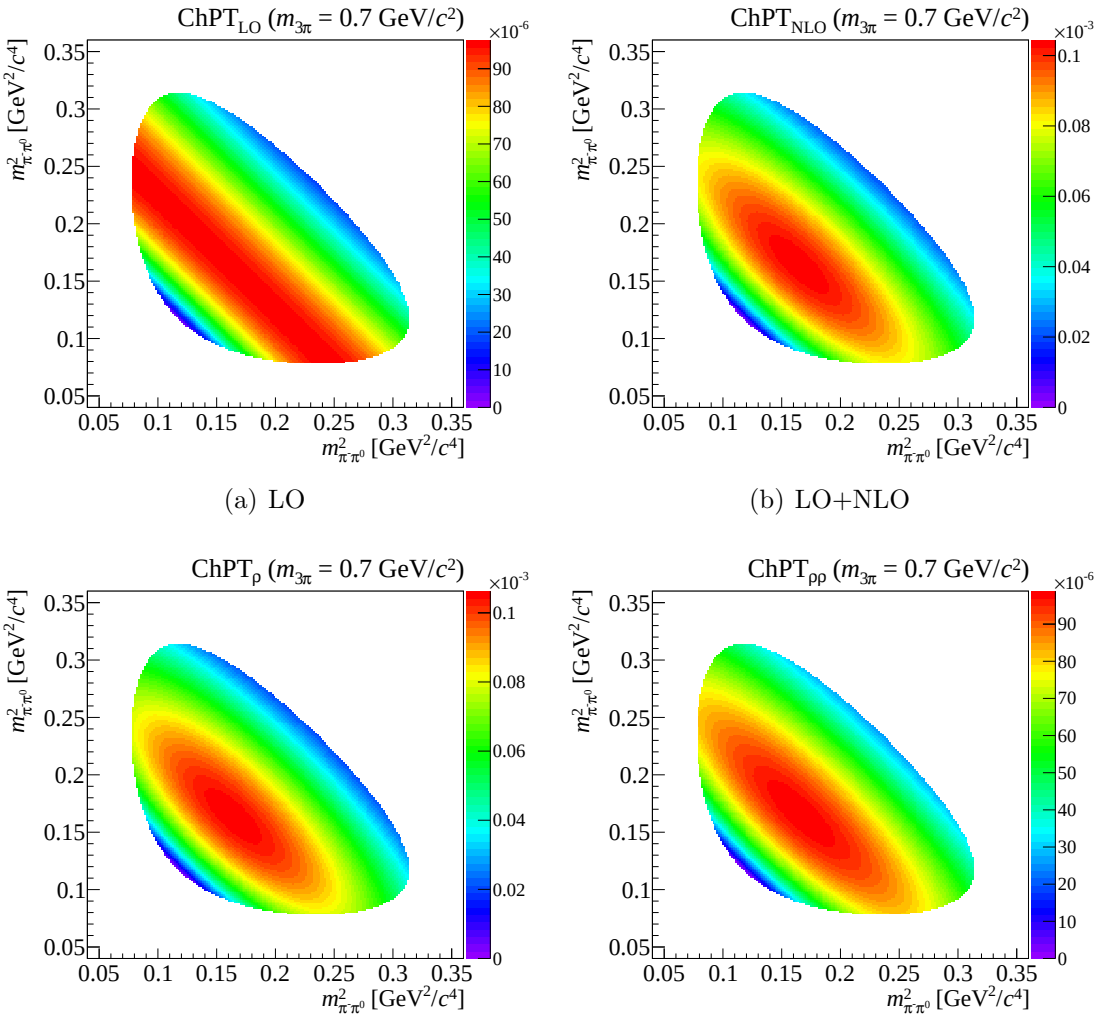

(a) LO (b) LO+NLO

(c) LO+NLO+single ρ (d) LO+NLO+single ρ+double ρ

Figure 11.1: Dalitz plots showing the invariant mass dependence of one charged $\pi\pi$ subsystems to the other for the partial-waves, which are based on calculations in the framework of ChPT at a three-pion $m_{3\pi} = 0.7\,\mathrm{GeV}/c^2$. Due to physical expectation the behavior for reflectivity $\epsilon = 1$ is shown.

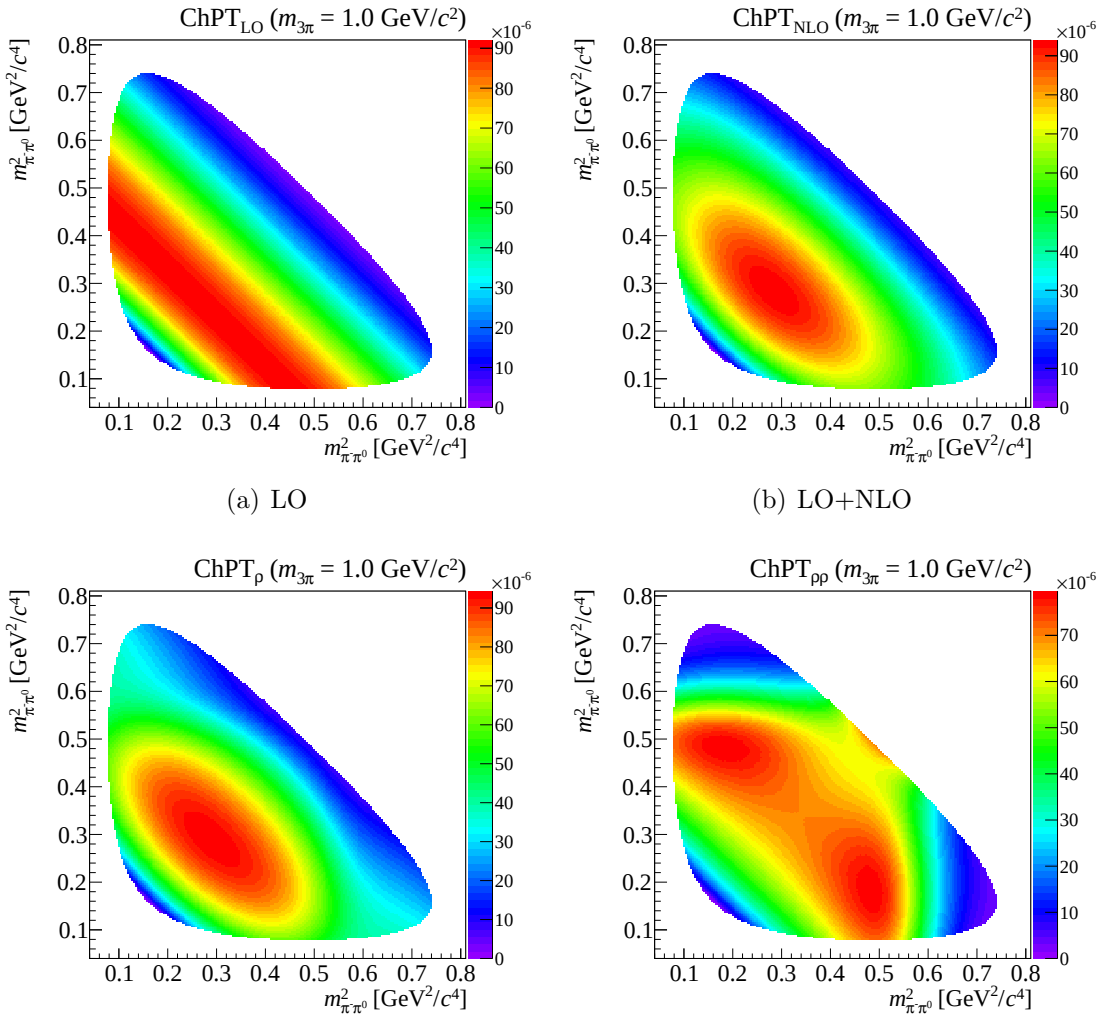

(a) LO

(b) LO+NLO

(c) LO+NLO+single ρ

(d) LO+NLO+single ρ+double ρ

Figure 11.2: Dalitz plots showing the invariant mass dependence of one charged $\pi\pi$ subsystems to the other for the partial-waves, which are based on calculations in the framework of ChPT at a three-pion $m_{3\pi} = 1.0\,\mathrm{GeV}/c^2$. Due to physical expectation the behavior for reflectivity $\epsilon = 1$.

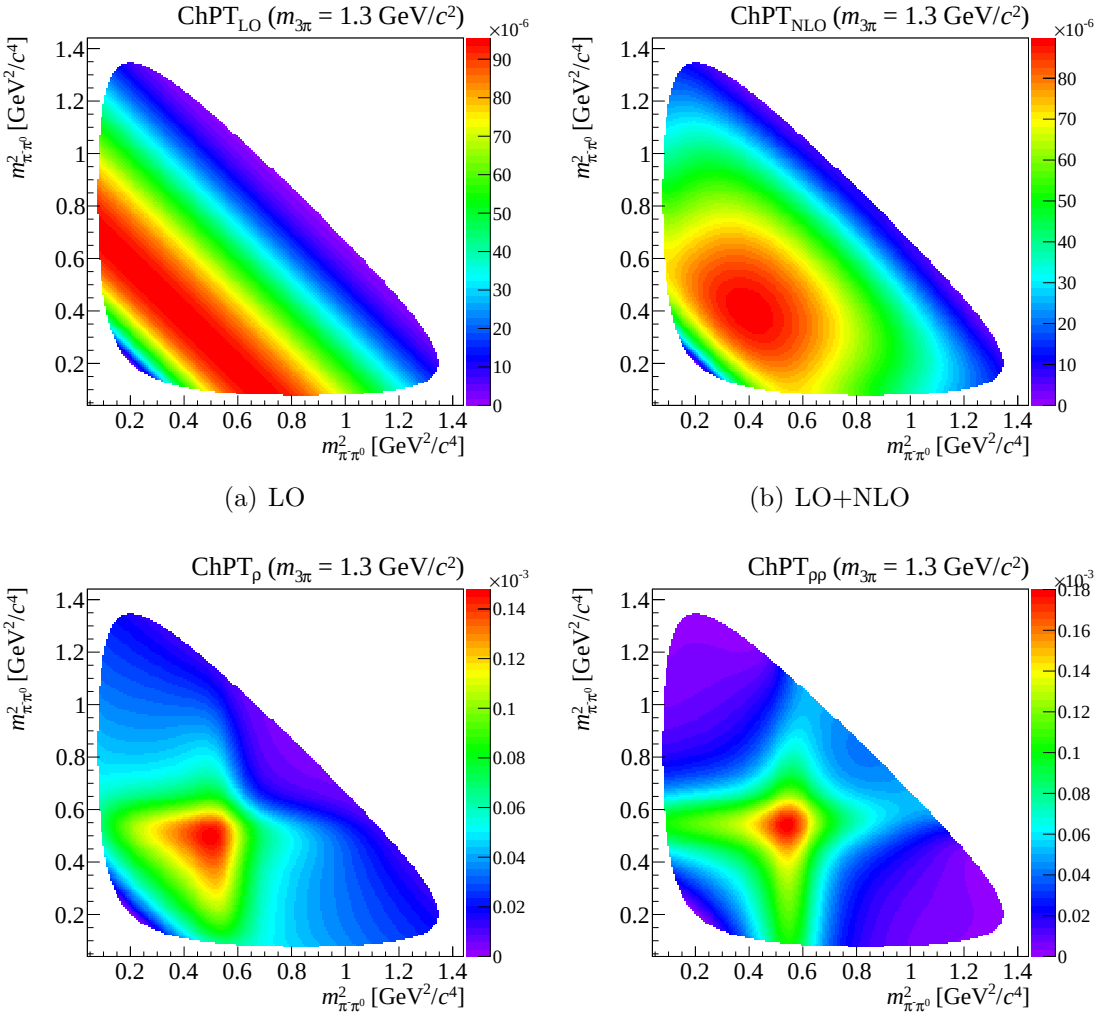

(a) LO (b) LO+NLO

(c) LO+NLO+single ρ (d) LO+NLO+single ρ+double ρ

Figure 11.3: Dalitz plots showing the invariant mass dependence of one charged $\pi\pi$ subsystems to the other for the partial-waves, which are based on calculations in the framework of ChPT at a three-pion $m_{3\pi} = 1.3\,\mathrm{GeV}/c^2$. Due to physical expectation the behavior for reflectivity $\epsilon = 1$.

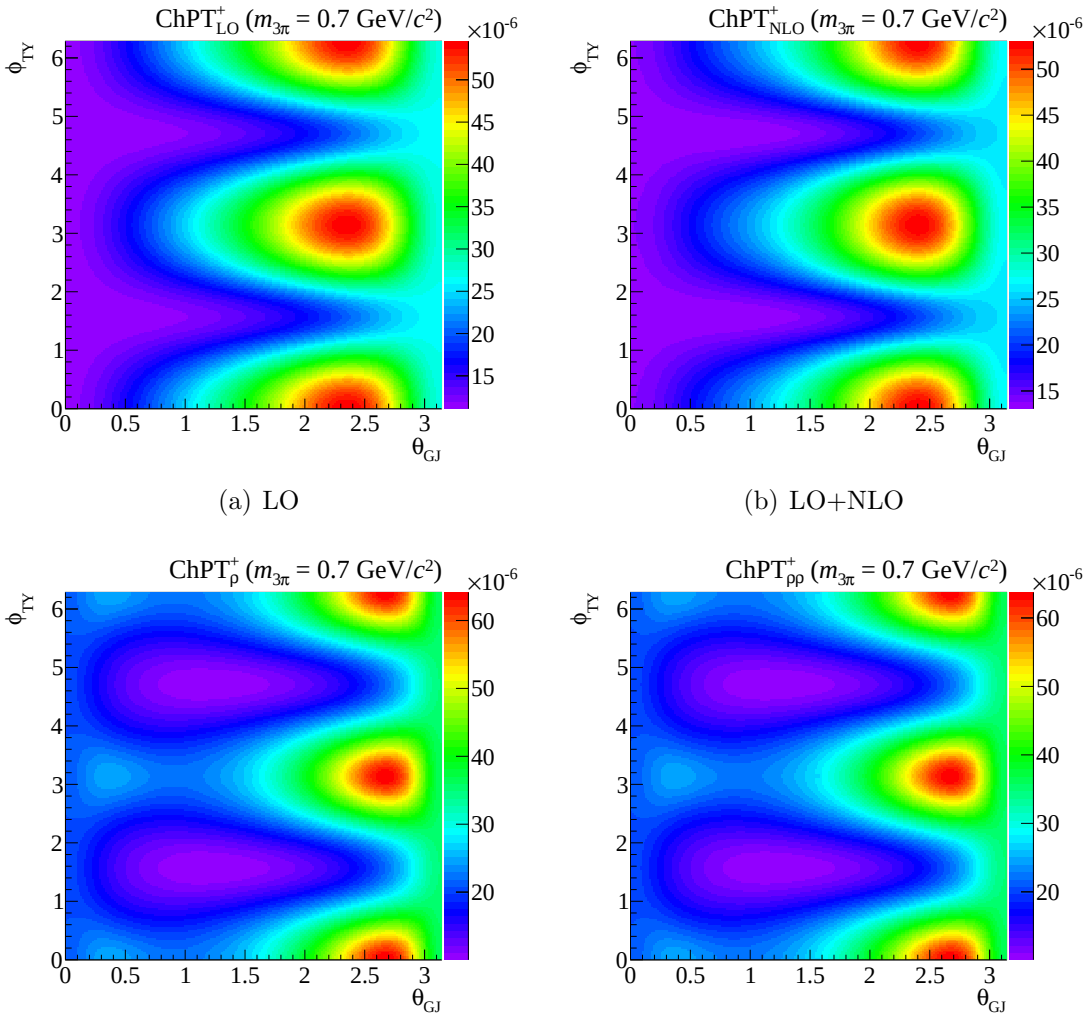

(a) LO (b) LO+NLO

(c) LO+NLO+single ρ (d) LO+NLO+single ρ+double ρ

Figure 11.4: Dependence of the normalized intensity of chiral waves on the decay angle θ_{GJ} and ϕ_{TY} at $m_{3\pi} = 0.7\,\mathrm{GeV}/c^2$. The dependence is shown for the different flavors of chiral-waves with positive reflectivity $\epsilon = 1$.

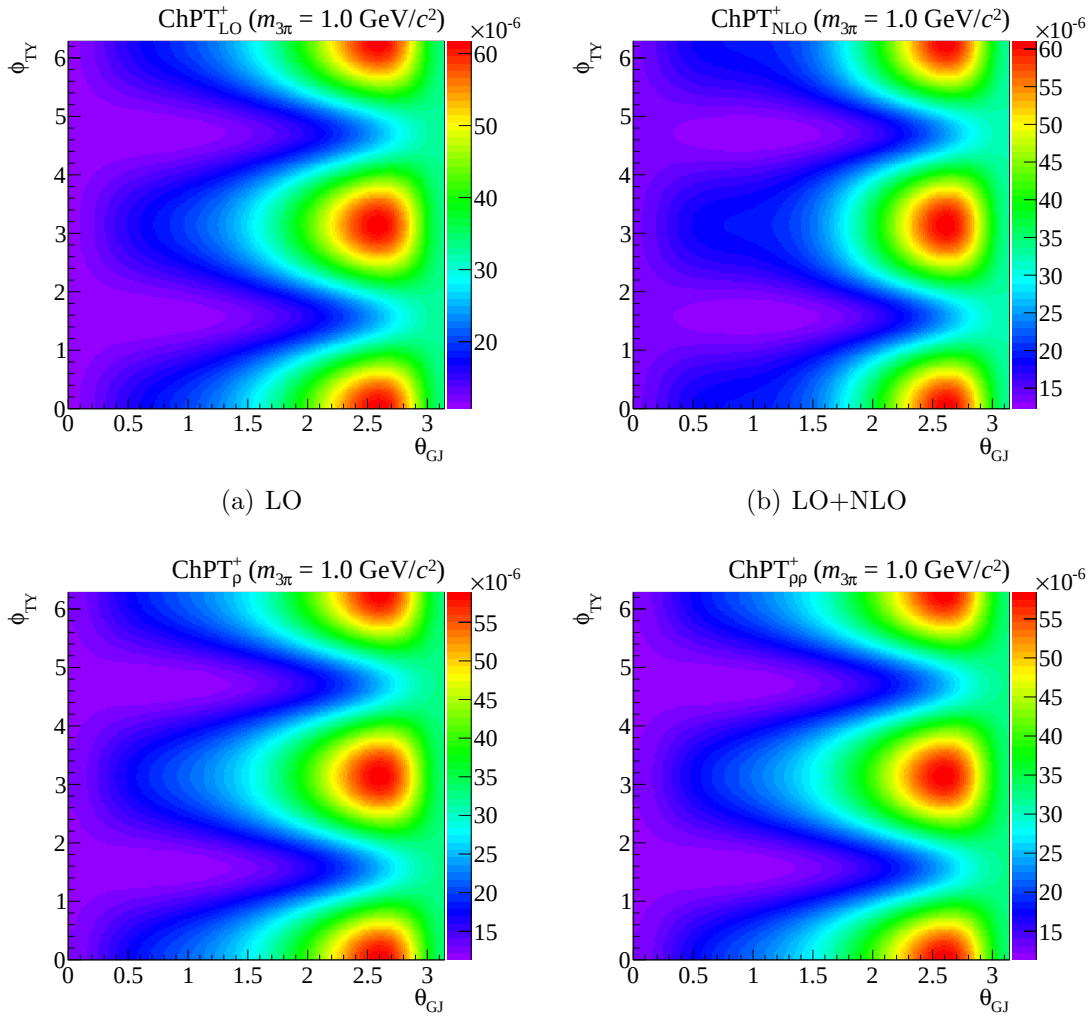

(a) LO

(b) LO+NLO

(c) LO+NLO+single ρ

(d) LO+NLO+single ρ+double ρ

Figure 11.5: Dependence of the normalized intensity of chiral waves on the decay angle θ_{GJ} and ϕ_{TY} at $m_{3\pi} = 1.0\,\mathrm{GeV}/c^2$. The dependence is shown for the different flavors of chiral-waves with positive reflectivity $\epsilon = 1$.

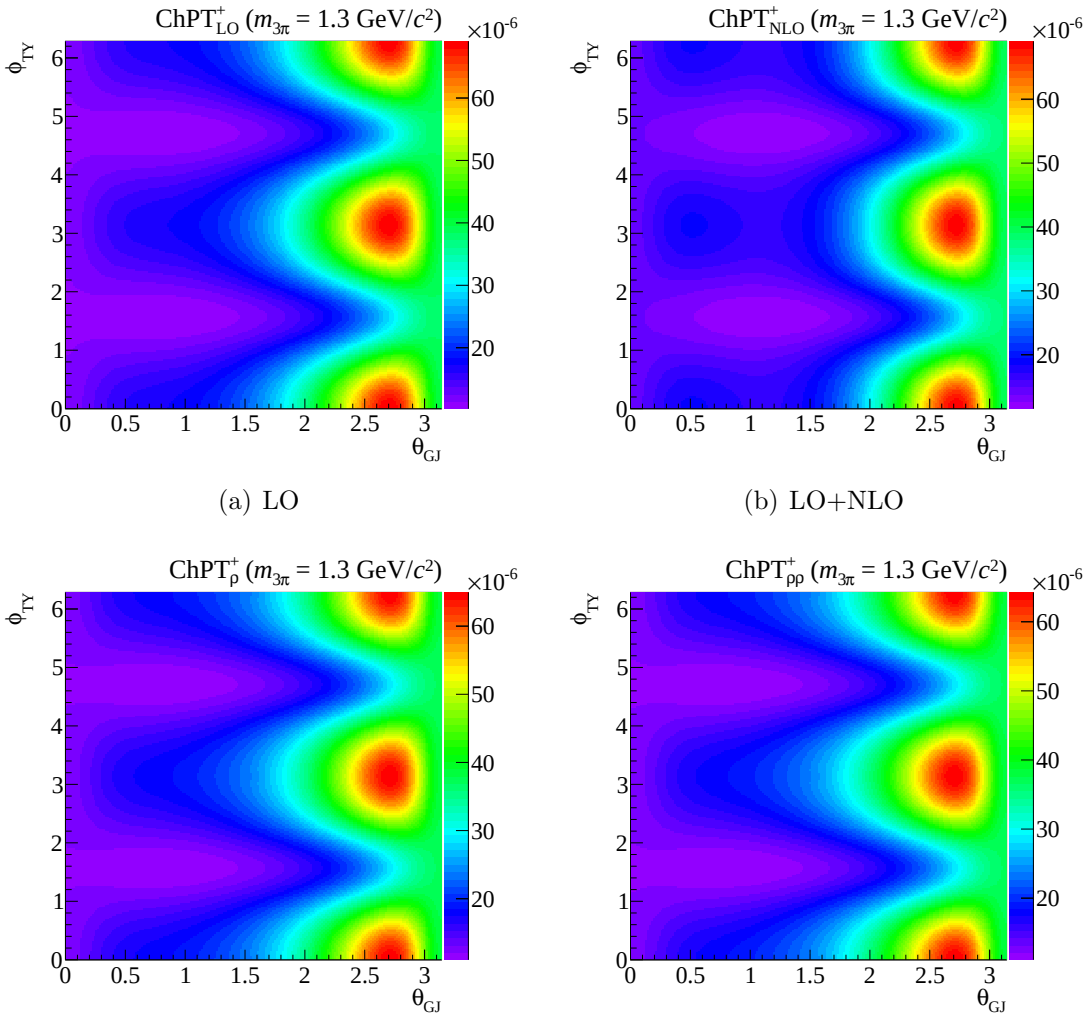

(a) LO (b) LO+NLO

(c) LO+NLO+single ρ (d) LO+NLO+single ρ+double ρ

Figure 11.6: Dependence of the normalized intensity of chiral waves on the decay angle θ_{GJ} and ϕ_{TY} at $m_{3\pi} = 1.3\,\mathrm{GeV}/c^2$. The dependence is shown for the different flavors of chiral-waves with positive reflectivity $\epsilon = 1$.

Chapter 12

Acceptance

Following the discussion in section 10.2 another important input to the mass-independent PWA fit, is the understanding and modeling of the acceptance[1] introduced by the imperfection of the apparatus. This is taken into account by means of Monte-Carlo integration. Each Monte-Carlo event is processed through the full COMPASS Monte-Carlo chain and it is determined weather the event is accepted or not. The events are generated by an external event generator, which simulates events distributed flat in phase-space by choosing kinematic variables randomly within the allowed kinematic range. The kinematics of the event are defined by the kinematics chosen from the event generator. The use of a beam file with recorded beam trajectories accounts for the properties of the beam, which are imposed by the beam optics. In order to overcome the statistical limitation imposed by the limited number of recorded beam trajectories, the parameters are randomly smeared within their uncertainties. The COMGEANT software, then propagates the final state particles of the generated event through the spectrometer, simulating interaction and decays of the produced particles. The detector response obtained by this simulation is processed with CORAL reconstructing events. The acceptance is determined by reconstructed events imposing the same selection criteria as established in chapter 8.

12.1 Properties of the Acceptance

In contrast to other COMPASS date sets, which are analyzed doing a partial-wave decomposition (see for example [Haa14, Gra12]), the acceptance of the present data-set, is not expected to be uniform due to the geometrical properties of the calorimeter trigger. The acceptance is defined as the fraction of accepted Monte-Carlo events, i.e. events, which are reconstructed and pass the event selection. This fraction can be studied by investigating the dependence on a wide variety

[1] Here the definition of acceptance does not only contain the angular acceptance of the apparatus, but also the event reconstruction efficiency, where the detection efficiency for particles and resolution effects enters.

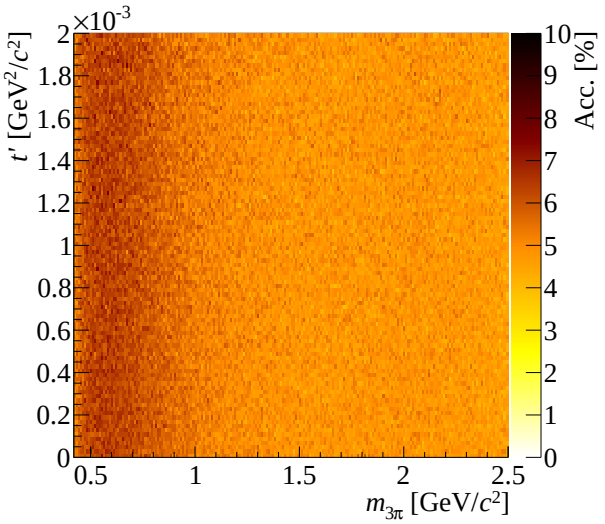

Figure 12.1: Dependence off the acceptance on the three-pion mass $m_{3\pi}$ and the transferred momentum t'.

of kinematic variables. The dependence of the acceptance on a small selection of kinematic variables, will be discussed here. Some of the more important kinematic variables are the invariant mass $m_{3\pi}$ and the transferred momentum t'. The dependence of the acceptance on these variables is shown in figure 12.1. A noticeable dependence of the acceptance on the three-pion $m_{3\pi}$ is revealed, while within the relevant kinematic range the acceptance does not vary with t'. The dependence of the acceptance on the invariant mass of the charged and neutral subsystem is shown in figure 12.2 and 12.3, respectively. The entire mass range of the three-pion final state is divided into four equally large mass bins with a width of $0.5\,\mathrm{GeV}/c^2$, each. On the upper bound of the allowed phase space, which depends upon the three-pion mass, high statistical fluctuations are observed due to the fact that only a few events are observed at this boarder. However, as this is true for Monte Carlo and recorded events, no significant effect is expected. Especially in the lowest three-pion mass bin from $0.5\,\mathrm{GeV}/c^2$ to $1.0\,\mathrm{GeV}/c^2$, a non uniform behavior of the acceptance in terms of the dependence on the invariant mass of the two pion systems is observed. In this mass region the acceptance value varies by approximately 20%. Looking at higher three-pion mass the dependence of the acceptance on the invariant mass of the two pion subsystems becomes more uniform. Still large distortions at the upper edges of the allowed kinematic range remain.

Besides the mass dependence of the acceptance, of course, the dependencies on many other kinematic variables are studied. Their study is not limited to the Gotfried-Jackson and Helicity frame, which are discussed below. The discussion of all studied dependencies, which are used to check the agreement of simulated and recorded events, would exceed the scope of this work. Thus, in the follow-

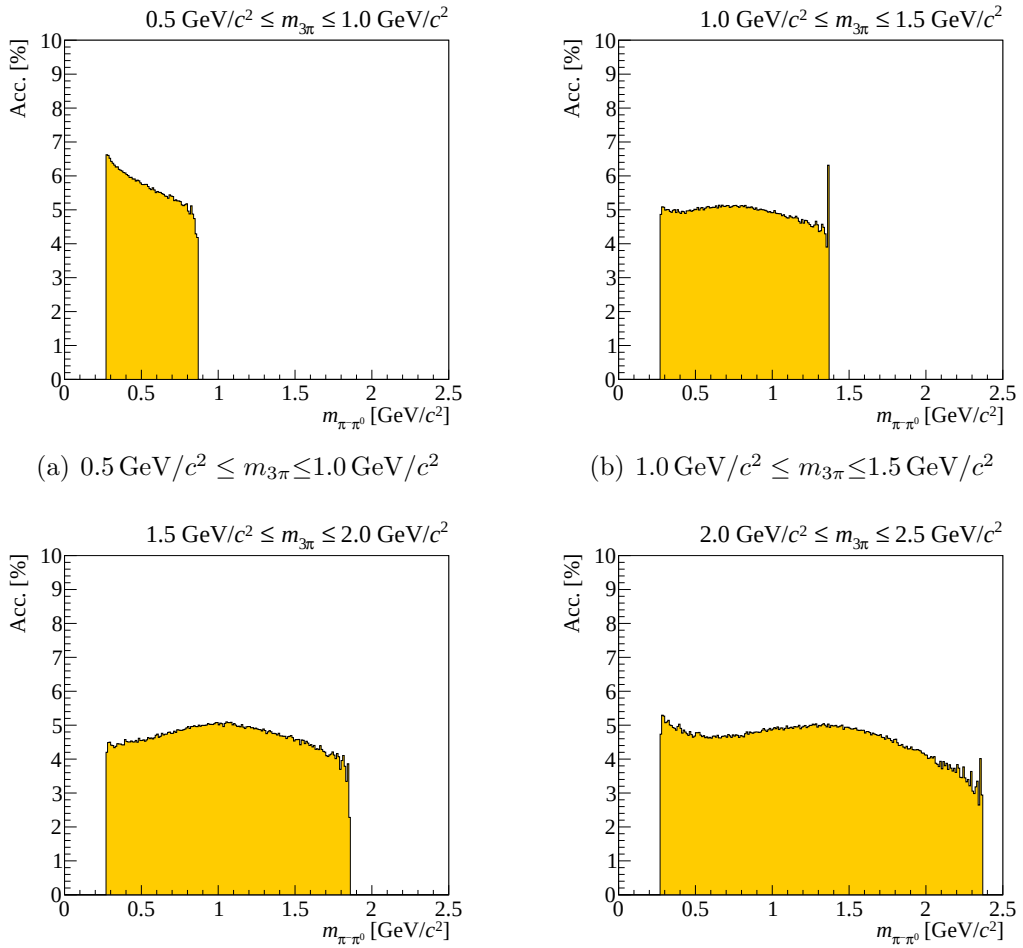

(a) $0.5\,\mathrm{GeV}/c^2 \leq m_{3\pi} \leq 1.0\,\mathrm{GeV}/c^2$

(b) $1.0\,\mathrm{GeV}/c^2 \leq m_{3\pi} \leq 1.5\,\mathrm{GeV}/c^2$

(c) $1.5\,\mathrm{GeV}/c^2 \leq m_{3\pi} \leq 2.0\,\mathrm{GeV}/c^2$

(d) $2.0\,\mathrm{GeV}/c^2 \leq m_{3\pi} \leq 2.5\,\mathrm{GeV}/c^2$

Figure 12.2: Dependence of the acceptance on the invariant mass $m_{\pi^-\pi^0}$ of the charge two pion subsystem. The dependence is shown in $0.5\,\mathrm{GeV}/c^2$ mass bins of the three-pion mass $m_{3\pi}$.

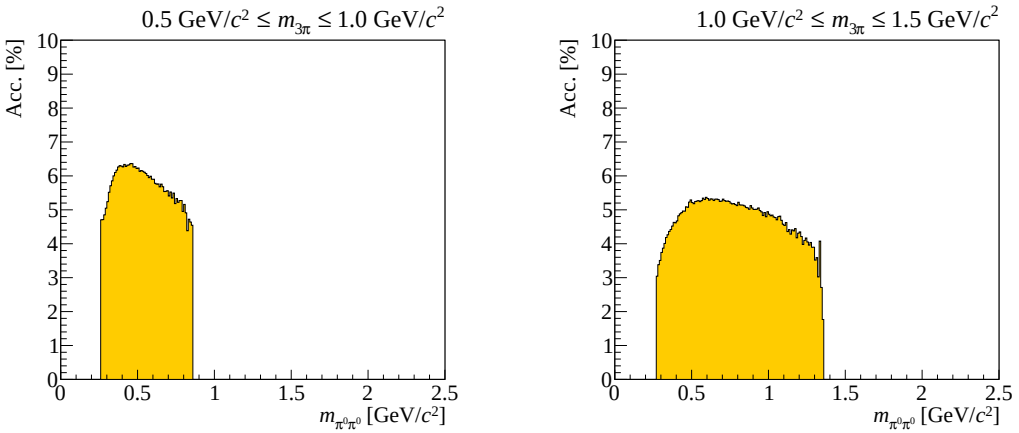

(a) $0.5\,\mathrm{GeV}/c^2 \leq m_{3\pi} \leq 1.0\,\mathrm{GeV}/c^2$

(b) $1.0\,\mathrm{GeV}/c^2 \leq m_{3\pi} \leq 1.5\,\mathrm{GeV}/c^2$

(c) $1.5\,\mathrm{GeV}/c^2 \leq m_{3\pi} \leq 2.0\,\mathrm{GeV}/c^2$

(d) $2.0\,\mathrm{GeV}/c^2 \leq m_{3\pi} \leq 2.5\,\mathrm{GeV}/c^2$

Figure 12.3: Dependence of the acceptance on the invariant mass $m_{\pi^0\pi^0}$ of the charge two pion subsystem. The dependence is shown in $0.5\,\mathrm{GeV}/c^2$ mass bins of the three-pion mass $m_{3\pi}$.

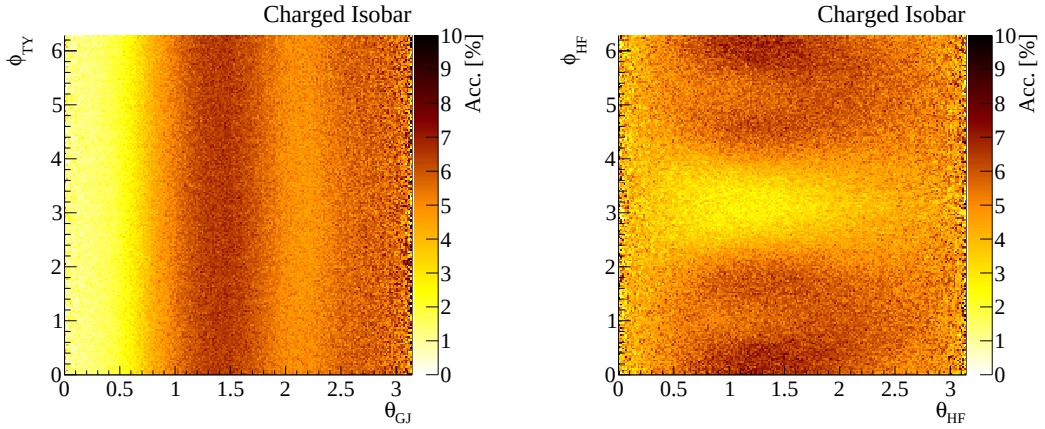

(a) Gottfried-Jackson frame (b) Helicity frame

Figure 12.4: Dependence of the acceptance on the decay angles in the Gottfried-Jackson and helicity frame of the charged two pion subsystem.

ing the discussion is limited to some dependencies, which are closely connected with the parametrization of decay amplitudes. These are the dependencies of the acceptance on the decay angles, which play an important role for the parametrization of isobaric amplitudes. Following the discussion in section 11.4, the charged two-pion system is now regarded as a quasi bound system, i.e. as isobar, and used to define the Gottfried-Jackson and helicity frame. The dependencies on the decay angles in the Gottfried-Jackson frame are shown in figure 12.4. The azimuthal angle in the Gottfried-Jackson frame chosen randomly in respect to laboratory coordinate system. Thus, geometric effects cancel and the acceptance does not depend on the Treiman-Yang angle ϕ_{TY} (see figure 12.4(a)). On the other hand a high energy deposit in the central region of ECAL2 is required. Thus a clear dependency on the polar angle θ_{GJ}, preferring backward scattering of the charged subsystem, is observed due to the boost from the rest to the laboratory frame. Qualitatively this behavior can be deduced, considering that the trigger is sensitive to the energy deposit in the center of ECAL2. The main contribution to the deposited energy comes from photons, which are produced in decays of π^0. Due to the geometry of the trigger and the boost to the laboratory frame, the energy contribution to the trigger energy is largest, when these photons are scattered forward. The scattering angle of the π^0, however, is connected with the scattering angle of the charged two pion subsystems. Thus the energy deposit in ECAL2 is loosely connected to θ_{GJ} of the charged two pion subsystem. The acceptance in the helicity frame of the charged isobar shows a more complicated structure (see figure 12.4(b)) and in general cannot be easily deduced from simple considerations. Doing the same for the neutral $\pi\pi$ system, i.e. looking at the neutral isobar (see figure12.5), the suppression of backward scattering of the $\pi\pi$ system due to the calorimetric trigger becomes apparent. However other

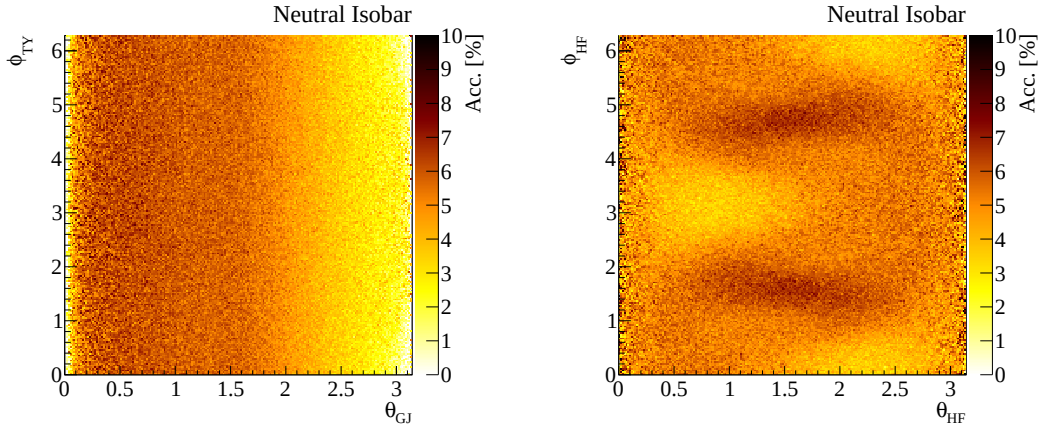

(a) Gottfried-Jackson Frame

(b) Helicity Frame

Figure 12.5: Dependence of the acceptance on the decay angles in the Gottfried-Jackson and Helicity Frame of the neutral two pion subsystem.

structure seen in the charged case do not show up in the Gottfried-Jackson frame, but propagate to the Helicity frame, which shows a more complicated structure. Taking into account, that the π^0 cannot be distinguished, a forward-backward symmetry with a shift of π in ϕ_{HF} is observed.

The described features of Primakoff production are not trivially recognized, when studying data. This has several reasons. At the one hand the dominating process is diffractive dissociation, which serves not only as large experimental background, but may also introduce interference effects changing the features of Primakoff production. On the other hand the described shape as discussed above do not account for experimental resolution and acceptance. Thus the observed shape are expected to be distorted. Last but not least one has to take into account, that in order to generate Dalitz distributions for data (see figure 8.15), one has to integrate over a certain $m_{3\pi}$-range. As this integrals contains the $m_{3\pi}$, which is to be studied, this integration is not easily reproduced for the hypothetical changes. However, the presented method of partial-wave decomposition accounts the discussed effects, except for the distortion by experimental resolution, and makes it possible to study the contribution and the features of Primakoff production in the investigated final state (see section 13).

12.2 Limitation of the Monte-Carlo

The Monte-Carlo tools, which are available to simulate the COMPASS spectrometer and to determine the acceptance, account for the material budget and the positioning and response of detectors and are well suited to simulate the angular acceptance of the spectrometer. However, with the currently available meth-

ods, not all aspects are taken into account. The simulation of background effects, which are introduced by pile-up events[2] or detector noise, for example lacks a good description. The presented analysis and event selection is sensitive to additional signals in ECAL2. In order to overcome this issue, the event selection, which supersedes the calorimetric trigger, does only account electromagnetic showers connected with the actual event. Thus the effect on the trigger can be neglected. However, the reconstruction algorithm is still sensitive to additional calorimetric clusters, which increase combinatorial background. The additional signals, which effective lowers the acceptance, are independent from the events and their kinematics. Therefore the angular properties of the acceptance are maintained, and the normalized acceptance integrals are unchanged.

As consequence the relative strength of different partial-wave does not change, while the total number of acceptance corrected number of events change. Thus, in principle an absolute measurement, like the measurement of cross section, is affected. However, using the $K \to \pi^-\pi^0\pi^0$ to determine the integrated luminosity, where the acceptance of the Kaon decay enters, the systematic introduced by the limited knowledge of the absolute scale of the acceptance cancel, assuming that the kinematics of the Kaon decay and the pion-target interactions are similar.

[2]Events origin from other beam particles or interaction, which due to their temporal appearance can interfere with the investigated event.

Chapter 13

Partial Wave Analysis

Applying the amplitude analysis technique described in chapter 10 to the data sample obtained by the event selection introduced in chapter 8, several resonating and non-resonating states and their contribution to the observed spectra are investigated. The regime of low momentum transfer with $t' \leq 0.002\,\mathrm{GeV}^2/c^2$ is studied with a mass-independent PWA. For this purpose the event sample is divided into $40\,\mathrm{MeV}/c^2$ mass bins (see section 13.2.1). At small $t' \leq 0.002\,\mathrm{GeV}^2/c^2$, $M = 1$ amplitudes are predominantly produced via Primakoff production with only a small contribution of strong production. Studies, which investigate the data in bins of t', are used to understand the t' dependence of the different amplitudes (see section 13.2.2) and therefore reveal insights to the contribution of diffractive production to $M = 1$ waves. This study, however, cannot use narrow mass bins due to statistical limitation. Thus the use of wider mass ranges is required. But first the wave-sets of the models are discussed.

13.1 The Model

Finding a PWA model, which is appropriated for a given data set well, is a delicate procedure. On the one hand all relevant contribution, which are present, have to be represented in the model. On the other hand the number of waves, which can be used, is limited by the amount of available events. Luckily it is possible to deduce some ideas about the contributing amplitudes by considering the quantum number and decay channel of known resonance. One important constraint, which applies to the present analysis, is the conservation of I^G in strong interactions, i.e. diffractive dissociation. Thus, the resonance X produced by diffractive dissociation must have the same $I^G = 1^-$ as the beam pion. This of course does not apply for Primakoff productions, which is a radiative process. As discussed before, these quantum numbers are omitted in the notation used here. Evaluating the three-pion mass spectrum signs of the $a_1(1260)$, $a_2(1320)$ and $\pi_2(1670)$ are observed. Thus the model has to contain waves with the corresponding quantum numbers, i.e. $J^{PC} = 1^{++}$, $J^{PC} = 2^{++}$ and $J^{PC} = 2^{-+}$.

Considering the coupling to radiative or strong production of this resonance either partial waves with $M = 1$ or $M = 0$ or both have to be considered. For strong production, i.e. diffractive dissociation, waves with $M \neq 0$ can in first approximation be neglected for the presented analysis due to the suppression at low t'. The reflectivity ϵ of $M = 0$ waves is positive. In the $M = 1$ sector at small values of t' and $m_{3\pi}$ only contributions from positive reflectivity amplitudes are expected. However, the production plane may not be measured correctly due to limited experimental resolution. This leads to a leakage from $M^\epsilon = 1^+$ into $M^\epsilon = 1^-$ waves, which otherwise have the same quantum numbers and decay modes. Thus, the $M^\epsilon = 1^-$ sector "mimics" the $M^\epsilon = 1^+$ waves by using the corresponding waves with negative reflectivity and applying the same thresholds. The question, which isobars to consider, can be attacked in different ways. The mass spectra of the $\pi\pi$ subsystems provides valuable information by revealing resonance structures. Additionally know decay modes taken from literature (see for example [B$^+$12]) are considered. This allows to develop a base model, which covers the most prominent contribution. The base model however has to be modified and extended to provide a good description of the event sample. Finding such a model by adapting the wave set and the thresholds, which are applied to the individual partial-waves and effectively reduce the wave set in certain mass ranges, is a complicated iterative procedure.

In the presented analysis several models are developed. In the following four models, with chiral-waves extended to high values of $m_{3\pi}$ are compared with a conservative model, which only contains isobaric waves. The presented isobaric model is the best model found to describe the data and only contain isobar amplitudes. The four models, which includes chiral waves, do only differ in *flavor* $\Lambda \in \{\mathrm{LO}, \mathrm{NLO}, \rho, \rho\rho\}$ of the isobaric waves. Here *flavor* is not to be confused with the flavor of the strong interaction. The models will therefore be named after the flavor of the chiral waves. Table 13.1 and 13.2 describe the complete wave set for both the chiral models and isobaric model.

13.2 Results

The mass-independent PWA in mass bins, which is presented below, restricts to low values of transferred momentum $t' \leq 0.002\,\mathrm{GeV}^2/c^2$ and events with the beam particle tagged as pion. The PWA allows to study the presence of resonances, which are not only identified by peaks or bumps in the intensity spectrum of amplitudes, but also by their phase. A first separation of different production mechanism is achieved by selecting the spin projections. In order to study the contribution of diffractive production to $M = 1$ waves, a PWA fit in bins of t' is done.

Wave	$m_{\min}$ in GeV/c^2
$0^{-+}0^{+}$ $(\pi\pi)_S$ S π	
$0^{-+}0^{+}$ $f_0(980)$ S π	1.10
$0^{-+}0^{+}$ ρ P π	
$0^{-+}0^{+}$ f_2 D π	1.22
$0^{-+}0^{+}$ $f_0(1500)$ S π	1.62
$1^{++}0^{+}$ ρ S π	
$1^{++}0^{+}$ ρ D π	0.78
$1^{++}0^{+}$ $(\pi\pi)_S$ P π	
$1^{++}0^{+}$ $f_0(980)$ P π	1.22
$1^{++}0^{+}$ f_2 P π	1.38
$2^{-+}0^{+}$ f_2 S π	1.22
$2^{-+}0^{+}$ ρ P π	0.78
$2^{-+}0^{+}$ $(\pi\pi)_S$ D π	0.78
$2^{-+}0^{+}$ f_2 D π	1.50
$2^{-+}0^{+}$ ρ F π	1.22
$3^{++}0^{+}$ ρ D π	1.50
$3^{++}0^{+}$ f_2 P π	1.50
$3^{++}0^{+}$ $(\pi\pi)_S$ F π	1.50

Table 13.1: Partial-waves with $M = 0$ and the applied thresholds. Threshold, which are not set explicitly, are omitted. In this sense, as no upper thresholds are set for $M = 0$ waves, only the lower threshold is given. Please note, that the model in the $M = 0$ sector is identical for all presented chiral and isobaric models.

13.2.1 Mass-Independent PWA in Mass-Bins

Considering the regime of small momentum transfer $t' \leq 0.002\,\mathrm{GeV}^2/c^2$, amplitudes with $M = 1$ are considered to mainly origin from Primakoff production. $M = 0$ waves are produced by strong interaction. Thereby the diffractive dissociation is expected to dominate the observed spectrum. This expectation is confirmed by the applied mass-independent PWA. The $M = 0$ spin total, which is the coherent sum of all waves with $M = 0$ (see figure 13.1(a)), has significant similarities with the mass spectrum shown in figure 8.12(b). However due to the acceptance correction the total scale differs and the enhancement at $\sim 1.7\,\mathrm{GeV}/c^2$, which corresponds to the $\pi_2(1670)$, is more pronounced. Studying the available fit models only little differences are observed in the $M = 0$ spin total. The different flavors of chiral models are almost identical concerning intensity and uncertainty. The isobaric models, still maintaining the coarse features observed in chiral models, show significant deviations in a wide mass range. The uncertainties are in general larger for the isobar model, when compared to the chiral model. This behavior becomes even more striking, when looking at the $M = 1$ spin total (figure 13.1(b)), where the radiatively produced $a_2(1320)$ shows up as a narrow peak. The $a_2(1320)$ sits on a broad structure. The obvious increase of error bars at $0.78\,\mathrm{GeV}/c^2$ is explained by the properties of the model as shortly discussed in the following. Below this threshold the model is restricted to a few $M = 0$ waves and the chiral-waves or in case of the isobaric model a few isobaric waves with $M = 1$. Above this threshold a bunch of amplitudes opens up, where most of the amplitudes feature $M = 1$. Thus, the number of degrees of freedom gets significantly larger, which is reflected by increased error bars. Similar to the $M = 1$ spin total the difference between the different flavors of the chiral model is small.

The spin totals give a first overview of the present amplitudes and their contribution, however, the strength of a fully featured PWA is the ability to investigate the intensity and phase of individual amplitudes. As deduced from the mass spectrum and the spin totals, the dominant contribution comes from the diffractively produced $a_1(1260)$ resonance[1]. The a_1 has $J^{PC} = 1^{++}$ and in the given kinematic region its predominant decay channel is know to be the $(\rho\pi)_S$ channel. The intensity of the corresponding partial-wave, the $(1^{++})0^+\,\rho\,S\,\pi$, is shown in figure 13.2(a). At this point it should be mentioned, that due to its large intensity the a_1 is expected to be observed in other decay channels as well. Thus, it is no surprise, that studying the intensity of the $1^{++}0^+\,(\pi\pi)_S\,P\,\pi$ wave a similar spectrum, but with lower intensity, is observed (see figure 13.2(b)). Looking at the relative phase between both waves a phase lock in the mass range of the a_1 is observed (figure 13.2(c)), i.e. a mass range where the relative phase between the waves is approximately constant. This is a strong indication, that both waves are connected by the same intermediate state a_1. The offset, how-

[1] In the following also the abbreviation a_1 will be used for the $a_1(1260)$.

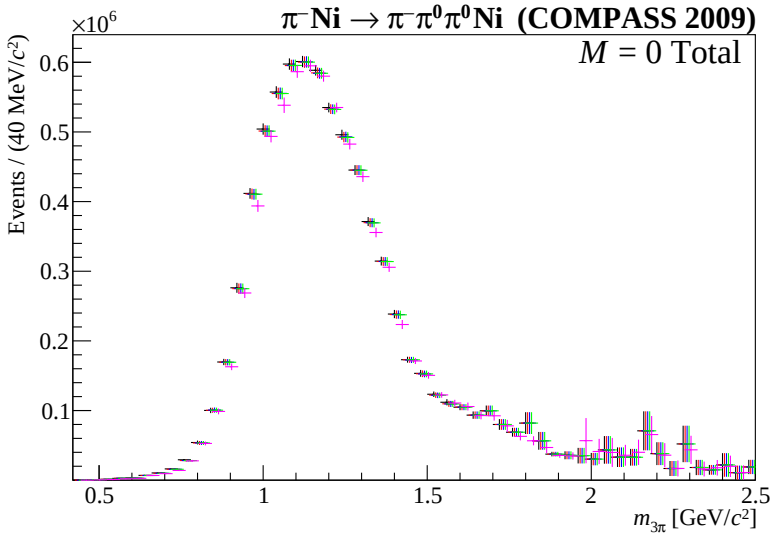

(a) $M = 0$ spin total

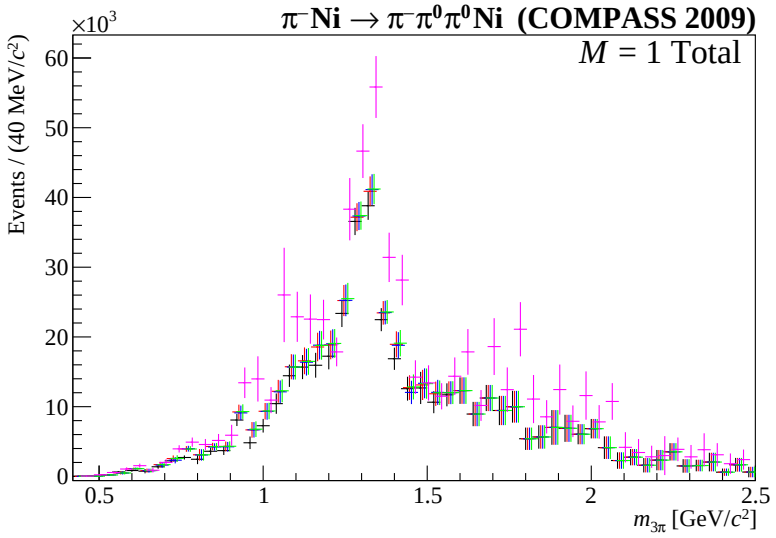

(b) $M = 1$ spin total

Figure 13.1: Total waves intensities of partial-waves with spin projection (a) $M = 0$ and (b) $M = 1$. The result for the chiral model up to LO (black), NLO (red), single ρ (blue) and double ρ exchange (green) are shown. For comparison a fit using the isobaric model is shown in magenta. The colored spectra are shifted to the right, the original position is given by the black curve.

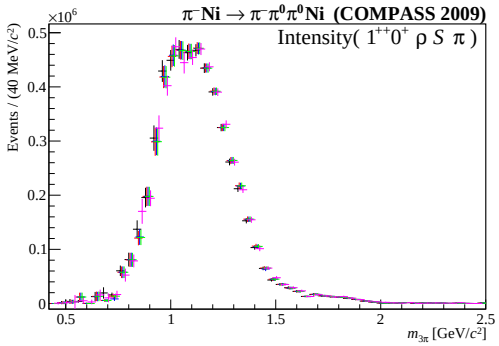

(a) $1^{++}0^{+}\,\rho\,S\,\pi$ Intensity

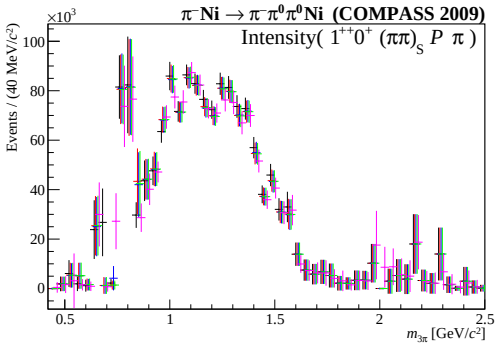

(b) $1^{++}0^{+}\,(\pi\pi)_S\,P\,\pi$ Intensity

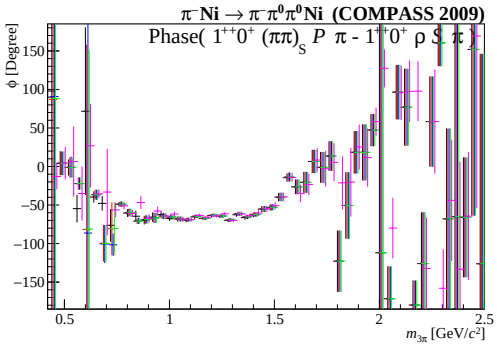

(c) Phase($1^{++}0^{+}\,(\pi\pi)_S\,P\,\pi\;-\;1^{++}0^{+}\,\rho\,S\,\pi$)

Figure 13.2: Intensity of the $(1^{++})0^{+}\,\rho\,S\,\pi$ (a) and $1^{++}0^{+}\,(\pi\pi)_S\,P\,\pi$ (b) partial waves and the phase between this two waves (c). For the color coding please refer to figure 13.1.

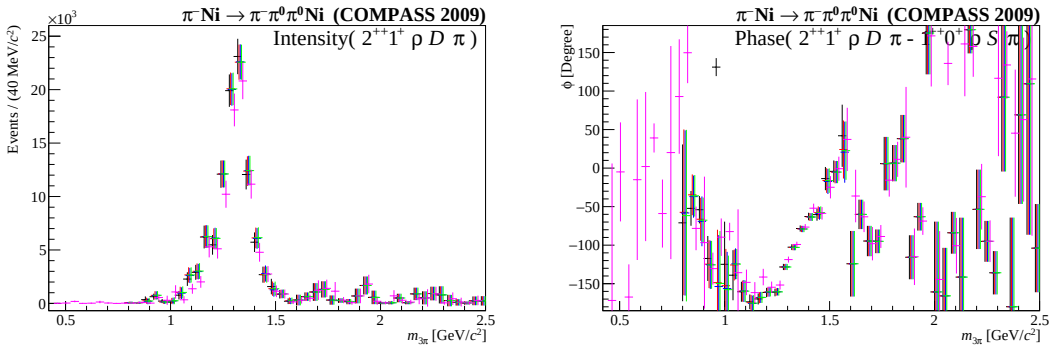

(a) $2^{++}1^{+}\,\rho\,D\,\pi$ Intensity (b) Phase($2^{++}1^{+}\,\rho\,D\,\pi - 1^{++}0^{+}\,\rho\,S\,\pi$)

Figure 13.3: Intensity of the $(2^{++})1^{+}\,\rho\,D\,\pi$ (a) partial waves and its relative phase to the $1^{++}0^{+}\,\rho\,S\,\pi$ (b). For the color coding please refer to figure 13.1.

ever, can be understood, considering interference or non-interference of different production mechanisms or final state interactions. While the $(1^{++})0^{+}\,\rho\,S\,\pi$ is believed to be dominated by diffractive dissociation, for the $1^{++}0^{+}\,(\pi\pi)_S\,P\,\pi$ the Deck-effect might play an important role. Thereby the Deck-effect being no resonance has no phase-motion itself, but can modify the phase and phase-motion of $1^{++}0^{+}\,(\pi\pi)_S\,P\,\pi$ by introducing a shift of the complex amplitude. Up to here it is shown, that the spectrum of the $(1^{++})0^{+}\,\rho\,S\,\pi$ and $1^{++}0^{+}\,(\pi\pi)_S\,P\,\pi$ have the same origin. However, as the origin of these amplitudes is a resonance it should show the phase motion, which is typical for a resonance. In order to observe this phase motion, it is requires to study the relative phase of waves with different intermediate states. A good option to study the phase motion of the a_1 is another narrow resonance, which lies in the same mass range, i.e. the $a_2(1320)$ resonance[2]. As already mentioned this resonance with $J^{PC} = 2^{++}$ is produced in Primakoff reaction and therefore exhibits $M = 1$. Considering the quantum numbers and the decay channel of the a_2 it is expected to occur in the $(2^{++})1^{+}\,\rho\,D\,\pi$ amplitude, where indeed a narrow peak at the right mass is observed (see figure 13.3(a)). Now studying the relative phase between $(2^{++})1^{+}\,\rho\,D\,\pi$ and $(1^{++})0^{+}\,\rho\,S\,\pi$ (figure 13.3(b)) the expected phase motion between both resonances is observed. Due to the sign first a falling phase from the a_1 is observed, which is followed by a sharp rise at around $1.2\,\mathrm{GeV}/c^2$, which indicates the appearance of the a_2.

Figure 13.4(a) shows the intensity of the $(2^{-+})0^{+}\,f_2\,S\,\pi$, one of the waves, where the $\pi_2(1670)$ resonance shows up as a enhancement in the intensity. Additionally the phase behavior of this amplitude shows the presence of a resonance at the mass of the π_2. This can for example be studied using the $1^{++}0^{+}\,\rho\,S\,\pi$ as reference (see figure 13.4(b)). The $\pi_2(1670)$, however, is not only observed in strong production, but can also be produced by radiative coupling. Thus it is no surprise,

[2]Similar to the a_1, the abbreviation a_2 is used for the $a_2(1320)$.

Wave	$m_{\min}$ in GeV/c^2	$m_{\max}$ in GeV/c^2
$1^{++}1^{\pm}\ \rho\ S\ \pi$	0.78 (*)	*
$1^{++}1^{\pm}\ (\pi\pi)_S\ P\ \pi$	– (*)	– (*)
$1^{-+}1^{\pm}\ \rho\ P\ \pi$	1.42 (*)	*
$2^{++}1^{\pm}\ \rho\ D\ \pi$	0.78 (*)	*
$2^{-+}1^{\pm}\ f_2\ S\ \pi$	1.42 ($^{1.34}$)	*
$2^{-+}1^{\pm}\ \rho\ P\ \pi$	1.42 (*)	*
$2^{-+}1^{\pm}\ (\pi\pi)_S\ D\ \pi$	– (1.22)	– (*)
$2^{-+}1^{\pm}\ \rho\ F\ \pi$	1.52	*
$(\text{ChPT})^{\pm}_{\Lambda}$	* (–)	1.62 (–)

Table 13.2: Wave with spin projection $M = 1$ and their thresholds. As waves with positive and negative reflectivity are always used pairwise with identical threshold, the notation of both waves is done only once. All chiral models use identical thresholds. Diverting threshold in the isobaric model are given in brackets. The symbol * denotes the absence of a threshold, i.e. the wave is not threshold, while the symbol – denotes, that the wave is omitted in a model.

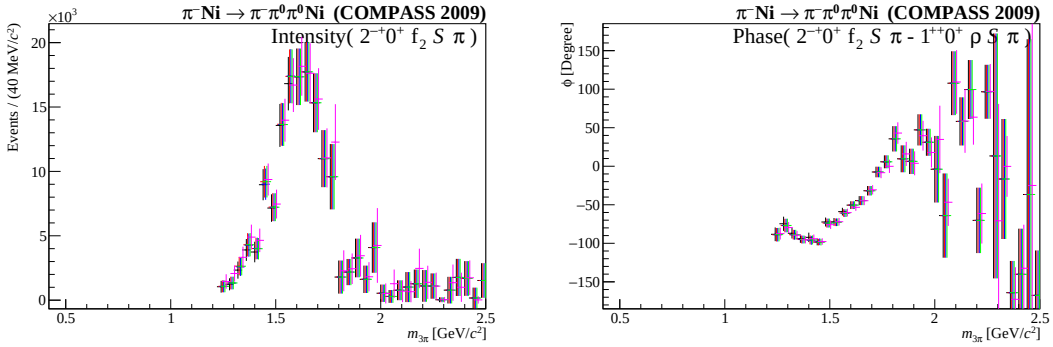

(a) $2^{-+}0^{+}\ f_2\, S\, \pi$ Intensity (b) Phase($2^{-+}0^{+}\ f_2\, S\, \pi\ -\ 1^{++}0^{+}\ \rho\, S\, \pi$)

Figure 13.4: Intensity of the $(2^{-+})0^{+}\ f_2\, S\, \pi$ (a) partial waves and its relative phase to the $1^{++}0^{+}\ \rho\, S\, \pi$ (b). For the color coding please refer to figure 13.1.

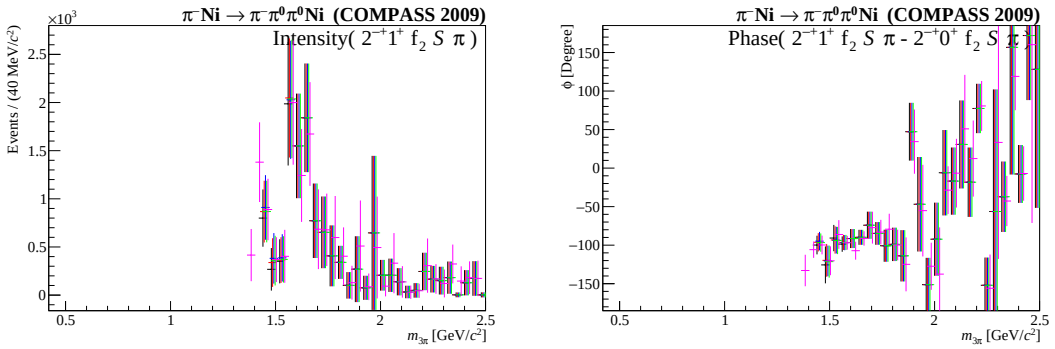

(a) $2^{-+}1^{+}\, f_2\, S\, \pi$ Intensity (b) Phase($2^{-+}0^{+}\, f_2\, S\, \pi$ − $2^{-+}1^{+}\, f_2\, S\, \pi$)

Figure 13.5: Intensity of the $2^{-+}1^{+}\, f_2\, S\, \pi$ (a) partial waves and its relative phase to the $2^{-+}1^{+}\, f_2\, S\, \pi$ (b). For the color coding please refer to figure 13.1.

that one observes a small peak at the mass of the $\pi_2(1670)$, when studying the intensity of the $(2^{-+})1^{+}\, f_2\, S\, \pi$ wave (figure 13.5(a)). At the same mass a phase lock at approximately $-100°$ between $(2^{-+})1^{+}\, f_2\, S\, \pi$ and the $(2^{-+})0^{+}\, f_2\, S\, \pi$ is observed (see figure 13.5(b)). At this place it should be mention, that neglecting further effects [FT09], the production phase difference between Primakoff production and diffractive dissociation is expected to be 90 Degree due to the properties of the photon and pomeron. Allowing for additional disturbances the observed relative phase difference of 100° is in good agreement with the picture of the $\pi_2(1670)$ produced either by diffractive dissociation or Primakoff reaction.

Besides the $a_1(1260)$, there is another known resonance with $J^{PC} = 1^{++}$ – the $a_1(1670)$. This resonance predominately decays via $\rho\pi$. As already shown the $1^{++}0^{+}\, \rho\, S\, \pi$ is dominated by the $a_1(1260)$, thus it is impossible to judge on a possible contribution of the $a_1(1670)$. However this picture changes when going to $(\rho\pi)_D$ decays. The intensity spectrum of the $1^{++}0^{+}\, \rho\, D\, \pi$ (see figure 13.6(a)) looks different from the one of the $1^{++}0^{+}\, \rho\, S\, \pi$ wave. The maximum of the broad spectrum lies approximately at the mass of the $a_1(1670)$, between 1.6 and 1.7 GeV/c^2. The long shoulder towards low mass however indicates, that there is also contribution from the $a_1(1260)$. This is confirmed by studying the phase between $1^{++}0^{+}\, \rho\, D\, \pi$ and $1^{++}0^{+}\, \rho\, S\, \pi$ wave (see figure 13.6(b)), where a plateau between roughly 1 and 1.3 GeV/c^2 is observed. The plateau is followed by a rise of the relative phase, which indicates the $a_1(1670)$ appearing in the $1^{++}0^{+}\, \rho\, D\, \pi$.

So far all waves, which were discussed, reveal negligible difference of the behavior of the fits with different models. However, studying the $1^{++}1^{+}\, \rho\, S\, \pi$ amplitude, where the radiatively produced $a_1(1260)$ can be observed, the situation changes. The PWA fit with the isobaric model show, as the intensity of the $1^{++}1^{+}\, \rho\, S\, \pi$ amplitude vanishes in the mass region of the $a_1(1260)$, no hints of a radiatively produced $a_1(1260)$ (figure 13.7(a)). On the other hand all chiral

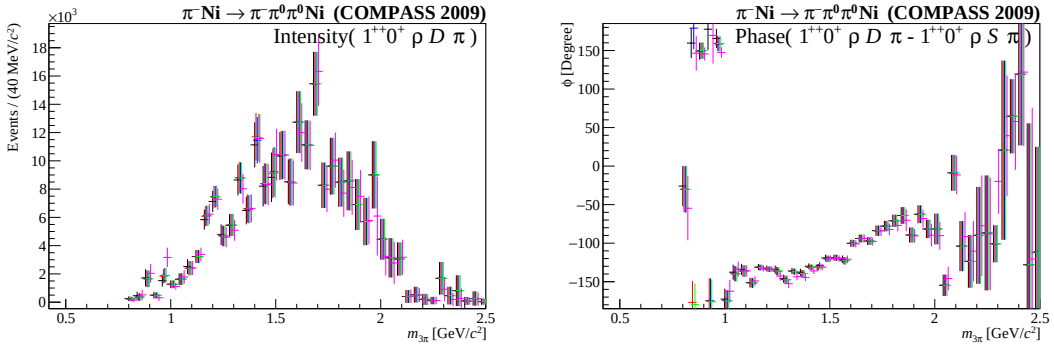

(a) $1^{++}0^{+}\,\rho\,D\,\pi$ Intensity (b) Phase($1^{++}0^{+}\,\rho\,D\,\pi - 1^{++}0^{+}\,f_2\,S\,\pi$)

Figure 13.6: Intensity of the $1^{++}0^{+}\,\rho\,D\,\pi$ (a) partial waves and its relative phase to the $1^{++}0^{+}\,\rho\,S\,\pi$ (b). For the color coding please refer to figure 13.1.

model show a clear enhancement of intensity between 1 and 1.3 GeV/c^2. The behavior of all chiral models, except the LO model, is almost identical. This grouping of chiral models is later on observed several times. Thus for practical reasons the chiral waves and models, which are based on ChPT calculation beyond leading-order calculations, are referred as advanced chiral waves and models, respectively. The LO model, however, reveal a significant higher intensity, which have a similar shape, in the same mass region. Studying the phase between the dominating $1^{++}0^{+}\,\rho\,S\,\pi$ and the $1^{++}1^{+}\,\rho\,S\,\pi$ (figure 13.7(b)), in the mass range of the $a_1(1260)$ all chiral models show a phase lock between the two waves. This phase lock is at $\approx -90°$, which supports the picture of radiative and diffractive production of the a_1.

So far it had been demonstrated, that the applied partial-wave analysis is able to resolve amplitudes, which contribute with a few per-mill to the observed spectra. However, up to now the chiral amplitudes, which are introduced to describe non-resonant radiative process, had not been discussed. Studying their contributions is a central part of this work. Figure 13.8(a) shows the intensity of the chiral waves with positive reflectivity. Again there are no large differences between the advanced chiral models. At low three-pion masses for these models the observed shape follows roughly the shape expected from ChPT prediction, where the intensity increases towards high masses due to the increasing cross section. On the other hand the Weizsäcker-Williams approximation predicts a damping at high masses, which roughly explains the vanishing of the wave at high masses. However, considering the fundamental assumptions, ChPT is applicable up to a few pion masses. The fact, that the experimental data are obviously described well by ChPT waves, even at high center-of-mass energies, is an experimental finding, which requires further interpretation. This, however, goes beyond the scope of this work. The intensity of the LO chiral amplitude is up to 0.78 GeV/c^2

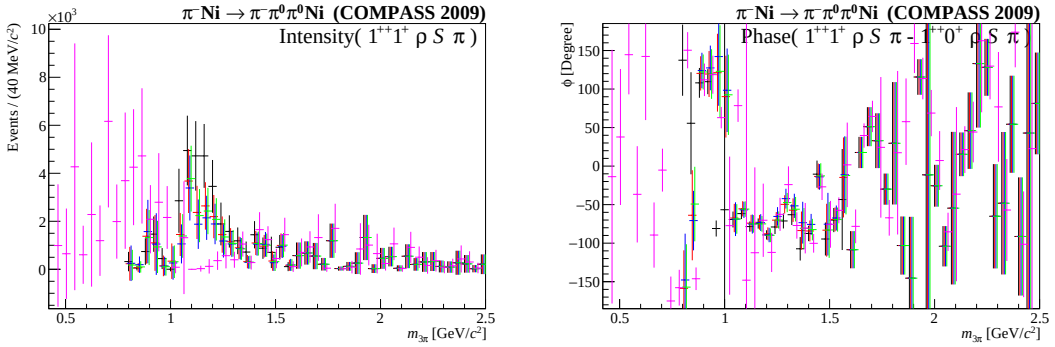

(a) $1^{++}1^{+}\,\rho\,S\,\pi$ Intensity (b) Phase($1^{++}1^{+}\,\rho\,S\,\pi - 1^{++}0^{+}\,f_2\,S\,\pi$)

Figure 13.7: Intensity of the $1^{++}1^{+}\,\rho\,S\,\pi$ (a) partial waves and its relative phase to the $1^{++}0^{+}\,\rho\,S\,\pi$ (b). For the color coding please refer to figure 13.1.

identical with the intensity found by the advanced chiral models. However, going to higher center-of-mass energy, the LO amplitude shows up to $\approx 1.2\,\mathrm{GeV}/c^2$ significantly less intensity than the other chiral waves. The observed intensity shows a plateau in the region form $0.78\,\mathrm{GeV}/c^2$ to $1.2\,\mathrm{GeV}/c^2$. This is the same mass range, where the intensity of the $1^{++}1^{+}\,\rho\,S\,\pi$ for the LO model is higher than for the advanced chiral models. Having a non-continuous behavior at the transition from the raising intensity below $0.78\,\mathrm{GeV}/c^2$ to the plateau above, seems to be unphysical as a continuous shape is expected. The identical behavior of all chiral waves up to $0.78\,\mathrm{GeV}/c^2$ can be understood by considering, that up to this threshold the chiral waves are the only $M = 1$ waves included in the models. In order to study the phase of the chiral waves, again the $1^{++}0^{+}\,\rho\,S\,\pi$ anchor wave is used (figure 13.8(b)). All chiral waves show falling phases with similar behavior. This matches the expectation for the phase between an amplitude describing non-resonant processes and one which contains a resonance. The curves, however, show different absolute values. Again the LO wave sticks out, revealing a phase, which differs by approximately 90° form the one of the advanced chiral models. The LO chiral amplitude is real, while the advanced amplitudes take on complex values due to loop and ρ contributions. Looking at the advanced chiral waves the NLO amplitude has a smaller phase than the other chiral amplitudes, which show almost identical phases. This can be understood as an effect of resonating pion-pion scattering as introduced by considering the ρ.

So far only amplitudes with positive reflectivity are discussed, which are physically expected. However, as discussed before, at small transferred momentum and masses the production plane is not always correctly resolved due to experimental resolution (see also section 11.3). As a consequence leakage into negative reflectivity waves with the same quantum number and the same decay channel is expected. For example studying the $2^{++}1^{-}\,\rho\,D\,\pi$ intensity (figure 13.9(a)) a

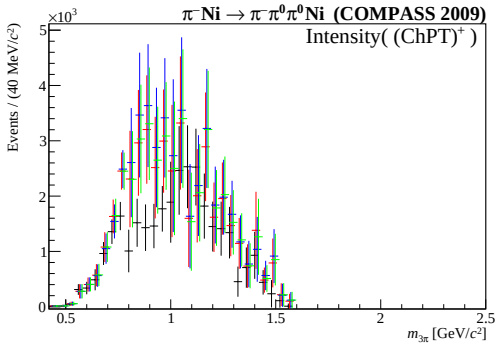

(a) $(\mathrm{ChPT})^{+}_{\Lambda}$ Intensity

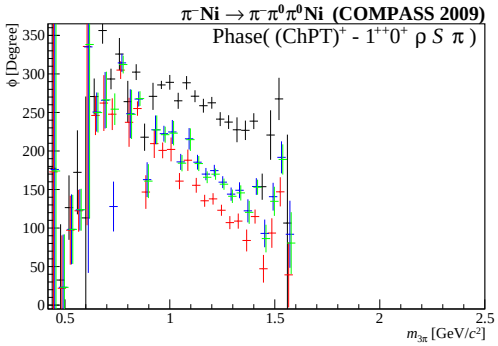

(b) Phase(ChPT)$^{+}$ − $1^{++}0^{+}\,\rho\,S\,\pi$)

Figure 13.8: Intensity of the different flavors of the chiral wave (a) partial waves and its relative phase to the $1^{++}0^{+}\,\rho\,S\,\pi$ (b). For the color coding please refer to figure 13.1.

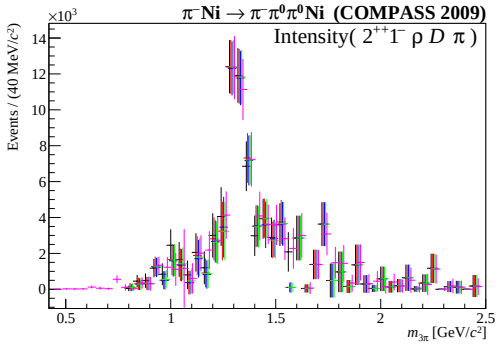

(a) $2^{++}1^{-}\,\rho\,D\,\pi$ Intensity

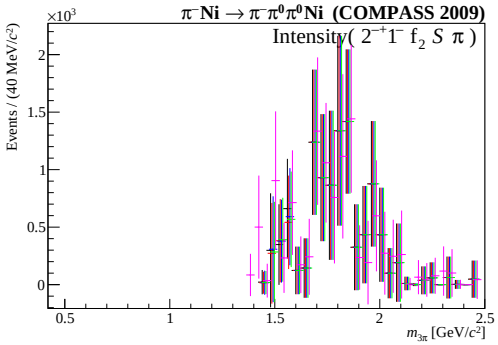

(b) $2^{-+}1^{-}\,f_2\,S\,\pi$ Intensity

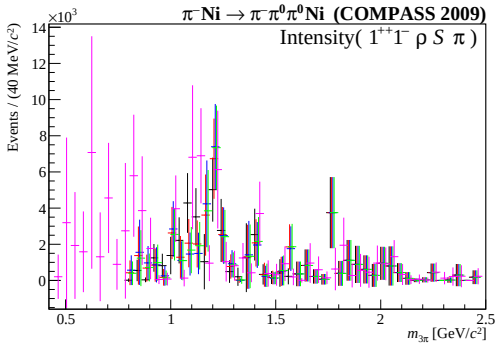

(c) $1^{++}1^{-}\,\rho\,S\,\pi$ Intensity

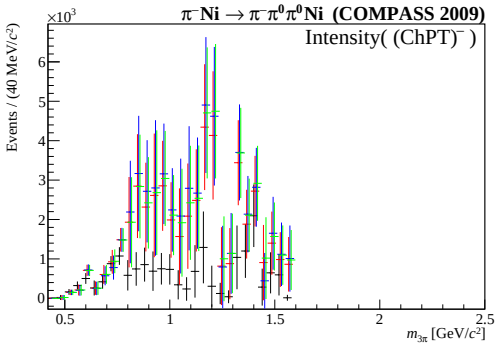

(d) $(\mathrm{ChPT})^{-}_{\Lambda}$ Intensity

Figure 13.9: Intensity of selected amplitudes with negative reflectivity $\epsilon = -$. For the color coding please refer to figure 13.1.

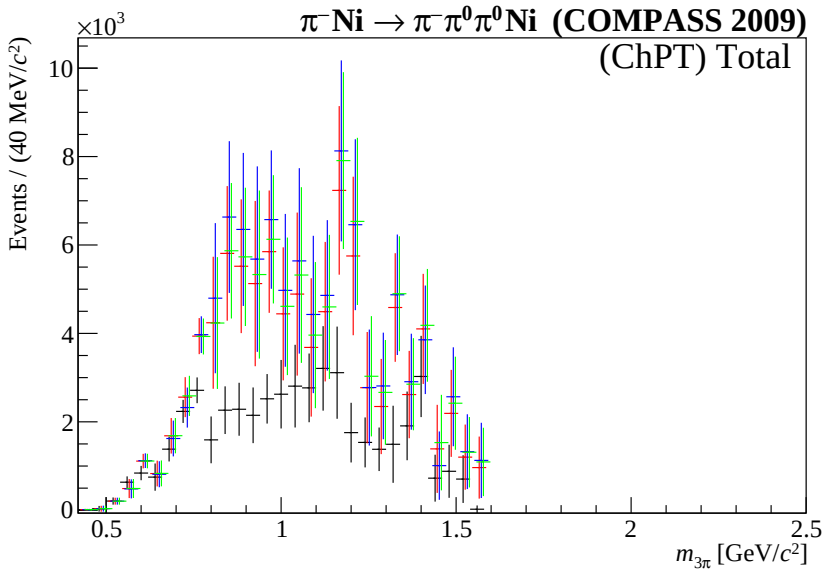

Figure 13.10: Total wave intensity of the chiral waves $(\text{ChPT})^{+}_{\Lambda}$ and $(\text{ChPT})^{-}_{\Lambda}$. For the color coding please refer to figure 13.1.

spectrum, which is similar to the one observed for the intensity of the $2^{++}1^{+}\,\rho\,D\,\pi$ amplitude, is observed. A prominent $a_2(1320)$ peak shows up. The intensity of the negative reflectivity wave however is smaller than for its counter part with positive reflectivity. The observed a_2 peak shows only 60% of the intensity, which is observed in the intensity of the positive reflectivity amplitude. Similar observations are true for the Primakoff produced $\pi_2(1670)$ (figure 13.9(b)). Considering the small intensity of the signal observed in the positive-reflectivity wave, the intensity in the negative-reflectivity wave gets very small. This is also true for the $1^{++}1^{-}\,\rho\,S\,\pi$ wave (see figure 13.9(c)). Thus, without knowing the positive reflectivity wave the enhancement of the intensity lacks significance. The small narrow peak at the position of the $a_2(1320)$ is probably an artifact of model leakage. Coming back to the chiral amplitudes the chiral wave with negative reflectivity (figure 13.9(d)) also resembles the behavior of its counter part with positive reflectivity. The drop of the LO amplitude at $780\,\text{MeV}/c^2$ is however much more pronounced. This, of course, also translates to the total wave intensity of chiral waves (see figure 13.10). Looking at the spin totals for $M^{\epsilon} = 1^{+}$ and $M^{\epsilon} = 1^{-}$ (figure 13.11) the intensity in the fit using the $(\text{ChPT})^{\pm}_{\text{LO}}$ waves for both reflectivity values recovers to the level of the other chiral models. This indicates, that the different behavior of LO and advanced models is due to model leakage between $M = 1$ waves with the same reflectivity. The isobaric fit mimics the behavior, which was already discussed when looking at the $M = 1$ spin total. But increased uncertainties are observed.

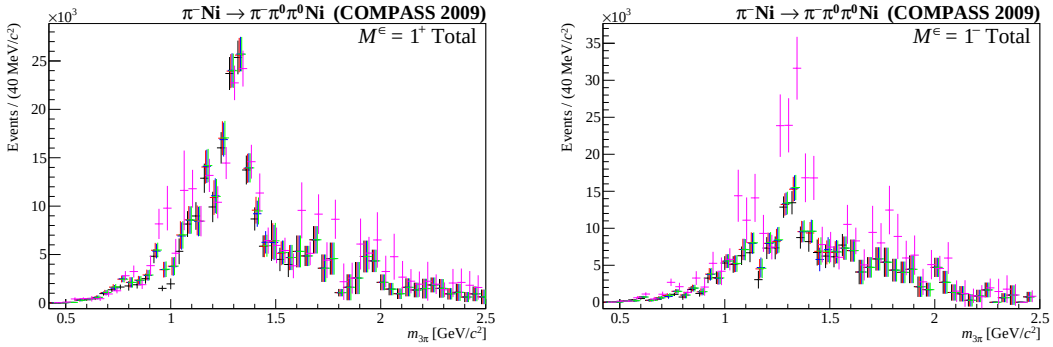

(a) $M^\epsilon = 1^+$ total waves intensity

(b) $M^\epsilon = 1^-$ total waves intensity

Figure 13.11: Total waves intensity of the $M^\epsilon = 1^+$ (a) and $M^\epsilon = 1^-$ partial waves. For the color coding please refer to figure 13.1.

While there is hardly any handle to make a statement regarding, which of the chiral models describes the data best, all chiral models show more continuous and therefore physical behavior and due to the smaller wave set smaller uncertainties as isobaric models. This is already visible at the level of spin totals. This leads to the conclusion, that the chiral wave describe the data better than isobaric waves. However, regarding the chiral models only the LO model show significant differences compared to the other chiral waves. Thereby, the behavior of the LO chiral waves itself may indicate, that the NLO, ρ or $\rho\rho$ chiral amplitude are better suited to describe the underlying physics, since a more continuous intensity of the chiral wave is observed[3]. However, in order to make a more substantial statement, a better understanding of the behavior of the different fit models is required. Thereby a central point is the understanding of the so-called model leakage, i.e. the leakage from a certain amplitude into other partial waves. A study aiming to investigate this behavior concerning different flavors of chiral waves is discussed in chapter 14.

13.2.2 Fit in Bins of t'

The PWA in mass bins allows first conclusions on the involved production mechanisms using the spin projection M and the phase of different waves. However, as $M = 1$ can be produced by Primakoff production and diffractive dissociation, this is only a rough classification. In order to study the contribution to $M = 1$, which is due to diffractive dissociation, a study of the t' dependence of the partial waves is required. This is achieved by doing a PWA in bins of t'. This study

[3]From a physics point of view a continuous development is expected and, assuming chiral perturbation theory applies, the low mass regime of $M = 1$ waves is, in the absence of resonance, completely described by the chiral amplitude.

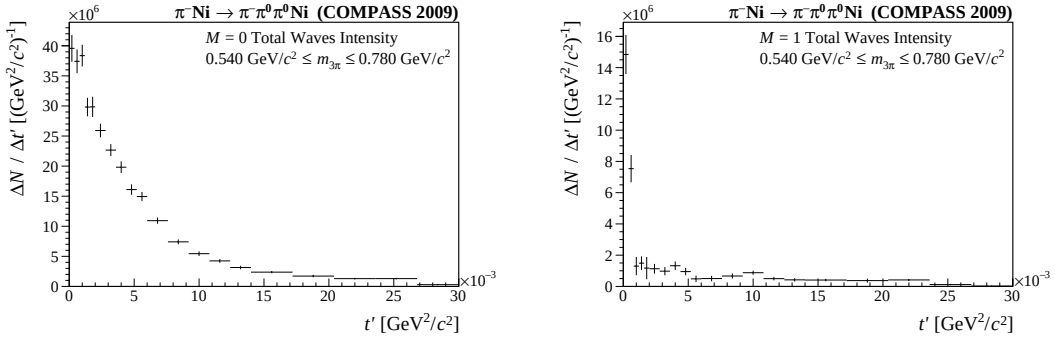

(a) $M = 0$ total waves intensity (b) $M = 1$ total waves intensity

Figure 13.12: Total waves intensity of $M = 0$ (a) and $M = 1$ (b) partial waves in a mass range $0.54\,\mathrm{GeV}/c^2 \leq m_{3\pi} \leq 0.78\,\mathrm{GeV}/c^2$.

cannot be applied in the narrow $40\,\mathrm{MeV}/c^2$ mass bins used before due to statistical limitations. Thus this study is done in broad mass ranges. In the following the results in the ranges from 0.54 to $0.78\,\mathrm{GeV}/c^2$, which is near the three-pion threshold, and from 1.22 to $1.38\,\mathrm{GeV}/c^2$, which covers the radiatively produced $a_2(1320)$ are discussed.

Similar to the fit in mass bins, the results of fits applying chiral models are describing the data in better than isobaric waves, showing a more continuous and therefore more physical shape and due to the smaller wave-set smaller uncertainties. Furthermore, the fits with one of the advanced chiral models describe the data best. These fits differ only marginally. Thus, in the following the discussion restricts to the most advanced chiral model, i.e. the one, which includes the chiral wave with double ρ exchange. Having said this the explicit notation of the flavor is omitted in the following discussion.

The t' Dependence Near the Three Pion Threshold

Later on, in the discussion in chapter 15 the partial-wave analysis technique will be used to measure the differential cross section of the process $\pi^-\gamma \to \pi^-\pi^0\pi^0$. This cross section is measured for masses $0.54\,\mathrm{GeV}/c^2 \leq m_{3\pi} \leq 0.78\,\mathrm{GeV}/c^2$. In this mass range the only $M = 1$ waves are the chiral waves $(ChPT)^{\epsilon=\pm}$. The chiral amplitudes refer to radiative production. However, the contribution from diffractive dissociation to the observed intensity has to be quantitatively understood. This is achieved by applying the partial-wave analysis in bins of t'. Considering only masses above $0.54\,\mathrm{GeV}/c^2$ contribution from $K^- \to \pi^-\pi^0\pi^0$ decays, which show up in the around the invariant mass of the K^-, are omitted. At this point it should be emphasized, that within the given mass range no resonant radiative processes are expected. This is reflected by the absence of isobaric $M = 1$ amplitudes. At small masses the overlap between $M = 1$ diffractive and

radiative production is minimal due to the sharp t' dependence of the Primakoff production, which is given by the Weizsäcker-Williams approximation (see section 3.3), and the relative phase of 90°. Thus, interference effects between the different production mechanisms is expected to be small.

Considering the simple structure of the $M = 1$ sector all important information is already contained in the spin totals. The $M = 0$ spin total (figure 13.12(a)) shows as expected an exponential shape, while the $M = 1$ spin total (figure 13.12(b)) shows a sharp peak at low t' followed by a long tail. The sharp peak matches the shape expected from the Monte-Carlo study of Primakoff events (see section 9.1). The tail can be used to constrain the contribution of diffractive dissociation, which is proportional to $t' \cdot \exp(-bt')$. Neglecting possible interference effects the observed spectrum can then be fitted by using the combined model

$$F(t') = a \cdot f(t', m_{3\pi}) + t' \cdot \exp(-bt'). \tag{13.1}$$

$f(t', m_{3\pi})$ is the expected Primakoff shape (equation 9.3). The parameters of the function depend on the three-pion mass $m_{3\pi}$. These parameters however change only slowly, thus they are allowed to vary within the limits of the mass range letting the fit determine the exact values. The parameters a and b are the parameters, which in leading order determine the amplitude of the Primakoff and diffractive production, respectively. These parameters are used to determine the corresponding contributions. The result of the fit is shown in figure 13.13. The observed t' shape is well described by the model and no signs of interference are observed. By integrating the individual contribution in a certain range of t' one can determine the admixture of diffractive and Primakoff production, respectively. The fraction of Primakoff events with transferred momentum $t'_{\text{low}} \leq t' \leq t'_{\text{high}}$ is then given by

$$\mathfrak{F}_{\text{Primakoff}}(t'_{\text{low}}, t'_{\text{high}}) = \frac{\int_{t'_{\text{low}}}^{t'_{\text{high}}} \mathrm{d}t'\, p_0 \cdot f(t', m)}{\int_{t'_{\text{low}}}^{t'_{\text{high}}} \mathrm{d}t'\, F(t')}. \tag{13.2}$$

The t' Dependence at the Mass of the $a_2(1320)$

Looking at three-pion masses larger than $1\,\text{GeV}/c^2$, several resonances are present and besides the small overlap of diffractive and radiative production the interference of the different production mechanisms might become significant. This is especially true for the $a_2(1320)$, which dominates the $M = 1$ spectrum. An important input to the understanding of these effects is the observed t' spectrum at the mass range of the $a_2(1320)$. A quantitative understanding of this inference is necessary to determine the absolute value of the radiative width of the $a_2(1320)$. Thus, a partial-wave analysis in t' bins is applied, considering three-pion masses from $1.22\,\text{GeV}/c^2 \leq m_{3\pi} \leq 1.38\,\text{GeV}/c^2$.

As in this particular mass region, multiple and partially narrow resonance ap-

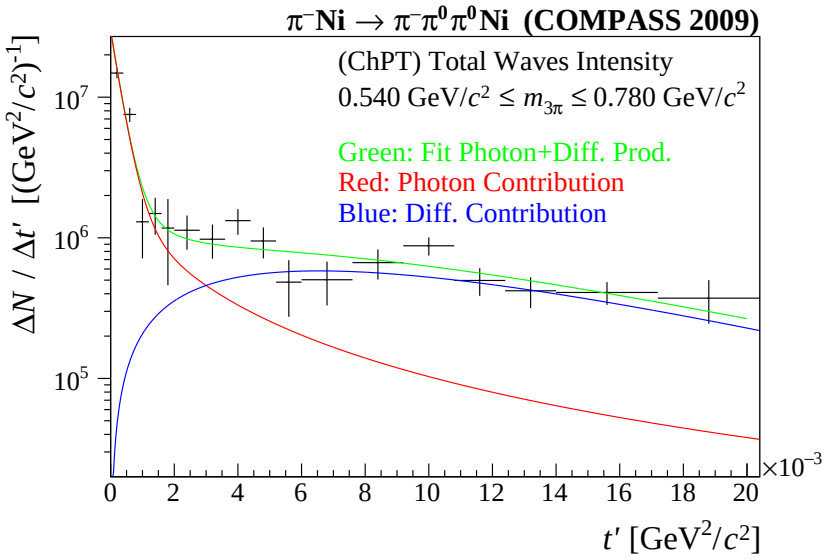

Figure 13.13: Contributions to the $M = 1$ total wave intensity in a mass range of $0.54\,\mathrm{GeV}/c^2 \leq m_{3\pi} \leq 0.78\,\mathrm{GeV}/c^2$. The histograms shows the data points and the fit (green) to the data. The contributions of Primakoff production (red) and diffractive dissociation (blue) are shown, which are added incoherently as described in the text.

pear, the assumption of the mass-independent PWA, that the mass-dependence in a certain analysis bin can be neglected, brakes down. Thus, the contribution of the resonances observed in different partial-wave has to be accounted. Neglecting the t'-dependence in the narrow t' bins this is achieved by introducing the mass-dependent decay amplitude $f_i^{\epsilon}(t', m_{3\pi}) = A_X(m_{3\pi})$ to the partial-waves (see equation 10.2 and 10.4), where X denotes the resonance with known parameters, which is observed in the amplitude i with reflectivity ϵ. Considering the results of the PWA in bins of $m_{3\pi}$ as well as the particle listing given in [B+12] the mass dependence of the $a_1(1260)$, $a_1(1420)$, $a_2(1320)$ and $\pi_2(1670)$ are modeled (see table 13.3). Table 13.4 lists which mass dependence is applied to which amplitude.

The $M = 0$ total waves intensity obtained with this method is shown in figure 13.14(a). Similar to the small mass an exponential dependence compatible with diffractive dissociation is observed. The $M = 1$ total waves intensity (figure 13.14(b)) shows, as expected, a sharp peak at low values of t' and a long tail. However, in contrast to lower masses, the transition between the peak at very low t' and the tail towards higher values shows an intensity, which cannot be described by equation 13.1. The intensity between roughly $0.001\,\mathrm{GeV}^2/c^2 \leq t' \leq 0.004\,\mathrm{GeV}^2/c^2$ is too high, to be described with this model. At this point it should be mentioned again, that equation 13.1 neglect interference

isobar	**paramters**	**comments**
$a_1(1260)$	$m_0 = 1.220\,\mathrm{Gev}/c^2$ $\Gamma_0 = 0.370\,\mathrm{GeV}/c^2$	According to [Bow86]
$a_1(1420)$	$m_0 = 1.412\,\mathrm{GeV}/c^2$ $\Gamma_0 = 0.155\,\mathrm{Gev}/c^2$	Using constant width
$a_2(1320)$	$m_0 = 1.314\,\mathrm{GeV}/c^2$ $\Gamma_0 = 0.120\,\mathrm{GeV}/c^2$ $\mathrm{BR}(\rho\pi)/\mathrm{BR}(\sigma\pi) = 4/1$	Decay channels: $\rho\pi$, $\sigma\pi$
$\pi_2(1670)$	$m_0 = 1.672\,\mathrm{GeV}/c^2$ $\Gamma_0 = 0.259\,\mathrm{GeV}/c^2$ $\mathrm{BR}(f_2\pi)/\mathrm{BR}(\rho\pi) = 7/3$	Decay channels: $f_2\pi$, $\rho\pi$

Table 13.3: Overview of parametrization of the mass dependence of three-pion resonances. The $a_1(1260)$ is parametrized according to [Bow86]. The $a_2(1320)$ and $\pi_2(1670)$ are parametrized using relativistic Breit-Wigner function considering the two most important decay modes.

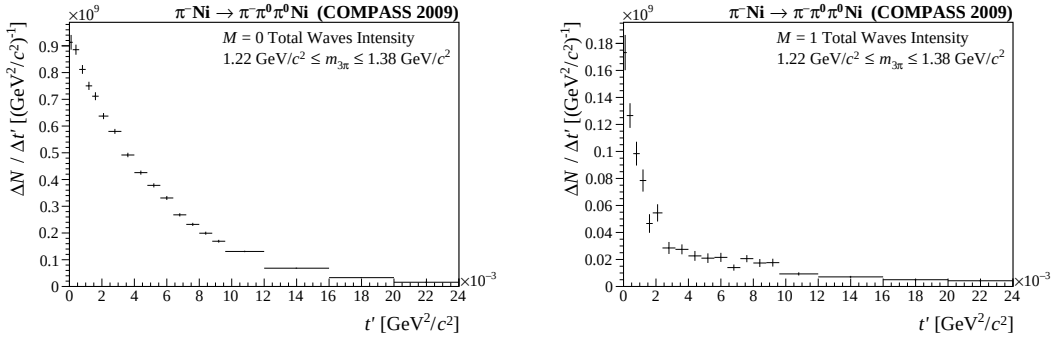

(a) $M = 0$ total waves intensity

(b) $M = 1$ total waves intensity

Figure 13.14: Dependence of the total waves intensity of $M = 0$ (a) and $M = 1$ (b) amplitudes on t' in the mass range $1.22\,\mathrm{GeV}/c^2 \leq m_{3\pi} \leq 1.38\,\mathrm{GeV}/c^2$.

Wave	**Mass dependence**
$1^{++}0^{+}\ \rho\ S\ \pi$	$a_1(1260)$
$1^{++}0^{+}\ \rho\ D\ \pi$	$a_1(1260)$
$1^{++}0^{+}\ (\pi\pi)_S\ P\ \pi$	$a_1(1260)$
$1^{++}0^{+}\ f_0(980)\ P\ \pi$	$a_1(1420)$
$1^{++}0^{+}\ f_2\ P\ \pi$	$a_1(1260)$
$2^{-+}0^{+}\ f_2\ S\ \pi$	$\pi_2(1670)$
$2^{-+}0^{+}\ \rho\ P\ \pi$	$\pi_2(1670)$
$2^{-+}0^{+}\ (\pi\pi)_S\ D\ \pi$	$\pi_2(1670)$
$2^{-+}0^{+}\ f_2\ D\ \pi$	$\pi_2(1670)$
$2^{-+}0^{+}\ \rho\ F\ \pi$	$\pi_2(1670)$
$1^{++}1^{\pm}\ \rho\ S\ \pi$	$a_1(1260)$
$1^{++}1^{\pm}\ (\pi\pi)_S\ P\ \pi$	$a_1(1260)$
$2^{++}1^{\pm}\ \rho\ D\ \pi$	$a_2(1320)$
$2^{-+}1^{\pm}\ f_2\ S\ \pi$	$\pi_2(1670)$
$2^{-+}1^{\pm}\ \rho\ P\ \pi$	$\pi_2(1670)$
$2^{-+}1^{\pm}\ (\pi\pi)_S\ D\ \pi$	$\pi_2(1670)$
$2^{-+}1^{\pm}\ \rho\ F\ \pi$	$\pi_2(1670)$

Table 13.4: Listing of the mass dependence applied to different partial waves, when doing the PWA fit in bins of transferred momentum t'. The mass dependencies are not used for three-pion masses bellow $0.78\,\mathrm{GeV7}c^2$. Waves with flat mass dependence are omitted.

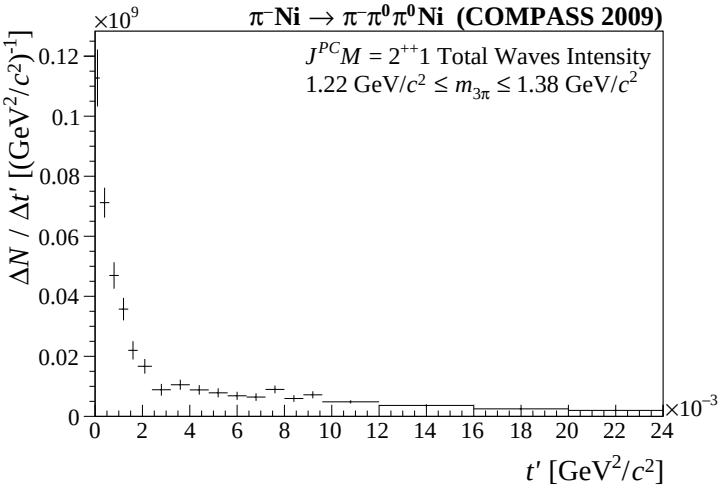

Figure 13.15: Dependence of the total waves intensity of $J^{PC}M = 2^{++}1$ amplitudes on t' in the mass range $1.22\,\mathrm{GeV}/c^2 \leq m_{3\pi} \leq 1.38\,\mathrm{GeV}/c^2$.

effects. This discrepancy cannot be resolved by looking at the $J^{PC}M = 2^{++}1$ total waves intensity (see figure 13.15). At the current state of understanding, the discrepancy is not introduced by experimental uncertainties, but is a evidence for the interference of production mechanisms. Lacking a suitable model the quantitative understanding of this effect, which is necessary for an absolute measurement in this mass region, is currently impossible. This includes the measurement of the radiative width of the $a_2(1320)$.

Nevertheless, the contributions to the $J^{PC}M = 2^{++}1$ total wave are studied. These are the $2^{++}1^+\,\rho\,D\,\pi$ wave (figure 13.16(a)) and its counter part with negative reflectivity, the $2^{++}1^-\,\rho\,D\,\pi$ wave (figure 13.16(b)). The suppression of high t' in the negative reflectivity is expected due to the fact, that negative reflectivity waves are populated through experimental uncertainties. Last but not least the phase difference between the $2^{++}1^+\,\rho\,D\,\pi$ and the $1^{++}0^+\,\rho\,S\,\pi$ should be discussed (figure 13.17). As seen in the PWA in mass bins the $1^{++}0^+\,\rho\,S\,\pi$ intensity comes from the $a_1(1260)$, while the $a_2(1320)$ shows up in the $2^{++}1^+\,\rho\,D\,\pi$. The phase between this two waves change from $\approx -100°$ to values of ≈ 20 with a continuous transition. This can be interpreted as the changeover from different productions mechanisms of the $a_2(1320)$, starting with radiative production at low t'. At higher t' the contribution of diffractive dissociation increases until it takes over completely and a constant phase is observed.

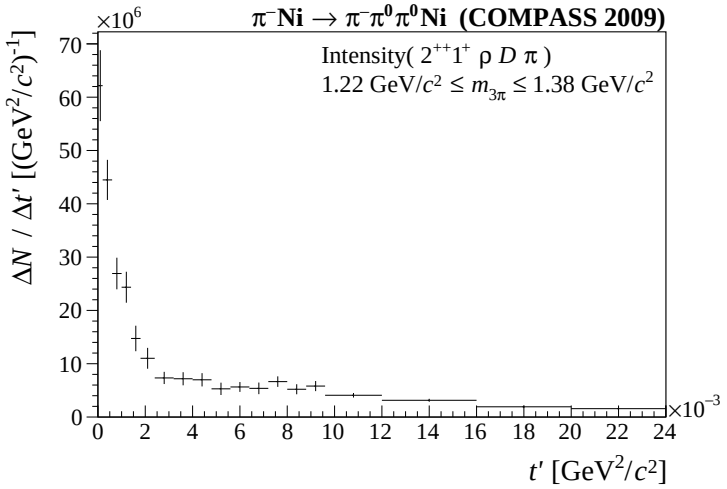

(a) Intensity($2^{++}1^{+}\,\rho\,D\,\pi$)

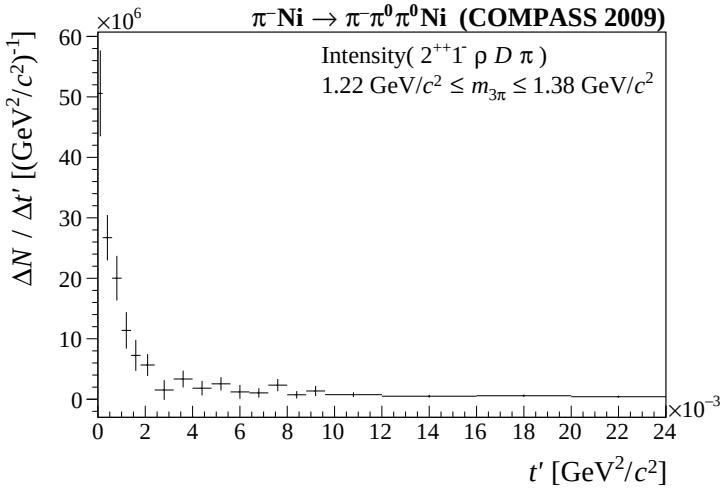

(b) Intensity($2^{++}1^{-}\,\rho\,D\,\pi$)

Figure 13.16: Dependence the intensity of the $2^{++}1^{+}\,\rho\,D\,\pi$ and $2^{++}1^{+}\,\rho\,D\,\pi$ amplitude on t' in the mass range $1.22\,\mathrm{GeV}/c^2 \leq m_{3\pi} \leq 1.38\,\mathrm{GeV}/c^2$.

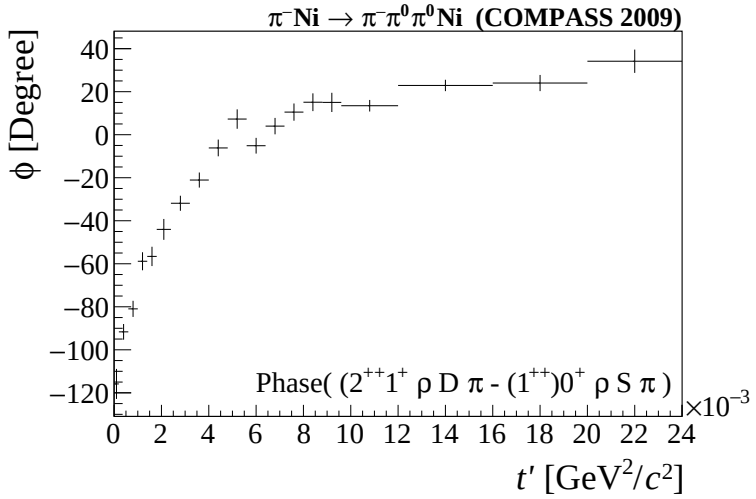

Figure 13.17: Dependence of the phase($2^{++}1^{+}\,\rho\,D\,\pi - 1^{++}0^{+}\,\rho\,S\,\pi$) on t' at the mass of the $a_2(1320)$.

Chapter 14

Systematic Studies

Demonstrating, that the presented partial-wave analysis is able to identify and characterize partial-waves with contributions on the sub-percent level, a careful analysis of systematic effects imposed by the model and apparatus is required. Besides a classical leakage study, where the obtained model is simulated and fed back to the PWA, a more comprehensive study of the chiral wave and their flavors has been carried out. For this study four event samples, one for each flavor of the chiral amplitudes, have been generated in the mass range of $0.42\,\mathrm{GeV}/c^2$ to $1.62\,\mathrm{GeV}/c^2$. Only a positive-reflectivity wave is taken into account. The event samples is generated in mass bins of $10\,\mathrm{MeV}/c^2$ width and follow a t' distribution imposed by the Weizsäcker-Williams approximation. The angular dependencies of the chiral wave are generated with a sample and reject algorithm. At the end, each mass bin with a width $10\,\mathrm{MeV}/c^2$ of provide the equal amount of 112 events, which have passed the selection. The generated event samples are than fitted with each of the chiral models, which are also used to fit the data (see chapter 13). Named after the underlying chiral wave, the event samples are referred as LO, NLO, single ρ and double ρ sample, respectively.

The visual presentation of the results uses the color scheme introduced in chapter 13. The LO model is plotted in black, the model including the NLO chiral wave in red. The models including chiral waves, which account for single and double ρ exchange, are printed in blue and green, respectively. For better distinction the colored points are increasingly shifted to the right. The bin center is always given by the black LO points.

14.1 The $(\mathrm{ChPT})^{+}_{\mathrm{LO}}$ Monte-Carlo Sample

First the behavior of the PWA fits to the event sample obtained by using the $(\mathrm{ChPT})^{+}_{\mathrm{LO}}$ chiral wave function to weight the Monte-Carlo events should be discussed. Figure 14.1 show the spin totals for $M = 0$, $M = 1$ as well as $M^{\epsilon} = 1+$ and $M^{\epsilon} = 1-$ total wave intensities, which are obtained by fitting with the different flavors of the chiral model. Fitting with the LO model, which contains the

chiral wave used to generate the sample, a significantly lower leakage into $M = 0$ waves than for other models is observed. Except for the lowest mass bins in the relevant kinematic range a leakage, which is in the order of ten percent, is found for this model. All other fits show significant more leakage, which increase towards higher masses. This behavior cannot be confirmed, when compared to the result of the PWA (see chapter 13), where all chiral model show a similar behavior of the spin totals. For the recorded data above $0.78\,\mathrm{GeV}/c^2$ the LO model reveals a significant lower intensity in the chiral wave than other chiral models. This is the behavior, which is opposite to the one observed studying the LO event sample. Here the fit with LO model reveal a higher intensity of the chiral wave due to the smaller leakage into $M = 0$ waves. Furthermore, at masses from 0.78 to $0.98\,\mathrm{GeV}/c^2$ a non-continuity in the intensity of the advanced chiral is observed. This is not observed for the COMPASS 2009 data. The model leakage from positive to negative reflectivity of the advanced model vanishes at higher masses, where for the COMPASS data an almost constant ratio of positive and negative reflectivity waves is observed for all models. For the LO Monte-Carlo this ratio of 10/7 is only reproduced with the LO fit. Thus, from these observations the conclusion is drawn, that the chiral amplitude observed in the COMPASS data does not follow the angular dependencies, which are predicted by the LO ChPT calculation.

14.2 The $(\mathbf{ChPT})^{+}_{\mathbf{NLO}}$ Monte-Carlo Sample

The spin totals obtained by the fit to the NLO sample are shown in figure 14.3. Similar to the fits to the real data and the previously discussed LO sample again a grouping of the advanced models is observed. Below $m_{3\pi} = 1\,\mathrm{GeV}/c^2$ the fits with advanced models show a comparatively small leakage into $M = 0$ waves, which is in the order of 10-20%. Above $1\,\mathrm{GeV}/c^2$ this leakage is continuously increased. For the LO model a similar increase can be observed. However this increase extend over the hole mass range, where the starting value is with approximately 30% much higher. The model leakage from positive to negative reflectivity is again found to be compatible with recorded data. Looking at the chiral amplitudes (figure 14.4) some principle similarities of the PWA applied to the COMPASS data are found. The fits for advanced chiral models still group together having a higher intensity than the LO chiral model. This is the behavior observed in the PWA of the COMPASS data for masses above $0.78\,\mathrm{GeV}/c^2$. However, at lower masses, where for the real data set no significant difference between LO and advanced chiral models exists, the intensity of chiral amplitude in the LO model is still lower than the intensity obtained for advanced models. Thereby the difference is smaller than at large values of $m_{3\pi}$. At this place one should emphasize, that in the recorded data set there might be additional contribution, which might modify the behavior of the fit. Thus no final conclusion can be

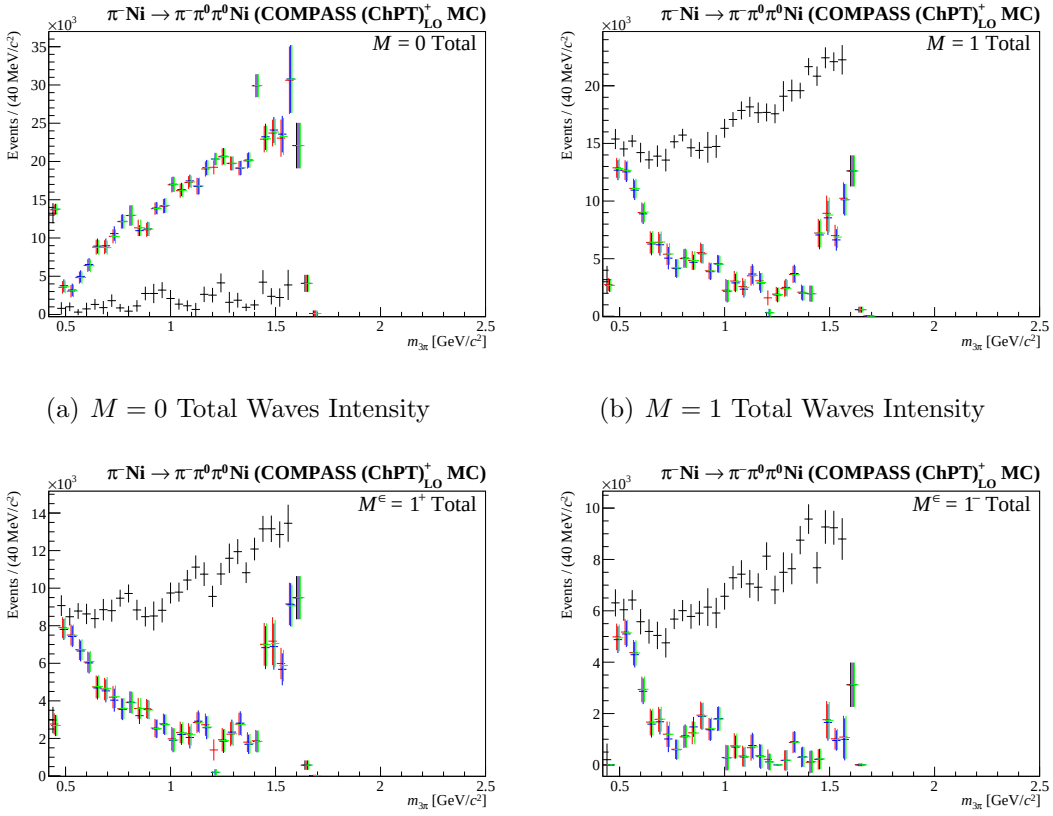

(a) $M = 0$ Total Waves Intensity

(b) $M = 1$ Total Waves Intensity

(c) $M^\epsilon = 1^+$ Total Waves Intensity

(d) $M^\epsilon = 1^-$ Total Waves Intensity

Figure 14.1: Total wave intensity fitted to Monte-Carlo sample, weighted with the $(\text{ChPT})^+_{\text{LO}}$ chiral wave. The different color represents different fit models (details given in the text).

drawn from this difference. Looking even more closely to the mass range from $0.78\,\text{GeV}/c^2$ to $1.22\,\text{GeV}/c^2$ the fit using the single ρ exchange model (blue) has a slightly higher intensity in the chiral wave than observed for the NLO or double ρ exchange model. This matches the observation made for COMPASS data (see chapter 13).

14.3 The $(\text{ChPT})^+_\rho$ Monte-Carlo Sample

Advancing further figure 14.5 shows the spin totals obtained by fitting the Monte-Carlo sample featuring single ρ exchange. The intensities of the chiral waves are shown in figure 14.6. Similar to the fit to the NLO sample, the coarse features observed in the analysis of recorded data are observed. However a close look to the chiral wave intensity of the different fit models show a wider spread of advanced

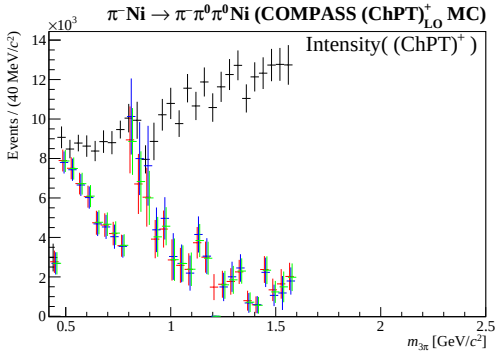

(a) Intensity($(\mathrm{ChPT})^{+}$)

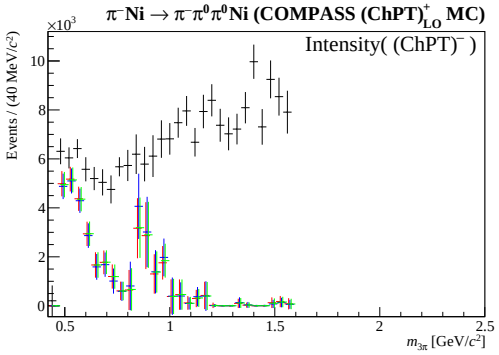

(b) Intensity($(\mathrm{ChPT})^{-}$)

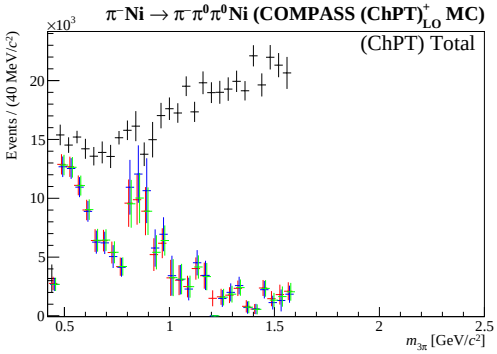

(c) Total Waves Intensity of Chiral Waves

Figure 14.2: Intensity of the chiral waves $(\mathrm{ChPT})^{+}$ and $(\mathrm{ChPT})^{-}$ fitted to the chiral event sample of LO calculations and their coherent sum, the ChPT Total wave intensity. The different fitting models are indicated with the color code discussed in the text.

chiral models at high values of $m_{3\pi}$. This is not observed for the recorded data. Thus, the NLO sample produces a behavior, which matches the behavior observed in the PWA analysis of the COMPASS data, better than the single ρ sample. This is, however, no strong evidence.

14.4 The $(\mathrm{ChPT})^{+}_{\rho\rho}$ Monte-Carlo Sample

Introducing double ρ exchange into the weighted Monte Carlo, it is found, that the coarse feature of the analysis of the COMPASS data are reproduced (see figure 14.7). Also investigating the chiral waves (figure 14.8) do reveal a very similar behavior as observed for COMPASS data and the NLO sample. This

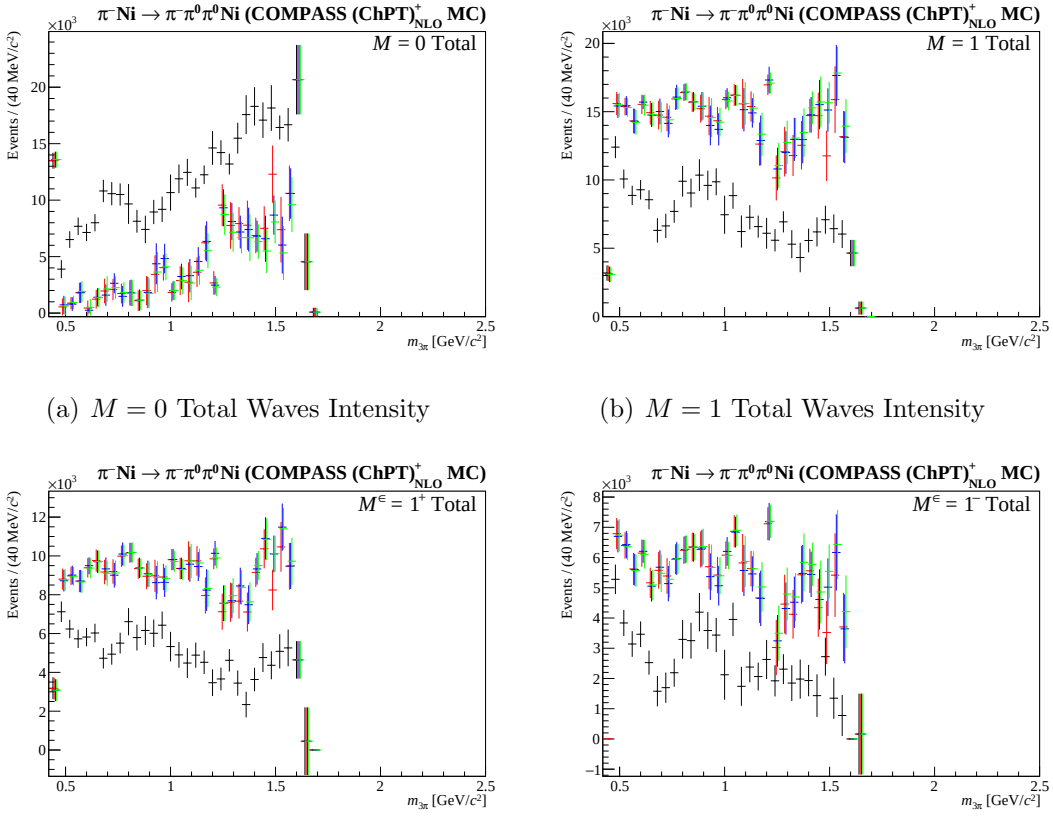

(a) $M = 0$ Total Waves Intensity

(b) $M = 1$ Total Waves Intensity

(c) $M^\epsilon = 1^+$ Total Waves Intensity

(d) $M^\epsilon = 1^-$ Total Waves Intensity

Figure 14.3: Total wave intensity fitted to Monte-Carlo sample, weighted with the $(\text{ChPT})^+_{\text{NLO}}$ chiral wave. The different color represents different fit models (details given in the text).

makes it impossible to determine, which model fits the data best. However, as the model is based on the most advanced ChPT calculations and no significant difference of advanced models are observed, the $\rho\rho$ model is regarded as the leading model. Thus all measurements are based on the results obtained with this model.

14.5 Conclusion of the Leakage Study

The study of PWA fits to the Primakoff data recorded at COMPASS in 2009 already revealed, that PWA models, which contain an amplitude based on ChPT calculations, produces superior fit results than pure isobar models. These fits however revealed, that the difference between available chiral models are comparably small, with only the LO model sticking out. Thus, a comprehensive study, which reveals the behavior of the different fit models, when used to describe

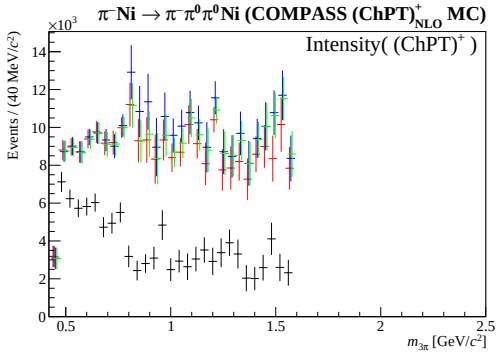

(a) Intensity($(\mathrm{ChPT})^{+}$)

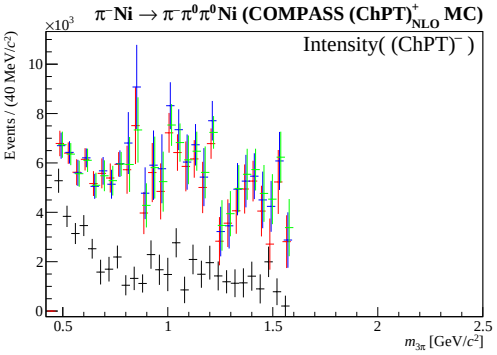

(b) Intensity($(\mathrm{ChPT})^{-}$)

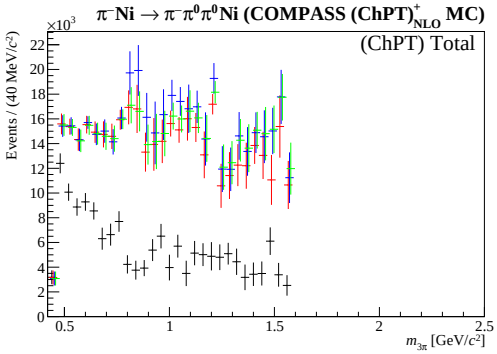

(c) Total Waves Intensity of Chiral Waves

Figure 14.4: Intensity of the chiral waves $(\mathrm{ChPT})^{+}$ and $(\mathrm{ChPT})^{-}$ fitted to the chiral event sample of NLO calculations and their coherent sum, the ChPT Total wave intensity. The different fitting models are indicated with the color code discussed in the text.

hypothetical chiral waves, had been conducted and discussed.

This study revealed, that for angular dependence produced by advanced models many of the features observed for COMPASS data are not only qualitatively, but also quantitatively reproduced, as it is the case for the leakage from positive to negative reflectivity. However, all advanced chiral waves behave very similar. This is also true, when the available number of Monte-Carlo events is increased by an order of magnitude. A study using larger event sample, which do not follow the t' distribution imposed by the Weizsäcker-Williams approximation, did not reveal further insights (see appendix C). Fits to the Monte Carlo truth, i.e. to the four-vectors generated by the event generator with acceptance being applied, show no model leakage. Thus, the observed model leakage is due to experimental resolution.

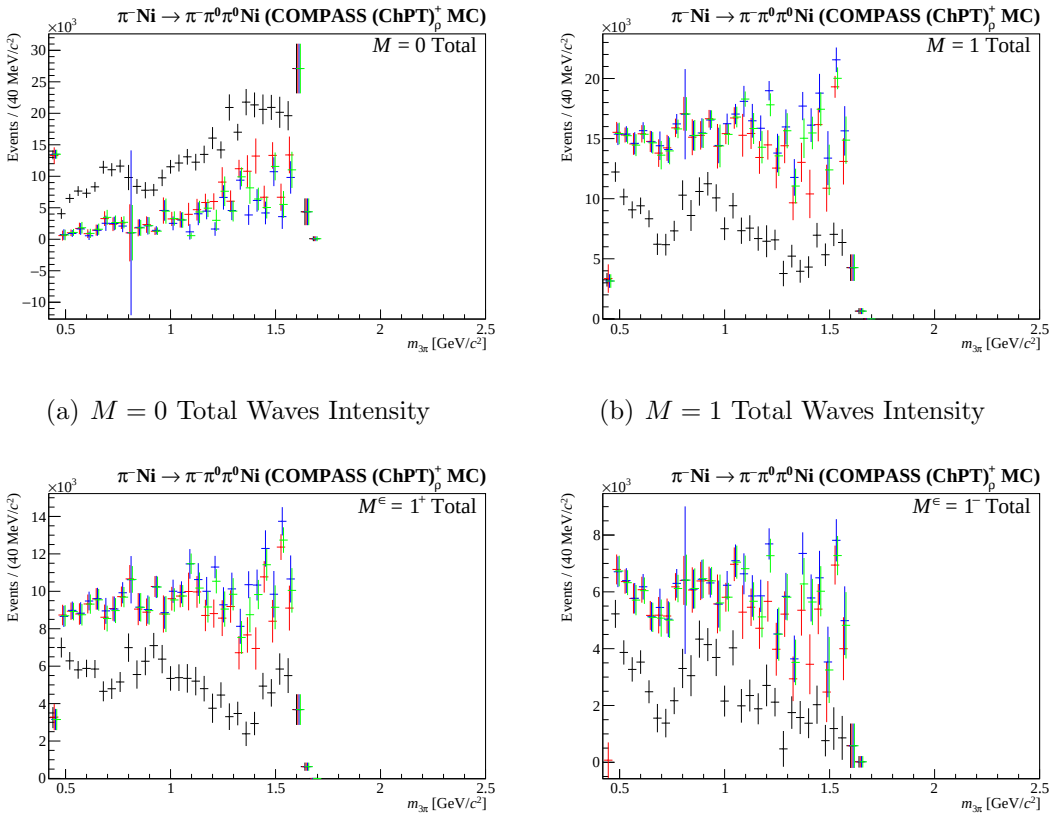

(a) $M = 0$ Total Waves Intensity

(b) $M = 1$ Total Waves Intensity

(c) $M^\epsilon = 1^+$ Total Waves Intensity

(d) $M^\epsilon = 1^-$ Total Waves Intensity

Figure 14.5: Total wave intensity fitted to Monte-Carlo sample, weighted with the $(\text{ChPT})^+_\rho$ chiral wave. The different color represents different fit models (details given in the text).

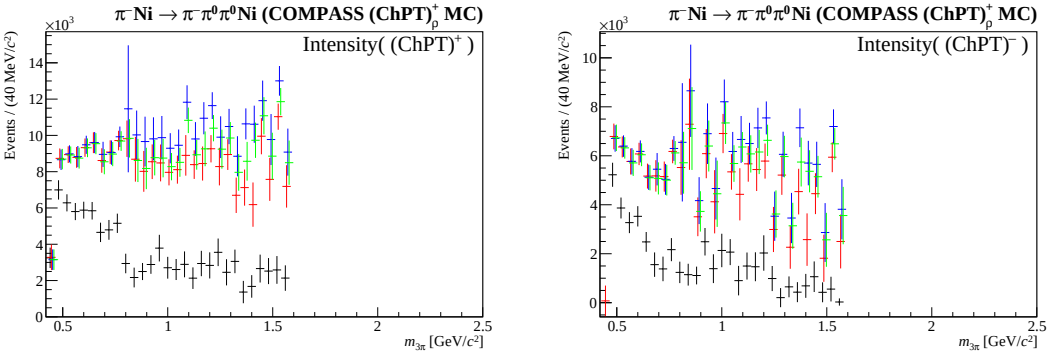

(a) Intensity($(\text{ChPT})^+$) (b) Intensity($(\text{ChPT})^-$)

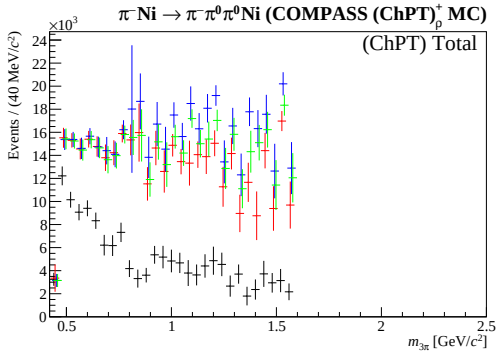

(c) Total Waves Intensity of Chiral Waves

Figure 14.6: Intensity of the chiral waves $(\text{ChPT})^+$ and $(\text{ChPT})^-$ fitted to the chiral event sample of calculations including single ρ exchange diagrams and their coherent sum, the ChPT Total wave intensity. The different fitting models are indicated with the color code discussed in the text.

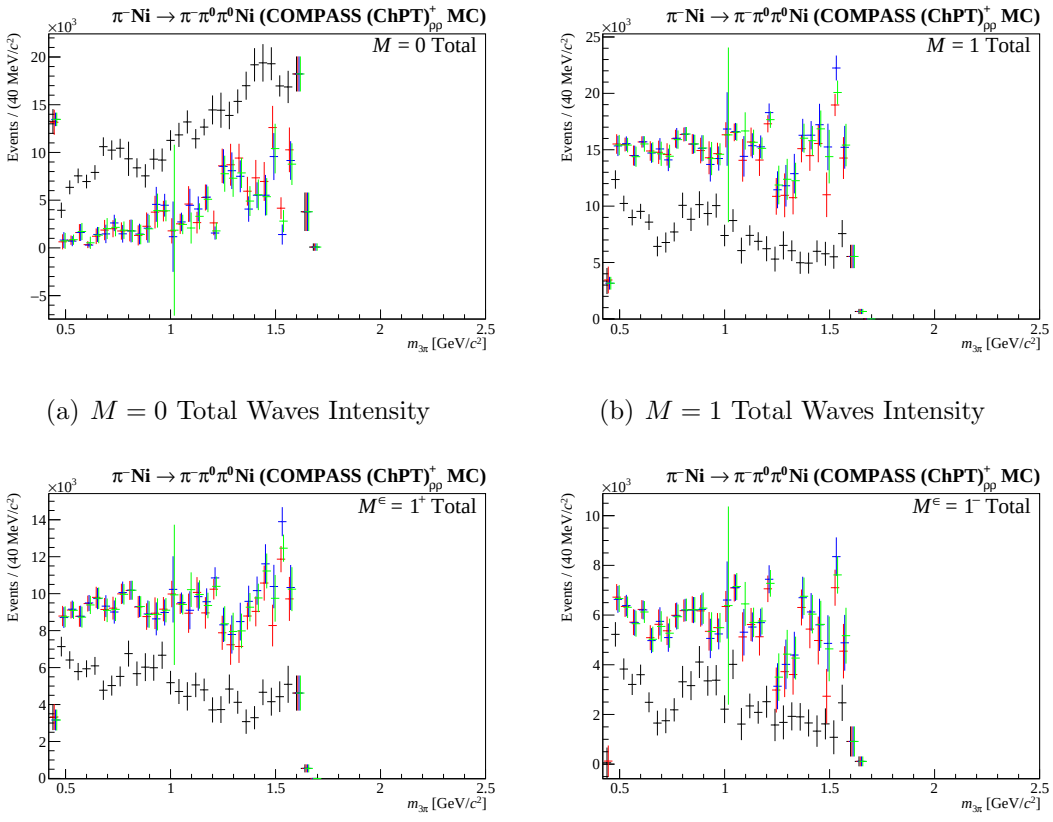

(a) $M = 0$ Total Waves Intensity

(b) $M = 1$ Total Waves Intensity

(c) $M^\epsilon = 1^+$ Total Waves Intensity

(d) $M^\epsilon = 1^-$ Total Waves Intensity

Figure 14.7: Total wave intensity fitted to Monte-Carlo sample, weighted with the $(\text{ChPT})^+_{\rho\rho}$ chiral wave. The different color represents different fit models (details given in the text).

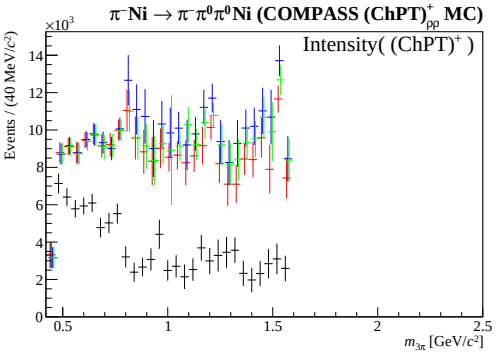

(a) Intensity($(\text{ChPT})^{+}$)

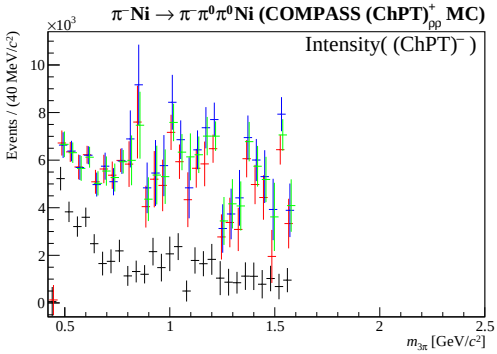

(b) Intensity($(\text{ChPT})^{-}$)

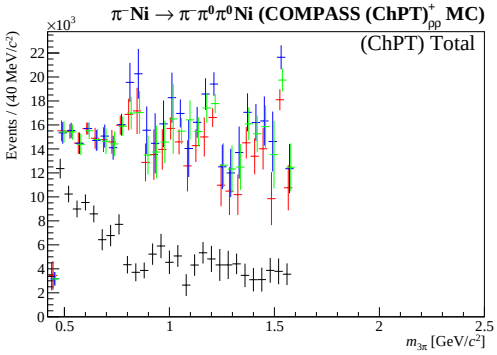

(c) Total Waves Intensity of Chiral Waves

Figure 14.8: Intensity of the chiral waves $(\text{ChPT})^{+}$ and $(\text{ChPT})^{-}$ fitted to the chiral event sample of calculations including double ρ exchange diagrams and their coherent sum, the ChPT Total wave intensity. The different fitting models are indicated with the color code discussed in the text.

The LO event sample in contrast to the advanced sample, could not reproduce the fit behavior observed for COMPASS data. Thus, the hypothesis, that the recorded data contain a chiral amplitude with pure leading-order behavior can be rejected.

Since none of the advanced chiral waves stick out, from this study no clear preference for one of the advanced wave can be deduced. Thus, the preference for the chiral amplitude which includes double ρ exchange is deduced from the fact, that it is based on the most advanced ChPT calculations.

Last but not least it should be recalled, that not all features of the behavior of the fit, like the similar behavior of all chiral models at large masses or the almost identical behavior all models for $m_{3\pi} < 0.78\,\mathrm{GeV}/c^2$, of the fit with different chiral models are reproduced. This leaves room for further clarification and improvements, which, however, exceeds the scope of this work.

Chapter 15

Cross Section of $\pi^-\gamma \to \pi^-\pi^0\pi^0$

Absolute measurement like the determination of the cross section require besides a good understanding of the apparatus and involved systematic, a normalization. The normalization is obtained through the integrated luminosity. At COMPASS decays of kaons, which are contained in the beam, are used to measure the integrated luminosity. The details of this measurement are discussed, before discussing how the differential cross section is obtained and which correction are necessary to compensate for known systematic effects.

15.1 Determination of Luminosity

The life time of the K^- is known with high precision. Thus by measuring the number of kaon decay within a certain period the integrated kaon flux can be determined. By accounting for the $BR(K^- \to f)$ not all kaon decays, but only kaon decays into a certain final state f have to be measured. The integrated flux of kaons is related to the integrated pion flux by the fraction of kaons and pions contained in the hadron beam at COMPASS. The hadron beam at COMPASS contains 2.4% kaons[1] and 0.8% anti-proton [AAA+15a]. The remaining particles are pions. The fraction of the kaon, thereby, is known by a relative uncertainty of 5%. Combining the integrated flux of pions with the target properties the integrated luminosity $\mathcal{L}$, which enters the calculation of the differential cross section, is determined.

In the following this method, which is used for the measurement of $\pi^-\gamma \to \pi^-\pi^0\pi^0$ cross section at COMPASS, is discussed in more details. In order to account for unknown systematic effects the final state of the kaon decays, which are used for normalization, is chosen to be identical to the final state of the reaction, which is under investigation. Thus, although there are other decay

[1] Currently an analysis of spectrometer aiming to measurement the beam composition is ongoing. Intermediate results revealed hints for a slightly larger kaon contribution. This would increase the absolute values of the measured cross section.

channels with higher branching fraction and better acceptance, the $K^- \to \pi^-\pi^0\pi^0$ is used to determine the pion luminosity.

15.1.1 $K^- \to \pi^-\pi^0\pi^0$ – Reconstruction and Selection

The selection of a clean $K^- \to \pi^-\pi^0\pi^0$ event sample requires only minimal modification of the event selection of pion-target interactions, which is descried in section 8.7. Thus the following discussion will concentrate on the necessary modification.

For the measurement of the integrated kaon flux a decay volume between the nickel and tungsten targets is selected. This decay volume, being close to the target, features similar systematics as the measurement of pion target interaction. Additionally, the influence of beam interaction is minimized due to the absence of solid material. The decay volume is selected by requiring the z position of the vertex to lie in a range of -65 to $-20\,\mathrm{cm}$[2] replacing the original target cut.

$$-65\,\mathrm{cm} \leq z_{\mathrm{vert}} \leq -20\,\mathrm{cm} \tag{15.1}$$

The assumption, that the reaction takes place at the position of the target is not applicable any more. Thus the vertex position is not constrained and the reconstructed coordinates are used. Figure 15.1 shows the distribution of reconstructed vertices along the z axis for the selected kaon decays as well as for simulated events. The distribution obtained by Monte-Carlo simulation is scaled down to match the amount of observed kaon decays. The observed distribution of kaon decays is in good agreement with simulations. Besides the overlap with the target cut, the contribution from beam-target interaction is negligible due to additional requirements. This is confirmed by the fact, that except a small enhancement at the nominal target position at $-72,5\,\mathrm{cm}$, which is not accounted for the measurement of the integrated flux, no target effects are observed in the distribution of vertices along the z-axis.

Decaying resonances and pseudo stable particles show up as peaks in the invariant mass spectrum of the final state. The peak position and width is defined by the mass and lifetime of the mother state, respectively. Thus by cutting on the invariant mass of the final state particles it is possible to select particle decays. Usually both the width and the peak position may also be effected by experimental resolution, which have to be taken into account, when defining the cut. Figure 15.2 shows the mass spectrum of the kaon decay discussed here. Kaon decays are selected by requiring

$$|m_{K^-} - m_f| \leq 15\mathrm{MeV}/c^2, \tag{15.2}$$

where $m_f = m_{3\pi}$ is the invariant mass of the three-pion system. The mass of the

[2]Coordinates given in the main reference system of the experiment.

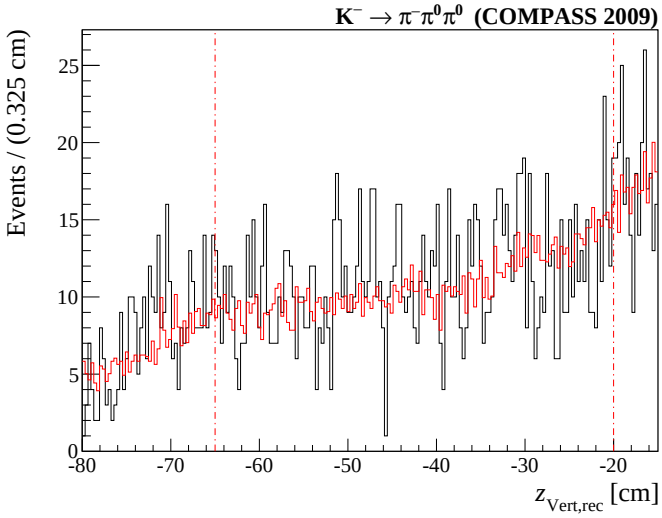

Figure 15.1: Reconstructed z position of the vertex for selected $K^- \to \pi^-\pi^0\pi^0$ events (Black: Data, Red: Scaled Monte Carlo). The vertical red lines indicate the selected range.

kaon m_{K^-} is taken from [B+12]. The selection is indicated by red lines.

For a particle decay like $K^- \to \pi^-\pi^0\pi^0$ four-momentum conservation require formally a transferred momentum $t' = 0$. However due to experimental resolution the measured value of t' for the kaon differs from zero and the distribution shown in figure 15.3 is observed. This observation is incorporated in the Kaon decay selection by requiring

$$t' \leq 0.001(\mathrm{GeV}/c)^2. \tag{15.3}$$

Applying the event selection with the modification discussed above to the present data set of $N_{K^-,\mathrm{rec}} = 1515$ kaon decays $K^- \to \pi^-\pi^0\pi^0$ are found. Thereby, of course, double counting of beam particles is avoided.

15.1.2 Acceptance Correction for $K^- \to \pi^-\pi^0\pi^0$

In order to determine the integrated flux of kaons the found number of kaon decays $N_{K,\mathrm{rec}}$ has to be corrected for acceptance effects. Thus in order to maintain proper normalization, having a good understanding of the acceptance of the experimental setup is important. Thereby the limitations of the COMPASS Monte-Carlo framework are taken into account by using the same final state for the normalization and the measurement itself. Thus the systematic, introduced by uncorrelated background, cancel due to the similarities of the kinematics (see chapter 12). Besides not describing the uncorrelated background, the observed properties and therefore angular distributions are correctly described by the Monte-Carlo. This

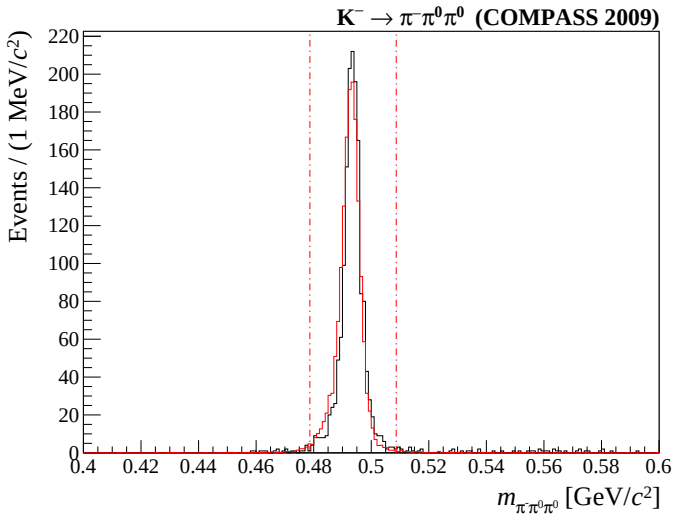

Figure 15.2: Reconstructed m_f spectrum of selected $K^- \to \pi^-\pi^0\pi^0$ events (Black: Data, Red: Scaled Monte Carlo). The vertical red lines indicate the selected range.

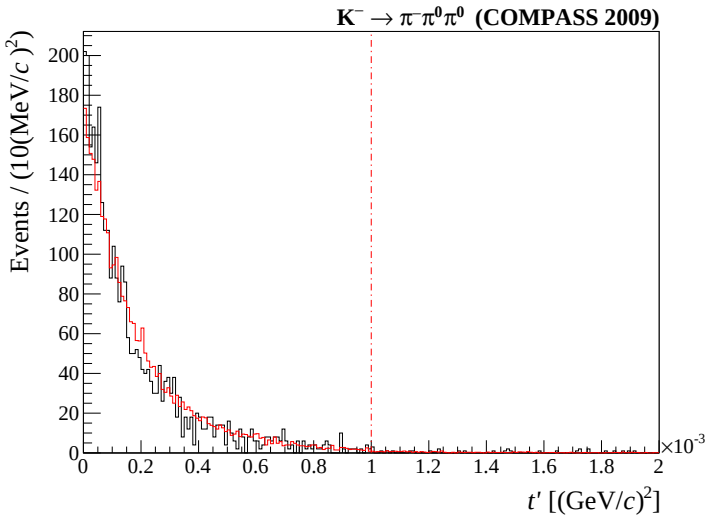

Figure 15.3: Reconstructed t' spectrum of selected $K^- \to \pi^-\pi^0\pi^0$ events (Black: Data, Red: Scaled Monte Carlo). The vertical red lines indicate the selected range.

can for example be seen by studying the distribution discussed in section 15.1.1. At this place it should be mentioned, that the Monte-Carlo event sample accounts for the angular dependence of the kaon decay, which is described by dalitz plot variables (see [B$^+$12]). The acceptance $A(K^- \to \pi^-\pi^0\pi^0)$ is then given by the fraction $N_{\mathrm{rec}}/N_{\mathrm{sim}}$ of accepted events and events, which are simulated within the decay volume.

$$A(K^- \to \pi^-\pi^0\pi^0) = \frac{N_{\mathrm{MC,rec}}}{N_{\mathrm{MC,sim}}} \tag{15.4}$$

Bin migration is accounted by simulating decays in a sufficiently large range of z values.

15.1.3 Luminosity of the Primakoff Measurement with Pion Beam

Using the obtained results for the number of observed kaon decays the integrated flux of pions is

$$\int \phi_\pi \mathrm{d}t = \frac{N_{K^-,\mathrm{rec}}/A(K^- \to \pi^-\pi^0\pi^0)}{\left(1 - e^{\frac{s}{c\beta\gamma\tau}}\right) BR(K^- \to \pi^-\pi^0\pi^0) \frac{N_{K^-,\mathrm{beam}}}{N_{\pi^-,\mathrm{beam}}}}, \tag{15.5}$$

with s being the length of the volume used to observe kaon decay. τ is the life time of the kaon taken from [B$^+$12]. $\beta = v/c$ and $\gamma = 1/\sqrt{1 - v^2/c^2}$ are the velocity in units of the speed of light c and the Lorentz factor, respectively. Where γ is calculated dividing the average beam energy $\overline{E}_{\mathrm{beam}} = 191\,\mathrm{GeV}$ by the rest energy of the kaon $m_K c^2 = 493.667\,\mathrm{MeV}$.

$$\gamma = \frac{\overline{E}_{\mathrm{beam}}}{m_K c^2} \qquad , \qquad \beta = \sqrt{1 - \gamma^{-2}} \tag{15.6}$$

The first factor of the quotient in equation 15.5 accounts for the decay volume, the lifetime of the kaon and the velocity of the kaon. The branching fraction $BR(K^- \to \pi^-\pi^0\pi^0) = 1.761(22) \cdot 10^{-2}$ (from [B$^+$12]) accounts for decays to other final states. $N_{K^-,\mathrm{beam}}/N_{\pi^-,\mathrm{beam}} = \frac{2.4}{97}$ finally is relation between the kaon and pion contributions to the beam. Connecting the integrated beam flux with the target properties the integrated luminosity is given by

$$\int \mathcal{L}_\pi \mathrm{d}t = \int \phi_\pi \mathrm{d}t \cdot \frac{\text{target particles}}{\text{area}}. \tag{15.7}$$

For the 4.2 mm thin nickel disc, which served as target for the present measurement, the number of target particles per area is determined as

$$\frac{\text{target particles}}{\text{area}} = \frac{d\,\rho_{\mathrm{Ni}}\,N_{\mathrm{A}}}{A W_{\mathrm{Ni}}} = 3.839\,\mu b^{-1} \tag{15.8}$$

with the nuclear density $\rho_{\mathrm{Ni}} = 8.908\,\mathrm{g/cm^3}$ of nickel and its average atomic weight $AW_{\mathrm{Ni}} = 58.6934\,\mathrm{u}$. $N_{\mathrm{A}} = 6.022 \cdot 10^{23}\,\mathrm{mol}^{-1}$ denotes the Avogado constant. $d = 0.42\,\mathrm{cm}$ is the thickness of the target. The uncertainty arising from this quantity is 2.4%, which is dominated by the uncertainty, with which d is known. The relative uncertainty, with which the beam composition is known, is 5%. A statistical uncertainty of ≈2.6% is introduced by the measurement and the determination of acceptance correction. The integrated luminosity then is found to be

$$\int \mathcal{L}_\pi \mathrm{d}t = (4.52 \pm 0.28) \cdot 10^3 \, \frac{\mathrm{Events}}{\mu b}. \tag{15.9}$$

15.2 Beam Particle Identification Efficiency

As described in section 8.6 the beam particle identification is achieved with two CEDAR detectors. In order to reduce background arising from Kaon decays and interactions, only beam particles with a pion tag are considered. This, however, means, that possible mis- or unidentified pions are neglected. For the measurement of the cross section this fact has to be taken into account. The event selection presented in chapter 8 enrich the pion sample, such that 97.1% of the events have a pion tag and only 0.7% have a kaon tag. The remaining 2.2% have unknown beam PID. Having such a high pion content the efficiency of identifying pions is difficult to access, however knowing the efficiency $\epsilon_{\mathrm{CEDAR},K}$ of tagging kaons the number of pions can be determined as

$$N_\pi = N_{\mathrm{tot}} - \frac{N_{K,\mathrm{tag}}}{\epsilon_{\mathrm{CEDAR},K}} \tag{15.10}$$

with the total number of events N_{tot} and the number of events $N_{K,\mathrm{tag}}$ with a kaon tag. As the measurement of the beam PID is independent from the target interaction, the measured intensities can be corrected by using

$$c_{\mathrm{CEDAR}} = N_\pi / N_{\pi,\mathrm{tag}} \tag{15.11}$$

with $N_{\pi,\mathrm{tag}}$ being the number of events having a pion tag. As the mass dependence of kaon reaction differs from the one of pion reactions, this correction factor is calculated for each individual analysis bin. The kaon tag efficiency is determined by using the $K^- \to \pi^-\pi^0$. This channel features not only a larger branching fraction but also a better acceptance than the $K^- \to \pi^-\pi^0\pi^0$. Thus the number of available events is higher. Consequently the uncertainty of the measurement is smaller. This of course require modification of the event selection, which are discussed briefly.

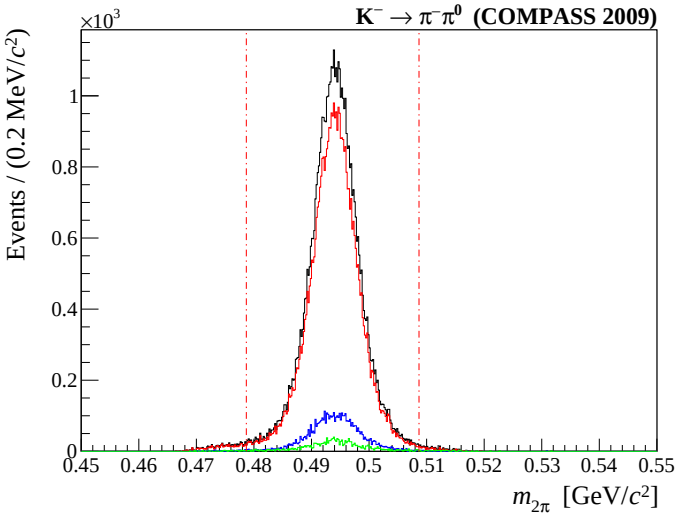

Figure 15.4: Invariant mass $m_{2\pi}$ of selected $K^- \to \pi^-\pi^0$ events (Black: All Events, Red: Beam tagged as Kaon, Green: Beam tagged as Pion, Blue: No decision).

15.2.1 $K^- \to \pi^-\pi^0$ – Reconstruction and Selection

Large extends of the reconstruction and selection of $K^- \to \pi^-\pi^0\pi^0$ can also be applied to the selection of $K^- \to \pi^-\pi^0$ due to similarities. Thus the event selection described in section 15.1.1 is taken as starting point and the discussion restricts to the necessary modifications.

There is only one π^0 in the final state. Consequently, the minimum required number of photons, i.e. electromagnetic showers, reduces to two. Each of these showers is still required to deposit more than 2 GeV in ECAL2. Similar to the selection of the three-pion final state only the two showers, which have the highest energy deposits, are considered. The pion mass cut is applied to the invariant mass of the $\gamma\gamma$ system, which is calculated with the energy conservation constrained applied. Equation 8.19 is adapted to the reduced number of photons.

$$u = \frac{E_{beam} - E_{\pi_f^-}}{\sum_{i=1}^{2} E_{\gamma,i,rec}}. \tag{15.12}$$

Besides the adaption of the reconstruction presented here the selection remains unchanged.

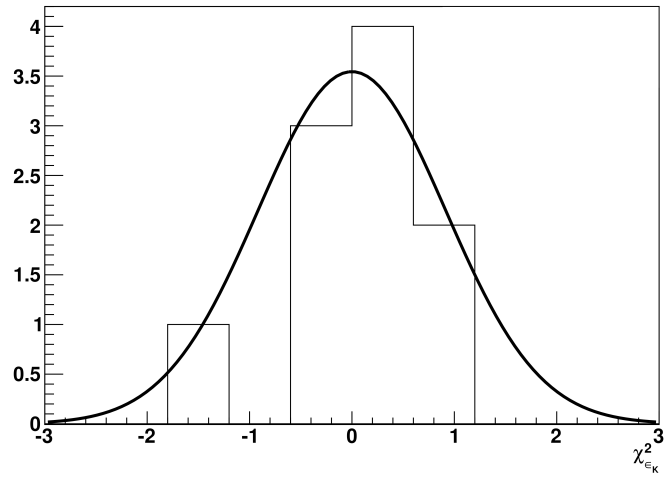

Figure 15.5: The χ^2-distribution of the kaon tag efficiency over time.

15.2.2 Kaon Tag Efficiency

Studying the mass distribution of the selected $K^- \to \pi^-\pi^0$ events (figure 15.4) a clean kaon decay peak is observed. The background beneath the peak is negligible. This allows to determine the efficiency of the beam particle tagging for kaon by looking at the decomposition of the spectrum regarding beam PID. Concentrating on the mass region around the peak center as indicated, it can be assumed, that independently from the measured beam particle ID the beam particle indeed is a K^-. On this base the efficiency of identifying a beam kaon as a kaon is

$$\epsilon_{\mathrm{CEDAR},K} = \frac{N_{\mathrm{kaon}}}{N_{\mathrm{tot}}} = 86.9\pm0.4\,(\mathrm{stat}). \tag{15.13}$$

The stability of this value is studied by dividing the data sample taken in 2009 into ten smaller samples of roughly equal amount of events. Each of these event sample corresponds to a continuous time period of the Primakoff run 2009. For each of the ten consecutive periods the kaon tag efficiency $\epsilon_{\mathrm{CEDAR},K,i}$ is determined and the

$$\chi^2 = \frac{\left(\epsilon_{\mathrm{CEDAR},K,i} - \epsilon_{\mathrm{CEDAR},K}\right)^2}{\epsilon_{\mathrm{CEDAR},K}} \tag{15.14}$$

is calculated. The χ^2 distribution of this independent measurements (see figure 15.5) is fitted with a Gaussian function, which reveals a width of $\sigma = 0.9\pm0.4$. This is in good agreement with the hypothesis of having statistical fluctuations, where $\sigma = 1$ is expected. As no systematic effects are observed one can conclude, that the tagging efficiency is stable throughout the 2009 Primakoff run and is only subjected to statistical fluctuations. The number $N'_{m,K}$ of kaon events, which con-

tribute in a certain mass bin, is then given by the quotient of the number of events $N_{m,K}$ with a kaon tag and the kaon tag efficiency $\epsilon_{\mathrm{CEDAR},K}$.

$$N'_{m,K} = \frac{N_{m,K}}{\epsilon_{\mathrm{CEDAR},K}} \tag{15.15}$$

15.3 t and m Dependence of the Primakoff Reactions

The Weizsäcker-Williams equivalent photon method connects the electromagnetic field of the nucleus with a flux of quasi free photons. The flux of photon described by this approximation has to be taken into account for the measurement of pion-photon reactions in pion-nucleus scattering. The t and m dependence of is given by [KF08, AAA+14b]

$$d_{\mathrm{WW}}(m,t) = \frac{2\alpha Z^2}{\pi} \frac{t'}{(t'+t_{\mathrm{min}})^2} \frac{m}{m^2 - m_\pi^2} F^2(t'+t_{\mathrm{min}}) \tag{15.16}$$

with Z being the charge of the the nucleus, $\alpha = 1/137$ the coupling strength and m_π the mass of the pion (from [B+12]). t_{min} is denoting the minimum squared transferred momentum.

$$t_{\mathrm{min}} = \frac{\left(m^2 - m_\pi^2\right)^2}{4 \cdot \left|\vec{p}_{\mathrm{beam}}\right|^2} \qquad \text{with } \left|\vec{p}_{\mathrm{beam}}\right| \approx E_{\mathrm{beam}}/c \tag{15.17}$$

t is then composed from the minimum squared transferred momentum and the reduced squared transferred momentum $t' = t - t_{\mathrm{min}}$ (see section 3.3). E_{beam} is the beam energy. $F(t)$ is the form factor of the nucleus. Here the elastic form factor

$$F(t) = \frac{3\left(\sin\left(\frac{tR}{\hbar c}\right) - \frac{tR}{\hbar c}\cos\left(\frac{tR}{\hbar c}\right)\right)}{\left(\frac{tR}{\hbar c}\right)^3}. \tag{15.18}$$

is used. $R = r_0 \cdot A^{1/3}$ denotes the radius of the nucleus. In order to calculate the cross section $d_{\mathrm{WW}}(m,t)$ has to be integrated over the mass m and transferred momentum t of each analysis bin. Thus the integral $D_{m,t}$ is considered. The indices m and t denote the analysis bin, which is defined by its borders m_{low}, m_{high}, t'_{low} and t'_{high}.

$$\begin{aligned} D_{m,t} = \int_{E_{\mathrm{beam}}} \int_{m_{\mathrm{low}}}^{m_{\mathrm{high}}} \int_{t'_{\mathrm{low}}}^{t'_{\mathrm{high}}} \mathrm{d}E_{\mathrm{beam}} \mathrm{d}m \, \mathrm{d}t' \\ \overline{\varrho}_{\mathrm{beam}}\left(E_{\mathrm{beam}}\right) \frac{2\alpha Z^2}{\pi} \frac{t'}{(t'+t_{\mathrm{min}})^2} \frac{m}{m^2 - m_\pi^2} F(t'+t_{\mathrm{min}}) \end{aligned} \tag{15.19}$$

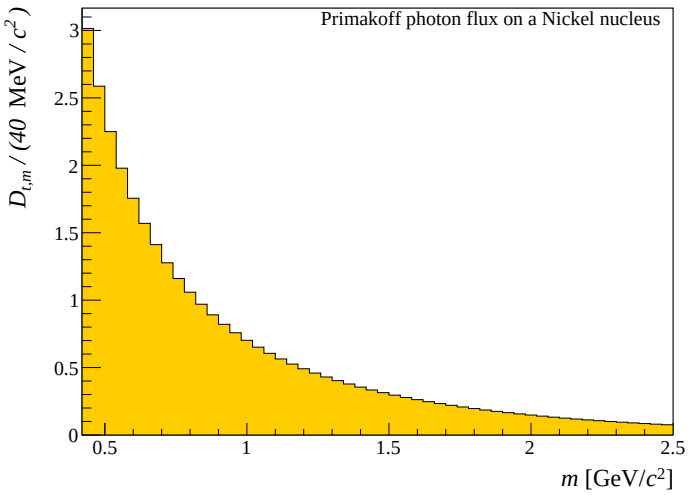

Figure 15.6: Dependence of $D_{m,t}$ calculated for $t'_{\text{low}} = 0$ and $t'_{\text{high}} = 0.002\,(\text{GeV}/c)^2$ on the three-pion mass $m_{3\pi}$. The calculation is done in narrow mass bins with $\Delta m = 40\,\text{MeV}/c^2$.

The integration over the beam energy E_{beam} respects the spread of the beam energy.

$$\overline{\varrho}_{\text{beam}}(E) = \frac{\varrho_{\text{beam}}(E)}{\int_{E_{\text{beam}}} \mathrm{d}E'\, \varrho_{\text{beam}}\,(E')} \tag{15.20}$$

is the normalized distribution of the beam energy distribution. The distribution of the beam energy $\varrho_{\text{beam}}(E)$ of the beam energy is in the current analysis approximated using the Gaussian function[3]

$$\varrho_{\text{beam}}(E) = \exp\left(-\frac{\left(E - \overline{E}_{\text{beam}}\right)^2}{2 \cdot \sigma^2_{\text{beam}}}\right) \tag{15.21}$$

with the mean beam energy $\overline{E}_{\text{beam}} = 191\,\text{GeV}$ and the width of $\sigma_{\text{beam}} = 2.0\,\text{GeV}$. For the given analysis the minimum $t'_{\text{low}} = 0$ and maximum $t'_{\text{high}} = 0.002\,(\text{GeV}/c)^2$ of the transferred momentum $t' = t + t_{\text{min}}$ is given by the range of t' considered for the PWA in mass bins. The mass range is chosen accordingly to the mass bin of the PWA. Figure 15.6 shows the dependence of $D_{m,t}$ on the invariant mass of the final state particle.

[3]The change introduced by using a Gaussian function instead of a delta function $\varrho_{\text{beam}}(E) = \delta\left(E - \overline{E}_{\text{beam}}\right)$ is in the order of one ($m_{3\pi} \approx 0.44\,\text{GeV}/c^2$) to four ($m_{3\pi} \approx 2.3\,\text{GeV}/c^2$) per-mil. Thus, a more detailed description of the beam is considered to have no significant impact.

15.4 Correction to the PWA Measurement

So far we discussed ingredients, which enters the calculation of the cross section, no matter weather the t' spectrum is fitted or the partial-wave analysis is applied. However, if the much more complex partial-wave analysis is used to determine the cross section, some specific effects have to be taken into account.

15.4.1 Bin Migration

Experimental uncertainties lead to an effect of bin migration, i.e. the measured m_f and t' differs from their real values. Therefore events migrate in or out of a certain analysis bin and leak into neighboring bins. The mass dependence is assumed to be shallow, thus in good approximation the net migration between neighboring mass bins vanishes. However this is not the case for leakage in t'. Especially for Primakoff events, which occur at very small values at t', a significant fraction of events will appear at higher values of t', while practically no events migrate from high to low t'. This effect is studied using a Monte-Carlo event sample. The t' distribution of the Monte-Carlo events follow the Weizsäker-Williams approximation. Events with $t'_{\text{sim}} \leq 0.0256\,\text{GeV}^2c^{-2}$ are generated and are required to fulfills all selection criteria except the t' cut. The correction factor, which accounts for the bin migration in t' is then given by the ratio of events with simulated transferred momentum $t'_{\text{sim}} \leq 0.002\,\text{GeV}^2c^{-2}$ and event with reconstructed transferred momentum $t'_{\text{rec}} \leq 0.002\,\text{GeV}^2c^{-2}$.

$$c_{\text{mig},m} = \frac{N_{\text{acc}}(t'_{\text{sim}} \leq 0.002\,\text{GeV}^2c^{-2})}{N_{\text{acc}}(t'_{\text{rec}} \leq 0.002\,\text{GeV}^2c^{-2})} \tag{15.22}$$

The index m indicates, that this fraction is not evaluated at global scale, but for each individual analysis bin.

15.4.2 Diffractive Background

Considering small values of t', the $M = 1$ waves are mainly produced by Primakoff reaction. However, contribution from diffractive dissociation remains. This contribution is an experimental background, which has to be considered, when measuring the radiative cross section. Studying the t' dependence of the $M = 1$ and also $M = 0$ by a partial-wave analysis in t' bins give access to this contribution (see section 13.2.2) and allows to subtract the introduced background. To obtain a quantitative description the different contributions and possible interference has to be modeled. This has been achieved for the t' spectrum of the total wave intensity of the chiral waves near the three-pion threshold (see figure 13.13). Following equation. 13.2 the correction factor c_{BG}, which has to be applied for the present measurement, is given by the fraction of Primakoff events

contributing to the observed intensity.

$$c_{\mathrm{BG}} = \mathfrak{F}_{\mathrm{Primaoff}}(0, 0.002\,\mathrm{GeV}^2/c^2) = 0.964 \tag{15.23}$$

15.4.3 Accounting for Model Leakage

Aiming to measure the differential cross section of $\pi^-\gamma \to \pi^-\pi^0\pi^0$, the leakage study presented in chapter 14 allows to determine a compensation factor, which accounts for leakage from chiral waves to waves with spin projection $M = 0$. This compensation factor is determined by the total intensity, i.e. square of the coherent sum of all amplitudes, divided by the $M = 1$ total waves intensity. In the relevant mass range from $0.54\,\mathrm{GeV}/c^2$ to $0.78\,\mathrm{GeV}/c^2$ the $M = 1$ total wave intensity is given by the sum of the chiral waves with positive and negative reflectivity. The best case (bc) is considered applying the model featuring double ρ exchange to the event sample, which is based on the corresponding calculation. In this case the resulting leakage fluctuates around a common value and no systematic are observed. A compensation factor for the model leakage is determined by the weighted mean of the leakage within each bin in the given mass range.

$$c_{\mathrm{leak,bc}} = 1.18 \pm 0.06 \tag{15.24}$$

The uncertainty is calculated using Gaussian error propagation. The leakage from $M = 1$ to $M = 0$ can be explained by experimental resolution washing out the ϕ_{TY} behavior of $M = 1$ waves. Thus a contribution from $M = 1$ amplitude with flat ϕ_{TY} dependence is observed. It is not expected, that experimental resolution can introduce non flat ϕ_{TY} components of $M = 0$ waves. This is especially true as the acceptance does not show a ϕ_{TY} dependence. Thus the leakage from $M = 0$ to $M = 1$ is believed to be small and therefore neglected.

The factor, which is obtained by applying fit models with different flavors to their corresponding event sample, is similar for all flavors of chiral waves. However looking at the case, where the simulated event sample is fitted with a different flavored model, the model leakage and therefore the required compensation factor can become large. Thereby a worst case scenario is considered to be the fit to the double ρ exchange event sample using the leading-order model. In this case a leakage compensation factor

$$c_{\mathrm{leak,wc}} = 2.30 \pm 0.15 \tag{15.25}$$

is found. However, all advanced fit models group together. Thus leakage is similar for these models. It is hard to imagine, that the leakage for the presented chiral models will become smaller, when applied to a event sample, which exploits chiral physics beyond the calculations presented here. The $c_{\mathrm{leak,bc}}$ should be regarded as a lower limit of the required correction. However, accounting for the similar leakage of the advanced fit model, it is also regarded as realistic value.

Consequently it is directly applied to the measurement. $c_{\text{leak,bc}}$ on the other hand is used to determine the upper bound of possible model leakage and the necessary correction.

Last but not least it should be mentioned, that summing over positive and negative reflectivity, the model leakage between the different reflectivities is accounted and does not require further corrections.

15.5 The Differential Cross Section

The differential cross section of $\pi^-\gamma \to \pi^-\pi^0\pi^0$ near the three-pion threshold is given by

$$\sigma(\pi^-\gamma \to \pi^-\pi^0\pi^0) = \frac{I_{\gamma,m} \cdot c_{\text{CEDAR},m} \cdot c_{\text{BG}} \cdot c_{\text{mig},m} \cdot c_{\text{leak}}}{D_{m,t} \cdot \int \mathcal{L}_\pi \mathrm{d}t}. \tag{15.26}$$

where the intensity $I_{\gamma,m}$ is either given by the total wave intensity of $M = 1$ amplitudes or by the acceptance corrected number of events determined by the fit to the observed t' distribution. In the second case the correction factors c_{BG}, $c_{\text{mig},m}$ and c_{leak} do not apply and are consequently set to one. Figure 15.7 shows the cross section measured with this method. For comparison the prediction from ChPT are also shown.

The resulting cross section lies between LO and NLO prediction being in better agreement with the NLO predictions. Still the uncertainty of the measured points is comparable large. Thus prediction, which accounts for ρ exchange, are still in agreement with the single points. However, the points lie on a rather smooth curve showing only small fluctuations. Thus a systematic deviation from this prediction is observed, which is not within the range of the common systematic uncertainty. This is a hint for possible contribution of effects, which are not yet modeled. This hypothesis is strengthen by the leakages studies for the partial-wave analysis. This studies, applying the currently available chiral models is able to produce a behavior, which is similar, but not identical, to the behavior observed studying the COMPASS data.

The result obtained by applying the partial-wave analysis (see chapter 13) is shown in figure 15.8. In general the cross section measured with this technique is smaller, then the one obtained by fitting the t' spectrum. However as discussed the systematic uncertainty towards a higher cross section arising from model leakage is huge. In the best case (bc) the uncertainty introduced by leakage is described by the solid blue area. The hatched area describes the upper limit given by the worst case (wc). Towards lower values the uncertainty is much smaller. Thus in conjunction with the results of the leakage study (see chapter 14), which shows that the observed angular dependencies are not reproduced by leading-order ChPT calculation, there is a strong preference for chiral models based on calculations beyond leading-order. The fact, that the observed fit behavior could

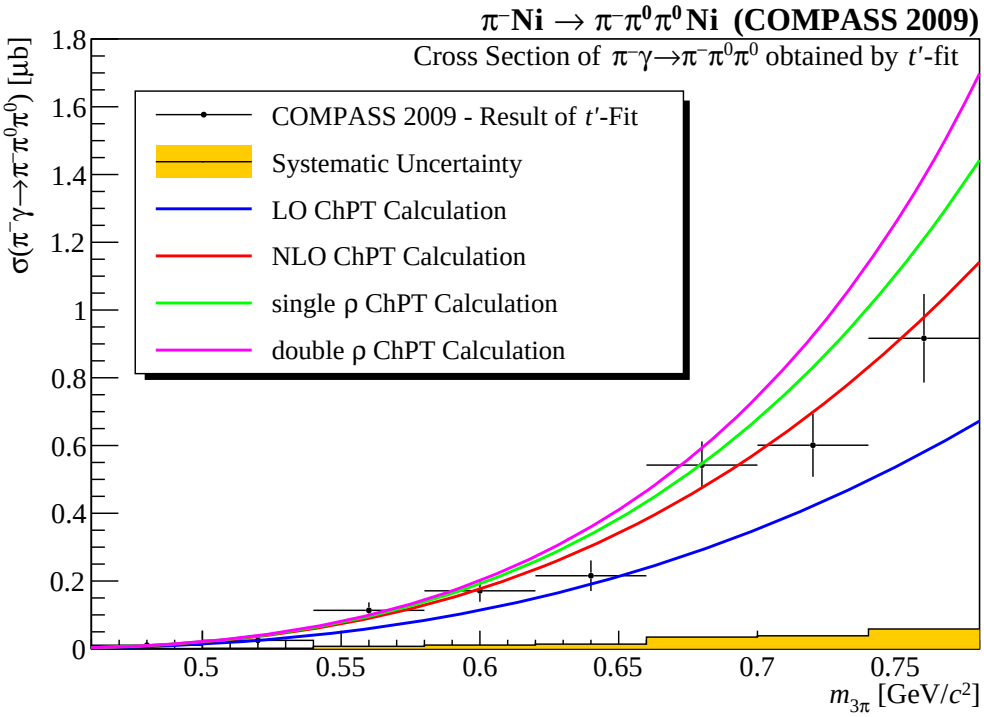

Figure 15.7: Total differential cross section measured by fitting the observed t' spectrum of $\pi^-\text{Ni} \to \pi^-\pi^0\pi^0\text{NI}$ events. The blue, red, green and magenta lines show the predictions of the ChPT calculation in leading order, next-to-leading order, including single and double ρ exchange, respectively. The error bars give the statistical uncertainty of the measurement, while systematic uncertainty coming from the determination of the luminosity is indicated by the yellow curve.

not be exactly reproduced with the MC event samples, delivers further evidence for contributions of effects beyond the available models. However, at this point, it should be stressed again, that the investigated chiral models are superior to isobaric models, when it comes to describe the angular distributions observed in the COMPASS data. Accounting for all systematic effects, not only the cross section predicted by NLO calculations but also the slightly higher prediction, which also accounts for ρ exchange, are in agreement with the measurement.

Last but not least one should mention, that both measurements of the cross section of $\pi^-\gamma \to \pi^-\pi^0\pi^0$ agree within their uncertainties. One should keep in mind, that the fit to the t' identifies Primakoff events by the properties of the production mechanisms, while the partial-wave analysis relies on properties of the decay. Thus these two method represent two distinguished approaches to identify pion-photon reactions, which, however, share the normalization via kaon decays and the selection of events. Thus a correction, which effects the measurement of the luminosity, will affect all measured point in the same way.

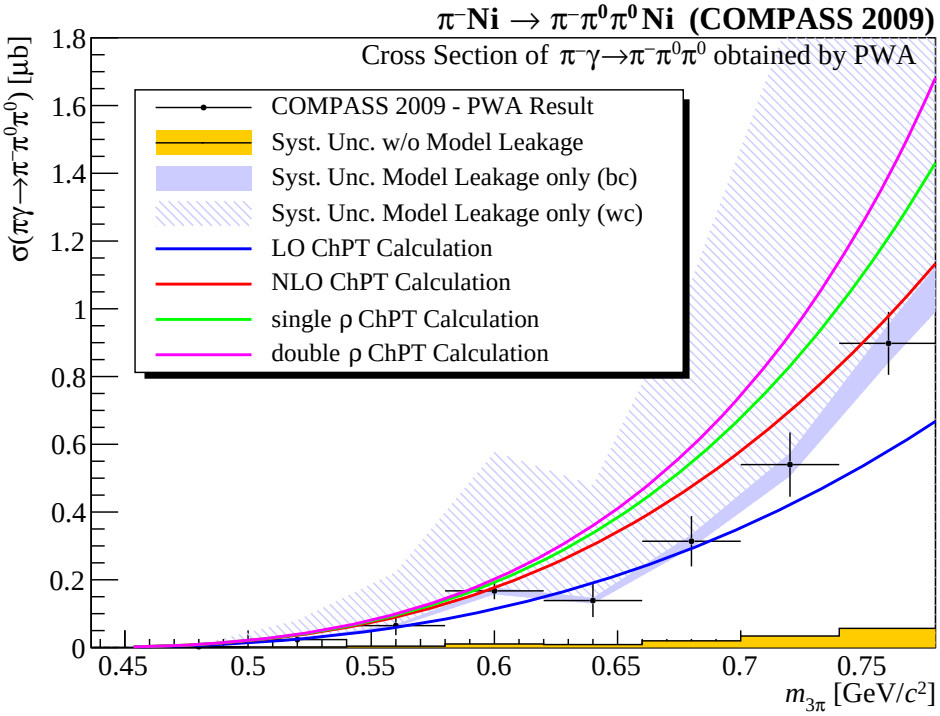

Figure 15.8: Total differential cross section measured by applying a PWA to the $\pi^-\mathrm{Ni} \to \pi^-\pi^0\pi^0\mathrm{NI}$ event sample . The blue, red, green and magenta lines show the predictions of the ChPT calculation in leading order, next-to-leading order, including single and double ρ exchange, respectively. The error bars give the statistical uncertainty of the measurement, while systematic uncertainty excluding model leakage effecting all data point in the same way is given by the yellow curve. The light blue area is showing the uncertainty due to model leakage, while the solid area indicate the uncertainty considering only the optimal case the hatched area includes also the worst case scenario.

Chapter 16

Conclusion

In 2009 a period of roughly two weeks was dedicated to a measurement of Primakoff reactions at COMPASS. For this measurement, a digital event trigger was developed, which enriches the sample of events with high energetic photons in the forward direction. The trigger scheme is not only suitable for the measurement of the pion polarizibility, for which it was optimized, but also for the measurement of events with π^0s in the final state. A clean sample of exclusive $\pi^-\pi^0\pi^0$ events is selected. A partial-wave decomposition of events in the low transferred momentum $t'\leq 0.002\,\mathrm{GeV}^2/c^2$ is used to analyze the event sample. Besides isobar amplitudes, partial-waves, which are based on calculations of $SU(2)$ chiral perturbation theory, are introduced and successfully used to describe the observed angular correlations. The ChPT calculations are available in leading order and next-to-leading order approximation as well as higher order approximations, which account for the exchange of up to one or two ρs. Iindependent from the flavor of the chiral it is found, that models, which include the newly introduced chiral amplitudes, are better suited to describe the data than models, which restrict to isobar amplitudes. It is shown, that the partial-wave analysis is able to resolve amplitudes, which contribute with a few per-mil. This shows, that not only a well defined wave-set is found, but also a good understanding of the experimental setup is achieved.

This finding is strength by the findings of extensive Monte-Carlo studies, which are used to determine systematic effects. This studies reproduce the model leakage between corresponding amplitudes with positive and negative reflectivity quantitatively. The same studies are also used to get further insights to the behavior of the different flavors of the chiral waves. Therefore events sample, which follow the angular distribution of different flavors of the chiral amplitude, are fitted with all available chiral models. This studies reveal, that based on the available experimental resolution chiral amplitudes and models, which include calculations beyond leading order, cannot be distinguished. The fits of event samples based on advanced chiral wave show a similar behavior as observed, when fitting the COMPASS data, while the event sample, which is based on the

leading order calculations, is not able to reproduce the observed behavior.

Analyzing the decay $K^- \to \pi^-\pi^0\pi^0$ of kaons, which are contained in the beam, the integrated luminosity is determined. Subsequently, the differential cross section $\pi^-\gamma \to \pi^-\pi^0\pi^0$ is obtained by combining the results of the partial-wave decomposition and the measurement of the luminosity. Using the same final state for both measurements systematic effects, which are not directly connected to the kinematic of individual events, cancel out. A complementary determination of the Primakoff contribution to the observed spectrum is achieved by analyzing the t' spectrum. This measurement concentrate on the production signature of Primakoff event distribution. The partial-wave decomposition, on the other hand, investigates the phase-space distribution of final state particles. The results of both measurements are within the given uncertainties compatible with each other. The measurements of the cross section $\pi^-\gamma \to \pi^-\pi^0\pi^0$ are compared to the prediction of chiral perturbation theory, which are available in the same four flavors as the chiral waves. Accounting for the uncertainties, the predictions of the next-to-leading order calculation matches the measurements best. Giving the large systematic uncertainty prediction from ChPT calculation, which accounts for the exchange of one or event two ρ are also compatible with the PWA results. Considering leading-order prediction, the situation is different. The systematic uncertainties towards smaller values are comparable small. Thus even-though some of the measured points are best compatible with the LO prediction, considering others the the deviation of measurement and leading-order prediction is slightly larger than the three sigma confidence level. Additionally most measured points are on a rather smooth curve, which roughly follows the ChPT predictions. Thus a systematic deviation is observed. Combining this results with the results of the partial-wave analysis and the study of systematic effects, which revealed that the observed angular distribution differs from the ones expected from LO ChPT calculations, the hypothesis of observing a leading order chiral amplitude can be rejected.

Most of the features, which are observed in the partial-wave decomposition of the recorded data, are reproduced, when studying Monte-Carlo sample based on ChPT calculation beyond leading order. One feature, however, is not. The recorded data revealed, that below $m_{3\pi} = 0.78\,\mathrm{GeV}/c^2$ all chiral models, including the leading order model, show similar intensity in the chiral waves. In the Monte-Carlo study, on the other hand, the leading order model shows a reduced intensity due to model leakage. The possibility, that this is caused by unaccounted properties of the apparatus, has been intensely studied, but no evidence are found. Thus it is likely caused by unaccounted physical effects. On the one hand this might be caused by missing contributions, i.e Feynman diagrams, to the chiral amplitude. On the other hand, the presence of strong processes may play an important role. The observed discrepancy may be caused by interference of strong and radiative production. This effects, which are clearly observed at higher masses, are currently not accounted due to the lack of a suitable model.

Being able to describe this interference quantitatively, also the radiative width of the observed radiative produced resonance can be determined.

Near the three-pion threshold no resonance exist. Thus not only radiative processes but also processes of the strong force should be described with non-resonant amplitudes. In case of the strong force, this processes are described by the Deck effect. This effect could analog to the chiral amplitude, be introduced to the partial-wave decomposition and potential replace several isobar waves. However, the currently available calculations treating the Deck effect are restricted to proton targets. Taken into account, that the Deck effect and its parametrization is under discussion and investigation for many years, the development of a suitable parametrization is beyond the scope of the thesis. Still it should be mentioned, that the use of such an amplitude could potentially reduce systematic effects and uncertainties.

The systematic uncertainties contribute significant to the uncertainty of the measurement. Thus for possible future measurements an important aspect would be to reduce the systematic uncertainties by improving the experimental setup. Obviously an improvement of calorimeter performance and vertex reconstruction would add. Additional it is observed, that the precise knowledge of the energy of the beam particles improve the quality of the measurement. Thus a beam momentum station, which allows to determine the energy of individual beam particles on a level below, the one achieved using the neural network, will help to reduce systematic uncertainties. Considering developments in detector technology, micro-pattern gaseous detector with pixel readout would allow to overcome the issue of interaction length.

Appendix A

Parmetrization of ρ-Exchange

In [EU02] the contribution of Feynman diagrams with a photon coupling to four pion are calculate for the production of a four pion final state in e^+e^- annihilation, i.e. $\gamma \to \pi\pi\pi\pi$. Due to the universality of this diagrams the same Feynman diagrams contribute to the pion-photon scattering $\pi\gamma \to \pi\pi\pi$. However as the given parametrization of this contribution is not well suited for the application, in the following the parametrization of the contribution of diagrams with a single ρ exchange and those featuring two ρ exchanges is given. The low energy constants, which are introduced to describe the ρ exchange, are the rest mass m_ρ of the ρ meson and the coupling constant g_ρ, describing the $\rho \to \pi\pi$ coupling. Using the Mandelstam variables introduced in 1.2, the following parametrization is provided by N. Kaiser. The contribution of diagrams featuring one ρ propagator is given by

$$
\begin{aligned}
A_1^{(\rho)} = \frac{1}{4m_\rho^2} \Bigg\{ & \frac{2}{3m_\pi^2 - s - t_1 - t_2} \Bigg[\frac{(2s + m_\pi^2 - 2s_1 - s_2 + t_2)(s - 2m_\pi^2 - s_2 + t_1)^2}{m_\rho^2 + s - 2m_\pi^2 - s_2 + t_1 - \Sigma_\rho\,(2m_\pi^2 - s + s_2 - t_1)} \\
& + \frac{(2s + m_\pi^2 - 2s_2 - s_1 + t_1)(s - 2m_\pi^2 - s_1 + t_2)^2}{m_\rho^2 + s - 2m_\pi^2 - s_1 + t_2 - \Sigma_\rho\,(2m_\pi^2 - s + s_1 - t_2)} \Bigg] \\
& + \frac{(m_\pi^2 + s - 2s_1 + 2t_2)(s - 2m_\pi^2 - s_2 + t_1)}{(m_\rho^2 + s - 2m_\pi^2 - s_2 + t_1 - \Sigma_\rho\,(2m_\pi^2 - s + s_2 - t_1))} \\
& + \frac{s_2(2s_1 + 2s_2 - 2s - t_2 - m_\pi^2)}{m_\rho^2 - s_2 - \Sigma_\rho(s_2)} + \frac{s_1(2s_1 - s + t_2)}{m_\rho^2 - s_1 - \Sigma_\rho(s_1)} \Bigg\}
\end{aligned}
\tag{A.1}
$$

with the complex selfenergy of the ρ meson

$$\begin{aligned}\Sigma_\rho(s) =& \frac{g_\rho^2 s}{24\pi^2}\left\{ 4m_\pi^2\left(\frac{1}{m_\rho^2}-\frac{1}{s}\right)-\left(1-\frac{4m_\pi^2}{s}\right)^{3/2}\ln\left(\frac{\sqrt{|s|}+\sqrt{|s-4m_\pi^2|}}{2m_\pi}\right)\right.\\ &+\left(1-\frac{4m_\pi^2}{m_\rho^2}\right)^{3/2}\ln\left(\frac{m_\rho+\sqrt{m_\rho^2-4m_\pi^2}}{2m_\pi}\right)\\ &\left.+\frac{i\pi}{2}\left(1-\frac{4m_\pi^2}{s}\right)^{3/2}\Theta\left(\frac{s}{m_\pi^2}-4\right)\right\}\end{aligned} \tag{A.2}$$

for $s<0$ or $s>4m_\pi^2$. $\Theta(x)$ denotes the heaviside function. $A_2^{(\rho)}$ is obtained by substitution of variables $s_1 \leftrightarrow s_2$ and $t_1 \leftrightarrow t_2$.

$$A_2^{(\rho)} = A_1^{(\rho)}|(s_1 \leftrightarrow s_2),\ (t_1 \leftrightarrow t_2) \tag{A.3}$$

The diagrams with two ρ propagators contribute with

$$\begin{aligned}A_1^{(\rho\rho)} =& \frac{(s-t_2)(s-2m_\pi^2-s_1+t_2)}{4\left[m_\rho^2-s_1-\Sigma_\rho(s_1)\right]\left[m_\rho^2-2m_\pi^2+s-s_1+t_2-\Sigma_\rho(2m_\pi^2-s+s_1-t_2)\right]}\\ &+\frac{2s_2^2+s_2(2m_\pi^2-5s+4s_1-2t_1-3t_2)+(s+t_1-2m_\pi^2)(2s+m_\pi^2-2s_1+t_2)}{4\left[m_\rho^2-s_2-\Sigma_\rho(s_2)\right]\left[m_\rho^2-2m_\pi^2+s-s_2+t_1-\Sigma_\rho(2m_\pi^2-s+s_2-t_1)\right]}\\ &+\frac{s-m_\pi^2}{m_\rho^2}+\frac{t_2-s}{4\left[m_\rho^2-s_1-\Sigma_\rho(s_1)\right]}+\frac{2m_\pi^2-s-t_2}{4\left[m_\rho^2-s_2-\Sigma_\rho(s_2)\right]}\\ &+\frac{t_2-s}{4\left[m_\rho^2-2m_\pi^2+s-s_1+t_2-\Sigma_\rho(2m_\pi^2-s+s_1-t_2)\right]}\\ &+\frac{2m_\pi^2-s-t_2}{4\left[m_\rho^2-2m_\pi^2+s-s_2+t_1-\Sigma_\rho(2m_\pi^2-s+s_2-t_1)\right]}\end{aligned} \tag{A.4}$$

and

$$A_2^{(\rho\rho)} = A_1^{(\rho\rho)}|(s_1 \leftrightarrow s_2),\ (t_1 \leftrightarrow t_2). \tag{A.5}$$

For the given analysis $m_\rho^2 = 30.4367 \cdot m_\pi^2$ and $g_\rho = 6.03$ are used.

Appendix B

PWA in Mass Bins: More Amplitudes

In chapter 13 the partial-wave analysis has been discussed and the intensity and phases of the most important waves are shown. The used wave-set however contains much more amplitudes. In order to give a more complete picture here the intensities of the remaining amplitudes as well as some selected phases are shown. However this is done without further discussion of the amplitude. Having different fit models, the color code introduced in 13 will be used. The different flavors of the chiral model, LO, NLO, ρ and $\rho\rho$ are drawn in black, red, blue and green, respectively. The isobaric reference model is shown in magenta.

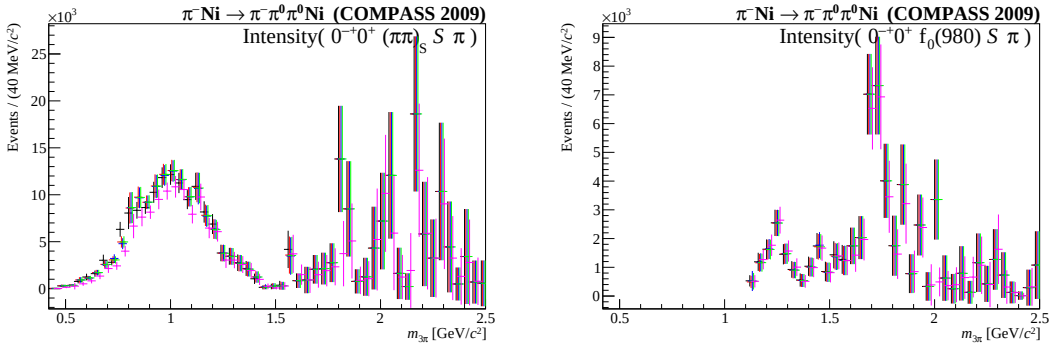

(a) Intensity($0^{-+}0^{+}\,(\pi\pi)_S\,S\,\pi$) (b) Intensity($0^{-+}0^{+}\,f_0(980)\,S\,\pi$)

Figure B.1: PWA in mass bins: More intensities (1).

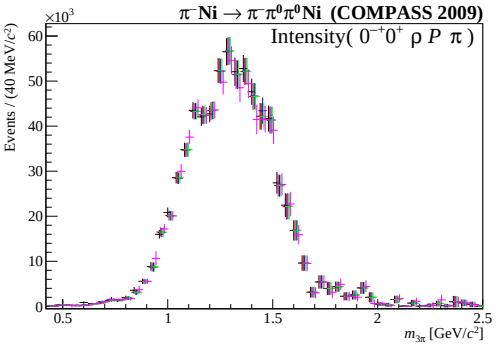

(a) Intensity($0^{-+}0^{+}\,\rho\,P\,\pi$)

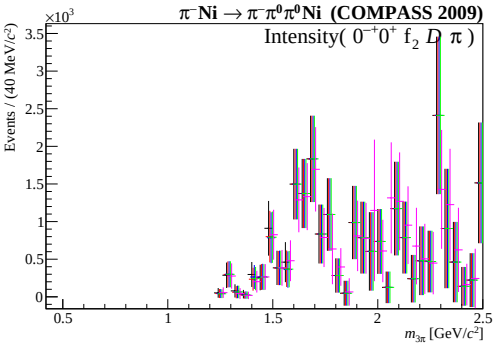

(b) Intensity($0^{-+}0^{+}\,f_2\,D\,\pi$)

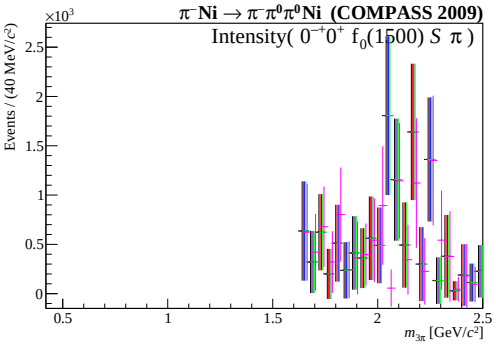

(c) Intensity($0^{-+}0^{+}\,f_0(1500)\,S\,\pi$)

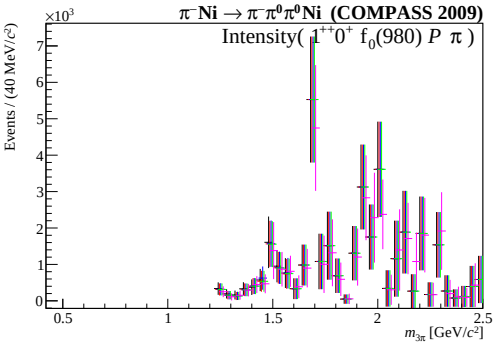

(d) Intensity($1^{++}0^{+}\,f_0(980)\,P\,\pi$)

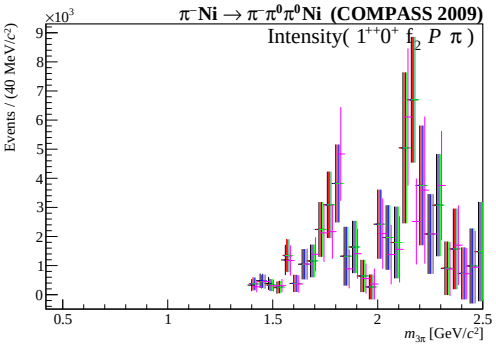

(e) Intensity($1^{++}0^{+}\,f_2\,P\,\pi$)

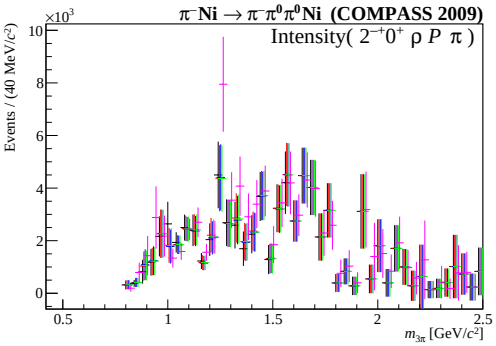

(f) Intensity($2^{-+}0^{+}\,\rho\,P\,\pi$)

Figure B.2: PWA in mass bins: More intensities (2).

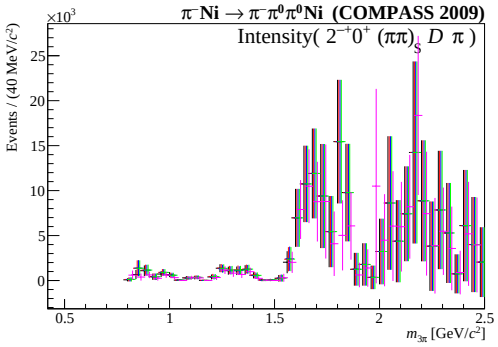

(a) Intensity($2^{-+}0^{+}\,(\pi\pi)_S\,D\,\pi$)

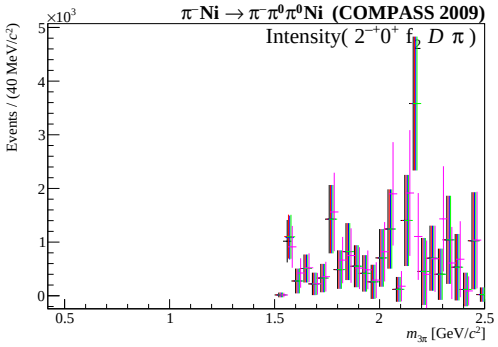

(b) Intensity($2^{-+}0^{+}\,f_2\,D\,\pi$)

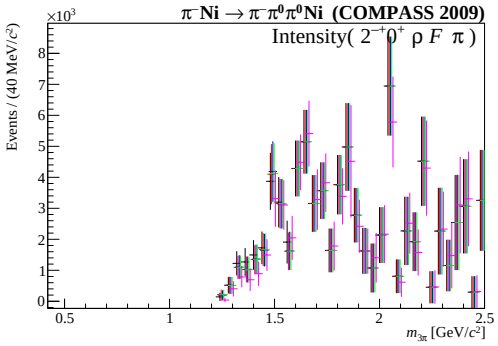

(c) Intensity($2^{-+}0^{+}\,\rho\,F\,\pi$)

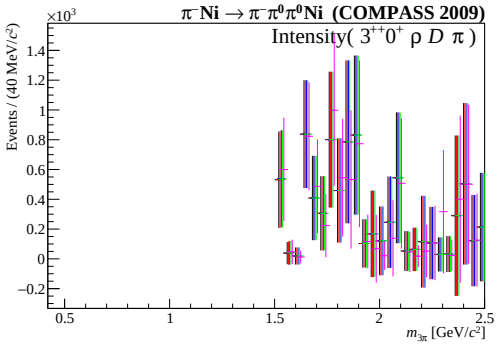

(d) Intensity($3^{++}0^{+}\,\rho\,D\,\pi$)

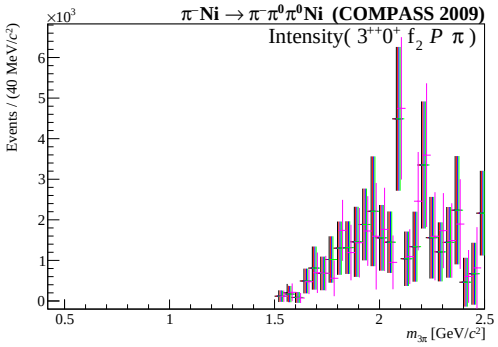

(e) Intensity($3^{++}0^{+}\,f_2\,P\,\pi$)

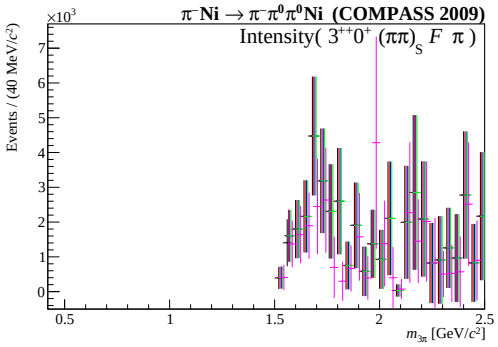

(f) Intensity($3^{++}0^{+}\,(\pi\pi)_S\,F\,\pi$)

Figure B.3: PWA in mass bins: More intensities (3).

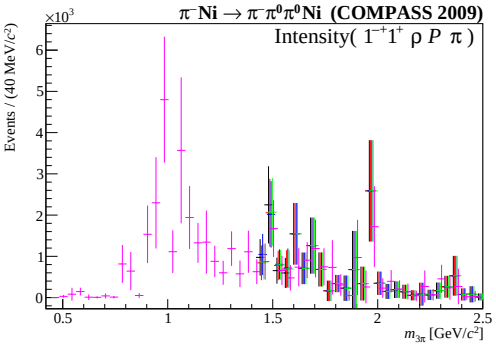

(a) Intensity($1^{-+}1^{+}\,\rho\,P\,\pi$)

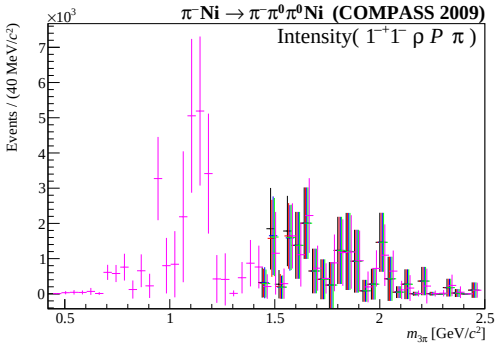

(b) Intensity($1^{-+}1^{-}\,\rho\,P\,\pi$)

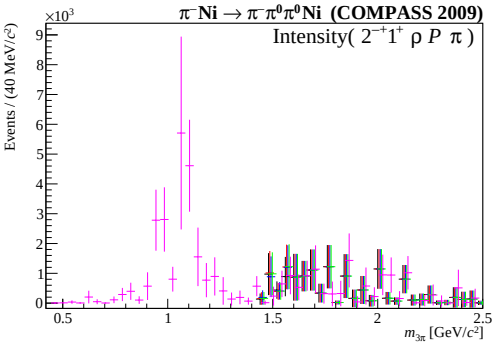

(c) Intensity($2^{-+}1^{+}\,\rho\,P\,\pi$)

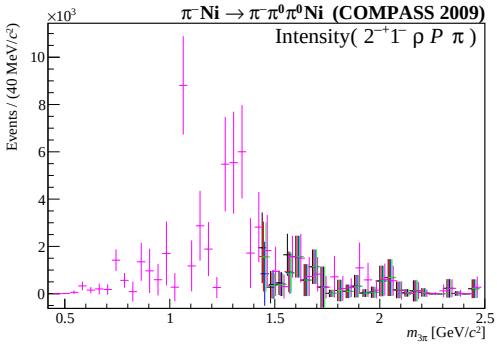

(d) Intensity($2^{-+}1^{-}\,\rho\,P\,\pi$)

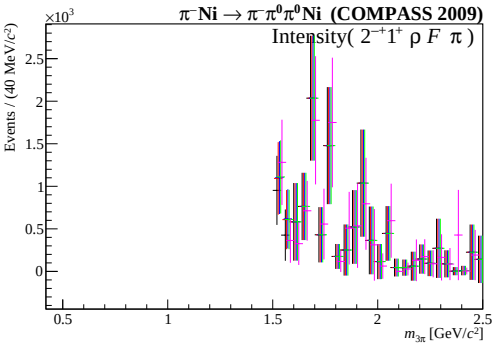

(e) Intensity($2^{-+}1^{+}\,\rho\,F\,\pi$)

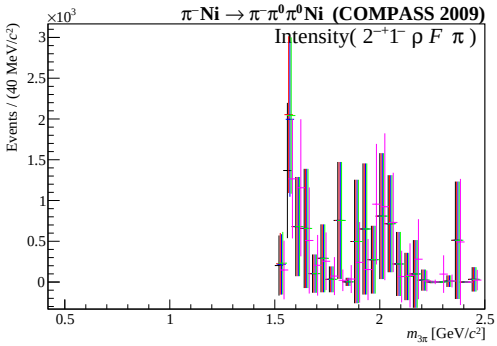

(f) Intensity($2^{-+}1^{-}\,\rho\,F\,\pi$)

Figure B.4: PWA in mass bins: More intensities (4).

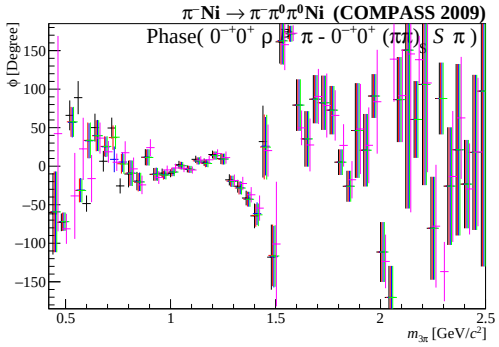

(a) Phase($0^{-+}0^{+}\,\rho\,P\,\pi\ -\ 0^{-+}0^{+}\,(\pi\pi)_S\,S\,\pi$)

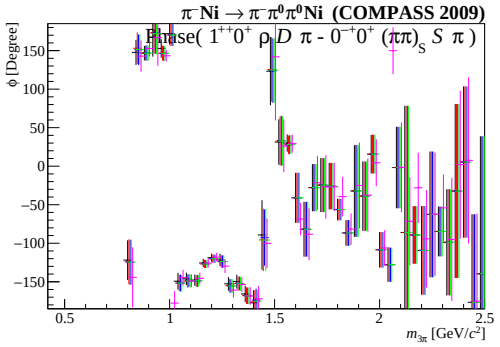

(b) Phase($1^{++}0^{+}\,\rho\,D\,\pi\ -\ 0^{-+}0^{+}\,(\pi\pi)_S\,S\,\pi$)

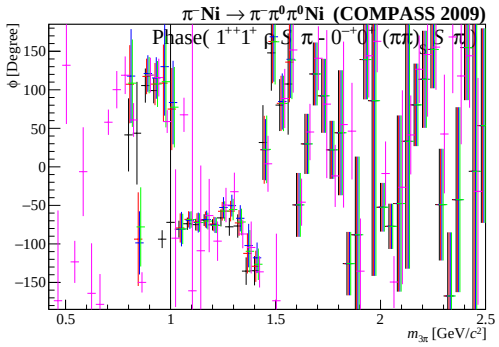

(c) Phase($1^{++}1^{+}\,\rho\,S\,\pi\ -\ 0^{-+}0^{+}\,(\pi\pi)_S\,S\,\pi$)

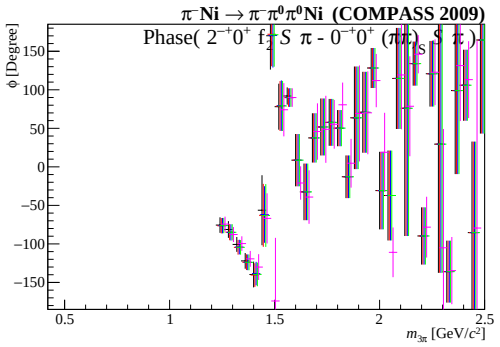

(d) Phase($2^{-+}1^{+}\,f_2\,S\,\pi\ -\ 0^{-+}0^{+}\,(\pi\pi)_S\,S\,\pi$)

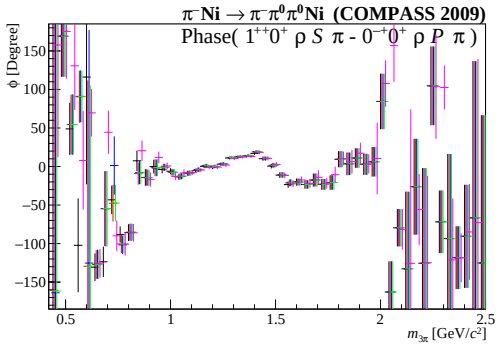

(e) Phase($1^{++}0^{+}\,\rho\,S\,\pi\ -\ 0^{-+}0^{+}\,\rho\,P\,\pi$)

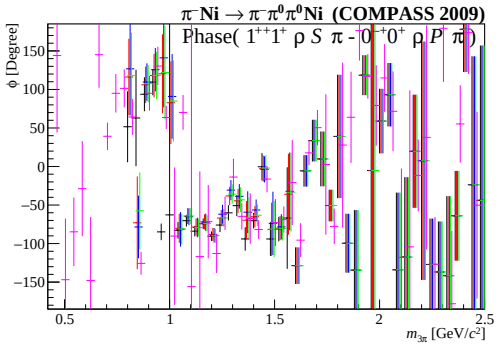

(f) Phase($1^{++}1^{+}\,\rho\,S\,\pi\ -\ 0^{-+}0^{+}\,\rho\,P\,\pi$)

Figure B.5: PWA in mass bins: More phases (1).

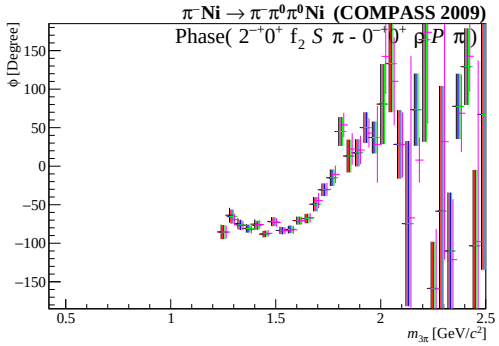

(a) Phase($2^{-+}0^{+}\, f_2\, S\, \pi\ -\ 0^{-+}0^{+}\, \rho\, P\, \pi$)

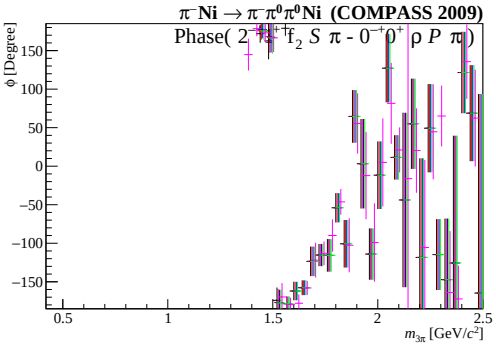

(b) Phase($2^{-+}1^{+}\, f_2\, S\, \pi\ -\ 0^{-+}0^{+}\, \rho\, P\, \pi$)

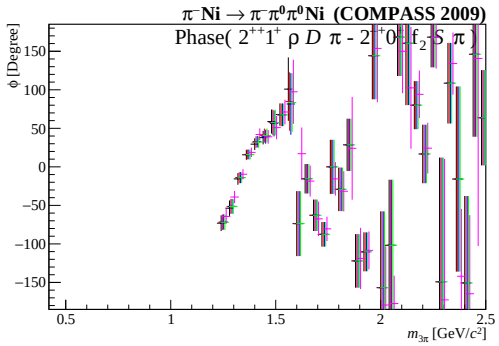

(c) Phase($2^{++}1^{+}\, \rho\, D\, \pi\ -\ 2^{-+}0^{+}\, f_2\, S\, \pi$)

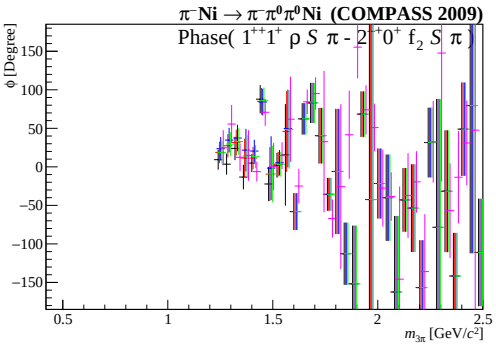

(d) Phase($1^{++}1^{+}\, \rho\, S\, \pi\ -\ 2^{-+}0^{+}\, f_2\, S\, \pi$)

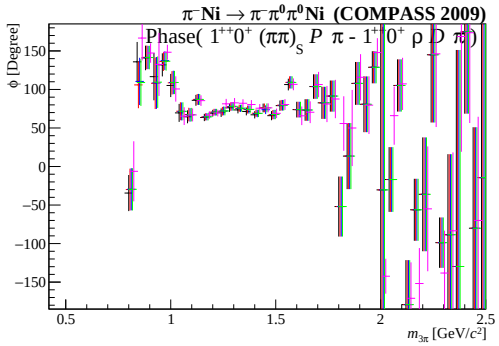

(e) Phase($1^{++}0^{+}\, (\pi\pi)_S\, S\, \pi\ -\ 1^{++}0^{+}\, \rho\, D\, \pi$)

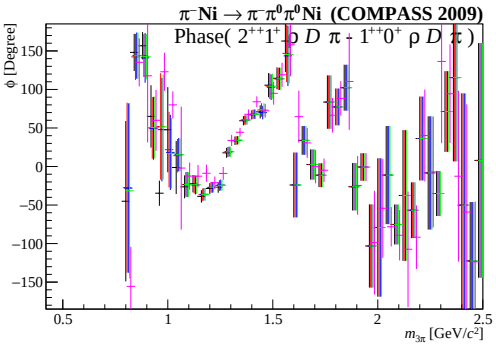

(f) Phase($2^{++}1^{+}\, \rho\, S\, \pi\ -\ 1^{++}0^{+}\, \rho\, D\, \pi$)

Figure B.6: PWA in mass bins: More phases (2).

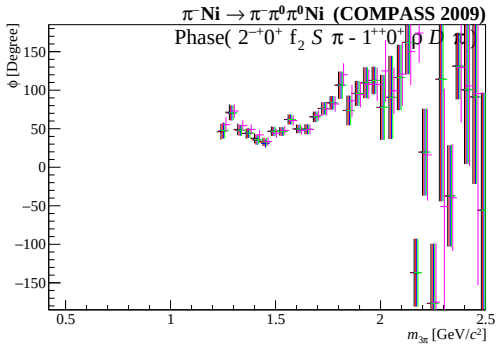

(a) Phase($2^{-+}0^{+}\, f_2\, S\, \pi\ -\ 1^{++}0^{+}\, \rho\, D\, \pi$)

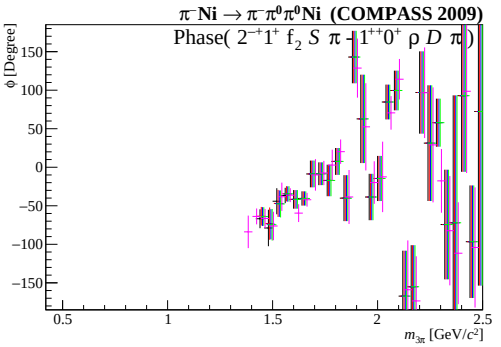

(b) Phase($2^{-+}1^{+}\, f_2\, S\, \pi\ -\ 1^{++}0^{+}\, \rho\, D\, \pi$)

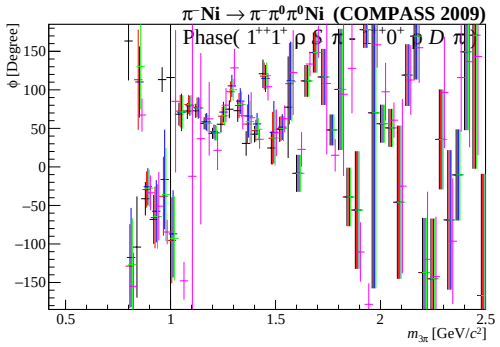

(c) Phase($1^{++}1^{+}\, \rho\, S\, \pi\ -\ 1^{++}0^{+}\, \rho\, D\, \pi$)

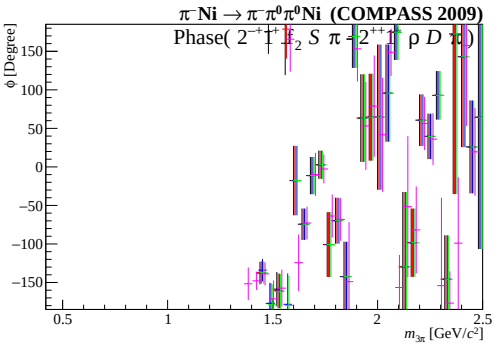

(d) Phase($2^{-+}1^{+}\, f_2\, S\, \pi\ -\ 2^{++}1^{+}\, \rho\, D\, \pi$)

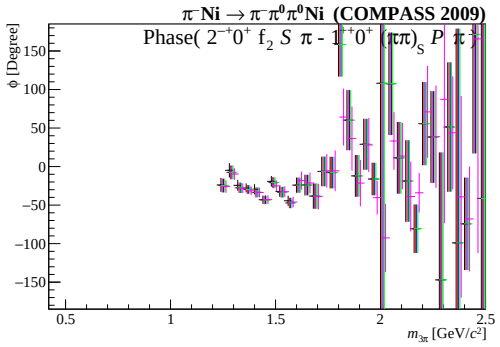

(e) Phase($2^{-+}0^{+}\, f_2\, S\, \pi\ -\ 21^{++}0^{+}\, (\pi\pi)_S\, P\, \pi$)

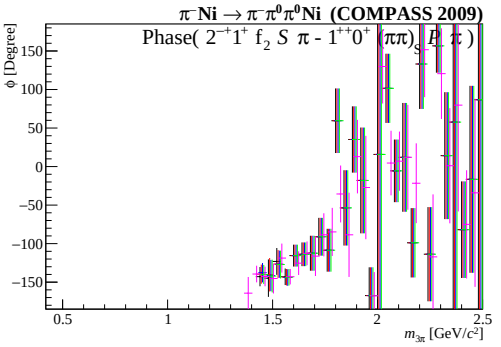

(f) Phase($2^{-+}1^{+}\, f_2\, S\, \pi\ -\ 21^{++}0^{+}\, (\pi\pi)_S\, P\, \pi$)

Figure B.7: PWA in mass bins: More phases (3).

Appendix C

Leakage Study with Extended Statistics

Similar to the leakage study, which is discussed in chapter 14 a leakage study based on a larger Monte-Carlo event samples has been conducted, aiming to study the effect of increased events sample. The event sample, however, do not follow the t' dependence of the Weizsäcker-Williams equivalent photon approximation. Due to computational limitation, the weights are imposed on the event sample, which is used to determine acceptance. This event sample follow a exponential t' distribution observed for recorded data. While the acceptance, as it does not depend on t', is not affected by this, the model leakage between positive and negative reflectivity waves is expected to be smaller. The observed behavior is in agreement with expectations and the previously discussed leakage study, revealing no further insides. Thus a detailed discussion is omitted. However for completeness in the following a selection of obtained intensities and total wave intensities are shown. The intensities are arrange according the chiral model used to generate the event samples. The fit models are marked with the color code introduced in chapter 14.

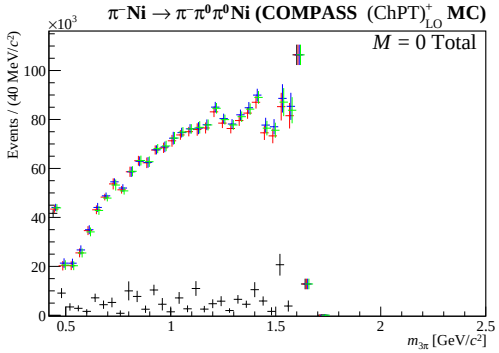

(a) $M = 0$ Total Waves Intensity

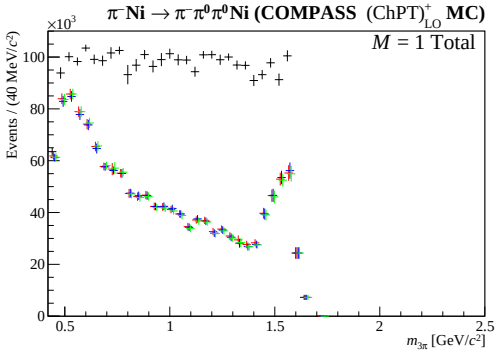

(b) $M = 1$ Total Waves Intensity

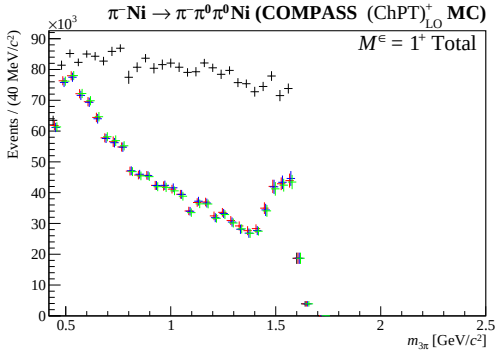

(c) $M^\epsilon = 1^+$ Total Waves Intensity

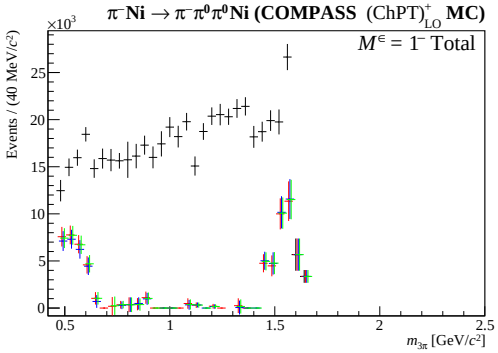

(d) $M^\epsilon = 1^-$ Total Waves Intensity

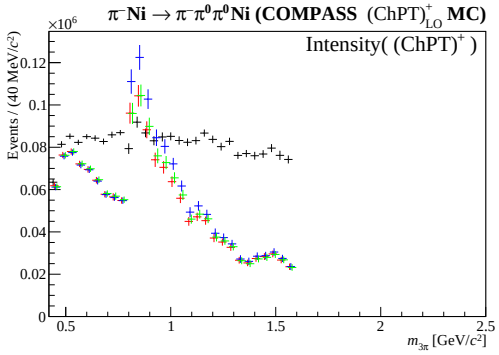

(e) Intensity($(\mathrm{ChPT})^+$)

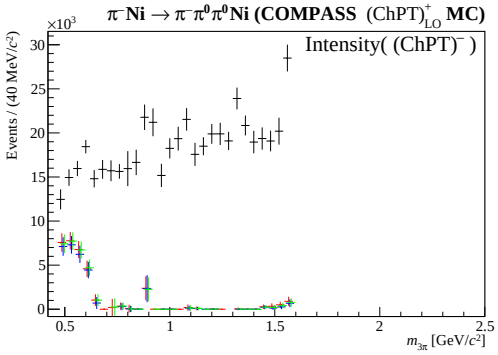

(f) Intensity($(\mathrm{ChPT})^-$)

Figure C.1: Intensities of coherent sums of waves as well as the chiral waves obtained with the extended LO event sample. The different colors introduced in chapter 14 refer to different fit models. Please see the text for more details.

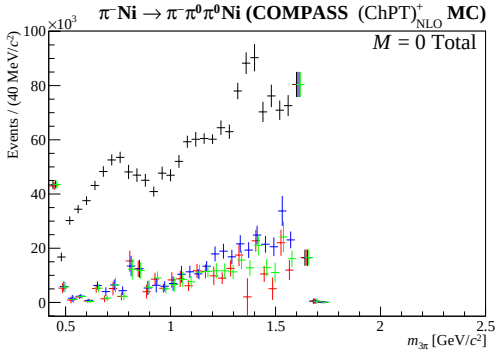

(a) $M = 0$ Total Waves Intensity

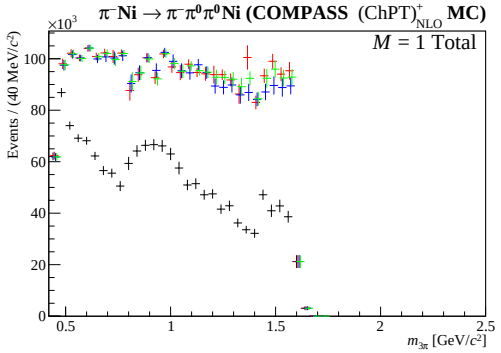

(b) $M = 1$ Total Waves Intensity

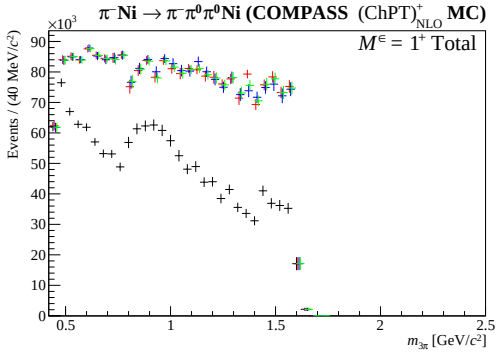

(c) $M^\epsilon = 1^+$ Total Waves Intensity

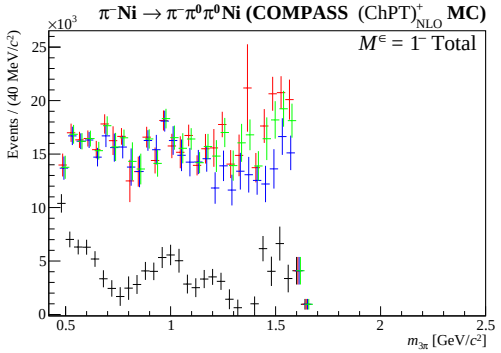

(d) $M^\epsilon = 1^-$ Total Waves Intensity

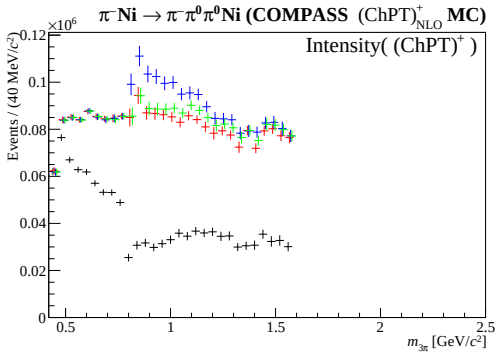

(e) Intensity($(\mathrm{ChPT})^+$)

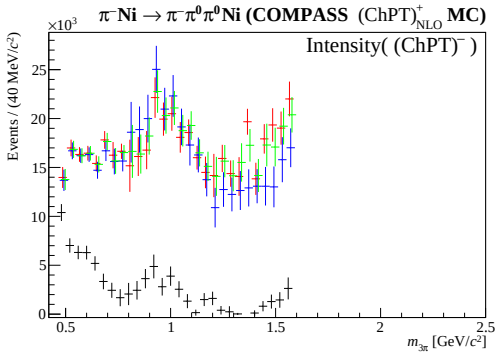

(f) Intensity($(\mathrm{ChPT})^-$)

Figure C.2: Intensities of coherent sums of waves as well as the chiral waves obtained with the extended NLO event sample. The different colors introduced in chapter 14 refer to different fit models. Please see the text for more details.

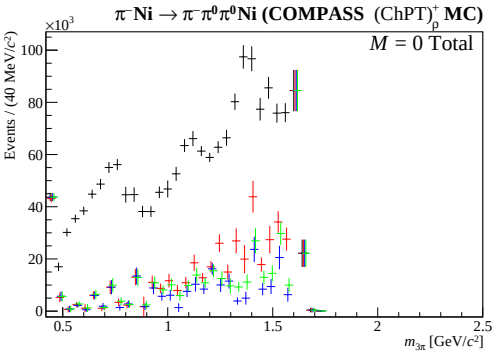

(a) $M = 0$ Total Waves Intensity

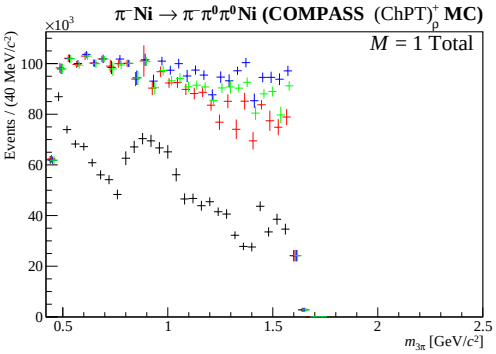

(b) $M = 1$ Total Waves Intensity

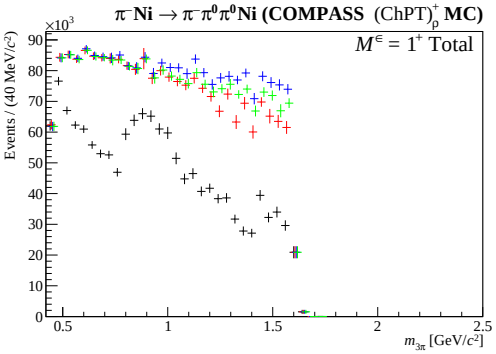

(c) $M^\epsilon = 1^+$ Total Waves Intensity

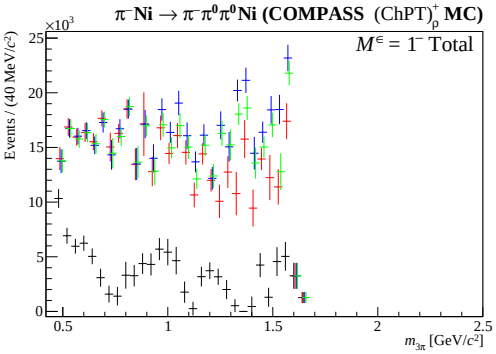

(d) $M^\epsilon = 1^-$ Total Waves Intensity

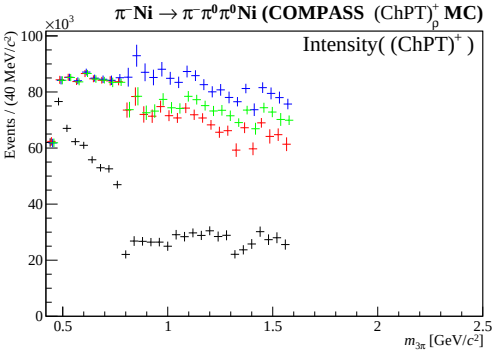

(e) Intensity($(\mathrm{ChPT})^+$)

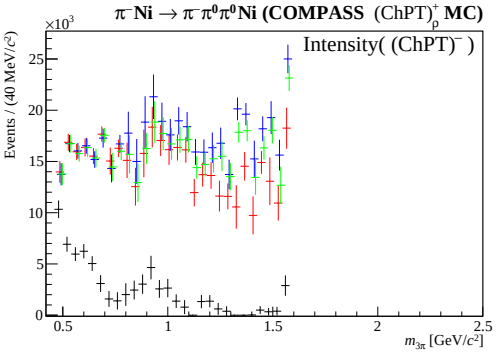

(f) Intensity($(\mathrm{ChPT})^-$)

Figure C.3: Intensities of coherent sums of waves as well as the chiral waves obtained with the extended ρ exchange event sample. The different colors introduced in chapter 14 refer to different fit models. Please see the text for more details.

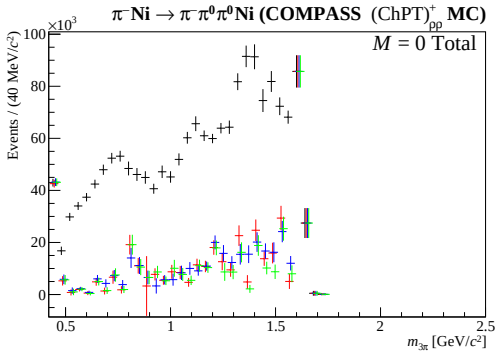

(a) $M = 0$ Total Waves Intensity

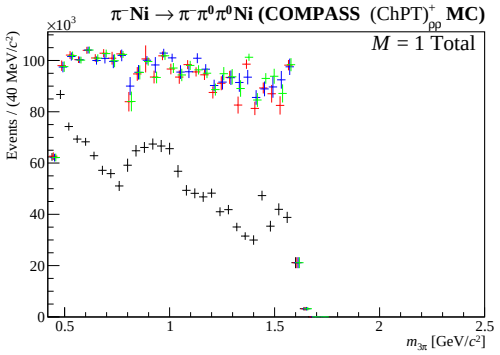

(b) $M = 1$ Total Waves Intensity

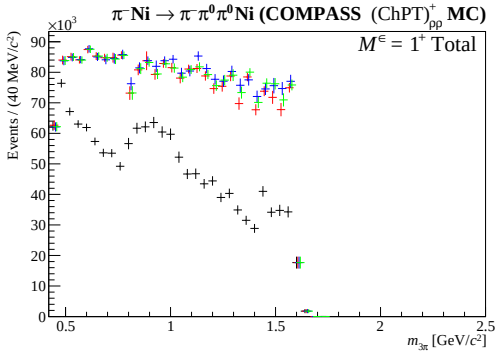

(c) $M^\epsilon = 1^+$ Total Waves Intensity

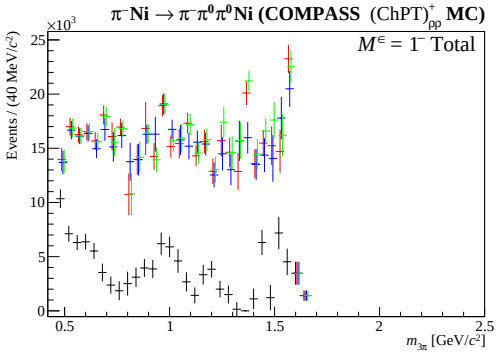

(d) $M^\epsilon = 1^-$ Total Waves Intensity

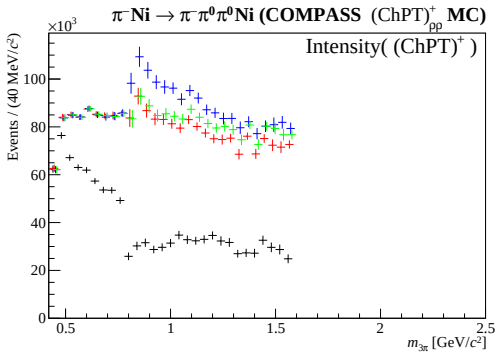

(e) Intensity($(\mathrm{ChPT})^+$)

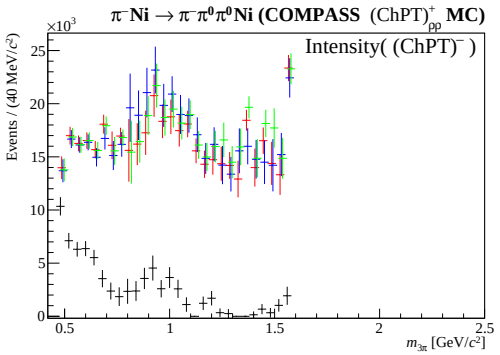

(f) Intensity($(\mathrm{ChPT})^-$)

Figure C.4: Intensities of coherent sums of waves as well as the chiral waves obtained with the extended double ρ exchange event sample. The different colors introduced in chapter 14 refer to different fit models. Please see the text for more details.

List of Figures

List of Tables

Bibliography

[AAA+07] Abbon P., Albrecht E., Alexakhin V. et al. (The COMPASS Collaboration). *The COMPASS experiment at CERN*. Nuclear Instruments and Methods in Physics Research Section A: Accelerators, Spectrometers, Detectors and Associated Equipment, 577(3):455–518, 2007. *Cited on pages 32 and 34.*

[AAA+12] Adolph C., Alekseev M. G., Alexakhin V. Y. et al. (The COMPASS Collaboration). *First Measurement of Chiral Dynamics in* $\pi^-\gamma \to \pi^-\pi^-\pi^+$. Phys. Rev. Lett., 108(19), 2012. *Cited on page 31.*

[AAA+14a] Abbon P., Adolph C., Akhunzyanov R. et al. (The COMPASS Collaboration). *COMPASS home page,* http://wwwcompass.cern.ch, 2014. *Cited on page 32.*

[AAA+14b] Adolph C., Akhunzyanov R., Alexeev M. G. et al. (The COMPASS Collaboration). *Measurement of radiative widths of* $a_2(1320)$ *and* $\pi_2(1670)$. The European Physical Journal A, 50(4), 2014. *Cited on pages 28, 29 and 173.*

[AAA+15a] Abbon P., Adolph C., Akhunzyanov R. et al. (The COMPASS Collaboration). *The COMPASS setup for physics with hadron beams*. Nuclear Instruments and Methods in Physics Research Section A: Accelerators, Spectrometers, Detectors and Associated Equipment, 779:69–115, 2015. *Cited on pages 32, 34, 41, 66 and 165.*

[AAA+15b] Adolph C., Akhunzyanov R., Alexeev M. G. et al. (The COMPASS Collaboration). *Measurement of the Charged-Pion Polarizability*. Phys. Rev. Lett., 114(6), 2015. *Cited on pages 28 and 68.*

[AAB+94] Abatzis S., Antinori F., Barberis D. et al. *Observation of a narrow scalar meson at 1450 MeV in the reaction at 450 GeV/c using the CERN Omega spectrometer*. Physics Letters B, 324(3-4):509–514, 1994. *Cited on page 19.*

[ABB95] Alexandrov Y. A., Balestra F. and Beck M. *CHEOPS: charm experiment with omni-purpose setup. Technical Report CERN-SPSLC-95-22. SPSLC-I-202*, CERN, Geneva, 1995. *Cited on page 27.*

[ABB+05] Ablikim M., Bai J., Ban Y. et al. *Resonances in $J/\Psi \to \phi\pi^+\pi^-$ and ϕK^+K^-*. Physics Letters B, 607(3-4):243–253, 2005. *Cited on page 112.*

[ABB+09] Antcheva I., Ballintijn M., Bellenot B. et al. *ROOT - A C++ framework for petabyte data storage, statistical analysis and visualization*. Comput. Phys. Commun., 180(12):2499–2512, 2009. *Cited on page 36.*

[AMP87] Au K. L., Morgan D. and Pennington M. R. *Meson dynamics beyond the quark model: Study of final-state interactions*. Phys. Rev. D, 35:1633–1664, 1987. *Cited on pages 110 and 113.*

[AO88] Aznauryan I. G. and Ogamesyan K. A. Sov. J. Nucl. Phys., 47:1097, 1988. *Cited on page 28.*

[B+12] Beringer J. et al. (The Particle Data Group). *Review of Particle Physics*. Phys. Rev. D, 86:010001, 2012. *Cited on pages 30, 66, 73, 78, 112, 132, 147, 167, 169 and 173.*

[Bar90] Barlow R. *Extended maximum likelihood*. Nuclear Instruments and Methods in Physics Research Section A: Accelerators, Spectrometers, Detectors and Associated Equipment, 297(3):496 – 506, 1990. *Cited on page 98.*

[BCK+08] Batley J., Culling A., Kalmus G. et al. *New high statistics measurement of Ke4 decay form factors and $\pi\pi$ scattering phase shifts*. The European Physical Journal C, 54(3):411–423, 2008. *Cited on page 6.*

[BCK+09] Batley J. R., Culling A. J., Kalmus G. et al. *Determination of the S-wave π π scattering lengths from a study of K $\pm\to\pi$ $\pm$ π 0 π 0 decays*. The European Physical Journal C, 64(4):589–608, 2009. *Cited on page 6.*

[BKT96] Baum G., Kyynäräinen J. and Tripet A. (The NA58 Collaboration). *COMPASS: a proposal for a common muon and proton apparatus for structure and spectroscopy*. *Technical Report CERN-SPSLC-96-14. SPSLC-P-297*, CERN, Geneva, 1996. *Cited on pages 5, 27 and 28.*

[Bow86] Bowler M. *The A1 revisited*. Physics Letters B, 182(3-4):400–404, 1986. *Cited on page 148.*

[BRo14] Brun R., Rademakers F. and other. *ROOT home page,* http://root.cern.ch, 2014. *Cited on page 36.*

[CBB+82] Cihangir S., Berg D., Biel J. et al. *Radiative width of the A2(1310)*. Physics Letters B, 117(1-2):119 – 122, 1982. *Cited on page 28.*

[CGL01] Colangelo G., Gasser J. and Leutwyler H. *$\pi\pi$ scattering*. Nuclear Physics B, 603(1-2):125–179, 2001. *Cited on page 6.*

[Chu71] Chung S. U. *SPIN FORMALISMS*. CERN Yellow Report, 1971. *Cited on page 108.*

[Chu08] Chung S. U. *Introduction to partial-wave analyses – II*. presented at TUM Workshop, March 17^{th}, 2008. *Cited on page 19.*

[Chu10] Chung S. U. *Formulas for Partial-Wave Analysis - Version V*. *Technical report*, Brookhaven National Laboratory, 2010. BNL-QGS-06-102. *Cited on pages 111 and 112.*

[DDLN02] Donnachie S., Dosch G., Landshoff P. et al. *Pomeron Physics and QCD*. Cambridge University Press, 2002. *Cited on page 19.*

[Dec64] Deck R. T. *Kinematical Interpretation of the First π - p Resonance*. Phys. Rev. Lett., 13(5):169–173, 1964. *Cited on page 22.*

[EH78] Efron B. and Hinkley D. V. *Assessing the Accuracy of the Maximum Likelihood Estimator: Observed Versus Expected Fisher Information*. Biometrika, 65(3):pp. 457–482, 1978. *Cited on page 102.*

[EU02] Ecker G. and Unterdorfer R. *Four-pion production in e^+e^- annihilation*. The European Physical Journal C - Particles and Fields, 24(4):535–545, 2002. *Cited on pages 8, 9 and 185.*

[FGM72] Fritzsch H. and Gell-Mann M. *Current algebra: Quarks and what else?*. eConf, C720906V2:135–165, 1972. *Cited on page 4.*

[FHK+09] Friedrich J., Huber S., Ketzer B. et al. *A digital calorimetric trigger for the COMPASS experiment at CERN*. In *Proceedings of "Topical Workshop on Electronics for Particle Physics (TWEPP09)"*, volume TWEPP 2009. 2009. *Cited on pages 42, 43, 45, 49 and 56.*

[FK12] Friedrich J. and Krämer M. *Reconstruction of the Pion Beam Energy from Beam Optics*, 2012. COMPASS Note 2012.2. *Cited on page 60.*

[Fla76] Flatté S. *Coupled-channel analysis of the $\pi\eta$ and $K\overline{K}$ systems near $K\overline{K}K$ threshold*. Physics Letters B, 63(2):224 – 227, 1976. *Cited on page 112.*

[Fri10] Friedrich J. *CEDAR performance in the 2009 Primakoff run*, 2010. COMPASS Note 2010.15. *Cited on pages 72 and 81.*

[Fro61] Froissart M. *Asymptotic Behavior and Subtractions in the Mandelstam Representation*. Physical Review, 123(3):1053–1057, 1961. *Cited on page 18.*

[FT09] Fäldt G. and Tengblad U. *Coulomb-nuclear interference in pion-nucleus bremsstrahlung*. Phys. Rev. C, 79:014607, 2009. *Cited on page 139.*

[Ger12] Gerassimov S. *Private communications*, 2012. *Cited on page 66.*

[GHK+10] Gautheron F., Heß C., Koivuniemi J. et al. (The COMPASS Collaboration). *COMPASS-II Proposal. Technical Report CERN-SPSC-2010-014. SPSC-P-340*, CERN, Geneva, 2010. *Cited on pages 5, 27 and 28.*

[GM56] Gell-Mann M. *The interpretation of the new particles as displaced charge multiplets*. Nuovo Cim, 4(S2):848–866, 1956. *Cited on page 4.*

[GM61] Gell-Mann M. *The Eightfold Way: A Theory of strong interaction symmetry*. 1961. *Cited on page 3.*

[GM64] Gell-Mann M. *A Schematic Model of Baryons and Mesons*. Phys.Lett., 8:214–215, 1964. *Cited on page 3.*

[Gra12] Grabmüller S. *Cryogenic Silicon Detectors and Analysis of Primakoff Contributions to the Reaction $\pi^- Pb \to \pi^-\pi^-\pi^+ Pb$*. Ph.D. thesis, Technische Universtität München, 2012. *Cited on pages 31 and 123.*

[Haa14] Haas F. *Two-dimensional partial-wave analysis of exclusive 190 GeV $\pi^- p$ scattering into the $pi^-\pi^-\pi^+$ final state at COMPASS (CERN)*. Ph.D. thesis, Technische Universtität München, 2014. *Cited on pages 15, 97 and 123.*

[HMC95] *Letter of intent: semi-inclusive muon scattering from a polarised target. Technical Report CERN-SPSLC-95-27. SPSLC-I-204*, CERN, Geneva, 1995. *Cited on page 27.*

[HQ72] von Hippel F. and Quigg C. *Centrifugal-Barrier Effects in Resonance Partial Decay Widths, Shapes, and Production Amplitudes*. Phys. Rev. D, 5:624–638, 1972. *Cited on page 111.*

[Hub10] Huber S. *Development of a Digital Trigger of Electromagnetic Calorimeter*. Master's thesis, Technische Universtität München, 2010. *Cited on pages 45, 51, 52, 53, 54 and 56.*

[IYO89] Ishida S., Yamada K. and Oda M. *Radiative decays of light-quark S- and P-wave mesons in the covariant oscillator quark model*. Physical Review D, 40(5):1497–1512, 1989. *Cited on page 28.*

[Jac62] Jackson J. D. *Classical Electrodynamics*. John Wiley & Sons Ltd., 1962. *Cited on page 23.*

[JR75] James F. and Roos M. *Minuit - a system for function minimization and analysis of the parameter errors and correlations*. Computer Physics Communications, 10(6):343–367, 1975. *Cited on page 101.*

[Kai10] Kaiser N. *Chiral corrections to $\pi^-\gamma \to 3\pi$ processes at low energies*. Nucl.Phys.A848:198-217,2010, 2010. *Cited on pages 6, 7, 8 and 9.*

[KF08] Kaiser N. and Friedrich J. *Cross-sections for low-energy $\pi\gamma$ reactions*. The European Physical Journal A, 36(2):181–188, 2008. *Cited on pages 6 and 173.*

[Krä14] Krämer M. *Measurement of radiative widths at COMPASS*. In *Proceedings of "XV International Conference on Hadron Spectroscopy"*, volume Hadron 2013. 2014. *Cited on page 28.*

[Kuh07] Kuhn R. *A Measurement of Spin Asymmetries in Quasi-Real Photo-Production of Hadrons with High Transverse Momentum at COMPASS*. Ph.D. thesis, Technische Universtität München, 2007. *Cited on page 35.*

[MAA+77] May E., Abramson J., Andrews D. et al. *Photoproduction of $\eta\pi^\pm$ resonances*. Physical Review D, 16(7):1983–1985, 1977. *Cited on page 28.*

[MAA+01] Molchanov V., Alkhazov G., Atamantchouk A. et al. *Radiative decay width of the a2(1320)-meson*. Physics Letters B, 521(3-4):171 – 180, 2001. *Cited on page 28.*

[Mar63] Martin A. *Unitarity and High-Energy Behavior of Scattering Amplitudes*. Physical Review, 129(3):1432–1436, 1963. *Cited on page 18.*

[MKA+09] Mann A. B., Konorov I., Angerer H. et al. *The universal sampling ADC readout system of the COMPASS experiment*. In *Nuclear Science Symposium Conference Record (NSS/MIC), 2009 IEEE*, pages 2225–2228. 2009. *Cited on page 43.*

[MKP07] Mann A., Konorov I. and Paul S. *A Versatile Sampling ADC System for On-Detector Applications and the AdvancedTCA Crate Standard*. In *Real-Time Conference, 2007 15th IEEE-NPSS*, pages 1–5. 2007. *Cited on page 42.*

[MYO+13] Maeda T., Yamada K., Oda M. et al. *Radiative $\pi^\pm\gamma$ transitions of excited light-quark mesons in the covariant oscillator quark model*. arXiv:1310.7507, 2013. *Cited on page 28.*

[Nag05] Nagel T. *Cinderella: an Online Filter for the COMPASS experiment*. Master's thesis, Technische Universtität München, 2005. *Cited on page 36.*

[Nag12] Nagel T. *Measurement of the Charged Pion Polarizability at COMPASS*. Ph.D. thesis, Technische Universtität München, 2012. *Cited on pages 66 and 69.*

[NN53] Nakano T. and Nishijima K. *Charge Independence for V-particles*. Progress of Theoretical Physics, 10(5):581–582, 1953. *Cited on page 4.*

[PAA+03] Pislak S., Appel R., Atoyan G. S. et al. *High statistics measurement of K_{e4} decay properties*. Phys. Rev. D, 67:072004, 2003. *Cited on page 6.*

[Pau96] Paul S. *The CHEOPS project*. Nuclear Physics B - Proceedings Supplements, 50(1-3):272–279, 1996. *Cited on page 27.*

[Per74] Perl M. *High energy hadron physics*. Wiley, Mew York, 1974. *Cited on page 21.*

[PS61] Pomeranchuk I. and Shumushkevich I. *On processes in the interaction of γ-quanta with unstable particles*. Nuclear Physics, 23:452–467, 1961. *Cited on page 23.*

[Reg59] Regge T. Il Nuovo Cimento, 14(5):951–976, 1959. *Cited on page 17.*

[Ros75] Rose M. E. *Elementary theory of angular momentum*. Wiley, Mew York, 1975. *Cited on page 108.*

[Ros81] Rosner J. *Decays of $L = 1$ mesons to $\gamma\pi$, $\gamma\rho$, and $\gamma\gamma$*. Physical Review D, 23(5):1127–1133, 1981. *Cited on page 28.*

[Rut11] Rutherford E. *The scattering of α ans β particles by matter and the structure of the atom*. Philosophical Magazine Series 6, 21(125):669 – 688, 1911. *Cited on page 3.*

[Rut20] Rutherford E. *Bakerian Lecture. Nuclear Constitution of Atoms*. Proceedings of the Royal Society of London, A97(686):374 – 400, 1920. *Cited on page 3.*

[Sch12] Schlüter T. *The $\pi^-\eta$ and $\pi^-\eta'$ system in exclusive 190 GeV π^-p reactions at COMPASS (CERN)*. Ph.D. thesis, Ludwig-Maximilians-Universität München, 2012. *Cited on page 114.*

[Wei34] v. Weizsäcker C. F. *Ausstrahlung bei Stößen sehr schneller Elektronen*. Z. Physik, 88(9-10):612–625, 1934. *Cited on page 22.*

[Wil33] Williams E. J. *Applications of the Method of Impact Parameter in Collisions*. Proceedings of the Royal Society of London A: Mathematical, Physical and Engineering Sciences, 139(837):163–186, 1933. *Cited on page 22.*

[Yuk35] Yukawa H. *On the Interaction of Elementary Particles*. Proc.Phys.Math.Soc.Jap., 17(48), 1935. *Cited on page 3.*

[Zwe64] Zweig G. *An SU(3) model for strong interaction symmetry and its breaking. Version 2*. pages 22–101, 1964. *Cited on page 3.*

Own Contribution

In order to match the requirements of the Primakoff measurement at COMPASS in 2009 a completely new trigger setup was developed under the supervision of Igor Konorov. As part of my work I optimized and evaluated the trigger scheme and algorithms for the calorimetric trigger setup. In preparation of the measurement I developed all parts of the software, which is necessary to operate and monitor the trigger. This includes but is not limited to the extension of the COMPASS online filter Cinderella and the ConfigServer, which is used for programming and controlling the trigger. During the Primakoff data taking in 2009 I was involved in all aspects of the commissioning and operation of the trigger, which is also true for a second Primakoff measurement in 2012. For this measurement I again got involved in the development and maintenance of necessary software components.

In the course of the production of the recorded data, I was involved in the revision and extension of the reconstruction software, CORAL. The work focused on the improvement of the performance of the calorimeters. Among the modification of the software, was the introduction of new calibrations, which rely on the knowledge of the mass of the neutral pion, so called π^0 calibrations. At that part I contributed to the determination of these calibrations.

In order to determine the relations of the energy of individual beam particles on the parameters of their trajectory, I developed a interface to the multilayer perceptron implementation of root. Based on a sample of exclusive $\pi^-\pi^-\pi^+$ events, which was provided by Jan Friedrich, I determined a suitable network topology and trained the neural network. I provided the outcome to the COMPASS collaboration, where it is used in several other analysis.

I developed a event selection fro exclusive $\pi^-\pi^0\pi^0$ events, which is presented here. Last but not least I carried out the analysis presented in this thesis, which lead to the measurement of the differential cross section of $\pi^-\gamma \to \pi^-\pi^0\pi^0$. The analysis was supervised by Stefan Paul and Jan Friedrich. The partial-wave decomposition has been carried out in close collaboration with Dima Ryabchikov, who maintains and develop the employed amplitude analysis framework. I adapted the software to the requirements of the analysis and added several features, which are unique to the presented analysis. I also added to the general improvements of the software.

The results of the partial-wave analysis were presented to the COMPASS collaboration, which agreed to release the results and present them to the public. The results have been shown at national and international conferences.

Acknowledgment

Above all I want to thank Prof. Stephan Paul for giving me the chance to work on this thesis. I greatly appreciate, that I had the freedom to pursue my own ideas under his supervision. He lead his chair to be a place of creative and fruitful work.
I would also like to thank Igor Konorov, who lead the development of the digital trigger, and Jan Friedrich, who supervised the analysis, for their guidance and numerous interesting discussion.
I am grateful to Dima Ryabchikov for introducing me into the art of amplitude analysis and with whom I worked in close collaboration on the partial-wave analysis. He maintains and develops the analysis framework, which was used for the amplitude analysis.
Thanks also to Stefan Huber, who worked on the digital trigger as an Diploma student and on who's work I partly rely on.
Let me also thank the COMPASS colleagues, who contributed to the experiment. In particular I want thank my Munich colleagues Alexander Austregesilo, Shu Urk Chung, Florian Haas, Stefanie Grabmüller, Boris Grube, Bernhard Ketzer, Alexander Mann, Thiemo Nagel, Sebastian Neubert and Sebastian Uhl for the valuable and free exchange of thoughts having many interesting discussions. Special thanks thereby go to Sergei Gerasimov, Thiemo Nagel and Sebastian Uhl, who worked with me on the improvement of the calorimeter reconstruction and its calibration.
I would like to thank Prof. Dr. Norbert Kaiser. He provided the parametrization of the chiral waves and helped me with many explanation and discussions on this topic.
I am grateful to Alexander Austregesilo and Jan Friedrich for proof-reading large parts of my thesis.
I would like to thank Karin Frank, who is the administrative backbone of the group.
Last but not least I want to thank my family and friends for their constant support and love. In particular I want to thank my parents, Ines and Ulla.